Collective Excitations in Bose-Einstein Condensates

im Fachbereich Physik der

Freien Universität Berlin

eingereichte Dissertation

von

Hamid Jabber Haziran Al-Jibbouri

September 2013

Die in vorliegender Dissertation dargestellte Arbeit wurde in der Zeit zwischen Oktober 2009 und September 2013 im Fachbereich Physik an der Freien Universität Berlin unter Betreuung von Priv.-Doz. Dr. Axel Pelster durchgeführt.

Erstgutachter: Priv.-Doz. Dr. Axel Pelster

Zweitgutachter: Prof. Dr. Jürgen Bosse

Tag der Disputation: 23. September 2013

Abstract

The experimental discovery of dilute ultracold quantum gases in 1995 has instigated a broad interest in ultracold atoms and molecules, and paved the way for extensive studies of a wide range of both experimental and theoretical topics. Various theories were developed to describe Bose-Einstein condensates (BECs) for different ranges of temperature and interaction strengths. This thesis focuses on studying the mean-field theory of the Gross-Pitaevskii (GP) equation which provides a good description for the macroscopic wave function when both quantum and thermal fluctuations are negligible. This means that the range of validity is restricted to small interaction strengths at zero temperature. Within the GP theory we study analytically and numerically the nonlinear dynamics of BECs which are induced by a harmonic modulation of either the interaction strength or the harmonic trapping potential. At first a detailed numerical investigation reveals that solving the partial differential equation of Gross and Pitaevskii can be reduced to solving ordinary differential equations for the condensate widths within a Gaussian variational approach. Despite this tremendous simplification the prominent nonlinearity of the underlying GP equation is inherited by the variational equations, which thus allow to describe a rich variety of nonlinear phenomena in different experimental setups. In order to describe them analytically we transfer the Poincaré-Lindstedt method, which represents a well-established tool in the field of nonlinear dynamics, to the Gaussian variational approach.

Modulation of some of the parameters of a BEC can give rise to prominent nonlinear features, such as shifts in the frequencies of collective oscillation modes, higher harmonics generation, and resonant mode coupling. As a first application we consider a recent Bose-Einstein condensate of ^{7}Li, which has been excited experimentally by a harmonic modulation of the atomic s-wave scattering length with the help of a Feshbach resonance. Combining an analytical perturbative approach with extensive numerical simulations, we analyze the emerging nonlinear dynamics. In particular, we present the resulting shift of collective excitation spectra close to parametric resonances where the driving frequency coincides with a collective mode frequency. Another application of experimental importance is to study geometric resonances in BECs with two-body and three-body contact interactions, where changing the geometry of the trapping potential leads to commensurate collective excitation frequencies with emerging nonlinear effects such as frequency shifts and resonant mode coupling. In this context we also show that a small repulsive three-body interaction is able to extend the stability region of the condensate for an attractive two-body interaction as it increases the critical number of atoms in the trap.

Apart from a periodic modulation of a system parameter the dipole mode frequency can be excited by introducing an abrupt change in the potential, where the center of mass oscillates according to the Kohn theorem back and forth in the trapping potential with the natural trap frequency irrespective of both the strength and the type of the two-particle interaction. To this end, we study the collective excitation modes of a Bose-Einstein condensate in a harmonic Ioffe-Pritchard in the vicinity of a Feshbach resonance for experimentally realistic parameters of a ^{85}Rb BEC, where the dipole mode is excited in z-direction. A linearization of the underlying equations of motions shows that the dipole mode frequency decreases when the bias magnetic field approaches the Feshbach resonance, so the Kohn theorem is violated.

Finally within a variational approach we discuss the physical properties of a BEC in an axially-symmetric harmonic trap with a single vortex in the center. At first we analyze the equilibrium configuration and determine the vortex size as well as the Thomas-Fermi radii of the condensate in the Thomas-Fermi limit. Then we calculate the critical rotation frequency for the emergence of the vortex and compare our findings with the literature. Finally, we investigate how the presence of the vortex changes the collective excitation frequencies and we discuss the free expansion of the BEC. All these results indicate how nonlinear dynamics properties could be made clearly observable in future experiments on the basis of our results.

Zusammenfassung

Die experimentelle Entdeckung verdünnter ultrakalter Quantengase im Jahre 1995 hat ein breites Interesse an ultrakalten Atomen und Molekülen hervorgerufen und den Weg zu intensiven weitreichenden Untersuchungen sowohl experimenteller als auch theoretischer Themen bereitet. Verschiedene Theorien wurden entwickelt, um Bose-Einstein-Kondensate (BECs) in verschiedenen Temperaturbereichen und mit unterschiedlichen Wechselwirkungsstärken zu beschreiben. Die vorliegende Doktorarbeit konzentriert sich auf die Gross-Pitaevskii (GP) Molekularfeldtheorie, die eine gute Beschreibung der makroskopischen Wellenfunktion darstellt, wenn sowohl quantenmechanische als auch thermische Fluktuationen vernachlässigbar sind. Das bedeutet, dass der Gültigkeitsbereich auf kleine Wechselwirkungsstärken am absoluten Temperaturnullpunkt beschränkt ist. Innerhalb der GP-Theorie studieren wir analytisch und numerisch die nichtlineare Dynamik von BECs, die durch eine harmonische Modulation von entweder der Wechselwirkungsstärke oder des harmonischen Fallenpotentials hervorgerufen wird. Zunächst zeigt eine detaillierte numerische Untersuchung, dass das Lösen der partiellen Differentialgleichung von Gross und Pitaevskii auf das Lösen von gewöhnlichen Differentialgleichungen für die Kondensatbreiten innerhalb eines Gaußschen Variationsansatzes zurückgeführt werden kann. Trotz der erheblichen Vereinfachung wird die Nichtlinearität der zugrundeliegenden GP-Gleichung auf die Variationsgleichungen übertragen, so dass eine Beschreibung der reichhaltigen nichtlinearen Phänomene in verschiedenen experimentellen Aufbauten möglich ist. Um diese analytisch zu beschreiben, übertragen wir die Poincaré-Lindstedt-Methode, die ein etabliertes Werkzeug im Gebiet der nichtlinearen Dynamik darstellt, auf den Gaußschen Variationszugang.

Die Modulation eines Parameters im BEC kann zu bedeutenden nichtlinearen Eigenschaften führen, wie z.B. Verschiebungen in den Frequenzen kollektiver Moden, Erzeugung höherer Harmonischer und resonate Modenkopplung. Als eine erste Anwendung betrachten wir ein neues Experiment mit einem ^{7}Li Bose-Einstein-Kondensat, das durch eine harmonische Modulation der s-Wellenstreulänge mit Hilfe einer Feshbach Resonanz angeregt wurde. Durch Kombination eines analytischen störungstheoretischen Zuganges mit aufwändigen numerische Simulationen analysieren wir die sich ausbildende nichtlineare Dynamik. Insbesondere untersuchen wir die resultierende Verschiebung der kollektiven Anregunsspektren in der Nähe einer parametrischen Resonanz, wo die antreibende Frequenz mit einer kollektiven Modenfrequenz zusammenfällt. Eine andere Anwendung von experimenteller Bedeutung besteht darin, geometrische Resonanzen in BECs mit Zwei- und Drei-Teilchen-Wechselwirkungen zu studieren, wo eine Veränderung der Geometrie des Fallenpotentials zu kommensurablen kollektiven Anregungsfrequenzen mit emergenten nichtlinearen Efekten wie Frequenzverschiedungen und resonanter Modenkopplung führt. In diesem Zusammenhang zeigen wir auch, dass eine kleine repulsive Drei-Teilchchen-Wechselwirkung die Stabilitätsregion eines Kondensates mit einer attraktiven Zwei-Teilchen-Wechselwirkung vergrößern kann, da dies die kritische Atomzahl in der Falle erhöht.

Abgesehen von einer periodischen Modulation eines Systemparameters kann die Dipolmodenfrequenz auch dadurch angeregt werden, dass man eine plötzliche Änderung des Potential bewirkt, so dass der Schwerpunkt gemäß des Kohn-Theorems im Fallenpotential unabhängig von der Stärke und von dem Typ der Zwei-Teilchen-Wechselwirkung mit der natürlichen Fallenfrequenz hin- und heroszilliert. Hierzu studieren wir die kollektiven Anregungsmoden eines Bose-Einstein-Kondensates in einer harmonischen Ioffe-Pritchard-Falle in der Umgebung einer Feshbach-Resonanz für experimentell realistische Parameter eines ^{85}Rb BECs, wo die Dipolmode in z-Richtung angeregt ist. Eine Linearisierung der zugrunde liegenden Bewegungsgleichungen zeigt, dass die Dipolmodenfrequenz kleiner wird, wenn das Magnetfeld die Feshbach-Resonanz erreicht, so dass das Kohn-Theorem verletzt wird.

Schließlich diskutieren wir innerhalb eines Variationszuganges die physikalischen Eigenschaften eines BECs in einer axialsymmetrischen harmonischen Falle mit einem einzelnen Vortex im Zentrum. Zunächst untersuchen wir die Gleichgewichtskonfiguration und bestimmen sowohl die Vortex-Größe als

auch die Thomas-Fermi-Radien des Kondensates im Thomas-Fermi-Limes. Dann berechnen wir die kritische Rotationsfrequenz für die Emergenz eines Vortex und vergleichen unsere Ergebnisse mit der Literatur. Schließlich untersuchen wir, wie die Anwesenheit eines Vortex die kollektiven Anregungsfrequenzen verändert und wir diskutieren die freie Expansion eines BECs. All diese Resultate zeigen, wie nichtlineare dynamische Eigenschaften auf der Grundlage unserer Resultate in künftigen Experimenten beobachtet werden können.

Contents

1. Introduction

1.1. Bose-Einstein Condensates

A Bose-Einstein condensate (BEC) is a particular state of matter of a system of bosons confined in an external potential. The atoms are cooled to temperatures very near to absolute zero. Under this condition, a large fraction of the bosons occupy the lowest energy level, which is when the bosons are reduced to a state of zero velocity.

This new state of matter was first predicted in 1924 by an Indian physicist and mathematician called Satayendra N. Bose who rederived that the thermal distribution of photons is not a Maxwell-Boltzmann but a Planck distribution [1]. Albert Einstein extended this work to a system of non-interacting massive Bose particles and presented the basic idea of a BEC in 1925 [2]. He realized that a large fraction of particles occupies the state of lowest energy at low temperature.

Immediately after the discovery of superfluidity in liquid helium in 1938 [3,4], F. London suggested the first approaches for realizing a BEC by using superfluid liquid ^{4}He [5,6]. However, interactions between particles in superfluid ^{4}He are stronger than an ideal gas system which was studied by A. Einstein [2]. Therefore, the connection between the two concepts of BEC and superfluidity was not straightforward. Theoretical and experimental results show that the fraction of condensed particles in superfluid liquid ^{4}He is less than about 7% at zero temperature [7–9]. The first microscopic theory of interacting Bose gases in the realm of BEC was formulated in 1947 by N.N. Bogoliubov [10]. He introduced quantum corrections on top of a mean-field theory in order to account for atom-atom interactions in the trapped gas.

The phenomenological theory of superfluidity in terms of the excitation spectrum of ^{4}He liquid was developed by L.D. Landau [11], which was later supported by the experimental confirmation for the postulated excitation spectrum [12]. The concept of the off-diagonal long-range order is one of the interesting effects which connect BEC and superfluidity. The subject has been extensively studied by many theorists, including Landau and Lifshitz [13], Penrose [14], and Penrose and Onsager [7]. Another important aspect of BEC and superfluidity is the occurrence of quantized vortices which were predicted by Onsager [15] and Feynman [16], and which were first observed in superfluid ^{4}He [17,18] and more recently in atomic BEC [19].

The first Bose-Einstein condensate of dilute atomic ^{87}Rb was produced by the JILA group led by E. Cornell and C. Wieman [20,21]. Two experimental achievements were reported in the same year by the Ketterle group in MIT for ^{23}Na [22] and the Hulet group in Rice University for ^{7}Li [23,24]. This was made possible by advancements in atom cooling and trapping techniques [25–27], that allowed experimentalists to cool dilute gases of neutral atoms down to extremely low temperatures. An atomic Hydrogen condensate was finally produced in the year 1998 [28]. There are two cooling techniques to create the dilute atomic BEC in laboratory by combining laser cooling and evaporative cooling [20,22]. The first cooling technique relies on trapping the atoms due to a Zeeman shift [20] in a magneto-optical trap and cooling them to about 10 μK. Afterwards, they are bombarded by photons of counter-propagating laser beams in all three spatial directions. The second cooling technique is performed by removing the high-energy tail of the thermal distribution from the trap, thus lowering the temperature below 1 μK [22].

In these experimental realizations of BECs the atoms were confined in magnetic traps and cooled

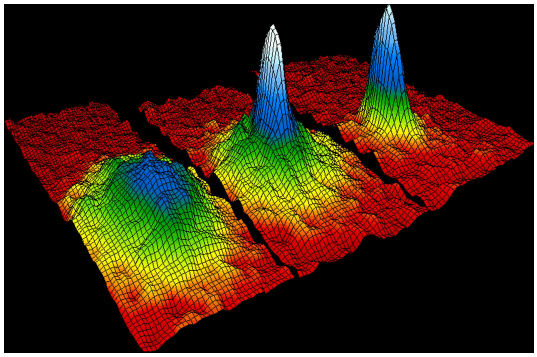

Figure 1.1.: Velocity distribution taken from JILA BEC Homepage [29]. The respective temperature is established by fitting two Gauss functions to the data, one for the thermal background and one for the condensate.

down to extremely low temperatures which are of the order of fractions of 10^{-6} kelvins. The first argument for condensation emerged from time-of-flight measurements, where the atoms were left to expand by switching off the confining trap and then they were imaged with optical methods. To this end a large peak in the velocity distribution was observed below a critical temperature, providing a clear signature for BEC. For their achievements Cornell, Wieman, and Ketterle were awarded the Nobel Prize in Physics in 2001. Figure 1.1 shows a velocity distribution at three different temperatures within the formation of a Rb BEC atoms, where the critical temperature T_c is of the order 1 μK. The colors in Fig. 1.1 show the number of atoms at various velocities, with red and white corresponding to the fewest and the greatest number, respectively. The left-hand figure shows a classical Maxwell-Boltzmann distribution at a temperature which is larger than the critical temperature, thus most of the atoms still have a finite velocity. The middle image indicates the emergence of a peak which describes that some of the atoms have reached a state of zero velocity and occupy the ground state. However, this image also shows that some atoms remain with non-zero velocities. Finally, the right-hand figure, taken at a temperature much below T_c, shows that a large fraction of the atoms now occupy the ground state and have zero velocity.

To date, dilute BEC's have been created with Rubidium [20], Sodium [22], Lithium [23], spin-polarized Hydrogen [28], metastable Helium [30], Potassium [31], Cesium [32], Ytterbium [33], Calcium [34], and Strontium [35,36]. In addition, other elements of special interest due to their large magnetic dipole-dipole interaction have also been condensed, such as Chromium [37], Dysprosium [38], and more recently Erbium [39].

Atomic systems present a high degree of control of both the external confinement and the strength of interactions between the constituents. The latter has become possible as the interaction strength between particles can be tuned by using Feshbach resonances [40–42] which allow control of the strength of s-wave and even higher order scattering between atoms through external fields. Theoretical predictions of the properties of a BEC such as the density profile [43], collective excitations [44] and the formation of vortices [45] can now be compared with experimental data [19,20,46] by adjusting some tunable external parameters, such as the trap frequencies. Needless to say, this dramatic progress on the experimental front has stimulated a corresponding wave of activity on both the theoretical and the numerical front.

From a theoretical point of view, and for a wide range of experimentally relevant conditions, the dynamics of a BEC can be well described by means of an effective mean-field theory. This approach is much simpler than dealing with the underlying full many-body theory and can describe quite accurately the static and dynamical properties of BECs. The relevant model is a classical nonlinear

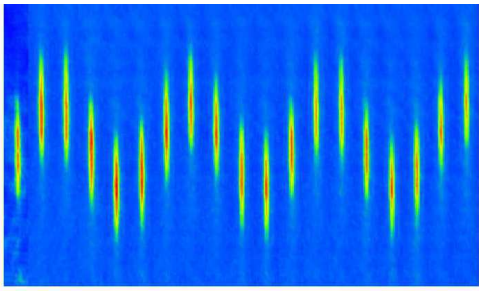

Figure 1.2.: An experimental measurement of the collective BEC modes, a figure taken from MIT BEC Homepage [68]. The time evolution of a BEC cloud is presented by a series of density profiles. Shape oscillations are coupled with the center of mass motion. The field of view in the vertical direction is about 200 μm and the time step is 10 ms per frame.

evolution equation, the so-called Gross-Pitaevskii (GP) equation [47–50]. In fact, this is a variant of the famous nonlinear Schrödinger (NLS) equation [51,52], which is a universal model describing the evolution of complex field envelopes in nonlinear dispersive media. In case of BECs, the nonlinearity is introduced by the interatomic interactions in the GP model and is accounted for through an effective mean-field. The results obtained by solving the GP equation show excellent agreement with most of the experiments. The GP equation is not generally applicable at finite temperatures; nonetheless, Ref. [53] has demonstrated a procedure in which this form may be used to represent the effect of thermal atoms within a mean-field approach [54–57]. GP also fails for quantum fluctuations [58–60].

1.2. Collective Excitations

Bose-Einstein condensation (BEC) in a dilute atomic vapor [20–24,61–63] has pathed the way for numerous experimental and theoretical works to study and understand ultracold quantum gases which can be regarded as a new state of matter. In particular, many experiments have focused on investigating collective excitations of harmonically trapped Bose-Einstein condensates BECs, as they can be measured very accurately on the order of less than 1% and thus provide a reliable method for extracting the respective system parameters of such ultracold quantum gas systems [64].

The experiments started with the condensate at very low temperature, where the thermal cloud of the condensate is not present, and the collective oscillation modes were induced by a modulation of the external trapping potential [46,64–67]. The collective modes were excited by applying a small time-dependent perturbation of a given frequency to the transversal component of the trap potential and the resulting real-time dynamics in terms of shape oscillations of the condensate was observed in Ref. [46]. Based on these measurements, two low-lying eigenmodes of different symmetry were identified. The same procedure was repeated at higher temperatures, when the condensate is not present, and, as expected, the thermal cloud has produced only a response corresponding to the excitations of a normal Bose gas. The condensate was also excited by a time-dependent modulation of the trapping potential experimentally, which additionally included a spatial displacement of the potential minimum [65]. In this case, shape oscillations coupled with the center of mass motion were observed. A typical experimental observation is given in Fig. 1.2.

The agreement between measured frequencies [46,65,69] and theoretical predictions [44,70–73] is one of the first important achievements in the investigation of these new systems. At the mean-field level, they can be successfully described by the time-dependent Gross-Piteavskii equation for the macroscopic wave function of a BEC at zero temperature [47–50].

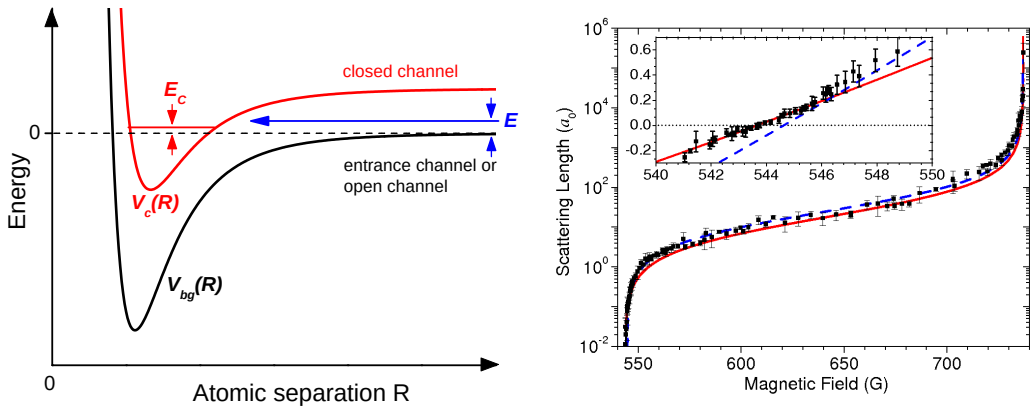

(a) (b)

Figure 1.3.: (a) Basic two-channel model for a Feshbach resonance. The phenomenon occurs when two atoms colliding at energy E in the entrance channel resonantly couple to a molecular bound state with energy E_c supported by the closed channel potential. In the ultracold domain, collisions take place near zero-energy, i.e. for $E \to 0$. Resonant coupling is then conveniently realized by magnetically tuning E_c near 0, if the magnetic moments of the closed and open channel differ. (b) Feshbach resonance of a ^{7}Li BEC: Dependence of the scattering length on the external magnetic field. Results are taken from Ref. [87].

The Gross-Piteavskii equation can be solved numerically. There has been a series of studies which deal with the numerical solution of the time-independent GP equation for the equilibrium shape of the condensate and the time-dependent GP equation for finding the dynamics of a BEC. In order to obtain a numerical solution of the time-dependent GP equation the Refs. [73–76] presented a time-splitting spectral method. Refs. [77–80] used the Crank-Nicolson finite difference method to compute the ground-state solution and the dynamics of the GP equation. For the ground-state solution of GP equation Refs. [71,81,82] presented a Runge-Kutta type method and used it to solve in 1D and in 3D with spherical symmetry, whereas Ref. [83] presented a general method to compute the ground-state solution via directly minimizing the energy functional. In particular, it can be solved variationally by assuming a Gaussian ansatz for the wave function [84,85]. The collective oscillation modes have been studied extensively due to the perfect control of atomic interactions using a Feshbach resonance. The Feshbach resonance is an important tool to experimentally investigate cold atomic gases. It allows to tune the scattering length to values much larger than the mean interatomic distance and even to change its sign by modifying the external magnetic field [86]. This resonance occurs when the energy associated with an elastic scattering process comes close to the energy of a bound state, see Fig. 1.3(a). This phenomenon was first investigated in the context of reactions forming compound nuclei [88] and later on, independently, for a description of configuration interactions in multielectron atoms [89]. In the context of cold atomic physics the Feshbach resonance was first used for bosonic systems [40,41]. Due to non-elastic processes the tuning of interaction strength is limited to the case of repulsive interactions [90]. In the case of fermions, due to the Pauli principle, three-body losses are suppressed and this causes a greater stability of the gas [91].

R. Hulet's group from the Rice University [87], demonstrated for a BEC of ^{7}Li an extreme tunability of interactions in the vicinity of a broad Feshbach resonance. In the mentioned experiment, atoms were trapped by the optical trap, while the bias magnetic field was used for tuning the scattering length via the Feshbach resonance. For the accessible range of values of magnetic field B, a ground-state condensate was produced and the corresponding density profiles were observed. By measuring the width of the condensate distribution and comparing these values with the corresponding numerical data

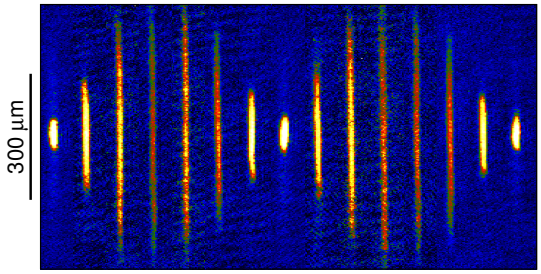

Figure 1.4.: Quadrupole oscillations of the BEC cloud, presented by a series of density profiles taken at equidistant time steps of 15 ms. Results are taken from Ref. [93].

based on the GP equation, information on the scattering length spanning seven orders of magnitude was extracted, as can be seen in Fig. 1.3(b). The Feshbach resonance can be described by an effective pseudopotential between atoms of the open channel with the scattering length:

$$a_s(B) = a_{\mathrm{BG}}\left(1 - \frac{\Delta}{B - B_{\mathrm{res}}}\right). \tag{1.1}$$

In this way, the following values of the parameters of the Feshbach resonance were obtained precisely: The background value amounts to $a_{\mathrm{BG}} = -24.5a_0$, where a_0 represents the Bohr radius the width is given by $\Delta = -192.3(3)$G and the resonance occurs at $B_{\mathrm{res}} = 736.8(2)$G.

In a recent experiment led by V. S. Bagnato and R. G. Hulet a quadrupole mode of a ^{7}Li condensate was excited by modulating the scattering length [92,93] through a broad Feschbach resonance [87] according to

$$a_s(t) = a_{\mathrm{av}} + \delta a \cos(\Omega t). \tag{1.2}$$

Here $a_{\mathrm{av}} \approx 3a_0$ represents the background s-wave scattering length, $\delta a \approx 2a_0$ the driving amplitude, and Ω the driving frequency. In Fig. 1.4, a quadrupole oscillation of the cloud is clearly observable [93]. The large oscillation amplitudes considered here extend over approximately 1 mm of the optical trap. A harmonic approximation of the trapping potential about the trap center is less than 10 % in error over this range. The cloud size in Fig. 1.4 as a function of time is modeled well by a variational calculation, which is consistent with negligible anharmonic contributions. Furthermore, no damping of the quadrupole mode was observed over many oscillation periods, which is consistent with a negligible thermal fraction.

Several recent experiments [94,95] have studied creation and interaction of solitons in the atomic BEC. Another subject of wide interest is the formation of Faraday patterns in a driven system [96–99]. An observation of this type of dynamics in a BEC was given in Ref. [100], where a density wave in the axial direction was produced by a strong modulation of the strength of the radial trapping potential. A further experimental research includes even a study of the quantum turbulent regime in a BEC [101] by a combination of rotation, strong modulation of trap strength and trap displacement. In essence, quantum turbulence is a superfluid turbulence characterized by the presence of tangled vortices. It was initially studied in superfluid Helium, but now it can be studied in a more controlled way in a BEC setup, as shown in Ref. [101].

In order to be able to keep up with the experimental advances, new theoretical approaches for the description of collective modes of a trapped system were developed. In the mean-field framework, a linearization of the GP equation around the ground-state was studied [102]. The collective oscillation modes can be induced in a BEC by modulating the external potential trap [46,65,103–107]. Alternatively, this can also be allowed by a modulation of the s-wave scattering length [87,93,108–111] or the strength of three-body interactions [108]. In the Thomas-Fermi (TF) limit, Stringari [70] has

analytically calculated frequencies of the collective modes, while Edwards et al. [44] extended these calculations via a numerical solution of the GP equation. Due to the inherent nonlinearity in this equation of motion, a wide variety of interesting phenomena are observed in collective excitations of BECs, including frequency shifts [105,109,112,113], mode coupling [105,112–115], damping [64,116] as well as collapse and revival of oscillations [105,117,118].

BEC systems are highly nonlinear and, therefore, a resonant coupling between collective modes is expected. It was experimentally observed [114,115] that, when the parity quadrupole mode is excited by changing the trap anisotropy parameter above a certain value, it is possible to achieve an energy transfer between modes at a rate which is comparable to the collective mode frequency. In Ref. [105], the frequency shift of collective modes was analytically studied due to the change of the trap anisotropy in a generic axially-symmetric geometry using the hydrodynamic equations in the Thomas-Fermi approximation [70]. When the frequencies of two collective modes are tuned to be commensurate by varying the trap anisotropy, which are called geometric resonances, strong nonlinear effects can be observed even for oscillations of relatively small amplitude. In Ref. [119], the authors studied the dynamics of large amplitude collective mode oscillations, frequency shifts and mode couplings for the case of a superfluid Fermi gas in the transition from a BCS superfluid to a BEC based on a superfluid hydrodynamic approach. The coupling rates between various modes were calculated analytically in Ref. [115], and it was shown that the coupling can be well described by a simple Hamiltonian, enabling quantitative studies of the squeezing effects which are related to harmonic-generation processes. The excitations of quadrupole and scissor modes in two-component BECs with a particular emphasis on the nonlinear dynamics due to the mode coupling between these modes were investigated in Ref. [120]. Recently, also a coupling of the dipole mode with the breathing and quadrupole mode was analyzed in the immediate vicinity of a Feshbach resonance [121,122].

1.3. Three-Body Interaction

It is well known that the majority of theoretical studies of collective excitations of a BEC is mainly focused on considering the two-body contact interaction due to the diluteness of the quantum gas [69,93,105,109,114,115,123]. On the other hand, in view of the experimental progress with BECs in atomic waveguides and on the surface of atomic chips, which involve a strong compression of the traps, a significant increase of the density of BECs can be achieved, thus also three-body interactions may play an important role [124–126]. Theoretical and experimental studies [124,127,128] for a BEC of ^{87}Rb atoms indicated that the real part of the three-body interaction term can be $10^3 - 10^4$ times larger than the imaginary part. The imaginary part, which arises from three-body recombinations, limits the lifetime of the condensate. However, even for a small strength of the three-body interaction, the region of stability for the condensate can be extended considerably according to Ref. [129]. Due to the three-body interaction, the density profile of the condensate changes [130] and, correspondingly, also the excitation spectrum of the collective oscillations is modified [131,132]. The modulation instability of a trapped BEC immersed in a highly elongated harmonic trap with two- and three-body interactions was studied both analytically and numerically [133]. The effect of the three-body interaction was furthermore studied in ultracold bosonic atoms in an optical lattice [126,134–141], in the BCS-BEC crossover [142], for complex solitons in BECs [143,144] and for a vortex in a BEC [145]. The properties of 2D Bose gases at large scattering lengths or near resonance are dictated by three-body effects in Ref. [146]. Universality in the three-body parameter in heteronuclear atomic systems have been predicted and analyzed in Ref. [147].

The collective excitations of a 1D BEC in a quadratic plus quartic trap are studied on the level of the Gross-Pitaevskii equation, and the collective excitation spectra are calculated as functions of

the two-body interaction as well as an anharmonic parameter in Ref. [148]. The collective excitations of a one-dimensional Bose-Einstein condensate trapped in an anharmonic potential were also studied in Ref. [149] by solving the time-dependent Tonks-Girardeau equation. In Ref. [150] the authors investigated the collective excitations of a 1D BEC with two- and three-body interactions in a harmonic trap with an anharmonic distortion up to a quintic term, by mainly focusing on the effect of the three-body interaction on the excitations by a variational analysis of the GP equation. The transition temperature, the depletion of the condensate atoms, and the collective excitations of a BEC with two- and three-body interactions in an anharmonic trap at finite temperature are studied in Ref. [151]. Reference [152] shows that the frequency of the collective excitation is also significantly affected by the strength of the three-body interaction and the anharmonicity of the potential. In Ref. [153] the authors investigated the collective excitations and the stability of a BEC in a one-dimensional trapping geometry for the case of a repulsive or attractive three-body interaction together with a repulsive two-body interactions by a standard variational approach.

An attractive two-body interaction has a profound effect on the stability of a BEC, since a large enough attractive interaction will cause the BEC to become unstable and collapse [63,154–157]. In Refs. [85,158–160] it was shown within the Gross-Pitaevskii formalism, that the critical particle number for a BEC in cylindrical traps can be obtained numerically. In Ref. [161] the GP equation for a system composed of attractive bosons confined in a harmonic trap was analyzed via a controlled perturbation theory. In this way it was shown that the critical particle number strongly depends on the anisotropy of the trap. In Ref. [162], an analytical solution of the Gross-Pitaevskii equation for a BEC with negative effective interaction strength was considered in a cylinder-symmetric trap. In particular, an analytical formula was derived which analyzes the critical particle number as a function of the anisotropy of the confining potential. Ref. [163] investigates how the critical particle number changes due to small anharmonic terms added to the confining potential of an atomic condensed system with negative two-body interaction. The dynamics of a recombination three-body Gross-Pitaevskii equation for trapped atomic systems with attractive two-body interaction was investigated numerically [164]. In Refs. [130,159] the authors show that, in a dilute gas, a small repulsive three-body interaction added to an attractive two-body interaction is able to stabilize the condensate such that the critical number of atoms in traps increases [154]. The maximal critical number of atoms occurs in a spherical trap according to various theoretical predictions [85,158,159,165,166], which agrees with experimental measurements [63].

1.4. Vortices in Atomic Bose-Einstein Condensate

The study of vortices has a long and illustrious scientific history reaching back to Helmholtz and Lord Kelvin in the nineteenth century [167]. The experimental achievement of Bose-Einstein condensation in trapped alkali-metal gases at low temperature [20,22,24] has stimulated intense experimental and theoretical activity. Vortices associated with quantized circulation are a central feature of superfluidity [168]. Singly- [19,169] and multiply-quantized [170] vortices have been observed in Bose-Einstein condensates (BECs) with repulsive atomic interactions. Complex vortex structures have been shown to be stable in repulsive BEC's, including vortex dipoles [171,172] and vortex rings [173]. In Ref. [174,175] BECs were studied both experimentally and theoretically in view of the creation and dynamics of single vortices as well as vortex lattices in ultracold atomic. These systems offer the possibility for a direct observation of vortex lines and their dynamics. They are thus excellent systems for a comprehensive theoretical study of vortex lines in three dimensions. Two basic experimental methods have been most effective in creating vortices in a BEC. The first approach [19] manipulates two hyperfine components of ^{87}Rb, spinning up one component with an external coherent electromagnetic

coupling beam [176]. The second nearly simultaneous approach [169] is similar to the rotating-bucket method of conventional low-temperature physics [168]. The starting point for studying the behavior of BECs is the theory of weakly interacting bosons which takes the form of the Gross-Pitaevskii theory. This theory is well suited to describe most of the effects of two-body interactions in the dilute gas at almost zero temperature and can be naturally generalized to explore thermal effects on the BEC [24,49,50,177–179]. The effect of vortices in the condensate for both positive and negative scattering lengths has been considered in Refs. [180,181]. For instance an analytical expression for the vortex critical frequency was found in the limit of a large particle number for positive scattering length, by approximately solving the time-independent GP equation. The vortex nucleation and the emergence of quantum turbulence, induced by oscillating magnetic fields, was introduced by Refs. [182,183].

A rotating Bose condensate state with a single vortex along the z-axis is studied in Refs [43,184]. There the superfluid coherence length was estimated, which determines the distance over which the condensate wave function can heal, by equating the kinetic energy term to the interaction energy and the critical angular frequencies required to create a vortex along the z-axis. Furthermore, analytic expressions for the monopole and the quadrupole excitation frequencies of a gravitationally self-bound BEC state with a single vortex induced by the electromagnetic wave were derived for a wide range of the dimensionless interaction, by considering two regimes, namely, the Thomas-Fermi-gravity (TF-G) and the gravity (G) regimes [184]. In these regimes, the lower bound of the ground-state energy, the sound velocity, and the monopole and quadrupole mode frequencies were calculated.

In Ref. [185] it was shown that a vortex appears in a BEC confined in a quadratic-plus-Gaussian laser potential due to the spontaneous shape deformation of the system in a BEC confined by harmonic trap only and the correct critical rotational frequency to create a single vortex was calculated. It was found that, by increasing the magnitude of the laser trap, a vortex can nucleate in a slowly rotating BEC. In the meantime, the quadratic-plus-quartic potential has been achieved experimentally by superimposing a blue detuned laser beam to the magnetic trap holding the atoms [186]. References. [187,188] showed that the shape deformation and consequently the formation of a quantized vortex in a rotating attractive and repulsive BEC depends on the strengths of both the atom-atom interaction and the anharmonical potential. The lowest energy surface mode excitation frequency and the critical rotational frequency of a BEC with both two- and three-body interactions confined in a quadratic-plus-quartic and harmonic-plus-Gaussian trap were discussed in Ref. [188]. It was found that the critical rotational frequency for a vortex formation in the harmonic-plus-Gaussian potential is lower than that in the quadratic-plus-quartic potential. The dynamics of vortex formation and the structure of vortex lattices in a Bose-Einstein condensate confined within a rotating double-well potential are numerically studied in Ref. [189]. In Ref. [190] the vortex-core structures according to the topology of the order parameter space were studied for a spin-1 Bose-Einstein condensate and it was shown that the vortex-core structures are classified by winding numbers that are locally defined in the core region. There was also shown that a vortex-core structure with a nontrivial winding number can be stabilized under a negative quadratic Zeeman effect.

A vortex in a rotating BEC with repulsive short-range interactions was extensively shown both analytically [191–193] and experimentally [19,169,194,195]. The motion of vortex lines and rings in BECs in harmonic traps are studied by a numerical solution of the GP equation in Ref. [196].

The effects of the dipole-dipole interaction on a condensate with a single vortex core were explored in Ref. [197]. The conditions for the generation of such dipolar BECs vortex are presented in Ref. [198]. The stability and excitations of harmonically trapped dipolar BECs with single and double quantized vortices were discussed in Ref. [199]. The low-lying excitations were calculated by using the Bogoliubov-de Gennes formalism and the dynamical stability was determined as a function of trap aspect ratio and dipole-dipole interaction strength. A single quantized off-axis straight vortex in a rotating dipolar BEC was studied in the Thomas-Fermi limit in Ref. [200]. In addition, the critical

rotation frequency at which a vortex state becomes energetically favorable over the vortex-free ground state in a harmonically trapped Bose-Einstein condensate, whose atoms have dipole-dipole interactions as well as the usual s-wave contact interactions, were calculated in Ref. [201]. In Ref. [202] the role of critical trap aspect ratios on both the critical angular velocity above which a vortex is energetically favorable and the precession velocity of an off-axis vortex was discussed. The influence of dipole-dipole interaction on the formation of vortices in a rotating dipolar BEC of ^{52}Cr and ^{164}Dy atoms in quasi two-dimensional geometry have explored in Ref. [203]. In Ref. [204] the authors discussed the properties of a vortex in a trapped dipolar BEC.

The frequency shifts of the quadrupole oscillations of a harmonically trapped Bose gas due to the presence of a quantized vortex were calculated by using a sum rule approach in Ref. [205] for positive scattering lengths and large particle number, where the shift relative to excitations of opposite angular momentum is proportional to the quantum circulation of the vortex. The normal modes of a two-dimensional rotating Bose-Einstein condensate confined in a quadratic plus quartic trap were studied in Ref. [206]. The hydrodynamic theory and sum rules were used to derive analytical predictions for the collective frequencies in the limit of high angular velocities where the vortex lattice produced by the rotation exhibits an annular structure. The collective excitations of a neutral atomic Bose-Einstein condensate with gravity-like interatomic attraction, which was induced by an electromagnetic wave, were studied in ref. [184]. By using a time-dependent variational approach, an analytical spectrum for monopole and quadrupole mode frequencies of a gravity-like self-bound BEC state at zero temperature was derived. The eigenfrequency of the single vortex precession about the centre of symmetry of the harmonic potential, as well as the eigenfrequencies of the oscillations of the dipole and quadrupole vortex cofigurations were obtained both analytically and numerically in Ref. [207] by using the Rayleigh-Ritz method.

In Ref. [208] it was shown that collective mode frequencies for both monopole and quadrupole modes and the critical rotational frequency for a single vortex nucleation are changed significantly when the system crosses from the BEC side to the BCS side. Furthermore, it was found that rotating Fermi gases are dramatically influenced by both the anisotropy and the anharmonicity of the trap. The vortex structures in the BCS-BEC evolution of p-wave resonant Fermi gases were investigated in Ref. [209] by using a fully microscopic theory based on the Bogoliubov-de Gennes equation. The properties of vortices at finite temperature, including decay rate, precession frequency and vortex core brightness were investigated by using the formalism Zaremba, Nikuni, and Griffin (ZNG) based on a dissipative Gross-Pitaevskii equation for the condensate coupled to a semi-classical Boltzmann equation for the thermal cloud in Ref. [210].

1.5. This Thesis

In this thesis, we study both analytically and numerically the nonlinear dynamics of BECs, in particular its collective oscillation modes, which are induced either by a harmonic modulation of the interaction strength or by changing by the geometry of the trapping potential. In addition we investigate how the dipole mode changes in the vicinity of a Feshbach resonance and how the collective excitations of a BEC change due to the presence of a single vortex.

Chapter 2 reviews the most important concepts of the theory of ultracold bosons. We begin with the second quantization Hamiltonian, and show how the GP equation can be obtained from the Heisenberg equation. We discuss the Thomas-Fermi limit for the case in an axially-symmetric trap. Then we review the variational description of low-lying modes in the linear regime for a system with both two- and three-body interaction and we discuss in detail the stability of a Bose-Einstein condensate in the presence of an attractive two-body and a repulsive three-body interaction strengths.

Furthermore, we investigate the behavior of the condensate during the free expansion after the trapping potential is turned off.

In **Chapter 3** we analyze the condensate dynamics induced by the harmonic modulation of the s-wave scattering length via a Feshbach resonance, yielding a time-dependent interaction strength. An external driving frequency is used for the modulation and, depending on its closeness to some of the condensate eigenfrequencies, either a resonant or a non-resonant behavior can be observed. This is a new venue for studying the nonlinear dynamical regime, since the equations governing the condensate dynamics on the mean-field level are nonlinear, and large amplitude oscillations are readily produced in the resonant regime. By combining different analytical and numerical methods we analyze how nonlinear effects influence the properties of the excited collective modes, which has important implications within parametric resonance for the interpretation of the actual experimental data. Prominent nonlinear features, such as mode coupling, higher harmonics generation, and significant shifts in the frequencies of collective modes are found and are quantitatively explained by using an analytic perturbative approach. In the non-resonant case, we have small-amplitude oscillations of the condensate size around the equilibrium widths, and we are in the regime of linear response. However, as the driving frequency approaches an eigenmode, we expect a resonant behavior which is characterized by large amplitude oscillations. In this case it is clear that a linear response analysis does no longer provide a quantitatively good description of the system dynamics [109].

By changing the geometry of the trapping potential we study in **Chapter 4** the dynamics of the condensate in general and its collective oscillation modes. In particular, the asymmetry of the confining potential leads to important nonlinear effects, including resonances in the frequencies of collective oscillation modes of the condensate [105,109,112]. We discuss in detail the resulting stability of the condensate. First, we consider the case of an attractive two-body interaction and a vanishing three-body interaction. Then we consider the case when we have attractive two-body and repulsive three-body interaction. We study in detail geometric resonances, when collective mode frequencies are commensurate, and derive explicit analytic results for the frequency shifts in the case of an axially-symmetric condensate with two- and three-body interactions based on a perturbative expansion within the Poincaré-Lindstedt method. Such a frequency shift is calculated for quadrupole and breathing modes, and the derived analytical results are then compared with numerical simulations. In addition, we also compare results of numerical simulations for radial and longitudinal widths of the condensate and the corresponding excitations spectra with the analytical results obtained using perturbation theory. Then, we analyze the resonant mode coupling and the generation of second harmonics of the collective modes, which are induced by nonlinear effects. To this end we consider a BEC in the initial state corresponding to the stationary ground state with a small perturbation proportional to the eigenvector of the quadrupole mode, which leads to quadrupole mode oscillations.

In **Chapter 5** we study the collective excitation modes of a harmonically trapped Bose-Einstein condensate in the vicinity of a Feshbach resonance [121]. To this end, we consider a Bose-Einstein condensate held in a trap composed of a harmonic potential plus a bias, where the potential is generated by the interaction of the atomic magnetic moment and an external magnetic field, yielding a spatially varying interaction strength. In the configuration, the dipole mode is excited in the z-direction, the center of mass oscillates periodically at the bottom of the trap. Within a variational ansatz we investigate how the dipole mode frequency changes once the bias magnetic field is sweeping through the Feshbach resonance, thus yielding a violation of the Kohn theorem.

In **Chapter 6** we study the static and dynamic properties of a single vortex in a Bose-Einstein condensate. Our starting point is the Gross-Pitaevski equation in the Thomas-Fermi limit where we show that the circulation of a vortex in a BEC is quantized. Within a variational approach we approximate the equations of motion for a condensate with a centered vortex and discuss equilibrium points as well as the frequencies of collective modes. Furthermore, we calculate the energies for a

condensate with and without a vortex and obtain the critical rotation frequency for a rotating trap at which a vortex state becomes stable. We then investigate the behavior of the condensate in free expansion after the trapping potential is turned off.

All these results indicate how nonlinear dynamics properties could be made clearly observable in future experiments on the basis of our results.

2. Gross-Pitaevskii Mean-Field Theory

In this chapter, we describe the theoretical basis of the Gross-Pitaevskii mean-field theory for BECs with two- and three-body interaction and present the notation that we will use throughout the remainder of this thesis. The starting point for our study is the second quantized Hamiltonian for a gas of interacting bosons from which we derive the mean-field Gross-Pitaevskii equation in Section 2.1. In Section 2.2, we review the variational approach from Refs. [84,85] which reduces the partial differential equation of Gross and Pitaevskii to a set of ordinary differential equations for the dynamics of the widths of the condensate. After having discussed the equilibrium positions in Section 2.3, we calculate in Section 2.4 the main results for the low-lying collective excitation modes of a BEC. On the basis of this we determine in Section. 2.5 the resulting stability of the condensate for both an attractive two-body and a repulsive three-body interaction strength. Furthermore, we discuss in Section 2.6 the behavior of the condensate in free expansion after the trapping potential is turned off.

2.1. Second Quantization Hamiltonian

The second quantised Hamiltonian for a gas of bosons interacting by two- and three-body collisions within an external trapping potential is given by [50,151,211–213]

$$\begin{aligned}\hat{H} &= \int d\mathbf{r}\hat{\Psi}^\dagger(\mathbf{r},t)h_0(\mathbf{r})\hat{\Psi}(\mathbf{r},t) + \frac{1}{2}\int d\mathbf{r}\int d\mathbf{r}'\hat{\Psi}^\dagger(\mathbf{r},t)\hat{\Psi}^\dagger(\mathbf{r}',t)\mathcal{V}_2(\mathbf{r}-\mathbf{r}')\hat{\Psi}(\mathbf{r}',t)\hat{\Psi}(\mathbf{r},t) \\ &+\frac{1}{3}\int d\mathbf{r}\int d\mathbf{r}''\int d\mathbf{r}'\hat{\Psi}^\dagger(\mathbf{r},t)\hat{\Psi}^\dagger(\mathbf{r}',t)\hat{\Psi}^\dagger(\mathbf{r}'',t)\mathcal{V}_3(\mathbf{r}-\mathbf{r}',\mathbf{r}'-\mathbf{r}'')\hat{\Psi}(\mathbf{r}'',t)\hat{\Psi}(\mathbf{r}',t)\hat{\Psi}(\mathbf{r},t),\end{aligned} \tag{2.1}$$

where $h_0(\mathbf{r}) = -\frac{\hbar^2}{2M}\Delta + V_{\text{ext.}}(\mathbf{r})$ denotes the single-atom Hamiltonian, M is the particle mass, $V_{\text{ext.}}$ is the external harmonic trap. Assuming homogeneity for the interactions, the tow-body interaction is denoted by $\mathcal{V}_2(\mathbf{r}-\mathbf{r}')$ and the three-body interaction reads $\mathcal{V}_3(\mathbf{r}-\mathbf{r}',\mathbf{r}'-\mathbf{r}'')$. Furthermore, $\hat{\Psi}^\dagger(\mathbf{r},t)$, and $\hat{\Psi}(\mathbf{r},t)$ are bosonic creation and annihilation field operators, respectively, which satisfy the equal-time Bose commutation relations [211]

$$\left[\hat{\Psi}(\mathbf{r},t),\hat{\Psi}(\mathbf{r}',t)\right] = \left[\hat{\Psi}^\dagger(\mathbf{r},t),\hat{\Psi}^\dagger(\mathbf{r}',t)\right] = 0, \qquad \left[\hat{\Psi}(\mathbf{r},t),\hat{\Psi}^\dagger(\mathbf{r}',t)\right] = \delta(\mathbf{r}-\mathbf{r}'). \tag{2.2}$$

The next step is to simplify the interatomic interaction potential $\mathcal{V}_2(\mathbf{r}-\mathbf{r}')$. At low temperatures s-wave scattering is the dominant collision process in dilute gases. If the s-wave scattering length a_s is small compared to the de-Broglie wavelength $\lambda_{dB} = \sqrt{2\pi\hbar^2/Mk_BT}$, then the interatomic potential can be replaced by an effective interaction which is well described by a delta-function potential [49,50,214],

$$\mathcal{V}_2(\mathbf{r}-\mathbf{r}') = g_2\delta(\mathbf{r}-\mathbf{r}'), \tag{2.3}$$

where the coupling two-body interaction g_2 is given by

$$g_2 = 4\pi\hbar^2 a_s/M\,. \tag{2.4}$$

Positive a_s corresponds to repulsive two-body interaction and negative a_s corresponds to attractive two-body interaction.

The three-body interaction becomes important for large values of the s-wave scattering length, but also for small values of a_s close to the ideal gas regime [215]. It is well known that the stability against the collapse of ^{85}Rb cannot be described by using only the two-body scattering [216]. The three-body scattering also plays an essential role in understanding the Efimov physics, where three bosons form a bound state [217,218]. Braaten and Nieto [215,219] have used an effective field theory to calculate the strength of the three-body interaction, which effectively arises from the two-body interaction, and obtained the result

$$\mathcal{V}_3(\mathbf{r}-\mathbf{r}',\mathbf{r}'-\mathbf{r}'') = g_3\delta(\mathbf{r}-\mathbf{r}')\delta(\mathbf{r}'-\mathbf{r}'')\,, \tag{2.5}$$

with the strength

$$g_3 = 32\pi(4\pi-3\sqrt{3})[\ln(\kappa a_s)+B]\hbar^2 a_s^4/M\,, \tag{2.6}$$

where κ denotes an arbitrary wave number within the renormalization procedure and B is a complex constant which is calculated for $a_s<0$ by Efimov [217] and for $a_s>0$ in Ref. [215]. The effective three-body coupling strength represents in general a complex number, where its imaginary part describes recombination effects. However, its real part is much larger, and the fit to experimental data for ^{85}Rb and ^{87}Rb gives typical values for $\mathrm{Re}(g_3)/\hbar$ of the order of $10^{-27}\mathrm{cm}^6\mathrm{s}^{-1}$ to $10^{-26}\mathrm{cm}^6\mathrm{s}^{-1}$ [151,158,220]. Near an Efimov resonance the imaginary part of B vanishes, and the real part amounts approximately to the value $B\approx 1$ [215]. Furthermore, it turns out that the $\ln(\kappa a_s)$ contribution is negligible for ultracold BECs with a particle density of the order 10^{13} cm^{-3}. Thus, the three-body interaction strength Eq. (2.6) reduces approximately to

$$g_3 = 39\pi(4\pi-3\sqrt{3})\hbar^2 a_s^4/M\,. \tag{2.7}$$

For instance, for ^{87}Rb atoms with an s-wave scattering length of $a_s = 100a_0$ we obtain the values $g_2 = 5\hbar\times 10^{-11}\mathrm{cm}^3\mathrm{s}^{-1}$ and $g_3 = \hbar\times 10^{-27}\mathrm{cm}^6\mathrm{s}^{-1}$ [126].

We now use this form of the Hamiltonian Eq. (2.2) to derive the resulting time evolution of $\hat{\Psi}(\mathbf{r},t)$. The Heisenberg equation of motion of the field operator $\hat{\Psi}(\mathbf{r},t)$ is given by

$$i\hbar\frac{\partial\hat{\Psi}(\mathbf{r},t)}{\partial t} = \left[\hat{\Psi}(\mathbf{r},t),\hat{H}\right], \tag{2.8}$$

so obtain with Eqs. (2.2), (2.3), and (2.5)

$$i\hbar\frac{\partial\hat{\Psi}(\mathbf{r},t)}{\partial t} = \left[-\frac{\hbar^2}{2M}\Delta + V_{\text{ext.}}(\mathbf{r}) + g_2\hat{\Psi}^\dagger(\mathbf{r},t)\hat{\Psi}(\mathbf{r},t) + g_3\hat{\Psi}^\dagger(\mathbf{r},t)\hat{\Psi}^\dagger(\mathbf{r},t)\hat{\Psi}(\mathbf{r},t)\hat{\Psi}(\mathbf{r},t)\right]\hat{\Psi}(\mathbf{r},t). \tag{2.9}$$

In 1947, N. N. Bogoliubov [10] formed the basis of a mean-field theory for dilute gases by decomposing the field operator $\hat{\Psi}(\mathbf{r},t)$ into a complex wave function $\psi(\mathbf{r},t)$, which corresponds to the macroscopic occupation of the ground state, and $\hat{\psi}(\mathbf{r},t)$, describing the non-condensed fraction, which corresponds either to thermally-excited atoms or quantum-mechanical fluctuations, where atoms are promoted into higher energy states due to interactions:

$$\hat{\Psi}(\mathbf{r},t) = \psi(\mathbf{r},t) + \hat{\psi}(\mathbf{r},t). \tag{2.10}$$

The equation of motion for the condensate wave function is obtained by substituting Eq. (2.10) into Eq. (2.9) and taking the expectation value of the field operator $\hat{\Psi}(\mathbf{r},t)$ in such a way that $\langle\hat{\psi}(\mathbf{r},t)\rangle = 0$,

so we obtain

$$
\begin{aligned}
i\hbar\frac{\partial\psi(\mathbf{r},t)}{\partial t} &= \Bigg\{ -\frac{\hbar^2}{2M}\Delta + V_{\text{ext.}}(\mathbf{r}) + g_2\Big[n_c(\mathbf{r},t) + 2\tilde{n}(\mathbf{r},t) + \tilde{m}(\mathbf{r},t)\Big] \\
&+ g_3\Big[n_c^2(\mathbf{r},t) + 3n_c(\mathbf{r},t)\tilde{m}(\mathbf{r},t) + 6n_c(\mathbf{r},t)\tilde{n}(\mathbf{r}) + n_c(\mathbf{r},t)\langle\hat{\psi}^\dagger(\mathbf{r},t)\hat{\psi}^\dagger(\mathbf{r},t)\rangle \\
&+ \langle\hat{\psi}(\mathbf{r},t)\hat{\psi}(\mathbf{r},t)\hat{\psi}(\mathbf{r},t)\rangle\psi(\mathbf{r},t) + 6\langle\hat{\psi}^\dagger(\mathbf{r},t)\hat{\psi}(\mathbf{r},t)\hat{\psi}(\mathbf{r},t)\rangle\psi(\mathbf{r},t) + 2\tilde{n}(\mathbf{r},t)\tilde{m}(\mathbf{r},t) \\
&+ 3\langle\hat{\psi}^\dagger(\mathbf{r},t)\hat{\psi}^\dagger(\mathbf{r},t)\hat{\psi}(\mathbf{r},t)\rangle\psi(\mathbf{r},t) + 3\langle\hat{\psi}^\dagger(\mathbf{r},t)\hat{\psi}^\dagger(\mathbf{r},t)\hat{\psi}(\mathbf{r},t)\hat{\psi}(\mathbf{r},t)\rangle\Big]\Bigg\}\psi(\mathbf{r},t) \\
&+ g_2\langle\hat{\psi}^\dagger(\mathbf{r},t)\hat{\psi}(\mathbf{r},t)\hat{\psi}(\mathbf{r},t)\rangle + g_3\langle\hat{\psi}^\dagger(\mathbf{r},t)\hat{\psi}^\dagger(\mathbf{r},t)\hat{\psi}(\mathbf{r},t)\hat{\psi}(\mathbf{r},t)\hat{\psi}(\mathbf{r},t)\rangle \qquad (2.11)
\end{aligned}
$$

with the condensate density $n_c(\mathbf{r},t) = |\psi(\mathbf{r},t)|^2$, the non-condensate density $\tilde{n}(\mathbf{r},t) = \langle\hat{\psi}^\dagger(\mathbf{r},t)\hat{\psi}(\mathbf{r},t)\rangle$ which represents the depletion of the condensate by collisional interactions, as well as the off-diagonal non-condensate density $\tilde{m}(\mathbf{r},t) = \langle\hat{\psi}(\mathbf{r},t)\hat{\psi}(\mathbf{r},t)\rangle$ which corresponds to the anomalous correlations between the non-condensed atoms.

The three-, four-, and five-field correlation functions $\langle\hat{\psi}^\dagger(\mathbf{r},t)\hat{\psi}(\mathbf{r},t)\hat{\psi}(\mathbf{r},t)\rangle$, $\langle\hat{\psi}(\mathbf{r},t)\hat{\psi}(\mathbf{r},t)\hat{\psi}(\mathbf{r},t)\rangle$, $\langle\hat{\psi}^\dagger(\mathbf{r},t)\hat{\psi}(\mathbf{r},t)\hat{\psi}(\mathbf{r},t)\rangle$, $\langle\hat{\psi}^\dagger(\mathbf{r},t)\hat{\psi}^\dagger(\mathbf{r},t)\hat{\psi}(\mathbf{r},t)\rangle$, $\langle\hat{\psi}^\dagger(\mathbf{r},t)\hat{\psi}^\dagger(\mathbf{r},t)\hat{\psi}(\mathbf{r},t)\hat{\psi}(\mathbf{r},t)\rangle$, and $\langle\hat{\psi}^\dagger(\mathbf{r},t)\hat{\psi}^\dagger(\mathbf{r},t)\hat{\psi}(\mathbf{r},t)\hat{\psi}(\mathbf{r},t)\hat{\psi}(\mathbf{r},t)\rangle$, respectively, have non-zero expectation values due to the broken $U(1)$ symmetry [55,56]. Eq. (2.11) reduces to the GP equation [214] if all the atoms are in the condensate i.e., the non-condensate density, the off-diagonal non-condensate density, and the correlation functions are ignored. This is a very good approximation at $T = 0$, for small enough interactions the non-condensate fraction in trapped atomic gases is estimated to be less than 1% [212,221,222]. Several approximations for the generalized Eq. (2.11) were discussed in case of a two-body interaction [55,56]: The Hartree-Fock-Bogoliubov (HFB) approximation for $\psi(\mathbf{r},t)$ corresponds to keeping the $n_c(\mathbf{r},t)$, $\tilde{n}(\mathbf{r},t)$, and $\tilde{m}(\mathbf{r},t)$ fluctuations, which have to be calculated self-consistently and neglecting the three-field correlation functions $\langle\hat{\psi}^\dagger(\mathbf{r},t)\hat{\psi}(\mathbf{r},t)\hat{\psi}(\mathbf{r},t)\rangle$ [223–225]. The dynamic Popov approximation corresponds to consider only the condensate and non-condensate densities $n_c(\mathbf{r},t), \tilde{n}(\mathbf{r},t)$, respectively and theories of this approximation were discussed in Ref. [226]. Furthermore, the static Popov approximation amounts to ignoring the fluctuations in the density $\tilde{n}(\mathbf{r},t)$ of the thermal cloud so that the non-condensate is always in static thermal equilibrium [212,214,222,223].

2.1.1. Time-Dependent Gross-Pitaevskii Equation

This thesis deals with the zero-temperature model for small enough interactions, in which the non-condensate atoms are completely neglected, so that Eq. (2.11) reduces to

$$
i\hbar\frac{\partial\psi(\mathbf{r},t)}{\partial t} = \left[-\frac{\hbar^2}{2M}\Delta + V_{\text{ext.}}(\mathbf{r}) + g_2 n_c(\mathbf{r},t) + g_3 n_c^2(\mathbf{r},t)\right]\psi(\mathbf{r},t). \qquad (2.12)
$$

This is the time-dependent Gross-Pitaevskii equation, which has become the main tool for theoretical studies of Bose-Einstein condensates. It was derived independently by E. P. Gross [47] and L. P. Pitaevskii [48] in 1961 and was originally used to investigate the presence of vortices in weakly interacting Bose gases. The wave function is normalized to the particle number N according to

$$
N = \int d\mathbf{r}\, |\psi(\mathbf{r},t)|^2 \ . \qquad (2.13)
$$

The GP equation has proven to be a very useful tool to describe the physics of weakly interacting atomic Bose-Einstein condensates in the early ages of this field.

2.1.2. Time-Independent Gross-Pitaevskii Equation

In order to study static properties of Bose-Einstein condensates, such as the equilibrium density for example, one uses the time-independent version of the Gross-Pitaevskii Eq. (2.12). To this end, we insert the factorization ansatz

$$\psi(\mathbf{r},t) = \psi(\mathbf{r})e^{-\frac{i}{\hbar}\mu t}\,, \tag{2.14}$$

where μ is called the chemical potential into Eq. (2.12), so $\psi(\mathbf{r})$ obeys the time-independent GP equation

$$\mu\psi(\mathbf{r}) = \left[-\frac{\hbar^2}{2M}\Delta + V_{\text{ext.}}(\mathbf{r}) + g_2 n_c(\mathbf{r}) + g_3 n_c^2(\mathbf{r})\right]\psi(\mathbf{r}). \tag{2.15}$$

2.1.3. Thomas-Fermi Approximation

The functional forms of quantities such as the condensate size are difficult to find analytically, so one has to use numerical method to solve the time-independent GP equation (2.15). The Thomas-Fermi (TF) solution represents an approximation for the density profile. In the case of comparatively strong interaction it is justified to neglect the kinetic energy term in the Eq. (2.15). In that situation, the density profile is approximated by the Thomas-Fermi solution, which corresponds to

$$n_c(\mathbf{r}) = |\psi(\mathbf{r})|^2 = \begin{cases} -\frac{g_2}{2g_3} + \sqrt{\left(\frac{g_2}{2g_3}\right)^2 + \frac{\mu - V_{\text{ext.}}(\mathbf{r})}{g_3}}, & \text{for } \mu - V_{\text{ext.}}(\mathbf{r}) \geq 0 \\ 0, & \text{otherwise.} \end{cases} \tag{2.16}$$

In the following we specialize the external potential to a tri-axial harmonic trap:

$$V_{\text{ext.}}(\mathbf{r}) = \frac{M}{2}\sum_{r=x,y,z}\omega_r^2 r^2\,. \tag{2.17}$$

We emphasize that the Thomas-Fermi solution of the harmonically trapped condensate given in Eq. (2.16), differs in many aspects from the non-interacting case. In particular, the boundaries of the cloud are determined by the condition $V_{\text{ext.}}(\mathbf{r}) = \mu$, which leads to the so-called Thomas-Fermi radii describing the extension of the cloud in the respective directions. In case of an axially-symmetric harmonic trap, when $\omega_x = \omega_y = \omega_\rho \neq \omega_z = \omega_\rho\lambda$ with the trap aspect ratio λ, the extension in radial and axial direction are given by

$$R_\rho = \sqrt{\frac{2\mu}{M\omega_\rho^2}}\,, \qquad R_z = \sqrt{\frac{2\mu}{M(\omega_\rho\lambda)^2}}. \tag{2.18}$$

The corresponding chemical potential μ has to be calculated by using the normalization condition Eq. (2.13), which leads to

$$N = \int d\mathbf{r}\left(-\frac{g_2}{2g_3} + \sqrt{\left(\frac{g_2}{2g_3}\right)^2 + \frac{\mu - V_{\text{ext.}}(\mathbf{r})}{g_3}}\right)\,, \tag{2.19}$$

where the integration is performed within the ellipsoid where the integrand is positive. This yields the following explicit result for the equation of state

$$N = \frac{\pi\mathcal{A}_2}{6}\left[-\sqrt{\mathcal{A}_1}\,(3\mathcal{A}_1 + 5) + 3\,(\mathcal{A}_1 + 1)^2\,\text{ArcSin}\left(\sqrt{\frac{1}{\mathcal{A}_1 + 1}}\right)\right]\,, \tag{2.20}$$

with the dimensionless parameters $\mathcal{A}_1 = g_2^2/4\mu g_3$ and $\mathcal{A}_2 = \mu/g_3\left(2\mu/M\tilde{\omega}^2\right)^{3/2}$, where $\tilde{\omega} = \lambda^{1/3}\omega_\rho$ denotes the geometric mean of the trap frequencies.

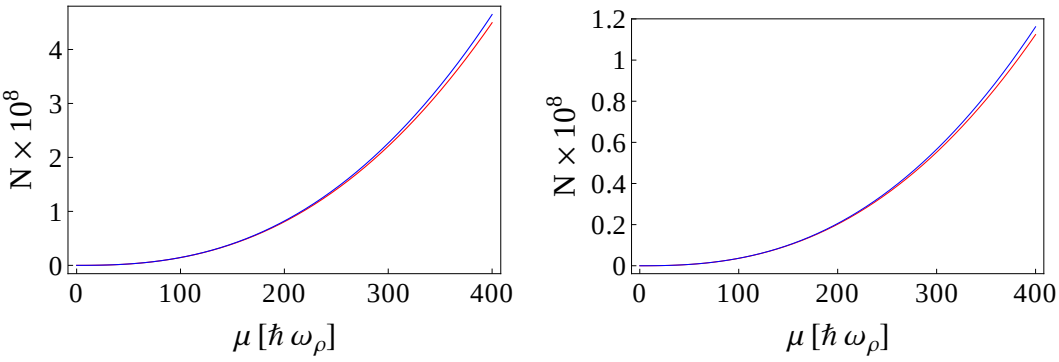

(a) (b)

Figure 2.1.: Equation of state (2.20) for ^{87}Rb gases with $\omega_\rho = 2\pi \times 112$ Hz, with a repulsive two- and three-body interaction strength versus the chemical potential for different trap anisotropies (a) $\lambda = 0.5$ and (b) $\lambda = 2$. Blue curve represents equation of state for vanishing three-body interaction strength g_3 and the red curve corresponds to Eq. (2.20) with three-body interaction strength from Eq. (2.7).

Figure 2.1 shows the equation of state of systems of repulsive two-body interaction strength as a function of chemical potential, where the red curve correspond to the exact result of Eq. (2.20) with the three-body interaction strength from Eq. (2.7), and the blue curve represents the case of vanishing three-body interaction strength. We read off from Fig. 2.1 that a non-vanishing three-body interaction strength g_3 yields for a pancake-like BEC lower particle numbers than a cigar-like BEC. Furthermore, it is clear that an additional three-body interaction for fixed particle number leads to an increase of the chemical potential and, thus according to Eq. (2.18) to an increase of the respective TF radii. The chemical potential μ and the Thomas-Fermi radius R_ρ and R_z up to first order of g_3 are defined by

$$\mu/\hbar\omega_\rho = \frac{1}{2}\left(\frac{15N\lambda a_s}{l}\right)^{2/5}\left[1 + \frac{4g_3}{35g_2^2}\left(\frac{15N\lambda a_s}{l}\right)^{2/5} + ...\right], \tag{2.21}$$

$$R_\rho/l = \left(\frac{15N\lambda a_s}{l}\right)^{1/5}\left[1 + \frac{2g_3}{35g_2^2}\left(\frac{15N\lambda a_s}{l}\right)^{2/5} + ...\right], \tag{2.22}$$

$$R_z/l = \frac{1}{\lambda}\left(\frac{15N\lambda a_s}{l}\right)^{1/5}\left[1 + \frac{2g_3}{35g_2^2\lambda^2}\left(\frac{15N\lambda a_s}{l}\right)^{2/5} + ...\right], \tag{2.23}$$

where l denotes the radial oscillating length

$$l = \sqrt{\hbar/M\omega_\rho}\,. \tag{2.24}$$

From Eq. (2.7) and Eqs. (2.22) and (2.23) we conclude that the TF radii depend more significantly on the three-body interaction near a Feshbach resonance, i.e. for large s-wave scattering length.

2.2. Variational Approach

In this section we use a variational approach to obtain approximate equations of motions for the parameters of a suitable trial function. This technique is well-established and has been successfully applied in several previous studies [70,85]. Our analytical method for studying nonlinear BEC dynamics is the variational approach introduced in Refs. [84,85].

The dynamics of a condensed Bose gas in a trap at zero temperature is described by the time-dependent GP Equation (2.12) with a harmonic trap potential defined in Eq. (2.17) and the parameters

g_2 and g_3 are defined in Eq. (2.4) and (2.7), respectively. There are two essential points where Eq. (2.12) differs from the Schrödinger equation. The first one is the nonlinear interaction terms $g_2 \left|\psi(\mathbf{r},t)\right|^2 \psi(\mathbf{r},t)$ and $g_3 \left|\psi(\mathbf{r},t)\right|^4 \psi(\mathbf{r},t)$. Additionally the wave function $\psi(\mathbf{r},t)$ is not normalized to 1 but to the total particle number as defined in Eq. (2.13).

The time-dependent Gross-Pitaevskii equation follows from the action

$$\mathcal{A}[\psi^*(\mathbf{r},t),\psi(\mathbf{r},t)] = \int dt \int d\mathbf{r}\mathcal{L}\left[\psi^*(\mathbf{r},t), \nabla\psi^*(\mathbf{r},t), \frac{\partial\psi^*(\mathbf{r},t)}{\partial t}; \psi(\mathbf{r},t), \nabla\psi(\mathbf{r},t), \frac{\partial\psi(\mathbf{r},t)}{\partial t}\right] \tag{2.25}$$

with the Lagrange density

$$\begin{aligned}\mathcal{L}(\mathbf{r},t) &= \frac{i\hbar}{2}\left(\psi^*(\mathbf{r},t)\frac{\partial\psi(\mathbf{r},t)}{\partial t} - \psi(\mathbf{r},t)\frac{\partial\psi^*(\mathbf{r},t)}{\partial t}\right) - \frac{\hbar^2}{2M}|\nabla\psi(\mathbf{r},t)|^2 \\ &\quad -V_{\text{ext.}}(\mathbf{r})|\psi(\mathbf{r},t)|^2 - \frac{g_2}{2}|\psi(\mathbf{r},t)|^4 - \frac{g_3}{3}|\psi(\mathbf{r},t)|^6.\end{aligned} \tag{2.26}$$

This, indeed, yields the Gross-Pitaevskii equation Eq. (2.12) if the Hamilton principle is applied

$$\delta\mathcal{A}[\psi^*(\mathbf{r},t),\psi(\mathbf{r},t)] = 0. \tag{2.27}$$

Inserting a suitable trial function with time-dependent parameters into equation Eq. (2.26) and integrating over space, leads to the Lagrange function of the system

$$L(t) = \int d\mathbf{r}\mathcal{L}(\mathbf{r},t)\,. \tag{2.28}$$

We follow Refs. [84,85] and use now the Gaussian variational ansatz

$$\psi(x,y,z,t) = \mathcal{N}(t)\exp\left\{\sum_{r=x,y,z}\left[\left(-\frac{1}{2u_r^2} - i\phi_r\right)r^2\right]\right\}, \tag{2.29}$$

with the normalization factor $\mathcal{N}(t) = \sqrt{N}/\sqrt{\pi^{\frac{3}{2}}u_x u_y u_z}$, while u_r and ϕ_r are variational parameters. The introduced parameters have a straightforward interpretation: u_r corresponds to the respective condensate width, while ϕ_r represents the corresponding phase. Therefore, Eq. (2.29) describes the dynamics of the condensate in terms of time-dependent condensate widths and phases, while no center of mass motion is considered here.

We start from the Lagrangian Eq. (2.28). For the Gaussian variational ansatz Eq. (2.29), the Lagrange function can be calculated

$$L = N\sum_{r=x,y,z}\left[-\frac{\hbar}{2}u_r^2\dot{\phi}_r - \frac{\hbar^2}{M}\left(\frac{1}{4u_r^2} + u_r^2\phi_r^2\right) - \frac{M}{4}\omega_r^2 u_r^2\right] - \frac{g_2 N^2}{2(2\pi)^{3/2}u_x u_y u_z} - \frac{g_3 N^3}{9\sqrt{3}\pi^3 u_x^2 u_y^2 u_z^2}\,. \tag{2.30}$$

The first part contains a time derivative, the second and the third part correspond to the kinetic and external potential trap, whereas the last two parts correspond to the two- and three-body interactions. From the Euler-Lagrange equations, we obtain the evolution equations for all variational parameters $q \in \{\phi_r, u_r\}$:

$$\frac{d}{dt}\frac{\partial L}{\partial \dot{q}} - \frac{\partial L}{\partial q} = 0\,. \tag{2.31}$$

The equations for the phases $\phi_r(t)$ can be solved explicitly in terms of the widths,

$$\phi_r = \frac{M\dot{u}_r}{2\hbar u_r}\,, \tag{2.32}$$

whereas the dynamics of the widths is given by

$$\hbar\dot{\phi}_r u_r - \frac{\hbar^2}{2M}\frac{1}{u_r^3} + \frac{2\hbar^2}{M}\phi_r^2 u_r + \frac{M\omega_r^2}{2}u_r - \frac{g_2 N}{(2\pi)^{3/2}u_r u_x u_y u_z} - \frac{2g_3 N^2}{9\sqrt{3}\pi u_r u_x^2 u_y^2 u_z^2} = 0. \tag{2.33}$$

By inserting Eq. (2.32) into Eq. (2.33) and introducing dimensionless parameters

$$\tilde{\omega}_i = \omega_i/\omega_\rho\,, \quad \tilde{u}_i = u_i/l\,, \quad \tilde{t} = t/\omega_\rho\,, \quad l = \sqrt{\frac{\hbar}{M\omega_\rho}}\,, \tag{2.34}$$

we obtain variational equations written in dimensionless form:

$$\ddot{u}_x + \lambda_x^2 u_x - \frac{1}{u_x^3} - \frac{\mathcal{P}}{u_x^2 u_y u_z} - \frac{\mathcal{K}}{u_x^3 u_y^2 u_z^2} = 0\,, \tag{2.35}$$

$$\ddot{u}_y + \lambda_y^2 u_y - \frac{1}{u_y^3} - \frac{\mathcal{P}}{u_y^2 u_x u_z} - \frac{\mathcal{K}}{u_x^2 u_y^3 u_z^2} = 0\,, \tag{2.36}$$

$$\ddot{u}_z + \lambda_z^2 u_z - \frac{1}{u_z^3} - \frac{\mathcal{P}}{u_x u_y u_z^2} - \frac{\mathcal{K}}{u_x^2 u_y^2 u_z^3} = 0\,. \tag{2.37}$$

Here, we have dropped for simplicity the tilde sign in the dimensionless widths and we have introduced the dimensionless two-body interaction strength

$$\mathcal{P} = g_2 N/(2\pi)^{3/2}\hbar\omega_\rho l^3 = \sqrt{2/\pi}Na_s/l\,, \tag{2.38}$$

and the dimensionless three-body interaction strength

$$\mathcal{K} = \frac{4g_3 N^2}{9\sqrt{3}\pi^3\omega_\rho\hbar l^6}\,, \tag{2.39}$$

where l denotes the radial oscillating length defined in Eq. (2.24). Both parameters Eqs. (2.38) and (2.39) are related to each other via

$$\mathcal{K} = \frac{32g_3\hbar\omega_\rho}{9\sqrt{3}g_2^2}\mathcal{P}^2\,. \tag{2.40}$$

Those equations of motion Eqs. (2.35)–(2.37) correspond to harmonic oscillators, which are modified by a kinetic term and an additional term that depends on the dimensionless parameter $\mathcal{P}$, which describes two-body interaction Eq. (2.38) and depends on the s-wave scattering length a_s, as well as on the dimensionless three-body interaction $\mathcal{K}$ defined in Eq. (2.39). From experimental data in Refs. [126,227], we read off that the two- and three-body interaction strengths are given by

$$\mathcal{P} = 426, \quad \mathcal{K} = 1050\,. \tag{2.41}$$

Note that the s-wave scattering length can be tuned to any value, large or small, positive or negative by applying an external magnetic field using the Feshbach resonance technique [126,130,131,152,153,228]. Therefore, in this thesis we will consider various of experimentally realistic values for dimensionless interaction strengths $\mathcal{P}$ and $\mathcal{K}$.

The dynamics of the width Eqs. (2.35)–(2.37) can be rewritten as

$$\ddot{u}_r = -\frac{\partial V_{\text{eff}}(u_x, u_y, u_z)}{\partial u_r}\,, \tag{2.42}$$

and can therefore be regarded as the motion of a fictitious point particle in the effective potential

$$V_{\text{eff}}(u_x, u_y, u_z) = \frac{1}{2}\left[u_x^2\lambda_x^2 + u_y^2\lambda_y^2 + u_z^2\lambda_z^2 + \frac{1}{u_x^2} + \frac{1}{u_y^2} + \frac{1}{u_z^2}\right] + \frac{\mathcal{P}}{u_x u_y u_z} + \frac{\mathcal{K}}{2u_x^2 u_y^2 u_z^2}\,. \tag{2.43}$$

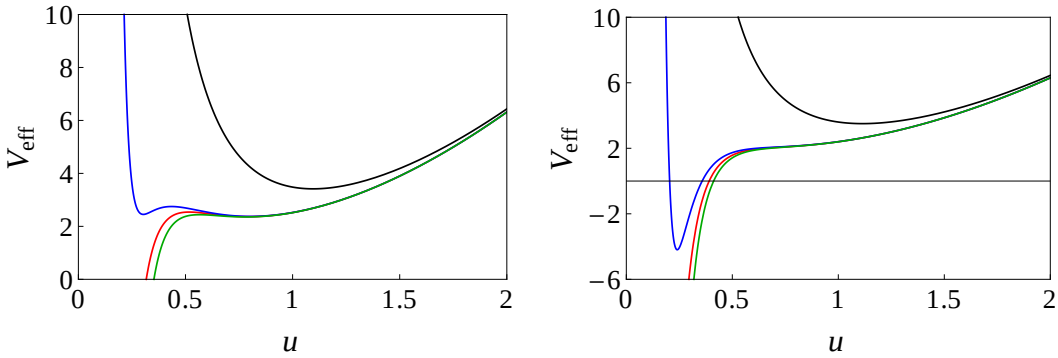

(a) (b)

Figure 2.2.: Effective potential Eq. (2.44) for systems with two-and three-body interaction strengths versus the width of the condensate u. Black curve corresponds to repulsive two- and three-body interactions, (a) $\mathcal{P} = 0.48$ and $\mathcal{K} = 0.005$ and (b) $\mathcal{P} = 0.6$ and $\mathcal{K} = 0.005$, red curve corresponds to attractive two-body interaction, (a) $\mathcal{P} = -0.48$ and $\mathcal{K} = 0$ and (b) $\mathcal{P} = -0.6$ and $\mathcal{K} = 0$, blue curve corresponds to attractive two-body and repulsive three-body interactions, (a) $\mathcal{P} = -0.48$ and $\mathcal{K} = 0.005$ and (b) $\mathcal{P} = -0.6$ and $\mathcal{K} = 0.005$, and green curve corresponds to attractive two- and three-body interactions, (a) $\mathcal{P} = -0.48$ and $\mathcal{K} = -0.005$ and (b) $\mathcal{P} = -0.6$ and $\mathcal{K} = -0.005$.

Small oscillations around a stable configuration are possible when there is a minimum in the effective potential. A detailed study of the effective potential Eq. (2.43) for systems of two- and three-body interaction strengths reveals, for instance, that an atomic condensate with attractive two-body interaction can be stabilized with a very small respective three-body interaction strength. In this way the stability region of the condensate can be extended considerably [129,160].

For the isotropic case the effective potential Eq. (2.43) has the following form

$$V_{\text{eff}}(u) = \frac{3}{2}\left(u + \frac{1}{u^2}\right) + \frac{\mathcal{P}}{u^3} + \frac{\mathcal{K}}{2u^6}\,. \tag{2.44}$$

The first and the second part correspond to the external potential trap and the kinetic energy, respectively, whereas the last two parts correspond to the two- and three-body interactions. It is clear that this functional form implies the asymptotics

$$V_{\text{eff}}(u) = \begin{cases} \frac{3}{2}u^2 \to \infty\,, & \text{for } u \gg 1 \\ \frac{3}{2}\frac{1}{u^2} + \frac{\mathcal{P}}{u^3} + \frac{\mathcal{K}}{2u^6} \to s\infty\,, & \text{for } u \ll 1 \end{cases} \tag{2.45}$$

with the parameter

$$s = \begin{cases} +1 & \text{if} \quad \mathcal{K} > 0 \bigvee \mathcal{K} = 0 \bigwedge \mathcal{P} > 0 \bigvee \mathcal{P} = 0 = \mathcal{K} \\ -1 & \text{if} \quad \mathcal{K} < 0 \bigvee \mathcal{K} = 0 \bigwedge \mathcal{P} < 0\,. \end{cases} \tag{2.46}$$

Figure 2.2 shows the effective potential Eq. (2.44) for systems of two- and three-body interaction strengths as a function of the condensate width u. For repulsive two- and three-body interactions (black curves) in Fig. 2.2 the effective potential has one local minimum, which means that the system is always stable. For the case of an attractive two-body interaction (red curves) and attractive two- and three-body interactions (green curves) as well as an attractive two-body interaction and a repulsive three-body interaction (blue curves) the situation in Fig. 2.2 is quite different. The system can either have none, one, or three equilibrium positions and we will discuss later on in detail the resulting stability diagram.

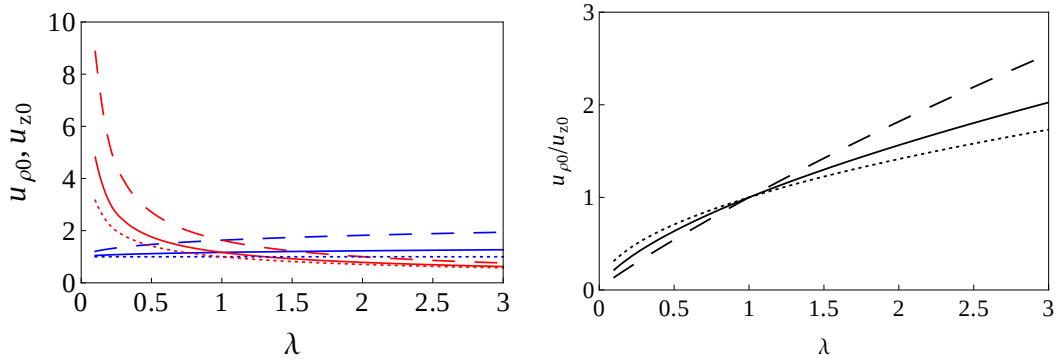

(a) (b)

Figure 2.3.: (a) Equilibrium positions $u_{\rho 0}$ (blue curves) and u_{z0} (red curves) from Eqs. (2.50) and (2.51) and (b) aspect ratio $u_{\rho 0}/u_{z0}$ (black curves) of systems with two- and three-body interaction strengths versus trap aspect ratio λ for non-interacting case $\mathcal{P} = \mathcal{K} = 0$ (dotted lines), while $\mathcal{P} = 1$, $\mathcal{K} = 0$ (solid lines) and $\mathcal{P} = 10$, $\mathcal{K} = 0.1$ (dashed lines).

2.3. Equilibrium Positions

The equilibrium positions can be calculated by setting the gradient of the potential Eq. (2.43) to zero, which yields

$$\lambda_x^2 u_{x0} - \frac{1}{u_{x0}^3} - \frac{\mathcal{P}}{u_{x0}^2 u_{y0} u_{z0}} - \frac{\mathcal{K}}{u_{x0}^3 u_{y0}^2 u_{z0}^2} = 0\,, \tag{2.47}$$

$$\lambda_y^2 u_{y0} - \frac{1}{u_{y0}^3} - \frac{\mathcal{P}}{u_{y0}^2 u_{x0} u_{z0}} - \frac{\mathcal{K}}{u_{x0}^2 u_{y0}^3 u_{z0}^2} = 0\,, \tag{2.48}$$

$$\lambda_z^2 u_{z0} - \frac{1}{u_{z0}^3} - \frac{\mathcal{P}}{u_{x0} u_{y0} u_{z0}^2} - \frac{\mathcal{K}}{u_{x0}^2 u_{y0}^2 u_{z0}^3} = 0\,. \tag{2.49}$$

We will consider the experimentally relevant case of an axially-symmetric trap, such that $\lambda_x = \lambda_y = 1$, $\lambda_z = \lambda$, $u_{x0} = u_{y0} = u_{\rho 0}$. This leads to the two algebraic equations

$$u_{\rho 0} = \frac{1}{u_{\rho 0}^3} + \frac{\mathcal{P}}{u_{\rho 0}^3 u_{z0}} + \frac{\mathcal{K}}{u_{\rho 0}^5 u_{z0}^2}\,, \tag{2.50}$$

$$\lambda^2 u_{z0} = \frac{1}{u_{z0}^3} + \frac{\mathcal{P}}{u_{\rho 0}^2 u_{z0}^2} + \frac{\mathcal{K}}{u_{\rho 0}^4 u_{z0}^3}. \tag{2.51}$$

Note that for given parameters $\mathcal{P}$, $\mathcal{K}$, and λ only positive real solutions $u_{\rho 0}$ and u_{z0} from Eqs. (2.50), (2.51) represent physically realized equilibrium widths. Although in Eq. (2.41) the value of $\mathcal{K}$ is larger than that of $\mathcal{P}$, the corresponding terms in Eqs. (2.50), (2.51), i.e. $\mathcal{K}/u_\rho^5 u_z^2$ and $\mathcal{K}/u_\rho^4 u_z^3$, are suppressed by the factor $u_\rho^2 u_z$ compared to the respective $\mathcal{P}$-terms. This factor can be estimated by taking into account the equilibrium positions $u_{\rho 0}$ and u_{z0}, which are obtained by solving the stationary equations (2.50) and (2.51). For the anisotropy $\lambda = 3/2$, one numerically obtains $u_{\rho 0} \approx 3.69$ and $u_{z0} \approx 2.47$, yielding the value $u_{\rho 0}^2 u_{z0} \approx 33.6$. This shows that the terms proportional to $\mathcal{K}$ have the effective coupling $\mathcal{K}/33 \approx 31.2$, which makes them small corrections of the order of 7% to the leading two-body interaction terms. However, if the system exhibits resonances, this may no longer be true anymore, and three-body interactions can play a significant role for the system dynamics.

Figure 2.3 shows the equilibrium positions Eqs. (2.50) and (2.51) as well as the aspect ratio $u_{\rho 0}/u_{z0}$ versus trap anisotropy λ for systems of repulsive two- and three-body interactions. We plot in Fig. 2.3(a) the equilibrium positions $u_{\rho 0}$ and u_{z0} as a function of trap anisotropy λ. A cigar-like

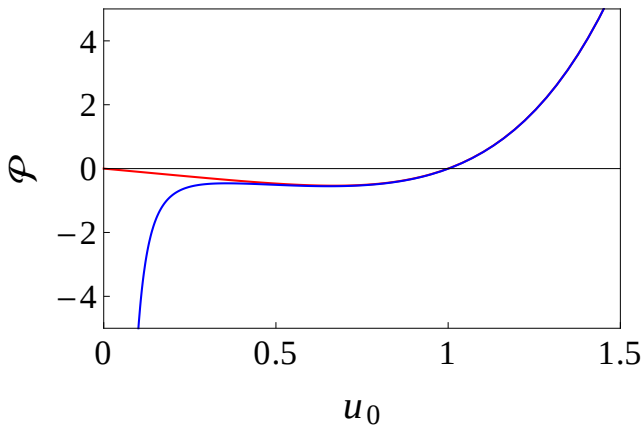

Figure 2.4.: Two-body interaction strength $\mathcal{P}$ as a function of the variational width parameter u_0 Eq. (2.53). Red curve corresponds to the systems of an attractive pure two-body and vanishing three-body interaction strength, while the blue curve corresponds to systems of attractive two-body and repulsive three-body $\mathcal{K} = 0.005$ interaction strengths.

shape occurs for $\lambda < 1$ because the axial size is larger than the radial size, while we have an isotropic shape for $\lambda = 1$ when $u_{\rho 0} = u_{z0}$, and we have a pancake-like shape for $\lambda > 1$. In Fig. 2.3(b) we plot the aspect ratio of $u_{\rho 0}/u_{z0}$ as a function of trap anisotropy λ and we see that repulsive interactions decrease (increase) the aspect ratio for cigar- (pancake-) condensates.

Furthermore, for the sake of simplicity, we also determine the isotropic equilibrium position determined from Eq. (2.44) via

$$-\frac{\mathrm{d}}{\mathrm{d}u} V_{\mathrm{eff}}(u)\bigg|_{u=u_0} = 0\,, \tag{2.52}$$

which leads to the condition

$$\mathcal{P} = u_0\left(u_0^4 - 1\right) - \frac{\mathcal{K}}{u_0^3}\,. \tag{2.53}$$

For the case of a pure repulsive two-body interaction, we can immediately see in Fig. 2.4 always one equilibrium solution exist. For the case of an attractive two-body and a repulsive three-body interaction, the problem is different: Eq. (2.53) can have up to three equilibrium solutions. Particular interesting is the stability of all these solutions. In order to determine their stability, the oscillation frequencies of the condensate around these equilibrium points have to be calculated.

2.4. Collective Modes

Frequencies of the low-lying collective modes are determined by linearizing Eq. (2.43) around the equilibrium positions Eqs. (2.47)–(2.49). If we insert the decompositions $u_{x0} = u_{x0} + \delta u_x$, $u_{y0} = u_{y0} + \delta u_y$ and $u_z = u_{z0} + \delta u_z$ into Eq. (2.43) and expand the effective potential into a Taylor series, we get

$$\begin{aligned} V_{\mathrm{eff}}(u_{x0} + \delta u_x, u_{y0} + \delta u_y, u_{z0} + \delta u_z) &= V_{\mathrm{eff}}(u_{x0}, u_{y0}, u_{z0}) \\ &+ \sum_{i=x,y,z}\left[\frac{\lambda_i^2}{2} + \frac{3}{2u_{i0}^4} + \frac{\mathcal{P}}{u_{i0}^2 u_{x0}u_{y0}u_{z0}} + \frac{3\mathcal{K}}{2u_{i0}^2 u_{x0}^2 u_{y0}^2 u_{z0}^2}\right]\delta u_i^2 + \frac{\mathcal{P}}{u_{x0}u_{y0}u_{z0}} \\ &\times\left[\frac{\delta u_x \delta u_y}{u_{x0}u_{y0}} + \frac{\delta u_z \delta u_x}{u_{x0}u_{z0}} + \frac{\delta u_y \delta u_z}{u_{y0}u_{z0}}\right] + \frac{2\mathcal{K}}{u_{x0}^2 u_{y0}^2 u_{z0}^2}\left[\frac{\delta u_x \delta u_y}{u_{x0}u_{y0}} + \frac{\delta u_z \delta u_x}{u_{x0}u_{z0}} + \frac{\delta u_y \delta u_z}{u_{y0}u_{z0}}\right] + \ldots\,, \end{aligned} \tag{2.54}$$

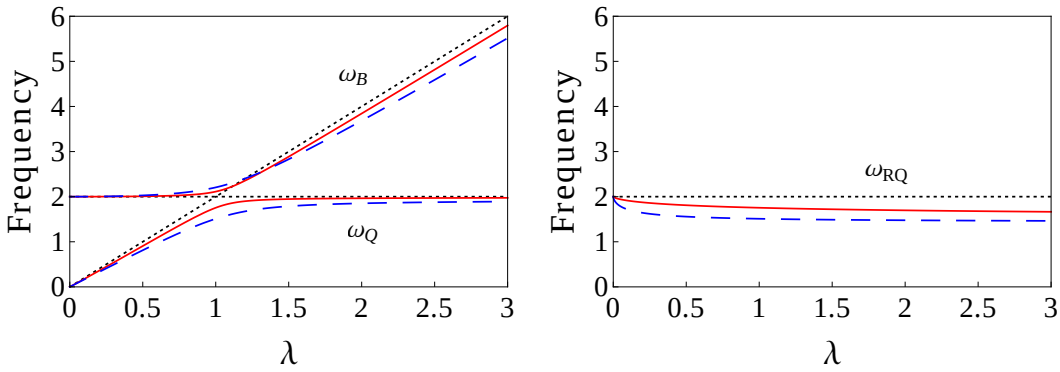

(a) (b)

Figure 2.5.: Frequencies of collective oscillation modes (in units of ω_ρ) for (a) breathing and quadrupole mode and (b) radial quadrupole mode versus trap aspect ratio λ for $\mathcal{P} = 1$, $\mathcal{K} = 0.001$ (solid red lines), $\mathcal{P} = 10$, $\mathcal{K} = 0.1$ (dashed blue lines), and $\mathcal{P} = 0$, $\mathcal{K} = 0$ (dotted black lines).

which can be written in case of an axially-symmetric harmonic trap as

$$V_{\text{eff}}(u_{x0} + \delta u_x, u_{y0} + \delta u_y, u_{z0} + \delta u_z) = V_{\text{eff}}(u_{\rho 0}, u_{z0}) + \frac{1}{2}\delta\mathbf{u}^T M \delta\mathbf{u} + \dots . \tag{2.55}$$

Thus the dynamics for small defections around the equilibrium positions is described by oscillations with the respective amplitudes δu_i. In the following it has to be analysed if the oscillation frequencies are real, complex or even pure imaginary, which would lead to non-stable equilibrium points. Additionally it is possible to determine the oscillation modes once the frequencies are known. Introducing the abbreviations

$$M = \begin{pmatrix} m_1 & m_2 & m_3 \\ m_2 & m_1 & m_3 \\ m_3 & m_3 & m_4 \end{pmatrix} , \quad \delta\mathbf{u} = \begin{pmatrix} \delta u_x \\ \delta u_y \\ \delta u_z \end{pmatrix} , \tag{2.56}$$

$$m_1 = 1 + \frac{3}{u_{\rho 0}^4} + \frac{2\mathcal{P}}{u_{\rho 0}^4 u_{z0}} + \frac{3\mathcal{K}}{u_{\rho 0}^6 u_{z0}^2} , \tag{2.57}$$

$$m_2 = \frac{\mathcal{P}}{u_{\rho 0}^4 u_{z0}} + \frac{2\mathcal{K}}{u_{\rho 0}^6 u_{z0}^2} , \tag{2.58}$$

$$m_3 = \frac{\mathcal{P}}{u_{\rho 0}^3 u_{z0}^2} + \frac{2\mathcal{K}}{u_{\rho 0}^5 u_{z0}^3} , \tag{2.59}$$

$$m_4 = \lambda^2 + \frac{3}{u_{z0}^4} + \frac{2\mathcal{P}}{u_{\rho 0}^2 u_{z0}^3} + \frac{3\mathcal{K}}{u_{\rho 0}^4 u_{z0}^4} , \tag{2.60}$$

the coupled set of differential equation Eq. (2.42) can be rewritten in matrix form:

$$\delta\ddot{\mathbf{u}}(t) + M\delta\mathbf{u}(t) = \mathbf{0} . \tag{2.61}$$

If we insert the solution ansatz

$$\delta\mathbf{u}(t) = \delta\mathbf{u} e^{i\omega t} , \tag{2.62}$$

the frequencies of the collective modes are related to the eigenvalues of the matrix M. The eigenvalue problem reads

$$\left(M - \omega^2 I\right)\delta\mathbf{u} = \mathbf{0} , \tag{2.63}$$

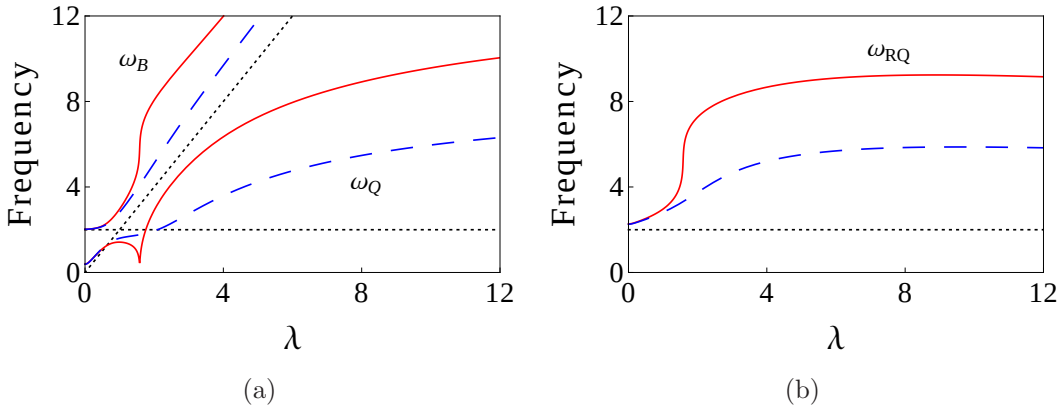

Figure 2.6.: Frequencies of collective oscillation modes (in units of ω_ρ) for (a) breathing and quadrupole mode and (b) radial quadrupole mode versus trap aspect ratio λ for $\mathcal{P} = -0.55$, $\mathcal{K} = 0.012$ (solid red lines), $\mathcal{P} = -0.55$, $\mathcal{K} = 0.02$ (dashed blue lines), and $\mathcal{P} = 0$, $\mathcal{K} = 0$ (dotted black lines).

and non-trivial solutions of Eq. (2.63) exist provided

$$\det(M - \omega^2 I) = 0\,. \tag{2.64}$$

To this end, the frequencies of collective modes are given by

$$\omega_{\mathrm{Q}}^2 = \frac{m_1 + m_2 + m_4 - \sqrt{(m_1 + m_2 - m_4)^2 + 8m_3^2}}{2}\,, \tag{2.65}$$

$$\omega_{\mathrm{B}}^2 = \frac{m_1 + m_2 + m_4 + \sqrt{(m_1 + m_2 - m_4)^2 + 8m_3^2}}{2}\,, \tag{2.66}$$

$$\omega_{\mathrm{RQ}}^2 = m_1 - m_2. \tag{2.67}$$

Note that in the non-interacting limit, the frequencies of the low-lying collective modes are given by

$$\omega_{\mathrm{B}} = \begin{cases} 2 & \lambda \leq 1 \\ 2\lambda & \lambda \geq 1 \end{cases}\,, \qquad \omega_{\mathrm{Q}} = \begin{cases} 2\lambda & \lambda \leq 1 \\ 2 & \lambda \geq 1 \end{cases}\,, \qquad \omega_{\mathrm{RQ}} = 2\,. \tag{2.68}$$

Figures 2.5 and 2.6 show the frequencies of all low-lying collective oscillation modes as functions of the trap aspect ratio λ for both a repulsive and an attractive two-body interaction, respectively. We see that the collective mode frequencies depend relative strongly on the trap anisotropy λ. However, for a repulsive two-body interaction variations of $\mathcal{P}$ and $\mathcal{K}$ yield only marginal changes, see Fig. 2.5, whereas for an attractive two-body interaction the frequencies in Fig. 2.6 depend strongly for varying parameters $\mathcal{P}$ and $\mathcal{K}$.

Inserting those collective frequencies in Eq. (2.63) yields the corresponding eigenvectors. Due to the linear dependence of Eq. (2.63), we use the first two lines in order to calculate the eigenvectors of the respective modes. With this we obtain

$$\delta\mathbf{u}_{\mathrm{RQ}} = \frac{1}{\sqrt{2}} \begin{pmatrix} 1 \\ -1 \\ 0 \end{pmatrix}\,, \tag{2.69}$$

i.e. the frequency ω_{RQ} is characterised by out-of-phase oscillations in the x and y directions, while in the z direction there are no oscillations, which is called 2D-quadrupole mode, see Fig. 2.7(a).

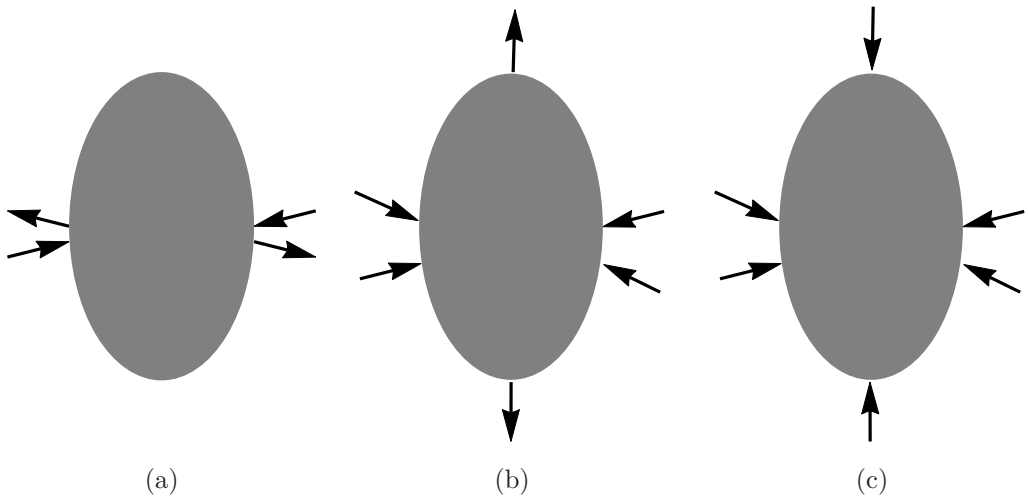

Figure 2.7.: Low-lying collective mode oscillations of the condensate in a cylindrical harmonic trap. (a) Radial quadrupole mode oscillates in x-y plane with frequency Eq. (2.67). (b) Quadrupole mode oscillates out-phase between ρ- and z-components with frequency Eq. (2.65). (c) Breathing mode oscillates in-phase between ρ- and z-components with frequency Eq. (2.66).

Furthermore, we get

$$\delta\mathbf{u}_{\mathrm{B,Q}} = \frac{m_3}{\sqrt{2m_3^2 + \left(m_1 + m_2 - \omega_{\mathrm{B,Q}}^2\right)^2}} \begin{pmatrix} 1 \\ 1 \\ \frac{m_1+m_2-\omega_{\mathrm{Q,B}}^2}{m_3} \end{pmatrix}, \tag{2.70}$$

where the quadrupole mode eigenvector $\delta\mathbf{u}_Q$ has the lower frequency and is characterized by out-of phase radial and axial oscillations, see Fig. 2.7(b), while the breathing mode eigenvector $\delta\mathbf{u}_B$ corresponds to in-phase radial and axial oscillations, see Fig. 2.7(c).

The TF limit corresponds to the limit $\mathcal{P} \to \infty$, so that Eqs. (2.50) and (2.51) for the equilibrium positions reduce to

$$u_{\rho 0} = \lambda u_{z0}, \qquad \mathcal{P} = \frac{-\mathcal{K} + u_{\rho 0}^6 u_{z0}^2}{u_{\rho 0}^2 u_{z0}}. \tag{2.71}$$

By using Eqs. (2.71) together with Eqs. (2.57)–(2.60) into Eqs. (2.65)–(2.67), we obtain

$$\begin{aligned} \omega_{\mathrm{B,Q}}^2 =& 2 + \frac{3\lambda^2}{2} - \frac{\mathcal{K}\lambda^2}{u_{\rho 0}^8} + \frac{\mathcal{K}\lambda^4}{2u_{\rho 0}^8} \\ & \pm \frac{1}{2}\sqrt{16 - 16\lambda^2 + 9\lambda^4 - \frac{16\mathcal{K}\lambda^2}{u_{\rho 0}^8} + \frac{4\mathcal{K}^2\lambda^4}{u_{\rho 0}^{16}} + \frac{4\mathcal{K}\lambda^4}{u_{\rho 0}^8} + \frac{4\mathcal{K}^2\lambda^6}{u_{\rho 0}^{16}} + \frac{6\mathcal{K}\lambda^6}{u_{\rho 0}^8} + \frac{\mathcal{K}^2\lambda^8}{u_{\rho 0}^{16}}}, \end{aligned} \tag{2.72}$$

$$\omega_{\mathrm{RQ}}^2 = 2 \tag{2.73}$$

The main result obtained by using the Gaussian approximation is an analytical estimate for the frequencies of the low-lying collective modes in the TF approximation, expressed by Eqs. (2.65)–(2.67) [84,85]. We emphasize that, although based on the Gaussian ansatz, the variational approximation reproduces the frequencies of collective modes not only for weakly interacting BEC, but also for the strongly interacting BEC in the Thomas-Fermi regime [70,84]. Therefore, it represents a solid

analytical description of the BEC dynamics. Most importantly, a reasonable quantitative agreement was obtained between the linear response theoretical results Eqs. (2.65)–(2.67) and experimental results for a BEC excited by using the trap modulation [65]. In general, a detailed experimental information on collective modes allows to test our theoretical understanding of the properties of an atomic BEC. The essential merit of testing theoretical predictions using collective oscillation modes stems from the possibility to measure frequencies of collective modes with a high accuracy on the order of less than 1% [64,66,67].

2.5. Stability Diagram

In this section we discuss the stability of a Bose-Einstein condensate in the mean-field framework for systems with two- and three-body contact interaction in an axially-symmetric harmonic trap. It is well known that BEC systems with an attractive two-body interaction are unstable against collapse above a critical number of atoms i.e. for sufficiently large negative value of $\mathcal{P}$ in the condensate [49,50]. For smaller numbers of atoms, the zero-point kinetic energy is able to counter the attractive inter-atomic interactions, however, when the number of atoms sufficiently increases, this is no longer possible, and the system collapses to the centre of the trapping potential.

We find that, for a pure two-body interaction, the condensate is stable only above a critical stability line $\mathcal{P}_c(\lambda)$, while the presence of even a small repulsive three-body interaction leads to a stabilisation of the condensate. On the other hand, we find that an attractive three-body interaction further destabilises the condensate.

To study in detail effects of three-body interaction on the stability of BEC systems, we consider several cases of interest: repulsive and attractive pure two-body interactions, attractive two-body and repulsive three-body interactions, and attractive two- and three-body interactions. If the corresponding system of equations does (not) have positive and bounded solutions of equations (2.35)–(2.37) in the vicinity of positive equilibrium widths determined by equations (2.50) and (2.51), then the condensate is considered stable (unstable). This is equivalent to performing a linear stability analysis and determining the stability of positive equilibrium widths by examining the frequencies of the low-lying collective oscillation modes (2.65)–(2.67). The solution is only stable if the frequencies of all low-lying collective modes are found to be real, otherwise the solution is unstable.

For the case of a pure repulsive two-body interaction, we will immediately see that the condensate is always stable. For the case of an attractive two-body interaction, the situation is quite different: the above system of equations can have no equilibrium, or it could have up to three equilibrium solutions. The results of a detailed numerical analysis are summarised in Fig. 2.8.

The dashed red line in Fig. 2.8(a) represents the critical stability line as a function of the trap aspect ratio λ for a pure two-body interaction ($\mathcal{K} = 0$). Below the critical stability line there are no stable solutions, and the system is unstable. Above the critical stability line, the system has one stable and one unstable solution for an attractive two-body interaction ($\mathcal{P} < 0$), and only one stable solution for a repulsive two-body interaction ($\mathcal{P} \geq 0$). For $\lambda = 0$, which corresponds to the limit of a cigar-shaped condensate, we have the critical value of two-body interactions $\mathcal{P}_c = -0.6204$, which coincides precisely with the value from Ref. [85]. For the isotropic case, when $\lambda = 1$, the critical value is $\mathcal{P}_c = -0.535$, which again coincides with the value from the literature [85,63,158,159]. Fig. 2.9(a) shows solutions for the isotropic condensate as a function of $\mathcal{P}$.

Now, if we consider the case of an attractive two-body interaction and a small repulsive three-body interaction, the results of the stability analysis are quite different. The system can either have one or three solutions, as shown in Fig. 2.8(b). The presence of a positive three-body interaction $\mathcal{K}$, however small, leads to the existence of at least one stable solution in the whole range of values of λ and $\mathcal{P}$. In

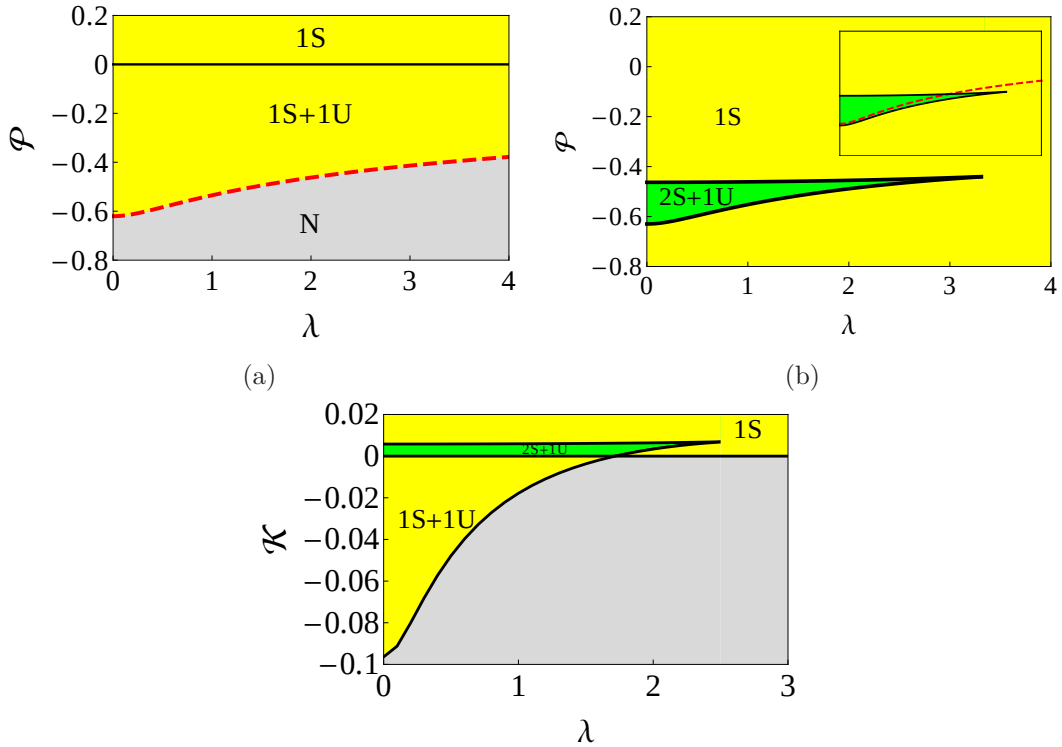

(a) (b) (c)

Figure 2.8.: Stability diagram of a BEC as a function of trap aspect ratio λ for different values of dimensionless two-body and three-body contact interaction strengths $\mathcal{P}$ and $\mathcal{K}$. (a) λ-$\mathcal{P}$ stability diagram for $\mathcal{K} = 0$, where the dashed red line represents the critical stability line, below which there are no solutions (N). Above this line, for $\mathcal{P} < 0$, there is one stable and one unstable solution (1S+1U), while for $\mathcal{P} \geq 0$ there is only one stable solution (1S). (b) λ-$\mathcal{P}$ stability diagram for $\mathcal{K} = 0.005$, where two cases exist: the small region with two stable and one unstable solution (2S+1U), while otherwise only one stable solution exists (1S). For comparison, in the inset we combine the critical stability line for $\mathcal{K} = 0$ with the stability diagram for $\mathcal{K} = 0.005$. (c) λ-$\mathcal{K}$ stability diagram for $\mathcal{P} = -0.5$. For $\mathcal{K} \leq 0$, there are two regions: the one without solutions (N), and the one with one stable and one unstable solution (1S+1U). For $\mathcal{K} > 0$, there are also two regions: the small region with two stable and one unstable solution (2S+1U), while otherwise there is only one stable solution (1S). As we can see, a non-vanishing value of the three-body interaction $\mathcal{K}$ substantially enhances the stability of a condensate.

the small area designated by 2S+1U in Fig. 2.8(b), two stable and one unstable solution exist. Out of these two stable solutions, only the one with the minimal energy is physically relevant and could be realised in an experiment. Figure 2.9(b) shows solutions for $\lambda = 1$, $\mathcal{K} = 0.005$ as a function of $\mathcal{P}$. As we can see, a minimal-energy stable solution exists for any value of $\mathcal{P}$. However, for large negative values of $\mathcal{P}$ this solution tends to zero, which practically represents a collapsed condensate. Therefore, although within the given mathematical model the condensate is always stable, physically this is valid only up to a critical number of atoms, which has to be determined by considering in detail the corresponding condensate density. However, as we can see from Fig. 2.9(b), the dependence $u_0(\mathcal{P})$ for large negative values of $\mathcal{P}$ is quite flat, which means that the stability region can be significantly extended in the presence of a small positive value of $\mathcal{K}$ compared to the case of pure two-body interaction.

We also analyse the stability of a BEC system as a function of three-body interaction $\mathcal{K}$. Figure

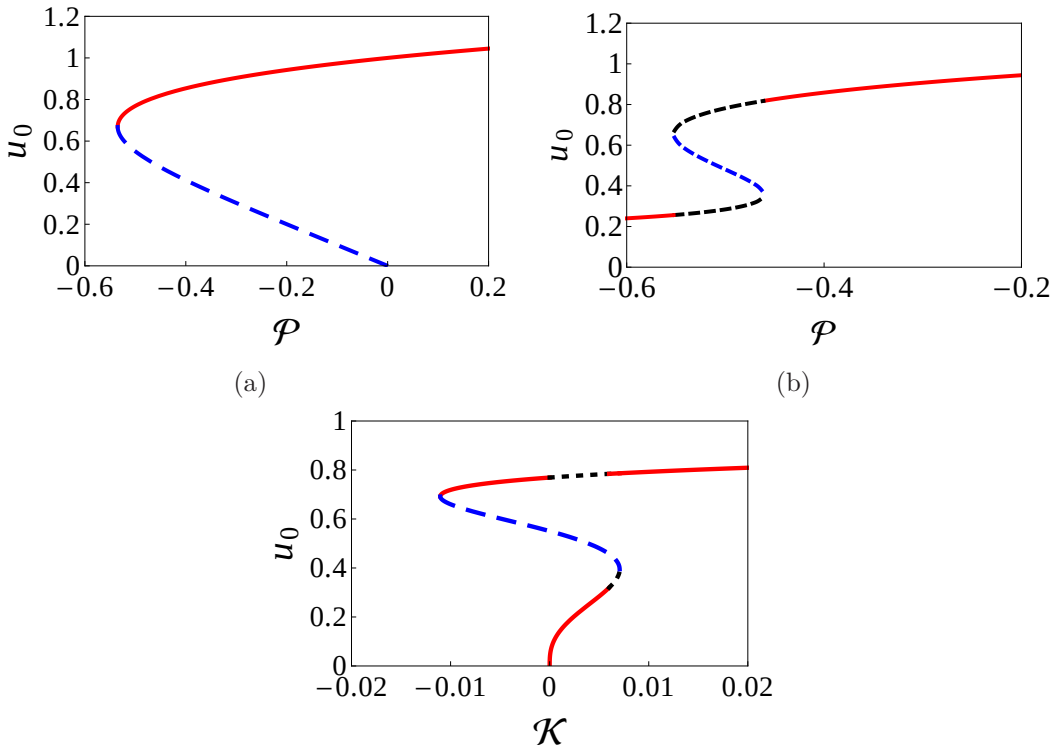

Figure 2.9.: Condensate width $u_{\rho 0} = u_{z0} = u_0$ for $\lambda = 1$ and (a) $\mathcal{K} = 0$, as a function of $\mathcal{P}$; (b) $\mathcal{K} = 0.005$, as a function of $\mathcal{P}$; (c) $\mathcal{P} = -0.5$, as a function of $\mathcal{K}$. Solid red lines represent the stable solution with minimal energy, dotted black lines represent another stable solution, dashed blue lines represent unstable solution.

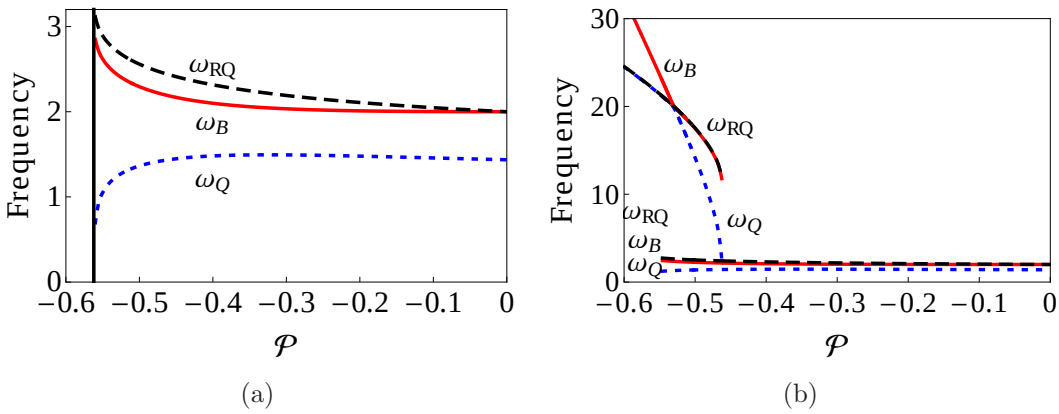

Figure 2.10.: Frequencies (in units of ω_ρ) of low-lying collective excitation modes: breathing (B), radial quadrupole (RQ), and quadrupole (Q) mode frequency, as functions of an attractive two-body interaction $\mathcal{P}$ for the trap anisotropy $\lambda = 117/163$ and (a) $\mathcal{K} = 0$, (b) $\mathcal{K} = 0.005$.

2.8(c) shows the corresponding stability diagram for an attractive two-body interaction $\mathcal{P} = -0.5$. For a repulsive three-body interaction ($\mathcal{K} > 0$), as expected, we see a small region with two stable and one unstable solution (2S+1U), as well as a region with only one stable solution (1S), similar to Fig. 2.8(b). For an attractive three-body interaction ($\mathcal{K} < 0$), the stability region with one stable and one unstable solution (1S+1U), which corresponds to the 1S+1U region in Fig. 2.8(a), gradually shrinks until it disappears as $\mathcal{K}$ becomes sufficiently negative. Therefore, we see that an attractive three-body

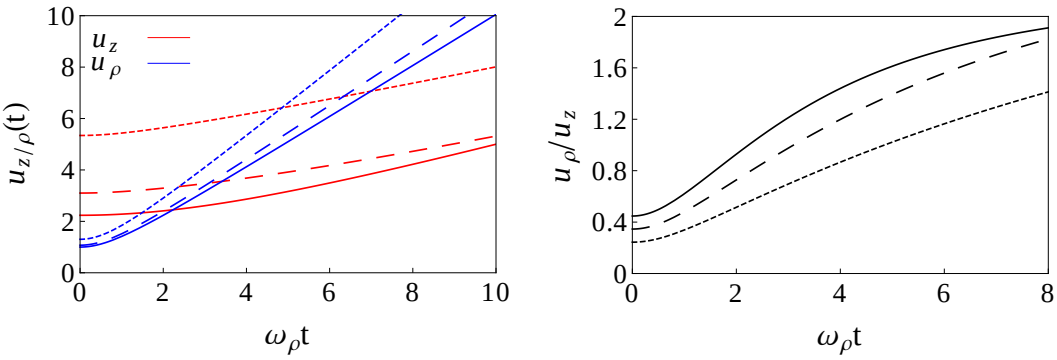

(a) (b)

Figure 2.11.: Evolution in time of (a) the spatial extensions u_ρ, u_z and (b) the aspect ratio u_ρ/u_z for the systems of two- and three-body interactions strength after turning off the trapping potential for trap anisotropy $\lambda = 0.2$. Solid curves correspond to the case of a no interaction $\mathcal{P} = 0$ and $\mathcal{K} = 0$, while dashed curves correspond to a system of repulsive two-body $\mathcal{P} = 1$ and three-body $\mathcal{K} = 0.001$ interaction strengths, and dotted curves correspond to the systems of repulsive two- and three-boy interaction strengths, $\mathcal{P} = 10$ and $\mathcal{K} = 0.1$, respectively.

interaction has the same destabilising effect on a BEC as an attractive two-body interaction. This can be also seen in Fig. 2.9(c), where the stable minimal-energy solution for $\mathcal{P} = -0.5$ exists only for a limited range of negative values of $\mathcal{K}$.

To further illustrate the findings of the above stability analysis, we plot in Fig. 2.10 the frequencies of the low-lying collective excitation modes as functions of an attractive two-body interaction for the trap anisotropy $\lambda = 117/163$ [24]. Fig. 2.10(a) corresponds to the case when three-body interactions are neglected, i.e. $\mathcal{K} = 0$, and we can see that the condensate collapses for $\mathcal{P}_c = -0.561$, when the expression for ω_Q^2 from equation (2.65) becomes negative. For a small repulsive three-body interaction $\mathcal{K} = 0.005$, Fig. 2.10(b) shows the frequencies corresponding to stable minimum-energy solutions. From Fig. 2.9(b) we see that for $\mathcal{P}_c = -0.486$ there is a jump from one to another solution branch due to the minimal energy condition, which is reflected in Fig. 2.10(b) by a corresponding jump in the frequencies of the collective modes.

2.6. Time-of-Flight Expansion

A time-of-flight experiment is one of the most interesting features in the realm of ultracold quantum gases. This technique was first demonstrated in 1995 for detecting Bose-Einstein condensation, where the atoms were allowed to expand after switching off the trap and imaged by absorption methods showing a characteristic peak in the momentum distribution [20,22,23].

We study in this section the free expansion of a BEC in case of an axially-symmetric harmonic trap by solving Eqs. (2.35)–(2.37) without the term, which represents the harmonic trap:

$$\ddot{u}_\rho - \frac{1}{u_\rho^3} - \frac{\mathcal{P}}{u_\rho^3 u_z} - \frac{\mathcal{K}}{u_\rho^5 u_z^2} = 0\,, \tag{2.74}$$

$$\ddot{u}_z - \frac{1}{u_z^3} - \frac{\mathcal{P}}{u_\rho^2 u_z^2} - \frac{\mathcal{K}}{u_\rho^4 u_z^3} = 0\,. \tag{2.75}$$

The initial condition needed for solving Eqs. (2.74) and (2.75) are obtained from the equilibrium

positions Eq. (2.50) and (2.51) and their vanishing derivatives at $t = 0$, i.e.

$$\dot{u}_\rho(t = 0) = \dot{u}_z(t = 0) = 0, \tag{2.76}$$

For the non-interacting case, one expects from Eqs. (2.74) and (2.75), that both radii will expand with a time scale which is given by respective inverse trap frequency. For systems of two- and three-body interaction strengths the expansions rate of the radii increases.

In Fig. 2.11 we show the resulting time-of-flight dynamics for systems of two- and three-body interaction strengths for the trap anisotropy $\lambda = 0.2$. We plot the radial and axial extensions as a function of time $\omega_\rho t$, where the solid curves are corresponding to the non-interacting case $\mathcal{P} = \mathcal{K} = 0$, while the dashed curves correspond to systems of two-body interaction strength $\mathcal{P} = 1$ and three-body interaction strength $\mathcal{K} = 0.001$ and the dotted dashed curves are corresponding to a system of two- and three-body interaction strengths $\mathcal{P} = 10$ and $\mathcal{K} = 0.1$. It becomes clear that a cigar-like condensate expands much faster in the radial than in the axial direction and that the condensate aspect ratio is inverted due to the Heisenberg principle.

3. Parametric Resonances

Parametric resonance is an interesting phenomenon in the realm of ultracold quantum gases. It occurs during a harmonic modulation of either the trapping potential [21,46,104] or the interaction [63,93,109,229,230], when the external driving frequency equals to the frequency of one collective oscillation mode of a Bose-Einstein condensate.

Such a resonance phenomenon in the oscillation of a BEC governed by the GP equation Eq. (2.12) can also be studied experimentally so that one can compare theoretical predictions with experimental measurements. In the experimental of Ref. [93], a new way of a condensate excitation has been demonstrated. The broad Feshbach resonance of ^{7}Li, see Ref. [87], allows a modulation of the atomic s-wave scattering length according to Eq. (1.2), with $N = 3 \times 10^5$ atoms, $\omega_\rho = 2\pi \times 4.85$ Hz, and $\omega_z = 2\pi \times 235$ Hz. The authors fit the axial time evolution of the cloud size after such a modulation to the function [93]

$$u_z(t) = u_{z0} + u_{z,\Omega} \sin(\Omega t + \Phi) + u_{z,Q} \sin(\omega_Q t + \phi), \tag{3.1}$$

where u_{z0} is the equilibrium size, $u_{z,\Omega}$ and $u_{z,Q}$ denote the respective amplitude of the driving and the quadrupole mode, respectively, and Φ and ϕ are corresponding phases. The main experimental result is the resonance curve shown in Fig. 3.1. The axial excitation amplitude as a function of the external driving frequency Ω reveals a double peak structure. The larger peak appears at the quadrupole mode frequency, i.e. at 9 Hz, and thus represents the main resonance, whereas a smaller peak occurs at twice the quadrupole mode, frequency i.e. at 18 Hz, and can, therefore, be identified with a parametric resonance in Fig. 3.1 [93].

Motivated by the experimental study, described in Ref. [93], we follow Ref. [109] and consider in this chapter dynamical features induced by a harmonic modulation of the s-wave scattering length. Our study is a step beyond the linear regime, toward the resonant behavior, and it is suited for the parametric region where low-lying collective modes can still be defined as in the linear regime, but their properties are modified by nonlinear effects. The obtained results are relevant for the proper interpretation of experimental data, and for an understanding of near-resonant properties of nonlinear systems. In the following, we study the nonlinear dynamical regime induced by a harmonic modulation of the s-wave scattering length, first for a spherically symmetric BEC in Sec. 3.1, afterwards, for an axially-symmetric BEC in Sec. 3.2. In both cases, we obtain excitation spectra as Fourier transforms of the time-dependent condensate sizes and from there we identify nonlinear features. In addition, we develop a perturbation theory based on the Poincaré-Lindstedt method which successfully explains the observed nonlinear effects. In particular, we discuss the relevance of our results for future experimental setups in the spirit of Ref. [93].

In order to study nonlinear BEC dynamics, we use an approach that is complementary to the recent theoretical considerations [231–234] of a BEC with harmonically modulated interaction. In Ref. [233] the real-time dynamics of a spherically symmetric BEC was numerically studied and analytically explained using the resonant Bogoliubov-Mitropolsky method [235]. On the other hand, in our approach in order to discern induced dynamical features, we look directly at the excitation spectrum obtained from a Fourier transform of the time-dependent condensate width. From this type of numerical analysis we find characteristic nonlinear properties: higher harmonic generation, nonlinear mode coupling, and significant shifts in the frequencies of collective modes with respect to their linear response coun-

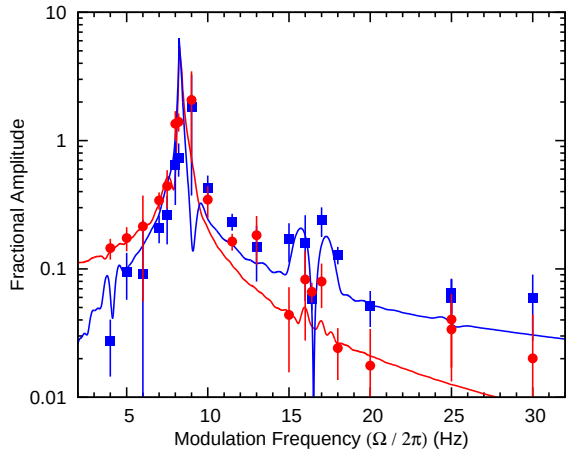

Figure 3.1.: Experimental resonance curve for the axial excitation amplitude of the driving $u_{z,\Omega}/u_{z0}$ (red circles) and the quadrupole mode u_{zQ}/u_{z0} (blue squares) as a function of the external driving frequency Ω [93].

terparts. In addition, we work out an analytic perturbative theory with respect to the modulation amplitude which is capable of capturing many of the mentioned nonlinear effects obtained numerically.

Nonlinearity-induced frequency shifts were considered previously in Ref. [105] for the case of bosonic collective modes excited by modulation of the trapping potential, and also in Ref. [119] for the case of a superfluid Fermi gas in the BCS-BEC crossover. Our analytical approach is based on the Poincaré-Lindstedt method [235–238], in the same spirit as presented in Refs. [105,119,238]. However, the harmonic modulation of the interaction strength introduces additional features that require a separate treatment. In Ref. [231] it was predicted that a harmonic modulation of the scattering length leads to the creation of Faraday patterns in BEC, i.e. density waves. Up to now, Faraday patterns have been experimentally induced by harmonic modulation of the transverse confinement strength [100], which is studied analytically and numerically in Ref. [239]. Here we focus only on the nonlinear properties of low-lying collective modes and do not consider possible excitations of Faraday patterns.

In order to obtain analytical insight into the condensate dynamics induced by the harmonic modulation of the s-wave scattering length described by Eq. (1.2), we use the Gaussian variational approximation by considering an axially-symmetric BEC, i.e. $\lambda_x = \lambda_y = 1, u_x = u_y = u_\rho$, excited by a modulation of the two-interaction strength, which preserves the axial symmetry of the condensate during its time evolution. As we do not take into the account the three-body interaction, i.e. we put $\mathcal{K} = 0$, the equations of the condensate widths Eqs. (2.35)–(2.37) can be written as

$$\ddot{u}_\rho + u_\rho - \frac{1}{u_\rho^3} - \frac{\mathcal{P}(t)}{u_\rho^3 u_z} = 0\,, \tag{3.2}$$

$$\ddot{u}_z + \lambda^2 u_z - \frac{1}{u_z^3} - \frac{\mathcal{P}(t)}{u_\rho^2 u_z^2} = 0\,. \tag{3.3}$$

In the previous set of equations and in all equations that follow, we have expressed all lengths in the units of the characteristic radial oscillator length $l = \sqrt{\hbar/m\omega_\rho}$ and the time in units of ω_ρ^{-1}. The dimensionless interaction parameter $\mathcal{P}(t)$ is defined in Eq. (2.38). Taking into account Eq. (1.2), we have

$$\mathcal{P}(t) = \mathcal{P} + \mathcal{Q}\cos\Omega t, \tag{3.4}$$

where $\mathcal{P} = \sqrt{2/\pi}Na_{\rm av}/l$ denotes the average interaction strength, $\mathcal{Q} = \sqrt{2/\pi}N\delta_a/l$ stands for a modulation amplitude, and Ω represents the driving frequency measured now in units of ω_ρ.

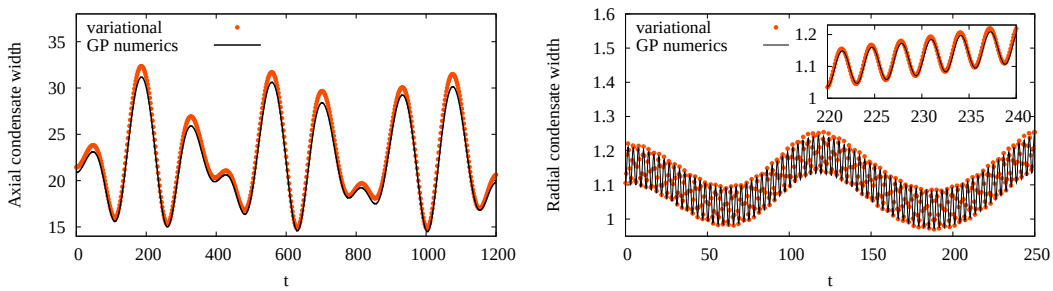

Figure 3.2.: Time-dependent axial and radial condensate widths calculated as root mean square averages. Comparison of the numerical solution of time-dependent GP equation with a solution obtained by using the Gaussian approximation for the actual experimental parameters $\lambda = 0.021$, $\mathcal{P} = 15$, $\mathcal{Q} = 10$, and $\Omega = 0.05$ [93].

To estimate the accuracy of the Gaussian approximation for describing the dynamics induced by the harmonic modulation of the interaction strength, we compare the solution of Eqs. (3.2), (3.3) with an exact numerical solution of the underlying GP equation. In Fig. 3.2, we plot the resulting time-dependent axial and radial condensate widths $\rho_{\rm rms}(t)$ and $z_{\rm rms}(t)$, calculated as root mean square values

$$\rho_{\rm rms}(t) = \sqrt{2\pi \int_{-\infty}^{\infty} dz \int_0^{\infty} \rho\, d\rho\, |\psi(\rho, z, t)|^2\, \rho^2}\,, \tag{3.5}$$

$$z_{\rm rms}(t) = \sqrt{2\pi \int_{-\infty}^{\infty} dz \int_0^{\infty} \rho\, d\rho\, |\psi(\rho, z, t)|^2\, z^2}\,, \tag{3.6}$$

of the solution of the GP equation, as well as the numerical solutions of Eqs. (3.2) and (3.3). We assume that, initially, the condensate is in the ground state. In the variational description, this translates into the initial conditions $u_\rho(0) = u_{\rho 0}$, $\dot{u}_\rho(0) = 0$, $u_z(0) = u_{z0}$, $\dot{u}_z(0) = 0$, where $u_{\rho 0}$ and u_{z0} are the time-independent solutions.

We plot in Fig. 3.2 the real-time dynamics where we observe the excitation of the slow quadrupole mode as an out-of phase oscillation in the axial and in the radial direction. In addition, in the radial direction we observe fast breathing mode oscillations. This is typical for highly elongated condensates [240] and our analysis for the experimental parameters shows a strong excitation of the quadrupole mode, but also a significant excitation of the breathing mode in the radial direction. Good agreement of real-time dynamics obtained from the variational approximation with the exact solution of the time-dependent GP simulation occurs even for long propagation times according to Fig. 3.2. This implies a good accuracy of the Gaussian approximation for calculating the frequencies of the excited modes.

3.1. Spherical-Symmetry Trap

Using a simple symmetry-based reasoning, we conclude that a harmonic modulation of interaction strength in the case of a spherically symmetric BEC, i.e. $\lambda = 1$, leads to the excitation of the breathing mode only, so that $u_\rho(t) = u_z(t) \equiv u(t)$ [109]. This fact simplifies numerical and analytical calculations and this is why we first consider this case before we embark on the study of a more complex axially symmetric BEC. Thus, the system of ordinary differential Eqs. (3.2) and (3.3) reduces to a single

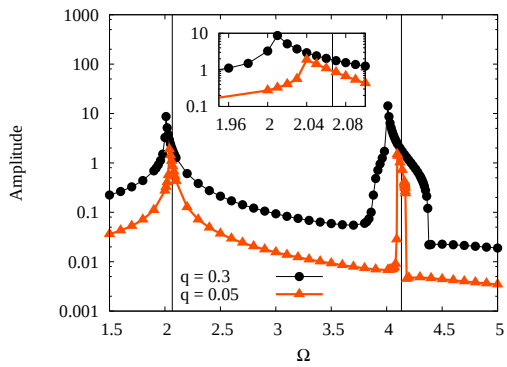

Figure 3.3.: Oscillation amplitude $(u_{\max} - u_{\min})/2$ versus driving frequency Ω for $\mathcal{P} = 0.4$. In the inset, we zoom to the first peak to emphasize that the shape and value of a resonance occur at a driving frequency Ω which differs from ω_0 and depends on the modulation amplitude $\mathcal{Q}$. The solid vertical lines correspond to ω_0 and $2\omega_0$.

equation:

$$\ddot{u} + u(t) - \frac{1}{u^3} - \frac{\mathcal{P}(t)}{u^4} = 0\,. \tag{3.7}$$

The equilibrium condensate width u_0 satisfies

$$u_0 - \frac{1}{u_0^3} - \frac{\mathcal{P}}{u_0^4} = 0\,, \tag{3.8}$$

and a linear stability analysis yields the breathing mode frequency

$$\omega_0 = \sqrt{1 + \frac{3}{u_0^4} + \frac{4\mathcal{P}}{u_0^5}}\,. \tag{3.9}$$

Note that the above result for the breathing mode can be also obtained from Eq. (2.66) if we set $\lambda = 1$, $u_{\rho 0} = u_{z0} \equiv u_0$, and take into account Eq. (3.8).

3.1.1. Numerical Simulations

The main feature of the modulation induced dynamics is that it strongly depends on the value of the driving frequency Ω. To illustrate this, we set $\mathcal{P} = 0.4$, $\mathcal{Q} = 0.1$ and solve Eq. (3.7) for different values of Ω. From the linear response theory, we have $u_0 = 1.08183$, $\omega_0 = 2.06638$ and we assume that the condensate is initially in equilibrium, i.e. $u(0) = u_0, \dot{u}(0) = 0$.

The phenomenology based on Eq. (3.7) is more systematically shown in Fig. 3.3 where we plot the oscillation amplitude defined as $(u_{\max} - u_{\min})/2$ versus the driving frequency Ω. A resonant behavior becomes apparent for both $\Omega \approx \omega_0$ and $\Omega \approx 2\omega_0$ in qualitative agreement with the experimental resonance curve of Fig. 3.1. In the same figure we also show the expected positions of resonances calculated using the linear stability analysis. Clearly, the prominent peaks exhibit shifts with respect to the solid vertical lines representing ω_0 and $2\omega_0$. As expected, a stronger modulation amplitude leads to a larger frequency shift, as can be seen from the inset. The curves presented in Fig. 3.3 are obtained by an equidistant sampling of the external driving frequency Ω. In addition to the expected resonances close to ω_0 and $2\omega_0$, a more thorough exploration of solutions of the variational equation Eq. (3.7) shows that also other "resonances" are present such as, e. g. at $\Omega \approx \omega_0/2$ and $\Omega \approx 2\omega_0/3$. This is further demonstrated in Fig. 3.4. These "resonances" are harder to observe

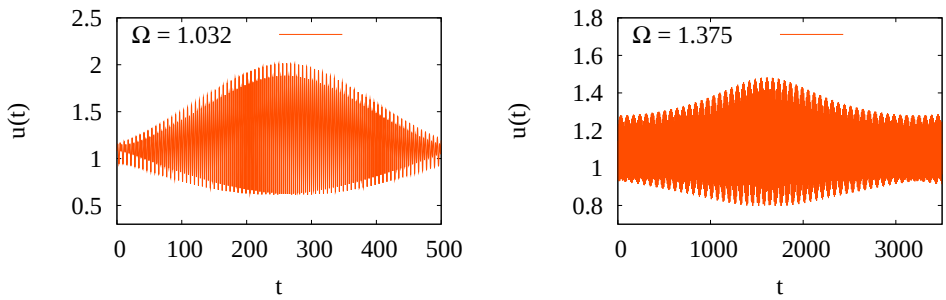

Figure 3.4.: Exact numerical solution of Eq. (3.7) for the condensate width $u(t)$ versus t for $\mathcal{P} = 0.4$, $\mathcal{Q} = 0.3$, corresponding to $\omega_0 = 2.06638$. We observe large amplitude oscillations for $\Omega \approx \omega_0/2$ in the top panel, while in the bottom panel a "resonant" behavior is also detected for $\Omega \approx 2\omega_0/3$.

numerically, since it is necessary to perform a fine tuning of the external frequency. However, their presence clearly demonstrates nonlinear BEC properties and an experimental observation of these phenomena is certainly of high interest. We note that the observed resonance pattern of the form $\Omega \approx 2\omega_0/n$ (where n is an integer) arises also in the case of a parametrically driven system described by the Mathieu equation, for instance, in the context of the Paul trap [241]. To examine such excited modes directly, we look at the Fourier transform of the condensate width $u(t)$.

To this end, we numerically solve Eq. (3.7) and find the Fourier transform of its solution using the Mathematica software package [242]. An example of such an excitation spectrum for $\mathcal{P} = 0.4$, $\mathcal{Q} = 0.1$, and $\Omega = 2$ is given in Fig. 3.5. The spectrum contains two prominent modes - a breathing mode of frequency ω (close, but not equal to ω_0) and a mode that corresponds to the driving frequency Ω, along with many higher-order harmonics which are of the general form $m\Omega + n\omega$, where m and n are integers. In Fig. 3.6 we juxtapose two zoomed Fourier spectra for two different driving frequencies for $\mathcal{P} = 0.4$ and $\mathcal{Q} = 0.2$. On the left plot, we show the zoomed spectrum for $\Omega = 1$. The vertical solid line corresponds to ω_0 and we find the peak in the spectrum that lies almost precisely at this position. On the contrary, from the right plot of Fig. 3.6, that corresponds almost to the resonant excitation $\Omega = 2$, we see that the prominent peak is displaced from the vertical line. This is the most clear-cut illustration of the shifted eigenfrequency arising due to the nonlinearity of the underlying dynamical equations. Our objective is now to develop an analytical approach, which is capable of taking into account these nonlinear effects.

3.1.2. Poincaré-Lindstedt Method

In its essence, our analytical approach represents the standard Poincaré-Lindstedt method [235,238,237,236]. Linearizing the variational equation (3.7) around the time-independent solution u_0 for vanishing driving $\mathcal{Q} = 0$, we obtain the zeroth-order approximation for the collective mode $\omega = \omega_0$ expressed by Eq. (3.9). To calculate the collective mode to higher orders, we explicitely introduce the sought-after eigenfrequency ω into the calculation by rescaling the time from t to $t = \omega t$, yielding the equation:

$$\omega^2\,\ddot{u}(t) + u(t) - \frac{1}{u(t)^3} - \frac{\mathcal{P}}{u(t)^4} - \frac{\mathcal{Q}}{u(t)^4}\cos\frac{\Omega t}{\omega} = 0\,. \tag{3.10}$$

In the next step, we assume the following perturbative expansions in the modulation amplitude $\mathcal{Q}$:

$$u(t) = u_0 + \mathcal{Q}\,u_1(t) + \mathcal{Q}^2\,u_2(t) + \mathcal{Q}^3\,u_3(t) + \dots\,, \tag{3.11}$$

$$\omega = \omega_0 + \mathcal{Q}\,\omega_1 + \mathcal{Q}^2\,\omega_2 + \mathcal{Q}^3\,\omega_3 + \dots\,, \tag{3.12}$$

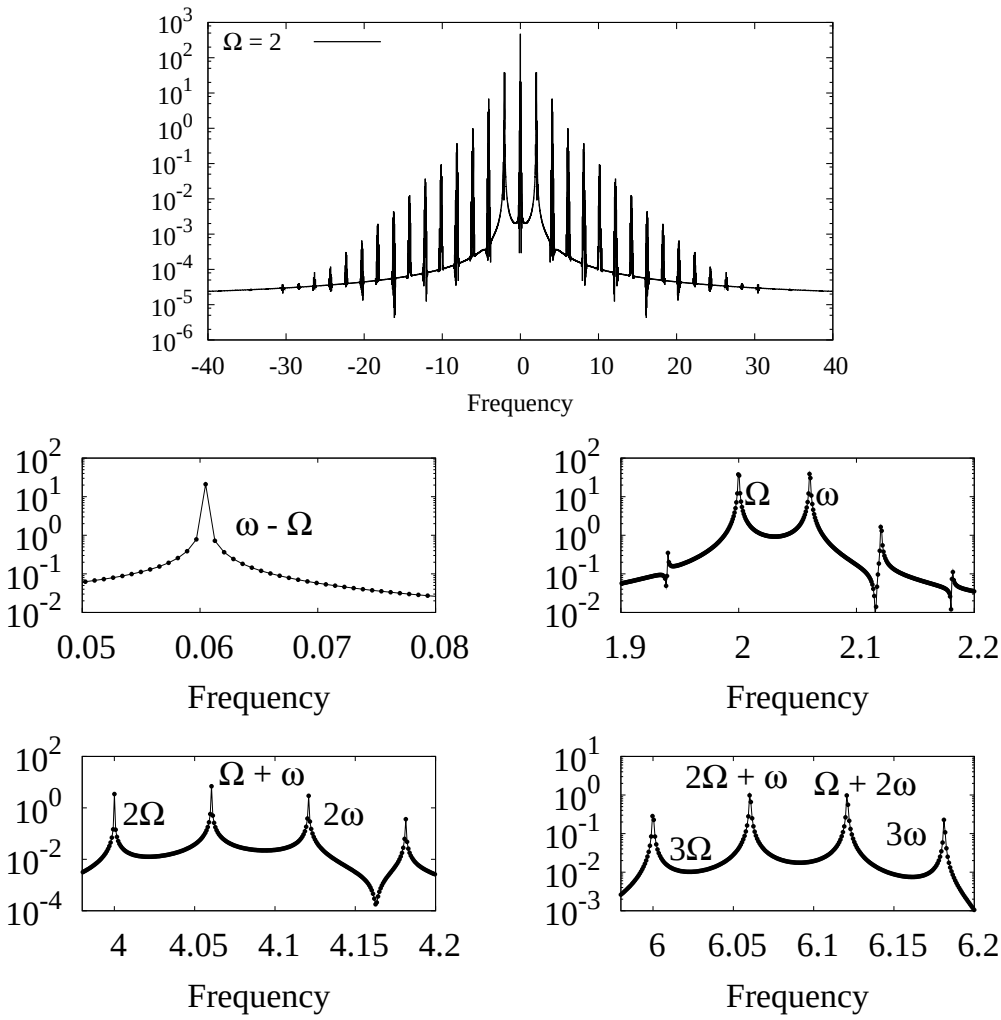

Figure 3.5.: Fourier transform of $u(t)$ for $\mathcal{P} = 0.4$, $\mathcal{Q} = 0.1$, and $\Omega = 2$. First plot presents the complete spectrum on a semi-log scale, while the subsequent plots focus on particular regions of interest in the spectrum.

where we expand ω around ω_0 and introduce frequency shifts $\omega_1, \omega_2, \ldots$ for each order in the expansion in $\mathcal{Q}$. By inserting the above expansions into the Eq. (3.10) and by collecting terms of the same order in $\mathcal{Q}$, we obtain a hierarchical system of linear differential equations. Up to the third order, we find:

$$\omega_0^2 \ddot{u}_1(t) + \omega_0^2 u_1(t) = \frac{1}{u_0^4} \cos \frac{\Omega t}{\omega}, \tag{3.13}$$

$$\omega_0^2 \ddot{u}_2(t) + \omega_0^2 u_2(t) = -2\omega_0\omega_1 \ddot{u}_1(t) - \frac{4}{u_0^5} u_1(t) \cos \frac{\Omega t}{\omega} + \alpha u_1(t)^2, \tag{3.14}$$

$$\begin{aligned} \omega_0^2 \ddot{u}_3(t) + \omega_0^2 u_3(t) = & -2\omega_0\omega_2 \ddot{u}_1(t) - 2\beta u_1(t)^3 + 2\alpha u_1(t) u_2(t) - \omega_1^2 \ddot{u}_1(t) \\ & + \frac{10}{u_0^6} u_1(t)^2 \cos \frac{\Omega t}{\omega} - \frac{4}{u_0^5} u_2(t) \cos \frac{\Omega t}{\omega} - 2\omega_0 \omega_1 \ddot{u}_2(t), \end{aligned} \tag{3.15}$$

where we have introduced $\alpha = 10\,\mathcal{P}/u_0^6 + 6/u_0^5$ and $\beta = 10\,\mathcal{P}/u_0^7 + 5/u_0^6$.

These equations disentangle in a natural way: we solve the first one for $u_1(t)$ and use that solution to solve the second one for $u_2(t)$ and so on. At the n-th level of the perturbative expansion with $n \geq 1$ we use the initial conditions $u_n(0) = 0, \dot{u}_n(0) = 0$. As is well known, the presence of the term $\cos t$ on

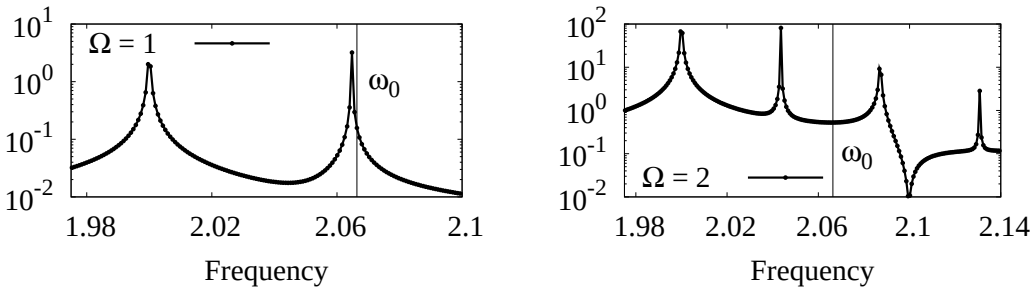

Figure 3.6.: Parts of the Fourier spectra for $\mathcal{P} = 0.4$, $\mathcal{Q} = 0.2$, and two different driving frequencies: $\Omega = 1$ (left) and $\Omega = 2$ (right). Position of a linear response result ω_0 is given by a vertical solid line.

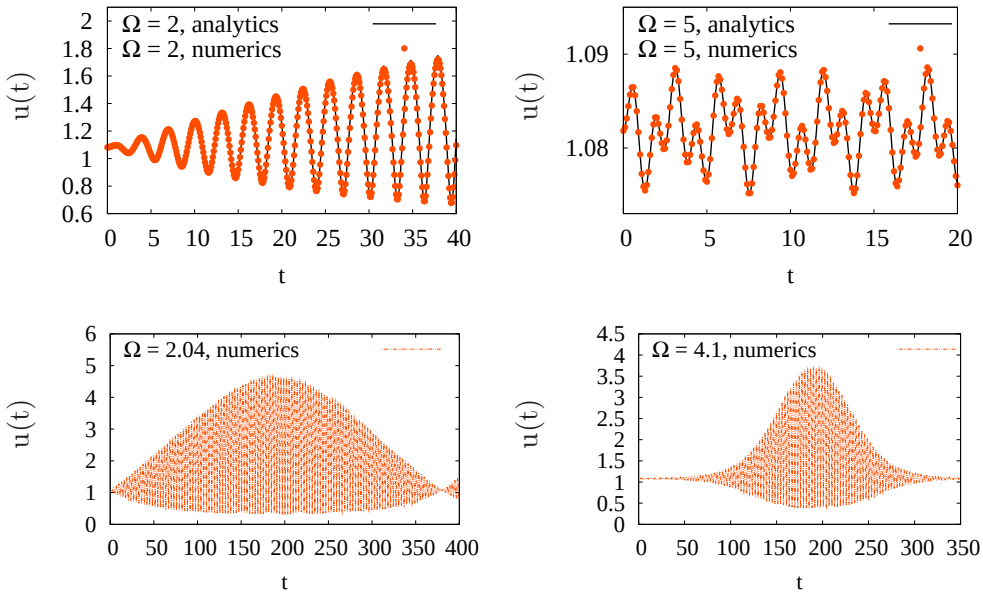

Figure 3.7.: Condensate dynamics $u(t)$ versus t within the Gaussian approximation for $\mathcal{P} = 0.4$, $\mathcal{Q} = 0.1$ and several different driving frequencies Ω. We plot the exact numerical solution of Eq. (3.7). For off-resonant driving frequencies Ω, we also show our analytical third-order perturbative result, as explained in Section 3.1.2.

the right-hand side of some of the previous equations would yield a solution that contains the secular term $t \sin t$. Such a secular term grows linearly in time, which makes it in the long-time limit the dominant term in the expansion (3.11) that otherwise contains only periodic functions in t. In order to ensure a regular behavior of the perturbative expansion, the respective frequency shifts ω_1, $\omega_2, \ldots$ are determined by imposing the cancellation of secular terms at the respective perturbative order.

This analytical procedure is implemented up to the third order in the modulation amplitude $\mathcal{Q}$ by using the software package Mathematica [242]. Although the calculation is straightforward, it easily becomes tedious for higher orders of perturbation theory. Note that it is necessary to perform the calculation to at least the third order since it turns out to be the lowest-order solution where secular terms appear and where a nontrivial frequency shift is obtained. We solve explicitely for $u_1(t)$, $u_2(t)$, and $u_3(t)$ and show an excellent agreement of our analytical solutions with a respective numerical solution of Eq. (3.7) in Fig. 3.7. Large amplitude oscillations and beating phenomena are present for

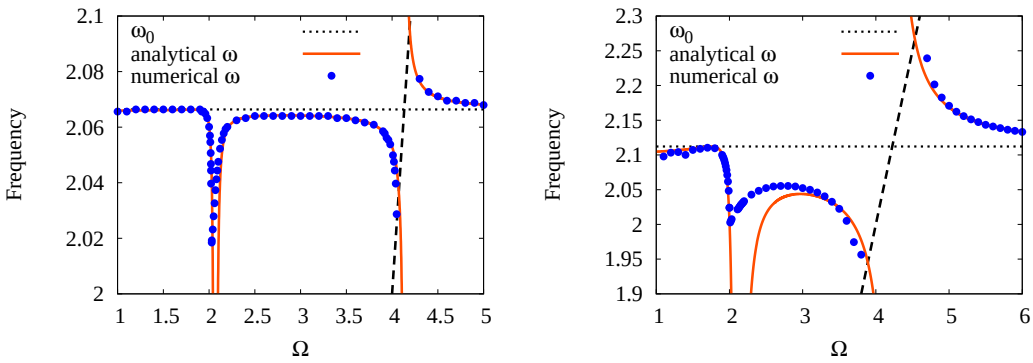

Figure 3.8.: Frequency of the breathing mode versus the driving frequency Ω for $\mathcal{P} = 0.4$ and $\mathcal{Q} = 0.1$ (left plot), and $\mathcal{P} = 1$ and $\mathcal{Q} = 0.8$ (right plot). The dashed line represents $\Omega/2$ and is given to guide the eye.

both $\Omega \approx \omega_0$ and for $\Omega \approx 2\omega_0$ which are close to the resonance. From the first-order solution $u_1(t)$ we read off only the two basic modes ω_0 and Ω, while the second-order harmonics $2\omega_0$, $\omega_0 - \Omega$, $\omega_0 + \Omega$ and 2Ω appear in $u_2(t)$. In the third order of perturbation theory, higher-order harmonics $\omega - 2\Omega$, $2\omega - \Omega$, $2\omega + \Omega$, $\omega + 2\Omega$, 3ω, and 3Ω are also present. Concerning the cancellation of secular terms, it turns out that the first-order correction ω_1 vanishes, yielding a leading frequency shift which is quadratic in $\mathcal{Q}$:

$$\omega = \omega_0 + \frac{\mathcal{Q}^2}{12 u_0^{20} \omega_0^3} \frac{\mathcal{P}(\Omega)}{(\Omega^2 - \omega_0^2)^2 \, (\Omega^2 - 4\omega_0^2)} + \dots \,, \tag{3.16}$$

where the polynomial $\mathcal{P}(\Omega)$ is given by

$$\begin{aligned} \mathcal{P}(\Omega) \;=\; & \Omega^4 \left[-240 \mathcal{P} u_0^5 + 36 u_0^6 (-4 + 3 u_0^4 \omega_0^2) \right] + \Omega^2 \left[-1100 \mathcal{P}^2 - 30 \mathcal{P} u_0 (44 - 65 u_0^4 \omega_0^2) \right. \\ & \left. + 9 u_0^2 (-44 + 127 u_0^4 \omega_0^2 - 44 u_0^8 \omega_0^4) \right] + 5600 \mathcal{P}^2 \omega_0^2 - 840 \mathcal{P} u_0 \omega_0^2 (-8 + 3 u_0^4 \omega_0^2) \\ & + 36 u_0^2 \omega_0^2 (56 - 39 u_0^4 \omega_0^2 + 8 u_0^8 \omega_0^4). \end{aligned} \tag{3.17}$$

A Mathematica notebook, which implements this analytical calculation is available at Ref. [243].

3.1.3. Discussion

The result given by Eq. (3.16) is the main achievement of our analytical analysis. It is obtained within a perturbative approach up to the second order in $\mathcal{Q}$ and it describes the breathing mode frequency dependence on Ω and $\mathcal{Q}$ as a result of nonlinear effects. Due to the underlying perturbative expansion, we do not expect Eq. (3.16) to be meaningful at the precise position of the resonances. However, by comparison with numerical results based on the variational equation, we find that Eq. (3.16) represents a reasonable approximation even close to the resonant region.

To illustrate this, we show in Fig. 3.8 two such comparisons. In the left figure we consider the parameter set $\mathcal{P} = 0.4$ and $\mathcal{Q} = 0.1$ and observe significant frequency shifts only in the narrow resonant regions. We notice an excellent agreement of numerical values with the analytical result given by Eq. (3.16). In the right figure we consider the parameter set $\mathcal{P} = 1$ and $\mathcal{Q} = 0.8$ with a much stronger modulation amplitude. In this case we observe significant frequency shifts for the broader range of modulation frequencies Ω. In spite of a strong modulation, we still see a qualitatively good agreement of numerical results with the analytical prediction given by Eq. (3.16). In principle, better agreement can be achieved using higher-order perturbative approximations. The dashed line on both

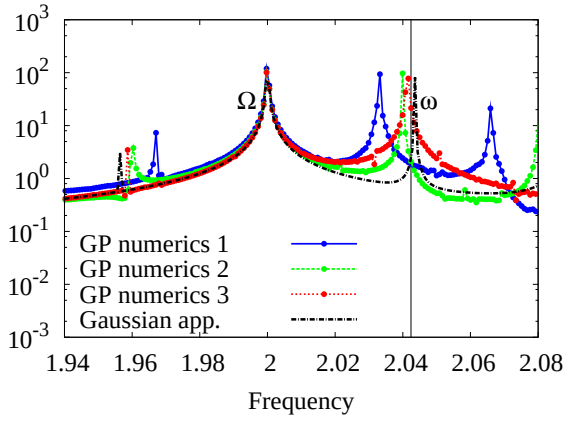

Figure 3.9.: Part of the Fourier spectrum of the time-dependent condensate width for $\mathcal{P} = 0.4$, $\mathcal{Q} = 0.2$, $\Omega = 2$. For numerical solution of GP equation we used several discretization schemes: GP numerics 1 (time step $\varepsilon = 10^{-3}$, spacing $h = 4 \times 10^{-2}$), GP numerics 2 ($\varepsilon = 5 \times 10^{-4}$, $h = 2 \times 10^{-2}$), GP numerics 3 ($\varepsilon = 5 \times 10^{-5}$, $h = 5 \times 10^{-3}$). For comparison we also show the corresponding spectrum obtained from the Gaussian approximation (dotted-dashed line) and analytical result (3.16) for the position of breathing mode (solid vertical line).

figures represents $\Omega/2$, given as a guide to the eye. It also serves as a crude description of what we observe numerically in the range $\Omega \approx 2\omega_0$.

The presence of two poles at $\Omega = \omega_0$ and $\Omega = 2\omega_0$ in Eq. (3.16) implies the possible existence of real resonances in the BEC with a harmonically modulated interaction. A perturbative expansion to higher orders would probably introduce additional poles, which are responsible for higher-order "resonant" behavior observed at $\Omega \approx 2\omega_0/n$, with $n \geq 3$. Still, the poles seem to be only an artefact of our approximative perturbative scheme, and thus may not be present in the exact description. For example, a simple resummation performed by using the second-order perturbative result removes these effects, although this is only an ad-hoc approximation. We stress that this issue concerning the true resonant behavior can not be settled either by relying on a numerical calculation due to inherent numerical artefacts related to finite numerical precision and finite computational time. To resolve it, one should rely on an analytical consideration along the lines of Ref. [104] or use some analytical tool applicable at resonances, such as the resonant Bogoliubov-Mitropolsky method [235]. However, this is out of the scope of the present thesis.

In addition to comparing our analytical results with numerical solutions based on the Gaussian variational approximation, we present a comparison with the full numerical solution of the GP equation. In order to be able to perform a Fourier analysis with a sufficiently good resolution, it is necessary to obtain an accurate solution for long evolution times. We do this by using the split-step method in combination with the semi-implicit Crank-Nicolson method [244]. As we refine the GP numerics by using finer space and time discretization parameters, our numerical results become stable as shown in Fig. 3.9. From the same figure, we observe quantitatively good agreement between GP numerics and Gaussian approximation, which is reflected in close values obtained for the breathing mode frequency. In addition, numerical values for the breathing mode approach closely the analytical result of Eq. (3.16), which is shown by a solid vertical line in Fig. 3.9.

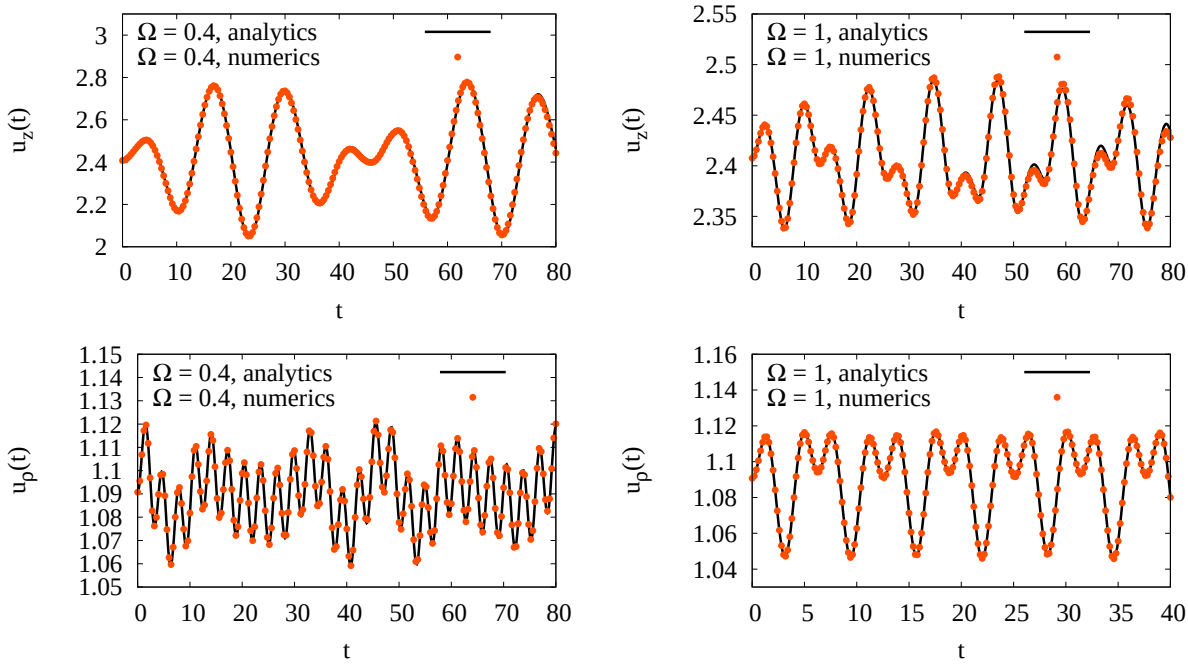

Figure 3.10.: Condensate dynamics within the Gaussian approximation for $\mathcal{P} = 1$, $\mathcal{Q} = 0.2$, $\lambda = 0.3$ and two different driving frequencies $\Omega = 0.4$ (left plot) and $\Omega = 1$ (right plot). We compare the exact numerical solution of Eqs. (3.2) and (3.3) with the analytical second-order perturbative result, as explained in Section 3.2.1

3.2. Axially-Symmetric BEC

To obtain experimentally more relevant results, we now study an axially symmetric BEC [109]. An illustration of the condensate dynamics is shown in Fig. 3.10 for $\mathcal{P} = 1$, $\mathcal{Q} = 0.2$, and $\lambda = 0.3$. We plot numerical solutions of Eqs. (3.2) and (3.3) obtained for the equilibrium initial conditions $u_\rho(0) = u_{\rho 0}$, $\dot{u}_\rho(0) = 0$, $u_z(0) = u_{z0}$, and $\dot{u}_z(0) = 0$. For the specified parameters, the equilibrium widths are found to be $u_{\rho 0} = 1.09073$, $u_{z0} = 2.40754$ and from the linear stability analysis we find both the quadrupole mode frequency $\omega_{Q0} = 0.538735$ and the breathing mode frequency $\omega_{B0} = 2.00238$. For a driving frequency Ω close to ω_{Q0}, we observe large amplitude oscillations in the axial direction. An example of excitation spectra is shown in Fig. 3.11. Here, we have the three basic modes ω_Q, ω_B, Ω, and many higher-order harmonics.

3.2.1. Poincaré-Lindstedt Method

In order to extract information on the frequencies of the collective modes beyond the linear stability analysis, we apply the perturbative expansion in the modulation amplitude $\mathcal{Q}$:

$$u_\rho(t) = u_{\rho 0} + \mathcal{Q}\, u_{\rho 1}(t) + \mathcal{Q}^2\, u_{\rho 2}(t) + \mathcal{Q}^3\, u_{\rho 3}(t) + \ldots, \tag{3.18}$$

$$u_z(t) = u_{z0} + \mathcal{Q}\, u_{z1}(t) + \mathcal{Q}^2\, u_{z2}(t) + \mathcal{Q}^3\, u_{z3}(t) + \ldots, \tag{3.19}$$

By inserting these expansions in Eqs. (3.2) and (3.3) and by performing expansions in $\mathcal{Q}$, we obtain a system of linear differential equations of the general form:

$$\ddot{u}_{\rho n}(t) + m_{11} u_{\rho n}(t) + m_{12} u_{zn}(t) + f_{\rho n}(t) = 0, \tag{3.20}$$

$$m_{21} u_{\rho n}(t) + \ddot{u}_{zn}(t) + m_{22} u_{zn}(t) + f_{zn}(t) = 0, \tag{3.21}$$

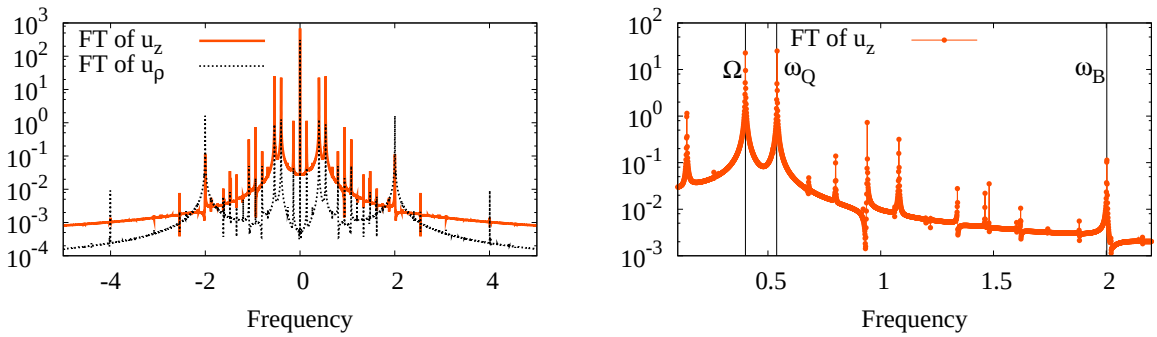

Figure 3.11.: Fourier transformed $u_\rho(t)$ and $u_z(t)$ for $\mathcal{P} = 1$, $\mathcal{Q} = 0.2$, $\lambda = 0.3$, and $\Omega = 0.4$. left plot gives complete spectrum, while in the right plot we show part of the spectrum together with positions of prominent peaks.

where $n = 1, 2, 3, \ldots$, $m_{11} = 4$, $m_{12} = \mathcal{P}/u_{\rho 0}^3 u_{z0}^2$, $m_{21} = 2\,\mathcal{P}/u_{\rho 0}^3 u_{z0}^2$, and $m_{22} = \lambda^2 + 3/u_{z0}^4 + 2\,\mathcal{P}/u_{\rho 0}^2 u_{z0}^3$. The functions $f_{\rho n}(t)$ and $f_{zn}(t)$ depend only on the solutions $u_{\rho i}(t)$ and $u_{zi}(t)$ of lower order, i. e. $i < n$. For $n = 1$ we have

$$f_{\rho 1}(t) = -\frac{\cos \Omega t}{u_{\rho 0}^3 u_{z0}}, \quad f_{z1}(t) = -\frac{\cos \Omega t}{u_{\rho 0}^2 u_{z0}^2},$$

and for $n = 2$ we get correspondingly

$$\begin{aligned} f_{\rho 2}(t) &= \frac{3}{u_{\rho 0}^4 u_{z0}} \cos \Omega t\, u_{\rho 1}(t) - \frac{6}{u_{\rho 0}^5} u_{\rho 1}(t)^2 - \frac{6\mathcal{P}}{u_{\rho 0}^5 u_{z0}} u_{\rho 1}(t)^2 + \frac{1}{u_{\rho 0}^3 u_{z0}^2} \cos \Omega t\, u_{z1}(t) \\ &\quad - \frac{3\mathcal{P}}{u_{\rho 0}^4 u_{z0}^2} u_{\rho 1}(t) u_{z1}(t) - \frac{\mathcal{P}}{u_{\rho 0}^3 u_{z0}^3} u_{z1}(t)^2, \end{aligned} \tag{3.22}$$

$$\begin{aligned} f_{z2}(t) &= \frac{2}{u_{\rho 0}^3 u_{z0}^2} \cos \Omega t u_{\rho 1}(t) - \frac{3\mathcal{P}}{u_{\rho 0}^4 u_{z0}^2} u_{\rho 1}(t)^2 - \frac{3\mathcal{P}}{u_{\rho 0}^2 u_{z0}^4} u_{z1}(t)^2 + \frac{2}{u_{\rho 0}^2 u_{z0}^3} \cos \Omega t\, u_{z1}(t) \\ &\quad - \frac{6}{u_{z0}^5} u_{z1}(t)^2 - \frac{4\mathcal{P}}{u_{\rho 0}^3 u_{z0}^3} u_{\rho 1}(t) u_{z1}(t). \end{aligned} \tag{3.23}$$

The linear transformation

$$u_{\rho n}(t) = x_n(t) + y_n(t), \tag{3.24}$$

$$u_{zn}(t) = c_1\, x_n(t) + c_2\, y_n(t), \tag{3.25}$$

with the coefficients

$$c_1 = \frac{m_{22} - m_{11} - \sqrt{(m_{22} - m_{11})^2 + 4 m_{12} m_{21}}}{2 m_{12}}, \tag{3.26}$$

$$c_2 = \frac{m_{22} - m_{11} + \sqrt{(m_{22} - m_{11})^2 + 4 m_{12} m_{21}}}{2 m_{12}} \tag{3.27}$$

decouples the system at the n-th level and leads to:

$$\ddot{x}_n(t) + \omega_{Q0}^2 x_n(t) + \frac{c_2\, f_{\rho n}(t) - f_{zn}(t)}{c_2 - c_1} = 0, \tag{3.28}$$

$$\ddot{y}_n(t) + \omega_{B0}^2 y_n(t) + \frac{c_1\, f_{\rho n}(t) - f_{zn}(t)}{c_1 - c_2} = 0. \tag{3.29}$$

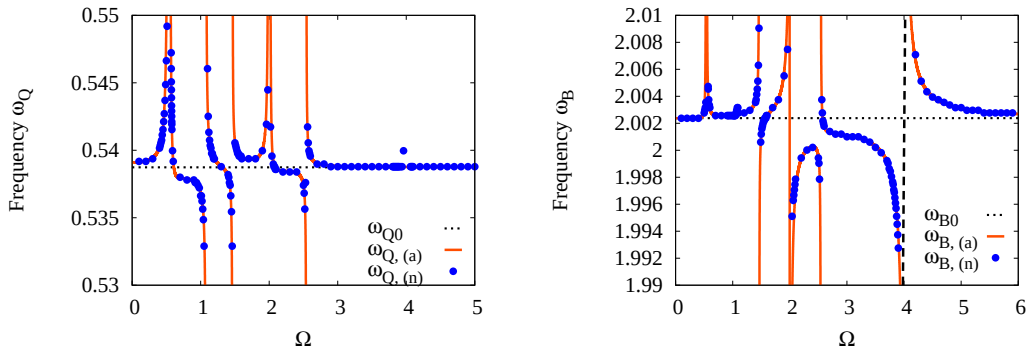

(a) (b)

Figure 3.12.: Frequency of the quadrupole mode ω_Q (a) and the breathing mode (b) versus driving frequency Ω for $\mathcal{P} = 1$, $\mathcal{Q} = 0.2$, and $\lambda = 0.3$. We plot linear response result ω_{Q0}, ω_{B0}, second-order analytical result $\omega_{Q,(\mathrm{a})}$, $\omega_{B,(\mathrm{a})}$ and numerical values $\omega_{Q,(\mathrm{n})}$, $\omega_{B,(\mathrm{n})}$.

Now it is clear how to proceed: we first solve Eqs. (3.28) and (3.29) for $x_1(t)$ and $y_1(t)$ and then using Eqs. (3.24) and (3.25) we obtain $u_{\rho 1}(t)$ and $u_{z1}(t)$. In the next step we use these solutions and solve for $x_2(t)$ and $y_2(t)$ and so on. At each level we impose the initial conditions $u_{\rho n}(0) = 0$, $\dot{u}_{\rho n}(0) = 0$, $u_{zn}(0) = 0$, and $\dot{u}_{zn}(0) = 0$. At the first level of perturbation theory, the equations for x and y are decoupled, i.e. $x_1(t)$ and $y_1(t)$ are normal modes: $x_1(t)$ describes quadrupole oscillations, while $y_1(t)$ describes breathing oscillations. However, at the second order of perturbation theory $y_1(t)$ enters the equation for $x_2(t)$ and also $x_1(t)$ appears in equation for $y_2(t)$, i.e. we have a nonlinear mode coupling.

The explicit calculation is performed up to the second order by using the software package Mathematica [242]. We obtain a good agreement of analytical results obtained in the second order of our perturbation theory and numerical results, as can be seen in Fig. 3.10 for a moderate value of a modulation amplitude $\mathcal{Q}$. The first secular terms appear at the level $n = 3$. The expressions are cumbersome, but the relevant behavior is obtained from the terms

$$\ddot{x}_3(t) + \omega_{Q0}^2 x_3(t) + C_Q \cos(\omega_{Q0} t) + \ldots = 0, \tag{3.30}$$

that leads to

$$x_3(t) = -\frac{C_Q}{2\omega_{Q0}} t \sin(\omega_{Q0} t) + \ldots . \tag{3.31}$$

The last term can be absorbed into the first-order solution

$$\begin{aligned} u_\rho(t) &= A_Q \cos(\omega_{Q0} t) - \frac{C_Q \mathcal{Q}^2}{2\omega_{Q0}} t \sin(\omega_{Q0} t) + \ldots \\ &\approx A_Q \cos[t(\omega_{Q0} + \Delta\omega_{Q0})], \end{aligned} \tag{3.32}$$

and can be interpreted as a frequency shift of the quadrupole mode to the order $\mathcal{Q}^2$:

$$\omega_Q = \omega_{Q0} + \Delta\omega_{Q0} = \omega_{Q0} + \mathcal{Q}^2 \frac{C_Q}{2\omega_{Q0} A_Q} + \ldots . \tag{3.33}$$

The coefficients A_Q and C_Q are calculated using the Mathematica code avaliable at the homepage [243], but their explicit form is too long to be presented here. Along the same lines we also calculate the frequency shift of the breathing mode.

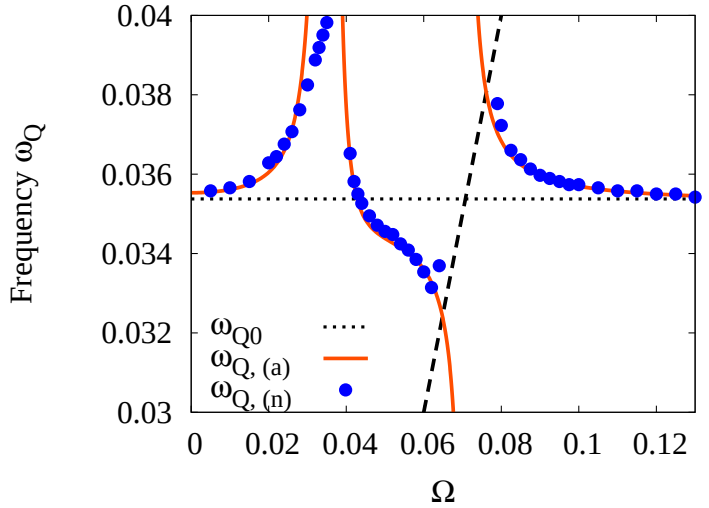

Figure 3.13.: Frequency of the quadrupole mode ω_Q versus driving frequency Ω for the experimental parameters $\lambda = 0.021$, $\mathcal{P} = 15$, $\mathcal{Q} = 10$ [93]. We plot linear response result ω_{Q0}, second-order analytical result $\omega_{Q,(a)}$, and numerical values $\omega_{Q,(n)}$.

3.2.2. Discussion

The main results of our calculation are shown in Fig 3.12. In Fig. 3.12(a) we plot the analytically obtained frequency of the quadrupole mode versus the driving Ω, using the second-order perturbation theory together with the corresponding numerical result based on the Fourier analysis of solutions of Eqs. (3.2) and (3.3). An analogous plot for the frequency of the breathing mode is given in Fig. 3.12(b). Our analytical perturbative result for the shifted quadrupole mode frequency contains poles at ω_{Q0}, $2\omega_{Q0}$, $\omega_{B0} - \omega_{Q0}$, $\omega_{Q0} + \omega_{B0}$ and ω_{B0}. Similarly, for the shifted frequency of the breathing mode poles in the perturbative solution are found at ω_{Q0}, ω_{B0}, $2\omega_{B0}$, $\omega_{B0} - \omega_{Q0}$ and $\omega_{Q0} + \omega_{B0}$. In both figures we see excellent agreement of the perturbatively obtained results with the exact numerics.

In the experiment of Ref. [93], excitations of a highly elongated and strongly repulsive BEC were considered for the system parameters $\lambda = 0.021$, $\mathcal{P} = 15$, and $\mathcal{Q} = 10$. For that case, according to $\omega_{Q0} = 0.035375$, $\omega_{B0} = 2.00002$, we have $\omega_{Q0} \ll \omega_{B0}$, and the driving frequency Ω was chosen in the range $(0, 3\omega_{Q0})$. Due to the large modulation amplitude $\mathcal{Q}$, many higher order harmonics are excited, and, most importantly, we find frequency shifts of the quadrupole mode of about 10% in Fig 3.13. From the same figure we notice that, due to the chosen frequency range for Ω, only resonances located at ω_Q and $2\omega_Q$ are observed in accordance with Fig. 3.1. The presence of nonlinear effects is already mentioned in Ref. [93]. However, we suggest that the frequency shifts calculated here have to be taken into account for extracting the resonance curves from the underlying experimental data.

To achieve a more clear-cut experimental observation of the nonlinearity-induced frequency shifts calculated in this chapter, we suggest a different trap geometry from the one used in Ref. [93]. Measurements of stable BEC modes can be performed for about 1 s and in order to extract precise values of the excited frequencies in the Fourier analysis, several oscillation periods should be captured within this time interval. A higher frequency of the quadrupole mode, that can be realized by using a larger trap aspect ratio λ, in combination with a higher modulation frequency would fulfill this condition. According to the results presented in Ref. [93], resonant driving may lead to condensate fragmentation. However, our numerical results indicate frequency shifts of about 10 % even outside the resonant regions according to Figs. 3.8 and 3.13, and this is where experimental measurements should be per-

formed. Although an increase in λ leads to a more pronounced nonlinear mixing of quadrupole and breathing mode and may complicate the condensate dynamics further, it may be possible to perform a Fourier analysis of experimental data, analogous to Ref. [67], and to compare it with the excitation spectra presented here. To achieve a complete matching of experimental data and our calculations, it may turn out that higher-order corrections to Eq. (1.2), that arise due to nonlinear dependence of scattering length on the external magnetic field, have to be taken into account.

4. Geometric Resonances

Theoretical studies of collective excitations are usually focused on two-body contact interactions due to the diluteness of quantum gases [69,93,105,109,114,115,123]. However, the experimental progress with BECs in atomic waveguides and on the surface of atomic chips, which involve a strong increase in the density of BECs, necessitates also the study of three-body interactions [124–126]. As reported in Ref. [129] and discussed in Section 2.5, even for a small strength of the three-body interaction, the region of stability for the condensate can be extended considerably.

Due to the nonlinearity of the underlying Gross-Pitaevskii equation, frequencies of collective oscillation modes of Bose-Einstein condensates exhibit resonances when their interaction is harmonically modulated [109]. Whereas such parametric resonances were analyzed in the previous chapter, here in this chapter we study the dynamics of the condensate in general and its collective oscillation modes in particular by changing the geometry of the trapping potential. The asymmetry of the confining potential leads to important nonlinear effects, including resonances in the frequencies of collective oscillation modes of the condensate [105,109,112,113].

The BEC dynamics at zero temperature is described by the nonlinear GP equation for the condensate wavefunction with two- and three-body interactions. Within a variational approach the partial differential equation of Gross and Pitaevskii Eq. (2.12) is transformed in Sec. 2.2 into a set of ordinary differential equations for the widths of the condensate in an axially-symmetric harmonic trap with both two- and three-body interactions:

$$\ddot{u}_\rho + u_\rho - \frac{1}{u_\rho^3} - \frac{\mathcal{P}}{u_\rho^3 u_z} - \frac{\mathcal{K}}{u_\rho^5 u_z^2} = 0\,, \tag{4.1}$$

$$\ddot{u}_z + \lambda^2 u_z - \frac{1}{u_z^3} - \frac{\mathcal{P}}{u_\rho^2 u_z^2} - \frac{\mathcal{K}}{u_\rho^4 u_z^3} = 0\,. \tag{4.2}$$

Although this represents a significant simplification in the description of a BEC, Ref. [109] demonstrates explicitly that these ordinary differential equations yield approximatively even for long evolution times the correct dynamics of the widths. In Sec. 4.1 we study in detail geometric resonances, which occur for commensurate frequencies of collective modes. To this end we derive an explicit analytic results for the frequency shifts for the case of an axially-symmetric condensate with two- and three-body interactions based on a perturbative expansion of the Poincaré-Lindstedt method. This frequency shift is calculated for a quadrupole mode in Sec. 4.1.1, for a breathing mode in Sec. 4.1.2, and the derived analytical results are then compared with the results of numerical simulations in Sec. 4.2. In that section we also compare results of numerical simulations for radial and longitudinal widths of the condensate and the corresponding excitations spectra with the analytical results obtained using perturbation theory. Then, in Sec. 4.3, we analyze the resonant mode coupling and the generation of second harmonics of the collective modes, which are induced by nonlinear effects. At first we consider a BEC in the initial state corresponding to the stationary ground state with a small perturbation proportional to the eigenvector of the quadrupole mode, which leads to quadrupole mode oscillations. In the linear case, we have small-amplitude oscillations of the condensate size around the equilibrium widths, and we are in the regime of linear stability analysis. However, when the frequencies of collective modes are approached, we obtain in the nonlinear case a resonant behavior, which is characterized

by large amplitude oscillations. In this case it is clear that a linear response analysis does no longer provide a qualitatively good description of the system dynamics [109].

4.1. Shifts in Frequencies of Collective Modes

Close to resonances, the nonlinear structure of the GP equation leads to shifts in the frequencies of collective oscillation modes compared to the respective values in Eqs. (2.65) and (2.66), which are calculated using the linear stability analysis. The resonances can be generated by two different mechanisms: they could be induced by an external, parametric driving of the system [109] as discussed in the previous chapter, or thus could emerge due to the geometry of the system [105]. The latter case of geometric resonances is further investigated in this section. In Sec. 4.3 we show that geometric resonances also induce a coupling of the collective modes, which is only possible due to the nonlinear nature of the system dynamics which is due to the interaction.

In order to analytically study both of these nonlinearity-induced effects, we apply the standard Poincaré-Lindstedt method [109,235,238,237,236] in order to develop a perturbation theory that describes the dynamics of a BEC with two- and three-body interactions.

4.1.1. Quadrupole Mode

We start with working out a perturbation theory for the BEC dynamic, which is based on a set of ordinary differential equations (4.1) and (4.2), by expanding the condensate widths in the series

$$u_\rho(t) = u_{\rho 0} + \varepsilon u_{\rho 1}(t) + \varepsilon^2 u_{\rho 2}(t) + \varepsilon^3 u_{\rho 3}(t) + \dots , \tag{4.3}$$

$$u_z(t) = u_{z0} + \varepsilon u_{z1}(t) + \varepsilon^2 u_{z2}(t) + \varepsilon^3 u_{z3}(t) + \dots , \tag{4.4}$$

where the smallness parameter ε stems from the respective initial conditions. Here we study the system dynamics with the initial condition in the form

$$\mathbf{u}(0) = \mathbf{u}_0 + \varepsilon \mathbf{u}_Q , \tag{4.5}$$

$$\dot{\mathbf{u}}(0) = \mathbf{0} , \tag{4.6}$$

when the system is close to the equilibrium position $\mathbf{u}_0$, and is perturbed in the direction of the quadrupole oscillation mode eigenvector $\mathbf{u}_Q$ determined by Eq. (2.70). By inserting the expansions (4.3) and (4.4) into Eqs. (4.1)–(4.2), we obtain the following system of linear differential equations:

$$\ddot{u}_{\rho n}(t) + m_1 u_{\rho n}(t) + m_2 u_{zn}(t) = \chi_{\rho n}(t) , \tag{4.7}$$

$$\ddot{u}_{zn}(t) + 2m_2 u_{\rho n}(t) + m_3 u_{zn}(t) = \chi_{zn}(t) , \tag{4.8}$$

where the index n takes integer values $n = 1, 2, 3, ..$, and the quantities m_1, m_2, and m_3 are already defined by the expressions (2.56). The functions $\chi_{\rho n}(t)$ and $\chi_{zn}(t)$ depend only on the solutions $u_{\rho i}(t)$ and $u_{zi}(t)$ of lower orders i, i.e. those corresponding to $i < n$. At first, for $n = 1$, we have $\chi_{\rho 1}(t) = \chi_{z1}(t) = 0$ and solve the above system of equations for $\mathbf{u}_1(t) = \begin{pmatrix} u_{\rho 1}(t) \\ u_{z1}(t) \end{pmatrix}$. Then, for $n = 2$, we use the previous solution, and solve the system for $\mathbf{u}_2(t)$, where the functions $\chi_{\rho 2}(t)$ and $\chi_{z2}(t)$ are given by

$$\chi_{\rho 2}(t) = \alpha u_{\rho 1}(t) u_{z1}(t) + \beta u_{z1}^2(t) + \gamma_\rho u_{\rho 1}^2(t) , \tag{4.9}$$

$$\chi_{z2}(t) = 4\beta u_{\rho 1}(t) u_{z1}(t) + +\gamma_z u_{z1}^2(t) + \alpha u_{\rho 1}^2(t) , \tag{4.10}$$

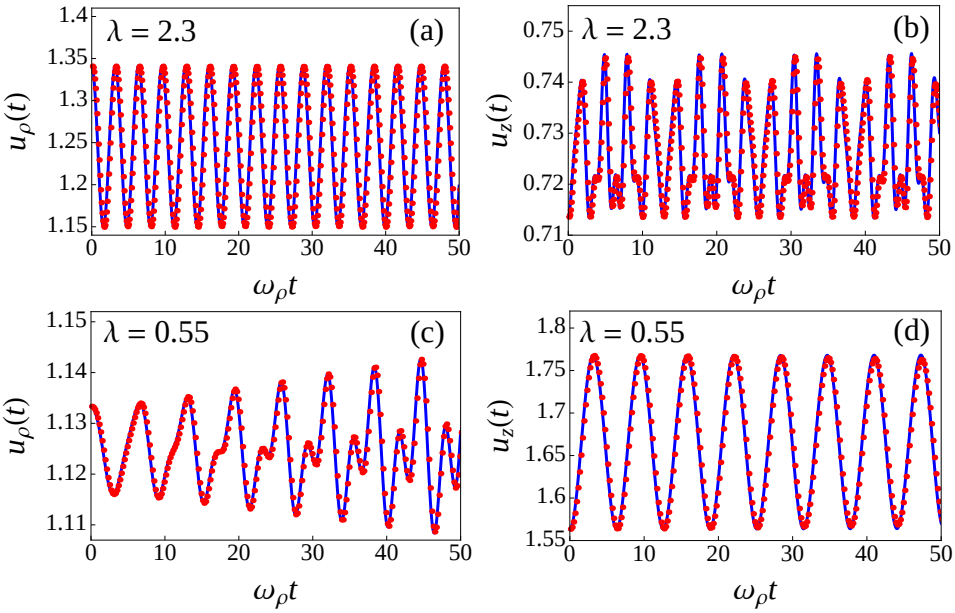

Figure 4.1.: A comparison of analytic (solid blue lines) and numeric (red dots) results for a BEC dynamics with a pure repulsive two-body interaction $\mathcal{P} = 1$, $\mathcal{K} = 0$, and $\varepsilon = 0.1$. Top panels show dynamics of (a) radial and (b) longitudinal condensate widths for the trap aspect ratio $\lambda = 2.3$ as a function of the dimensionless time $\omega_\rho t$; bottom panels show dynamics of (c) radial and (d) longitudinal BEC widths for $\lambda = 0.55$.

with the abbreviations

$$\alpha = \frac{3\mathcal{P}}{u_{\rho 0}^4 u_{z0}^2} + \frac{10\mathcal{K}}{u_{\rho 0}^6 u_{z0}^3}\,, \tag{4.11}$$

$$\beta = \frac{\mathcal{P}}{u_{\rho 0}^3 u_{z0}^3} + \frac{3\mathcal{K}}{u_{\rho 0}^5 u_{z0}^4}\,, \tag{4.12}$$

$$\gamma_\rho = \frac{6}{u_{\rho 0}^5} + \frac{6\mathcal{P}}{u_{\rho 0}^5 u_{z0}} + \frac{15\mathcal{K}}{u_{\rho 0}^7 u_{z0}^2}\,, \tag{4.13}$$

$$\gamma_z = \frac{6}{u_{z0}^5} + \frac{3\mathcal{P}}{u_{\rho 0}^2 u_{z0}^4} + \frac{6\mathcal{K}}{u_{\rho 0}^4 u_{z0}^5}\,. \tag{4.14}$$

At each level n of this procedure we use the initial conditions from Eqs. (4.5) and (4.6).

In order to decouple the system of equations (4.7)–(4.8), we use the linear transformation Eqs. (3.25) with the coefficients Eq. (3.27). It decouples the system at level n and leads to two independent linear second-order differential equations:

$$\ddot{x}_n(t) + \omega_Q^2 x_n(t) + \frac{c_2\chi_{\rho n}(t) - \chi_{zn}(t)}{c_1 - c_2} = 0\,, \tag{4.15}$$

$$\ddot{y}_n(t) + \omega_B^2 y_n(t) + \frac{\chi_{zn}(t) - c_1\chi_{\rho n}(t)}{c_1 - c_2} = 0\,. \tag{4.16}$$

From this we conclude that $x_n(t)$ and $y_n(t)$ correspond to quadrupole and breathing mode oscillations, respectively. Although the system is only perturbed in the direction of the quadrupole mode eigenvector, due to the nonlinearity of the system, the breathing mode is excited as well.

The solutions of the above equations depend essentially on the nature of the inhomogeneous terms, which are given by polynomials of harmonic functions of $\omega_Q t$, $\omega_B t$ and their linear combinations

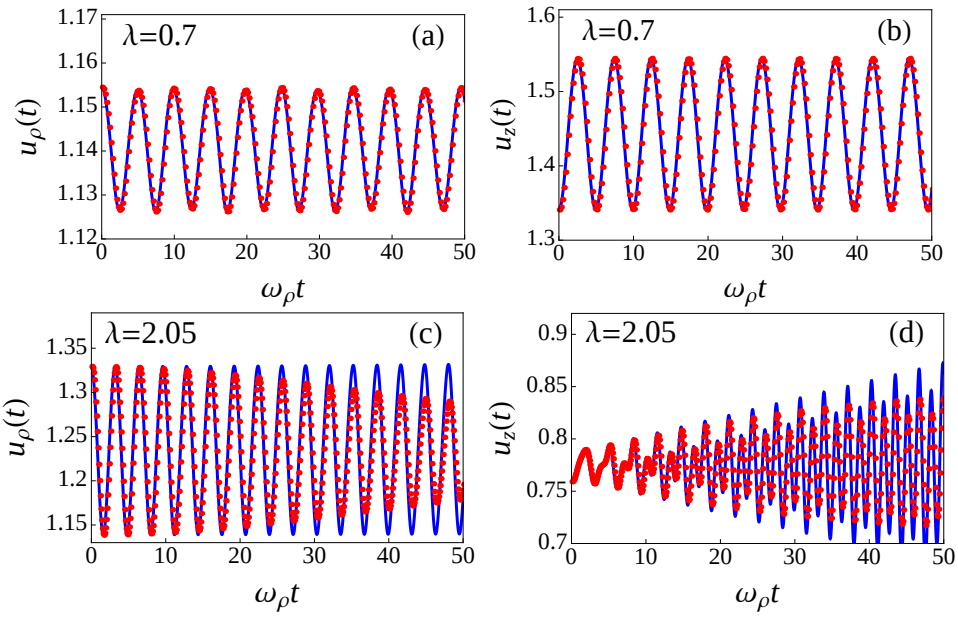

Figure 4.2.: A comparison of analytic (solid blue lines) and numeric (red dots) results for BEC dynamics for a repulsive two-body interaction $\mathcal{P} = 1$ and a repulsive three-body interaction $\mathcal{K} = 0.001$, with $\varepsilon = 0.1$. Top panels show dynamics of (a) radial and (b) longitudinal condensate widths for the trap aspect ratio $\lambda = 0.7$ as a function of the dimensionless time $\omega_\rho t$; bottom panels show dynamics of (c) radial and (d) longitudinal BEC widths for $\lambda = 2.05$.

$(k\omega_Q + m\omega_B)t$ with integers k and m. If the inhomogeneous part of the equation for x_n (y_n) does not contain a linear term proportional to the harmonic function in $\omega_Q t$ ($\omega_B t$), the particular as well as the homogeneous solutions will be again polynomials in harmonic functions of $\omega_Q t$, $\omega_B t$ and their linear combinations. In that case, the system exhibits usually small oscillations, which are characterized by the frequencies ω_Q and ω_B from the linear stability analysis. Compared to linear systems, the exception here is that higher harmonics and linear combinations of the modes emerge due to the inherent nonlinearity.

However, if the inhomogeneous part of the equation for x_n (y_n) contains a linear term proportional to the harmonic function in $\omega_Q t$ ($\omega_B t$), then the corresponding particular solution will contain a secular term, i.e. one proportional to t times a harmonic function of $\omega_Q t$ ($\omega_B t$), which turns out to be responsible for the frequency shift of the collective mode [109]. This happens for the first time at level $n = 3$, when Eqs. (4.7)–(4.8) can be written in vector form as

$$\ddot{\mathbf{u}}_3(t) + M\mathbf{u}_3(t) + \mathbf{I}_{Q,3}\cos\omega_Q t + \ldots = 0\,, \tag{4.17}$$

with the matrix

$$M = \begin{pmatrix} m_1 & m_2 \\ 2m_2 & m_3 \end{pmatrix}, \tag{4.18}$$

and the dots represent the inhomogeneous part of the equation, which does not contain linear terms proportional to harmonic functions in $\omega_Q t$. The expression for $\mathbf{I}_{Q,n}$ can be calculated systematically for any given level n with the help of the *Mathematica* software package [242]. The particular solution of Eq. (4.17) has the form

$$\mathbf{u}_{3,P}(t) = -\varepsilon^2 \frac{(\mathbf{u}_Q^L)^T \mathbf{I}_{Q,3}}{2\omega_Q}\mathbf{u}_Q t \sin\omega_Q t + \ldots\,, \tag{4.19}$$

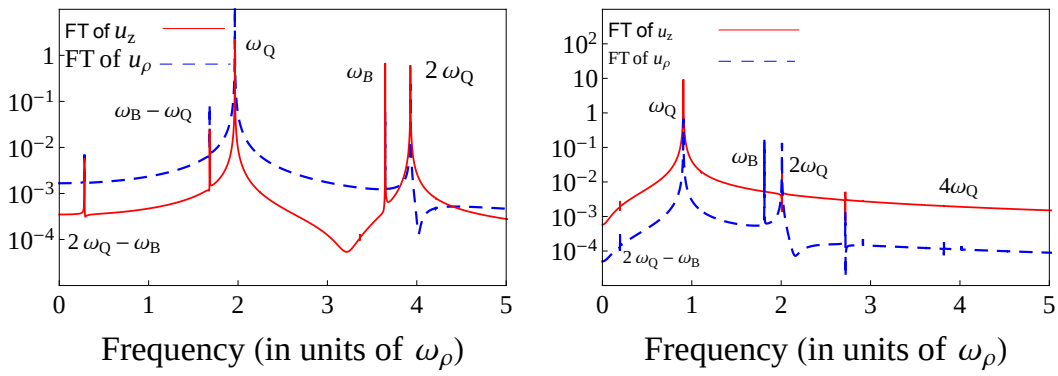

(a) $\lambda = 1.9$ (b) $\lambda = 0.5$

Figure 4.3.: Fourier spectra of the BEC dynamics obtained by numerically solving the system of equations (4.1) and (4.2) with the initial condition Eqs. (4.5) and (4.6) for a repulsive two-body interaction $\mathcal{P} = 1$, a repulsive three-body interaction $\mathcal{K} = 0.001$, and $\varepsilon = 0.1$. Each graph shows spectra of both longitudinal and radial condensate widths. The locations of all peaks are identified as linear combinations of the quadrupole and the breathing mode frequency, in correspondence with the analysis based on the developed perturbation theory.

with the left-hand eigenvector corresponding to the quadrupole mode

$$\mathbf{u}_Q^L = \frac{1}{\sqrt{4m_2^2 + \left(\omega_Q^2 - m_1\right)^2}} \begin{pmatrix} 2m_2 \\ \omega_Q^2 - m_1 \end{pmatrix}, \tag{4.20}$$

and, again, dots represent the part of the particular solution which is due to other inhomogeneous terms. The complete solution of Eq. (4.17) is given by the sum of the homogeneous solution $\mathbf{u}_Q \cos\omega_Q t$ and the particular solution $\mathbf{u}_{3,P}(t)$. The secular term can be now absorbed by a shift in the quadrupole mode frequency according to

$$\begin{aligned} \mathbf{u}_3(t) &= \mathbf{u}_Q \cos\omega_Q t - \varepsilon^2 \frac{(\mathbf{u}_Q^L)^T \mathbf{I}_{Q,3}}{2\omega_Q} \mathbf{u}_Q t \sin\omega_Q t + \dots \\ &\approx \mathbf{u}_Q \cos(\omega_Q + \Delta\omega_Q)t + \dots , \end{aligned} \tag{4.21}$$

which is quadratic in the smallness parameter ε:

$$\omega_Q(\varepsilon) = \omega_Q + \Delta\omega_Q = \omega_Q - \varepsilon^2 \frac{(\mathbf{u}_Q^L)^T \mathbf{I}_{Q,3}}{2\omega_Q} + \dots . \tag{4.22}$$

The expression for $(\mathbf{u}_Q^L)^T \mathbf{I}_{Q,3}$ is most easily calculated with the *Mathematica* software package [242], and reads

$$\mathbf{u}_Q^{T,L} \mathbf{I}_{Q,3} = \frac{f_{Q,3}(\omega_Q, \omega_B, u_{\rho 0}, u_{z0}, \mathcal{P}, \mathcal{K}, \lambda)}{(\omega_B - 2\omega_Q)(\omega_B + 2\omega_Q)}, \tag{4.23}$$

where $f_{Q,3}$ is a regular function without poles for real values of its arguments. Therefore, the frequency shift of a quadrupole mode to lowest order in ε is given by

$$\Delta\omega_Q = -\varepsilon^2 \frac{f_{Q,3}(\omega_Q, \omega_B, u_{\rho 0}, u_{z0}, \mathcal{P}, \mathcal{K}, \lambda)}{2\omega_Q(\omega_B - 2\omega_Q)(\omega_B + 2\omega_Q)} + \dots , \tag{4.24}$$

and depends explicitly on the trap aspect ratio λ, as well as implicitly through the λ-dependence of the frequencies ω_Q and ω_B according to Eqs. (2.65) and (2.66). The expression (4.24) for the

frequency shift has a pole for $\omega_B = 2\omega_Q$. Taking into account the fact that $\omega_Q < \omega_B$, as we can see from Eq. (2.65) and Fig. 2.5, this condition can, in principle, be satisfied. This is designated to be a geometric resonance, since it can be obtained just by tuning the geometry of the harmonic confining potential, i.e. the value of the trap aspect ratio λ. Higher-order corrections to $\Delta\omega_Q$ in ε can, in principle, be obtained systematically by using the developed perturbation theory. In Sec. 4.2 we compare the analytical result for the frequency shift of a quadrupole mode (4.24) with corresponding results of numerical simulations.

4.1.2. Breathing Mode

In a similar manner, we study the dynamics of a cylindrically-symmetric BEC system when initially only the breathing mode is excited, thus the initial condition reads now

$$\mathbf{u}(0) = \mathbf{u}_0 + \varepsilon \mathbf{u}_B \,, \tag{4.25}$$

$$\dot{\mathbf{u}}(0) = \mathbf{0} \,. \tag{4.26}$$

Applying again the Poincaré-Lindstedt perturbation theory, we calculate the breathing mode frequency shift,

$$\omega_B(\varepsilon) = \omega_B + \Delta\omega_B = \omega_B - \varepsilon^2 \frac{(\mathbf{u}_B^L)^T \mathbf{I}_{B,3}}{2\omega_B} + \dots \,, \tag{4.27}$$

where again the expression $(\mathbf{u}_B^L)^T \mathbf{I}_{B,3}$ is calculated in *Mathematica* software package [242]. In this way we finally yield the following analytic formula for the frequency shift of the breathing mode

$$\Delta\omega_B = -\varepsilon^2 \frac{f_{B,3}(\omega_Q, \omega_B, u_{\rho 0}, u_{z0}, \mathcal{P}, \mathcal{K}, \lambda)}{2\omega_B(2\omega_B - \omega_Q)(2\omega_B + \omega_Q)} + \dots \,, \tag{4.28}$$

where the function $f_{B,3}$ is a regular function of its arguments. Naively looking at this expression, one would say that it exhibits a pole for $2\omega_B = \omega_Q$. However, from Eq. (2.66) and Fig. 2.5 we see that $\omega_Q < \omega_B$, and, therefore, the condition $2\omega_B = \omega_Q$ is never satisfied. In the next section we numerically demonstrate, that a geometric resonance does not occur, and verify the analytical result for the frequency shift of the breathing mode.

4.2. Comparison with Numerical Results

In order to verify our analytical results, we perform high-precision numerical simulations [245–248]. At first we focus on a description of the BEC dynamics, and compare our analytical results for the radial and longitudinal widths of the condensate obtained perturbatively to the direct numerical solutions of equations (4.1)–(4.2). To this end we consider a BEC in the initial state corresponding to the perturbed equilibrium position, where the small perturbation is proportional to the eigenvector of the quadrupole mode according to equations (4.5) and (4.6). Examples of the condensate dynamics are shown in Fig. 4.1 for a pure two-body interaction $\mathcal{P} = 1$, $\mathcal{K} = 0$ with $\varepsilon = 0.1$, and in Fig. 4.2 for $\mathcal{P} = 1$, $\mathcal{K} = 0.001$, with $\varepsilon = 0.1$. In both figures we plot analytical and numerical solutions for u_ρ and u_z as functions of the dimensionless time parameter $\omega_\rho t$ for different values of the trap aspect ratio λ. Analytical solutions are calculated using the third-order perturbation theory developed in Subsection 4.1.1. We can see in Fig. 4.1 that the agreement is excellent, not only for the non-resonant value of the trap aspect ratio $\lambda = 2.3$ (top panels), but also for $\lambda = 0.55$ (bottom panels), which is close to a geometric resonance, as we will see later in Fig. 4.4(a). For these values of parameters, the relative shift in the quadrupole mode frequency is of the order of 0.3%, and therefore the third-order perturbation theory yields a quite accurate description of the system dynamics. The same applies to

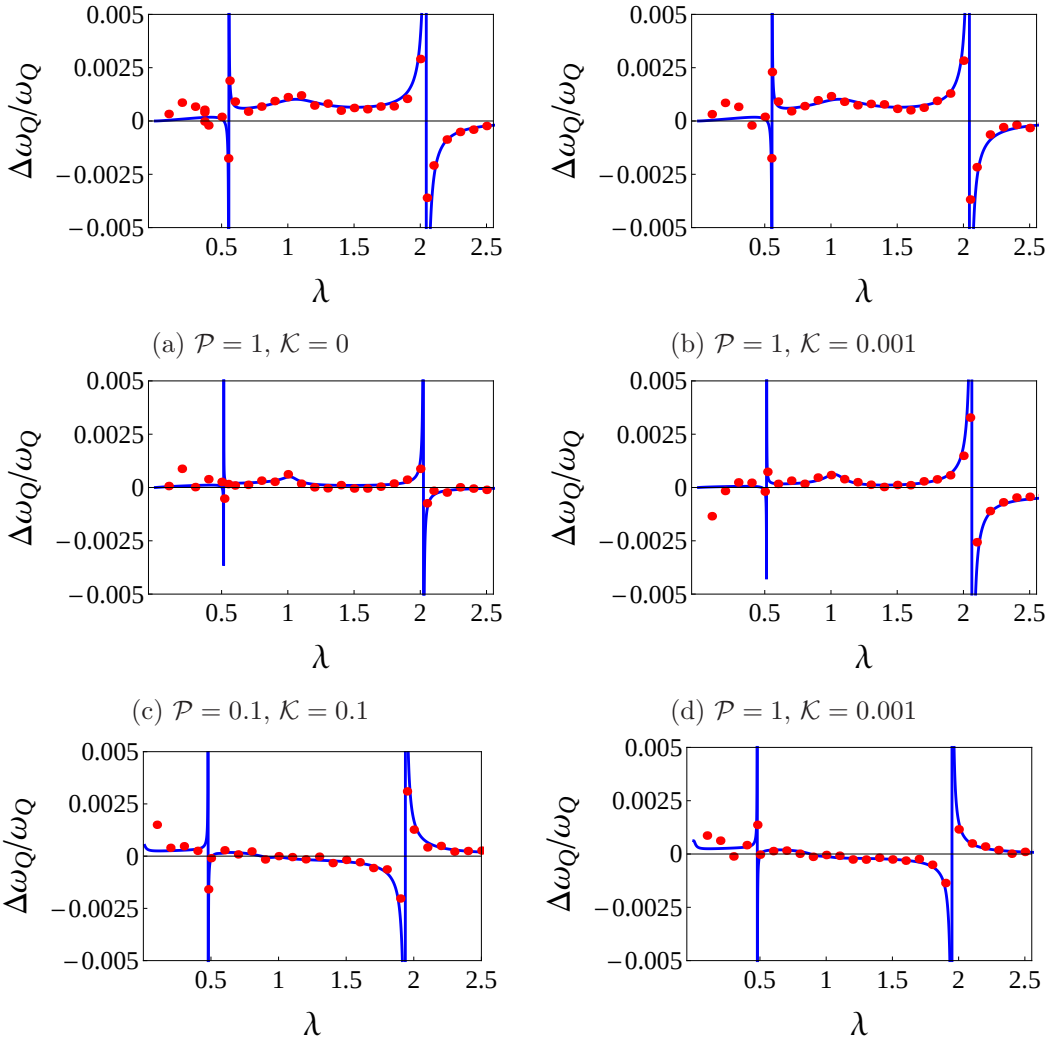

(a) $\mathcal{P} = 1$, $\mathcal{K} = 0$

(b) $\mathcal{P} = 1$, $\mathcal{K} = 0.001$

(c) $\mathcal{P} = 0.1$, $\mathcal{K} = 0.1$

(d) $\mathcal{P} = 1$, $\mathcal{K} = 0.001$

(e) $\mathcal{P} = -0.2$, $\mathcal{K} = 0$

(f) $\mathcal{P} = -0.2$, $\mathcal{K} = 0.005$

Figure 4.4.: Relative frequency shift of the quadrupole mode as a function of the trap aspect ratio λ for $\varepsilon = 0.1$ and different values of two-body and three-body interaction strengths. Solid lines represent the analytical result obtained from Eq. (4.24), while dots are obtained by a numerical analysis of the corresponding excitation spectrum for each value of λ, as described in Fig. 4.3.

the top panels of Fig. 4.2, where $\lambda = 0.7$ is far from any resonance. However, for $\lambda = 2.05$ (bottom panels) we observe some disagreement, which increases with propagation time. This is due to the fact that for $\mathcal{P} = 1$, $\mathcal{K} = 0.001$, the trap aspect ratio $\lambda = 2.05$ is close to a geometric resonance, as we will see in Fig. 4.4(b). In this case the perturbatively calculated shift in the quadrupole mode frequency is much larger than for the bottom panels of Fig. 4.1. For this reason, after a long enough time, the third-order perturbation theory is no longer sufficiently accurate. Although it gives a qualitatively correct description of the behavior of the system, one would have to go to higher orders in perturbation theory to get a more accurate agreement with the numerical results. Such a behavior in the bottom panels of Fig. 4.2 is just a tell-tale of the occurrence of a geometric resonance, and a subsequent analysis of frequency shifts is the only proper way to identify these resonances in a more quantitative way.

However, before we present this analysis, we show in Fig. 4.3 excitation spectra of the BEC dynamics

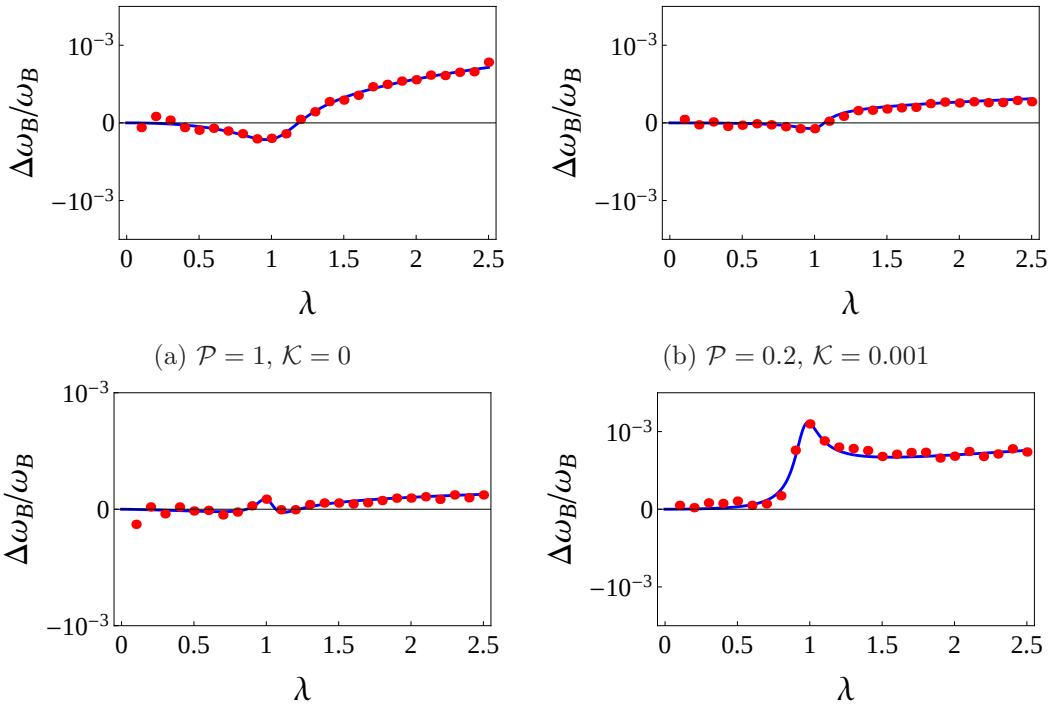

(a) $\mathcal{P} = 1$, $\mathcal{K} = 0$

(b) $\mathcal{P} = 0.2$, $\mathcal{K} = 0.001$

(c) $\mathcal{P} = 0.1$, $\mathcal{K} = 0.1$

(d) $\mathcal{P} = -0.2$, $\mathcal{K} = 0.005$

Figure 4.5.: Relative frequency shift of the breathing mode as a function of the trap aspect ratio λ for $\varepsilon = 0.1$ and different values of two-body and three-body interaction strengths. Solid lines represent the analytical result obtained from Eq. (4.28), while dots are obtained by a numerical analysis of the corresponding excitation spectrum for each value of λ, as described in Fig. 4.3.

which corresponds to the initial conditions Eqs. (4.5), (4.6) for $\mathcal{P} = 1$, $\mathcal{K} = 0.001$, and two values of the trap aspect ratio, $\lambda = 1.9$ and $\lambda = 0.5$. For the parameter values in Fig. 4.3(a), the linear stability analysis yields breathing and quadrupole mode frequencies Eqs. (2.65) and (2.66) with $\omega_B = 3.65$ and $\omega_Q = 1.96$, while for the parameters in Fig. 4.3(b) we obtain $\omega_B = 2.01$ and $\omega_Q = 0.905$, all expressed in units of ω_ρ. In both graphs we can see that the Fourier spectra contain two basic modes, ω_Q and ω_B, whose values agree well with those obtained from the linear stability analysis in equation Eqs. (2.65) and (2.66), and a multitude of higher-order harmonics, which are linear combinations of the two modes, as pointed out in Subsection 4.1.1.

Now we compare the derived analytical results for the frequency shifts of the quadrupole and the breathing mode with the results of numerical simulations for the BEC systems with two- and three-body contact interactions in a cylindrical trap. In particular, we note that the calculated frequency shifts close to geometric resonances reveal poles, which are an artefact of the perturbative approach. Indeed, our detailed numerical calculations show that the observed frequencies remain finite through the whole geometric resonance. In Figs 4.4 and 4.5 we present the comparison of analytic (solid lines) and numeric (dots) values of relative frequency shifts as functions of the trap aspect ratio λ. The analytical results are calculated from equation (4.24) and (4.28), respectively, while the numerical data are obtained from a Fourier analysis of the excitation spectrum, i.e. for each value of λ we have calculated the corresponding Fourier spectra, as in Fig. 4.3, and then extracted the frequency values of the quadrupole and the breathing mode.

In Fig. 4.4(a) we show a special case of a pure two-body interaction, when $\mathcal{K} = 0$. The condition for a geometric resonance $\omega_B = 2\omega_Q$ yields the trap aspect ratios $\lambda_1 = 0.55$ and $\lambda_2 = 2.056$, in

good agreement with the numerical data, as we can see from the graph. The existence of a geometric resonance at $\lambda_1 = 0.55$ is responsible for the violent dynamics seen in the bottom panels of Fig. 4.1, as we have pointed out earlier. However, by analyzing the frequency shifts we can conclusively show that, indeed, the geometric resonance is present. In further graphs we see that the excellent agreement between analytical and numerical results holds also for other values of $\mathcal{P}$ and $\mathcal{K}$, including the case of an attractive two-body interaction $\mathcal{P} = -0.2$, which is still within the BEC stability region. It is interesting to note the observation that the asymptotic approach to geometric resonances for the case of an attractive two-body interaction is reversed compared to the case of a repulsive two-body interaction. For instance, we can see in Fig. 4.4(d) that $\Delta\omega_Q/\omega_Q \to \infty$ when $\lambda \to \lambda_2^-$, and $\Delta\omega_Q/\omega_Q \to -\infty$ when $\lambda \to \lambda_2^+$, while for an attractive $\mathcal{P} = -0.2$ in Fig. 4.4(f) we see that the situation is reversed. However, our numerical results indicate frequency shifts of only about 1 %.

In Fig. 4.5 we compare analytic and numeric results for a frequency shift of the breathing mode. As for the quadrupole mode, the agreement is excellent for both repulsive and attractive two-body interaction. As pointed out in Section. 4.1.2, there are no geometric resonances for the breathing mode frequency, since the corresponding condition $\omega_Q = 2\omega_B$ cannot be satisfied.

Finally, we compare our derived analytic results with those from Ref. [105], where frequency shifts of collective modes were calculated in the Thomas-Fermi (TF) limit using a hydrodynamic approach. In terms of our variational approach, the TF limit corresponds to the limit $\mathcal{P} \to \infty$ for vanishing $\mathcal{K}$, so that Eqs. (2.72) for the frequencies of the breathing and the quadrupole mode reduces to

$$\omega_{B,Q}^2 = 2 + \frac{3}{2}\lambda^2 \pm \frac{1}{2}\sqrt{16 - 16\lambda^2 + 9\lambda^4}\,, \tag{4.29}$$

in agreement with Ref. [105]. The condition for a geometric resonance $\omega_B = 2\omega_Q$ yields trap aspect ratios $\lambda_{1,2} = (\sqrt{125} \pm \sqrt{29})/\sqrt{72}$, i.e. $\lambda_1 \approx 0.683$ and $\lambda_2 \approx 1.952$.

Figure 4.6 gives a comparison of the relative frequency shifts in the TF limit calculated in Ref. [105] using a hydrodynamic approach, and our analytical results obtained using the Poincaré-Lindstedt perturbation theory. Despite the good agreement, we observe small differences, which are due to the fact that reference [105] uses a parabolic variational ansatz for the condensate wave function, while we use the Gaussian ansatz in equation (2.29). We have confirmed that, when applied to the parabolic variational ansatz, our perturbative approach yields frequency shifts in perfect agreement with Ref. [105].

4.3. Resonant Mode Coupling

In this section we study the phenomenon of nonlinearity-induced resonant mode coupling. As already pointed out, even if a BEC system is excited precisely along the quadrupole or, equivalently, the breathing mode, the emerging dynamics will lead to small oscillations which initially involve only the corresponding mode, but then the other collective mode will eventually step in, as well as higher harmonics of the two modes and their linear combinations. This phenomenon is caused by the nonlinear nature of the system [109]. If the trap confinement of the system allows a geometric resonance, this could greatly enhance the mode coupling and speed up the emergence of those modes which are initially not excited, and therefore we designate it as a resonant mode coupling.

To demonstrate this phenomenon, we use the perturbative solution of Eqs. (4.1)–(4.2) with the initial conditions defined by Eqs. (4.5) and (4.6), for which the initial state coincides with the equilibrium with a small perturbation proportional to the quadrupole mode eigenvector. The second-order perturbative solution can then be written in the form

$$\mathbf{u}_2(t) = \mathbf{u}_0 + \begin{pmatrix} A_{\rho Q} \\ A_{zQ} \end{pmatrix} \cos\omega_Q t + \begin{pmatrix} A_{\rho B} \\ A_{zB} \end{pmatrix} \cos\omega_B t + \dots\,, \tag{4.30}$$

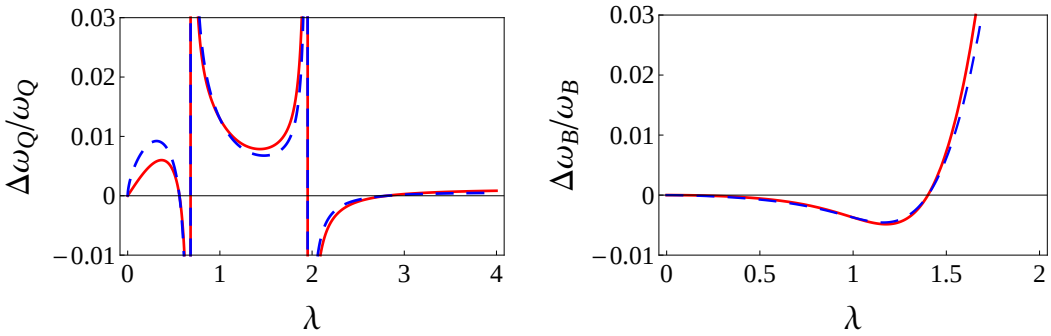

(a) (b)

Figure 4.6.: Comparison of the analytical results for the relative frequency shifts of (a) quadrupole and (b) breathing mode in the Thomas-Fermi limit from Ref. [105] derived using the parabolic variational ansatz (solid red lines) and the analytical results derived here using the Poincaré-Lindstedt perturbation theory with the Gaussian variational ansatz (dashed blue lines).

where dots represent higher harmonics and the respective amplitudes are given by

$$A_{\rho Q} = \varepsilon u_{\rho Q} + \varepsilon^2 \mathcal{A}_{\rho Q 2} \frac{u_{\rho Q}^2}{\omega_Q^2}\,, \tag{4.31}$$

$$A_{zQ} = c_1 A_{\rho Q}\,, \tag{4.32}$$

$$A_{\rho B} = \varepsilon^2 \mathcal{A}_{\rho B 2} \frac{u_{\rho Q}^2(\omega_B^2 - 2\omega_Q^2)}{\omega_B^2(\omega_B^2 - 4\omega_Q^2)}\,, \tag{4.33}$$

$$A_{zB} = c_2 A_{\rho B}\,. \tag{4.34}$$

Note that the absence of terms linear in ε in the expressions for $A_{\rho B}$ and A_{zB} is due to the initial condition, i.e. the fact that, initially, we only excite the quadrupole mode. The constants $c_{1,2}$ in the above expressions are defined by Eqs. (3.26) and (3.27), while $\mathcal{A}_{\rho Q 2}$ and $\mathcal{A}_{\rho B 2}$ are calculated to be

$$\mathcal{A}_{\rho Q 2} = \frac{c_2\gamma_\rho + c_1 c_2 \alpha + c_1^2 c_2 \beta - \alpha - 4c_1\beta - c_1^2\gamma_z}{3(c_1 - c_2)}\,, \tag{4.35}$$

$$\mathcal{A}_{\rho B 2} = \frac{-c_1^3\beta + \alpha - c_1\gamma_\rho + 4c_1\beta - c_1^2\alpha + c_1^2\gamma_z}{c_1 - c_2}\,, \tag{4.36}$$

with α, β, γ_ρ, and γ_z defined by Eqs. (4.11)–(4.14).

In Fig. 4.7 we see the comparison of the derived analytical results and numerical simulations for the amplitudes of the breathing mode, which emerge in the second order, as expected, due to nonlinear features of the system. The numerical results are obtained, as before, by extracting the amplitude of the breathing mode from the Fourier excitation spectra of the system for each value of the trap aspect ratio λ. The agreement is quite good, and we see again a resonant behavior, which occurs at the same trap aspect ratios as for the frequency shift of the quadrupole mode. From Eqs. (4.33) and (4.34) we actually see that the resonances occur when the condition $\omega_B = 2\omega_Q$ is satisfied, which is precisely the same condition as for the frequency shift. Therefore, geometric resonances are not only reflected in the resonances of frequency shifts of collective modes, but also in the resonant mode coupling.

In addition to the absolute values of the breathing mode amplitudes, which are excited through the nonlinear mode coupling, it is also interesting to look at their relative values, compared to the

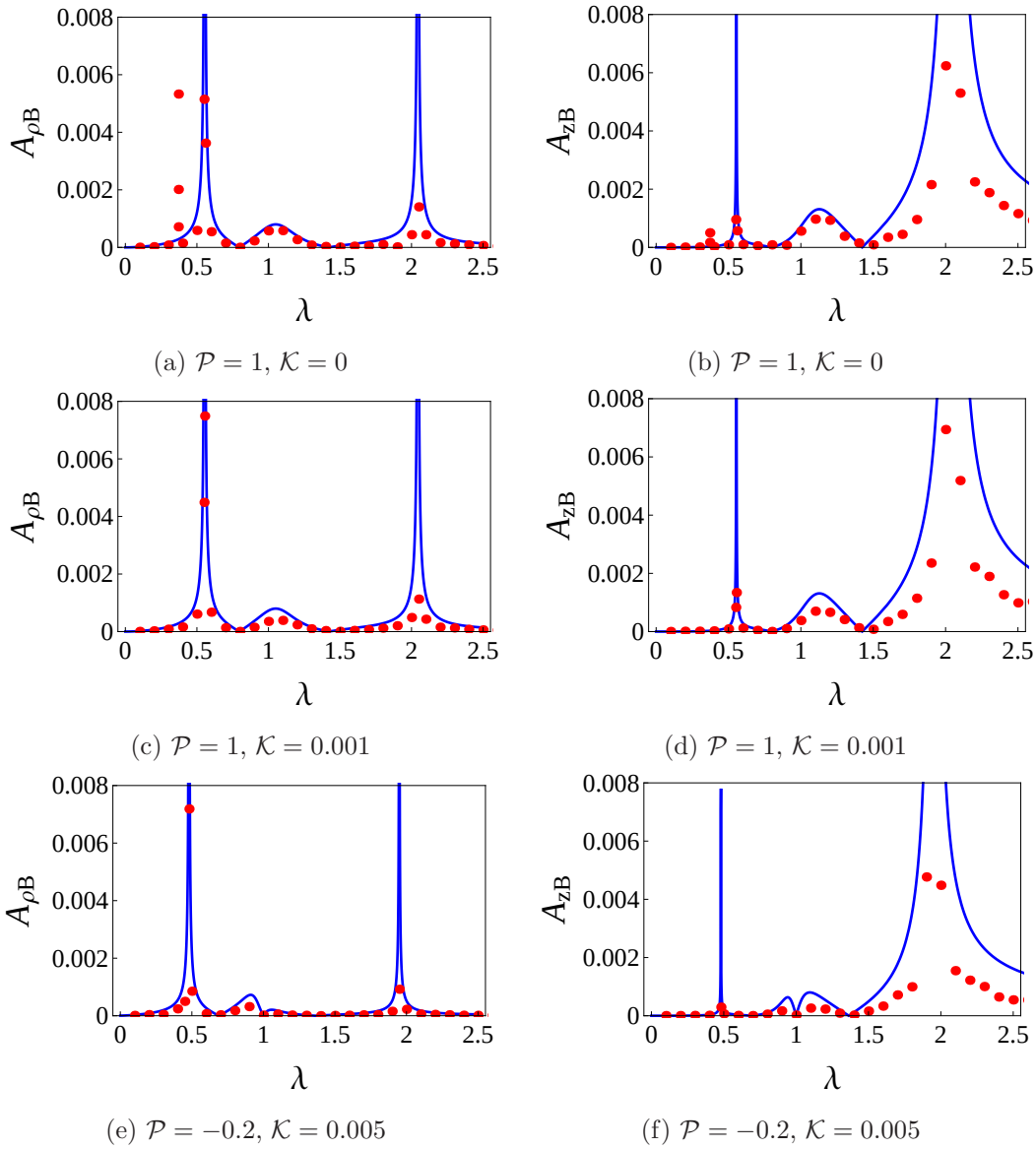

(a) $\mathcal{P} = 1$, $\mathcal{K} = 0$

(b) $\mathcal{P} = 1$, $\mathcal{K} = 0$

(c) $\mathcal{P} = 1$, $\mathcal{K} = 0.001$

(d) $\mathcal{P} = 1$, $\mathcal{K} = 0.001$

(e) $\mathcal{P} = -0.2$, $\mathcal{K} = 0.005$

(f) $\mathcal{P} = -0.2$, $\mathcal{K} = 0.005$

Figure 4.7.: Amplitudes of the breathing mode emerging in the second order of the perturbation theory from nonlinear BEC dynamics after initially only the quadrupole mode is excited, given as functions of the trap aspect ratio λ for $\varepsilon = 0.1$ and different values of two-body and three-body interaction strengths. The amplitudes $A_{\rho B}$ and A_{zB} from Eqs. (4.33) and (4.34) correspond to the condensate widths of the emerging breathing mode dynamics.

quadrupole mode amplitudes, i.e. the ratios

$$R_\rho = \frac{A_{\rho B}}{A_{\rho Q}} \propto \frac{\omega_B^2 - 2\omega_Q^2}{\omega_B^2 - 4\omega_Q^2}, \tag{4.37}$$

$$R_z = \frac{A_{zB}}{A_{zQ}} \propto \frac{\omega_B^2 - 2\omega_Q^2}{\omega_B^2 - 4\omega_Q^2}. \tag{4.38}$$

Figure 4.8 shows the comparison of analytical and numerical results for the relative amplitudes of the nonlinearity-excited breathing mode. Due to the geometric resonances, we see that the trap aspect ratio can be tuned in such a way that the resonant mode coupling excites the breathing mode with an amplitude which is even far larger than that of the quadrupole mode, which served as the source

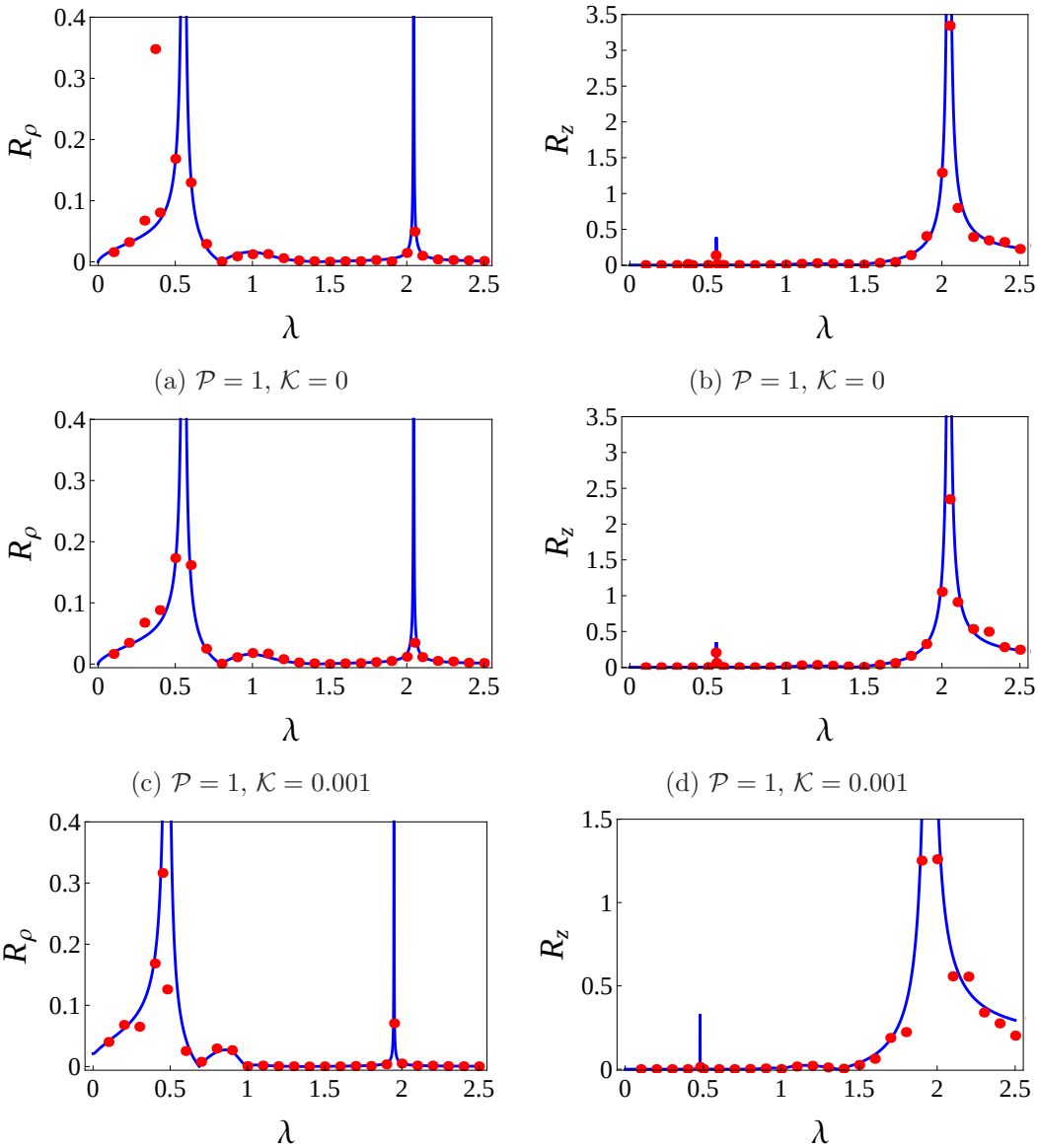

(a) $\mathcal{P} = 1$, $\mathcal{K} = 0$ (b) $\mathcal{P} = 1$, $\mathcal{K} = 0$

(c) $\mathcal{P} = 1$, $\mathcal{K} = 0.001$ (d) $\mathcal{P} = 1$, $\mathcal{K} = 0.001$

(e) $\mathcal{P} = -0.2$, $\mathcal{K} = 0.005$ (f) $\mathcal{P} = -0.2$, $\mathcal{K} = 0.005$

Figure 4.8.: Ratios of breathing and quadrupole mode amplitudes emerging in the second order of the perturbation theory after initially only the quadrupole mode is excited, given as functions of the trap aspect ratio λ for $\varepsilon = 0.1$ and different values of two-body and three-body interaction strengths. The quantity R_ρ and R_z from Eqs. (4.37) and (4.38) corresponds to the ratio of amplitudes of the breathing and the quadrupole mode in the radial and longitudinal condensate width.

of excitation.

Furthermore, from Eqs. (4.33) and (4.34) we see that, if the geometry of the trap is tuned such that $\omega_B = \omega_Q\sqrt{2}$, then the amplitudes of the breathing mode vanish simultaneously, i.e. $A_{\rho B} = A_{zB} = 0$. Although this is true only in second-order perturbation theory, it still represents a significant suppression of the nonlinear mode coupling. Therefore, the tunability of the trap aspect ratio offers a unique tool for enhancing and suppressing the mode coupling in a BEC, which might be of broad experimental interest.

In a similar way, we can initially excite only the breathing mode, which corresponds to Eqs. (4.1)–

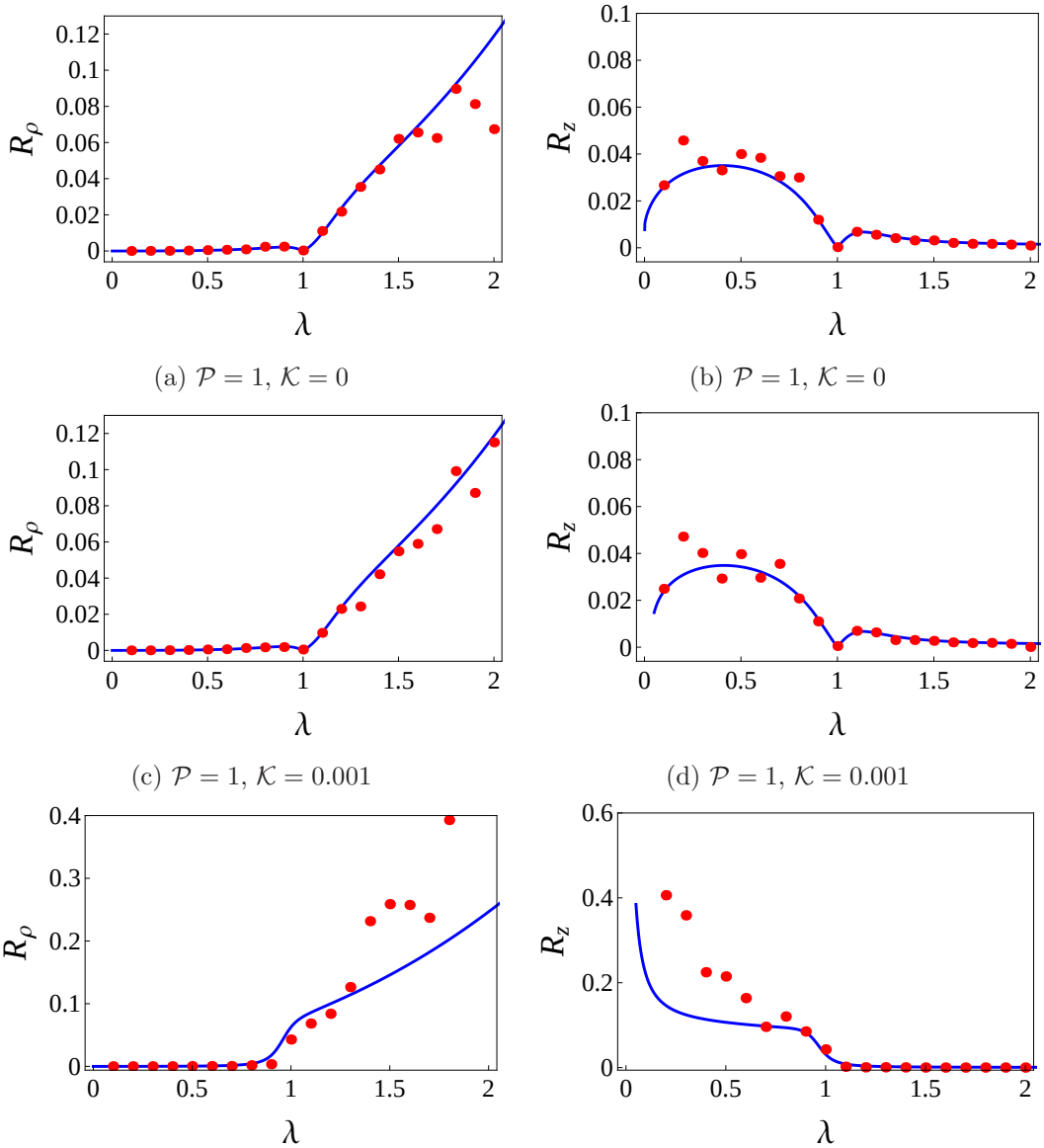

(a) $\mathcal{P} = 1$, $\mathcal{K} = 0$ (b) $\mathcal{P} = 1$, $\mathcal{K} = 0$

(c) $\mathcal{P} = 1$, $\mathcal{K} = 0.001$ (d) $\mathcal{P} = 1$, $\mathcal{K} = 0.001$

(e) $\mathcal{P} = -0.2$, $\mathcal{K} = 0.005$ (f) $\mathcal{P} = -0.2$, $\mathcal{K} = 0.005$

Figure 4.9.: Ratios of quadrupole and breathing mode amplitudes emerging in second order perturbation theory after initially only the breathing mode is excited, given as functions of the trap aspect ratio λ for $\varepsilon = 0.1$ and different values of two-body and three-body interaction strengths. The quantity R_ρ and R_z from Eqs. (4.46) and (4.47) corresponds to the ratio of amplitudes of the breathing and the quadrupole mode in the radial and longitudinal condensate width.

(4.2) with initial conditions defined in Eqs. (4.25) and (4.26). The solution in the second-order perturbation theory has again the form

$$\mathbf{u}_2(t) = \mathbf{u}_0 + \begin{pmatrix} A_{\rho B} \\ A_{zB} \end{pmatrix} \cos\omega_B t + \begin{pmatrix} A_{\rho Q} \\ A_{zQ} \end{pmatrix} \cos\omega_Q t + \dots , \tag{4.39}$$

but now the respective amplitudes read

$$A_{\rho B} \quad = \quad \varepsilon u_{\rho B} + \varepsilon^2 \mathcal{A}_{\rho B 2} \frac{u_{\rho B}^2}{\omega_B^2} , \tag{4.40}$$

$$A_{zB} = c_2 A_{\rho B}\,, \tag{4.41}$$

$$A_{\rho Q} = \varepsilon^2 \mathcal{A}_{\rho Q2} \frac{u_{\rho B}^2(2\omega_B^2 - \omega_Q^2)}{\omega_Q^2(4\omega_B^2 - \omega_Q^2)}\,, \tag{4.42}$$

$$A_{zQ} = c_1 A_{\rho Q}\,, \tag{4.43}$$

and the coefficients $\mathcal{A}_{\rho B2}$ and $\mathcal{A}_{\rho Q2}$ are given by

$$\mathcal{A}_{\rho B2} = \frac{-c_1\gamma_\rho - c_1c_2\alpha - c_1c_2^2\beta + \alpha + 4c_2\beta + c_2^2\gamma_z}{3(c_1 - c_2)}\,, \tag{4.44}$$

$$\mathcal{A}_{\rho Q2} = \frac{c_2^3\beta - \alpha + c_2\gamma_\rho - 4c_2\beta + c_2^2\alpha - c_2^2\gamma_z}{c_1 - c_2}\,. \tag{4.45}$$

In this case, the amplitude ratios are given by

$$R_\rho = \frac{A_{\rho Q}}{A_{\rho B}} \propto \frac{2\omega_B^2 - \omega_Q^2}{4\omega_B^2 - \omega_Q^2}\,, \tag{4.46}$$

$$R_z = \frac{A_{zQ}}{A_{zB}} \propto \frac{2\omega_B^2 - \omega_Q^2}{4\omega_B^2 - \omega_Q^2}\,. \tag{4.47}$$

Figure 4.9 compares analytical and numerical results for the mode coupling when initially only the breathing mode is excited, and then the quadrupole mode emerges due to the nonlinearity of the system. As for the case of the breathing mode frequency shift, there are no resonances, since $\omega_B > \omega_Q$, and the resonance condition $2\omega_B = \omega_Q$ cannot be satisfied, as we see from the graphs. Also, the condition $\omega_B\sqrt{2} = \omega_Q$ cannot be fulfilled, and therefore the amplitude of the quadrupole mode cannot be fully suppressed. For a repulsive two-body interaction in Fig. 4.9(a)–(d) we see that the ratios R_ρ and R_z are below 10%, and the mode coupling mechanism is not able to produce a significant amplitude for the quadrupole mode. For the case of an attractive two-body interaction in Fig. 4.9(e)–(f), the ratio increases and the generated quadrupole mode amplitude is stronger. Here the agreement between analytical and numerical results is only qualitative, so that the perturbation theory has to be carried out to higher orders in the small parameter ε in order to improve the agreement.

5. Breakdown of Kohn Theorem Near Feshbach Resonance in Magnetic Trap

Several studies showed that the excitation of low-lying collective modes can be achieved by modulating a system parameter. One example is to change the external potential trap [46,65,103–107] or, more specifically, the trap anisotropy of the confining potential [105,112–114,119,227]. Alternatively, this can also be achieved by a modulation of the s-wave scattering length [87,93,109,108,110,111] or possibly by modifying the three-body interaction strength [108,112,113].

In 1961 W. Kohn [249] first showed in a three-dimensional solid that the interaction between electrons does not change the cyclotron resonance frequency, i.e. the frequency of an electron moving in a static uniform magnetic field on a circle due to the Lorentz force [249]. In addition the Kohn theorem can be applied in the realm of the ultracold quantum gases where it states that the center of mass of the entire cloud oscillates back and forth in the trapping potential with the natural frequency of the trap irrespective of the strength and type of the two-body interaction. For instance, the Kohn theorem is discussed explicitly at zero temperature for a Bose gas in the Bogoliubov approximation in Ref. [250]. Furthermore, the Kohn theorem was shown to hold also at finite temperature, i.e. the dipole mode frequency does not change even at finite temperature [222,226,251–253]. The authors in Refs. [222,251] explored that the dynamics of a trapped Bose condensed gas at finite temperature is consistent with a generalized Kohn theorem and satisfies the linearized ZNG hydrodynamic equations. In particular the Kohn mode was studied in Ref. [252] by using and considering a nonlinear GP equation for the condensate wave function, which is coupled to a collisionless Boltzmann or Vlasov-Landau equation describing the dynamics of the noncondensed cloud in the collisionless regime. The validity of the Kohn theorem at finite temperature theory, based on a linear response formalism, was discussed in Ref. [226], afterwards, was examined in Ref. [253] for a specific finite temperature approximation within the dielectric formalism.

Another possible procedure to primarily excite the dipole mode consists in introducing an abrupt change in the potential. The experimental achievement [64,69] was confirmed by Refs. [50,70], where also the quadrupole frequency was determined as an eigenfrequency of the hydrodynamic equations. The internal and external dynamics of a Bose-Einstein condensate oscillating in an anharmonic magnetic waveguide was studied in Ref. [67]. There also several nonlinear effects including second and third harmonic generation of the center of mass motion, a coupling of the internal and external dynamics, and a nonlinear mode mixing were identified. Furthermore, the dipole mode frequency was studied by using a variational sum rule approach in Refs. [254–257]. The collective dipole oscillations in the Bose-Fermi mixture were studied theoretically in Refs. [255] and experimentally in Ref. [258]. In particular Ref. [255] investigated how the dipole mode frequency is affected by the unequal mases of bosons and fermion. Furthermore, the dipole mode frequency was studied by using a spin-orbit coupled Bose-Einstein condensate confined in a harmonic trap both experimentally [256] and theoretically [256,257] and it was shown that, due to spin-orbit coupling, the dipole mode frequency deviates from the trap frequency. The dipole mode was discussed in a fermionic mixture by using Boltzmann equation in Ref. [259].

In the recent work [121], the authors explored a different physical idea by investigating the coupling between dipole and quadrupole modes in the immediate vicinity of a Feshbach resonance. They

started with considering a Bose-Einstein condensate in a magneto-optical trap with a controlled bias field, where the dipole mode is excited. If the bias field is close enough to a Feshbach resonance, the oscillation of the entire cloud through the inhomogeneous bottom of the trap causes an effective periodic time-dependent modulation in the scattering length, which in turn excites other modes like the quadrupole or the breathing mode.

Although Ref. [121] introduces this appealing physical notion, it only provides a rough quantitative study. Therefore we calculate in this chapter in detail the collective excitation modes of a harmonically trapped Bose-Einstein condensate in the vicinity of a Feshbach resonance for experimentally realistic parameters of a ^{85}Rb BEC [260]. To this end, we consider the situation that a Bose-Einstein condensate oscillates within a dipole mode in z-direction and investigate how the dipole mode frequency changes when the bias magnetic field approaches the Feshbach resonance [261]. At first we follow Ref. [121] and transform the partial differential equation of Gross and Pitaevskii for the concentrate wave function in Section 5.2 within a variational approach [84,85] into a set of ordinary differential equations for the widths of the condensate and the center of mass oscillation in an axially-symmetric harmonic trap plus a bias potential. We then explore in Section 5.3 the heuristic approximation ansatz of Ref. [121] and determine the consequences for the frequencies of collective modes. Our own analysis is then based on an exact treatment as is explained in Section 5.4. With this we calculate in Section 5.5 the dipole mode frequency and the frequencies of collective modes on top of the Feshbach resonance. In contrast to the heuristic approximation of Ref. [121] we predict a finite dipole mode frequency on top of the Feshbach resonance. Then we discuss the corresponding results for the right-side of the Feshbach resonance in Section 5.6. In the limit that the bias field approaches the Feshbach resonance, we reproduce our previous results from Section 5.5. When the bias magnetic field is far away from the Feshbach resonance, however, we only partially recover the result of Ref. [121]. This shows that the heuristic approximation of Ref.[121] is not even correct far away from the Feshbach resonance despite its appealing physical motivation.

5.1. Near Feshbach Resonance

As mentioned in Chapter 2, the dynamics of a condensed Bose gas in a trap at zero temperature is described by the time-dependent GP equation Eq. (2.12). In the presence of a magnetic field, the s-wave scattering can be tuned by applying an external magnetic field due to the Feshbach resonance resulting in Eq. (1.1) [50,262]. Here in this chapter, we consider a Bose-Einstein condensate confined in a magneto-optical trap composed of a harmonic potential plus a bias

$$V_{\text{ext.}}(\mathbf{r}) = V_0 + \frac{M\omega_\rho^2}{2}\left(\rho^2 + \lambda^2 z^2\right). \tag{5.1}$$

This potential is generated by a corresponding magnetic field whose modulus is given by

$$B = B_0 + \frac{M\omega_\rho^2}{2\mu_{\text{B}}}\left(\rho^2 + \lambda^2 z^2\right), \tag{5.2}$$

where μ_{B} is the magnetic dipole moment and $B_0 = V_0/\mu_{\text{B}}$ is the bias field. This kind of field can be obtained, for instance, in a Ioffe-Pritchard trap [121,263]. From Eqs. (1.1) and (5.2), the interparticle interaction in the atomic cloud moving in this potential is controlled by the spatially dependent scattering length

$$a_{\text{s}} = a_{\text{BG}}\left[1 - \frac{\Delta}{\mathcal{H} + \frac{M\omega_\rho^2}{2\mu_{\text{B}}}\left(\rho^2 + \lambda^2 z^2\right)}\right], \tag{5.3}$$

where $\mathcal{H} = B_0 - B_{\text{res}}$ denotes the deviation of the bias magnetic field B_0 from the location of the Feshbach resonance at B_{res}. To this end, we consider the potential Eq. (5.1) loaded with a condensed

cloud whose dipole mode is excited in z-direction. In this configuration, far away from the Feshbach resonance the center of mass oscillates periodically at the bottom of the trap with the Kohn mode frequency $\omega_z = \lambda\omega_\rho$.

For experimental data, we follow Refs. [260,264] and consider $N = 4 \times 10^4$ atoms of a ^{85}Rb BEC in a harmonic trap with $\omega_\rho = 2\pi \times 156$ Hz along the radial direction and $\omega_z = 2\pi \times 16$ Hz along the axial direction. The Feshbach resonance parameters are given by the background value $a_{\rm BG} = -443\ a_0$, where a_0 is the Bohr radius, the width $\Delta = 10.7$ G, and the resonance location at $B_{\rm res} = 155$ G. The magnetic dipole moment $\mu_{\rm B}$ of a ^{85}Rb [265] is equal to one Bohr magneton $m_{\rm B} = \frac{e\hbar}{2M_e} = 9.27400968(20) \times 10^{-24}$ J/T, which represents the magnetic dipole moment of the Hydrogen atom with the electron charge e and the electron rest mass M_e.

Initially, we discuss qualitatively the consequences of the Thomas-Fermi approximation for a vanishing three-body interaction strength $g_3 = 0$. As we assume to have a strong two-body interaction, we can neglect the kinetic energy term in Eq. (2.15) and obtain

$$\mu = V_{\rm ext.}(\mathbf{r}) + g_2 n_c(\mathbf{r}). \tag{5.4}$$

Far away from the Feshbach resonance we can consider the potential in Eq. (5.3) to be small, thus we expand Eq. (5.3) up to the first order of the external potential, yielding

$$\mu = V_{\rm ext.}(\mathbf{r}) + \frac{4\pi\hbar^2 a_{\rm BG} n_c(\mathbf{0})}{M}\left[1 - \frac{\Delta}{\mathcal{H}} + \frac{\Delta}{\mathcal{H}^2\mu_{\rm B}}\frac{M\omega_\rho^2}{2}\left(\rho^2 + \lambda^2 z^2\right) + ...\right], \tag{5.5}$$

where $n_c(\mathbf{0})$ is the TF density at the trap center with the chemical potential μ being defined in Eq. (2.21) for vanishing three-body interaction. On the one hand we read off from Eq. (5.5) that the effective s-wave scattering length is given by

$$a_{\rm eff} = a_{\rm BG}\left(1 - \frac{\Delta}{\mathcal{H}}\right). \tag{5.6}$$

Thus, the BEC is unstable, i.e. $a_{\rm eff} < 0$, provided that $B_0 > B_{\rm crit} + \Delta$. Conversely, the TF approximation yields a stable BEC, i.e. $a_{\rm eff} > 0$, in the case that $B_{\rm res} < B_0 < B_{\rm crit} = B_{\rm res} + \Delta$. On the other hand, we obtain from Eqs. (2.17) and (5.5) the effective Kohn mode frequency

$$\omega_{D,\rm eff} = \lambda\omega_\rho\sqrt{1 + \frac{4\pi\hbar^2 a_{\rm BG} n_c(\mathbf{0})}{M}\frac{\mu\Delta}{\mathcal{H}^2\mu_{\rm B}}}. \tag{5.7}$$

On the right-hand side of the Feshbach resonance we expect for $B_{\rm res} < B_0 < B_{\rm crit} = B_{\rm res} + \Delta$ the expected Kohn mode frequency $\omega_{D,\rm eff}$ which is smaller than the corresponding one without the Feshbach resonance due to $a_{\rm BG} < 0$. In the following we will show that this initial qualitative finding is confirmed by a more quantitative analysis.

5.2. Variational Approach

In order to analytically study the dynamical system of a BEC with two-body contact interaction, where the dipole mode is excited in z-direction, we use a Gaussian variational ansatz which also coincides the center of mass oscillation in z-direction according to Refs. [84,85,121]. For an axially symmetric trap, this time-dependent ansatz reads

$$\psi^G(\rho, z, t) = \mathcal{N}\exp\left[-\frac{\rho^2}{2u_\rho^2} + i\rho\alpha_\rho + i\rho^2\beta_\rho\right]\exp\left[-\frac{(z-z_0)^2}{2u_z^2} + iz\alpha_z + iz^2\beta_z\right], \tag{5.8}$$

where $\mathcal{N} = 1/\sqrt{\pi^{\frac{3}{2}} u_\rho^2 u_z}$ is a normalization factor, while $u_{\rho,z}$, z_0, $\alpha_{\rho,z}$, and $\beta_{\rho,z}$ denote time-dependent variational parameters, which represent radial, axial condensate widths, the center of mass oscillation, and the corresponding phases. If we insert the Gaussian ansatz Eq. (5.8) into the Lagrange function (2.26), we obtain

$$\begin{aligned} L \;=\; & -\frac{\hbar}{2}\left[u_z^2\dot{\beta}_z + 2z_0^2\dot{\beta}_z + 2z_0\dot{\alpha}_z + 2u_\rho^2\dot{\beta}_\rho + \sqrt{\pi}u_\rho\dot{\alpha}_\rho\right] - \frac{\hbar^2}{2M}\left[\frac{1}{2u_z^2} + \frac{1}{u_\rho^2} + 2u_z^2\beta_z^2 + 4z_0^2\beta_z^2\right. \\ & \left. + 4z_0\beta_z\alpha_z + \alpha_z^2 + 4u_\rho^2\beta_\rho^2 + 2\sqrt{\pi}u_\rho\beta_\rho\alpha_\rho + \alpha_\rho^2\right] - V_0 - \frac{M\omega_\rho^2}{2}\left[u_\rho^2 + \frac{\lambda^2 u_z^2}{2} + \lambda^2 z_0^2\right] \\ & - \frac{\hbar^2 N a_{\mathrm{BG}}}{\sqrt{2\pi}M}\frac{1}{u_\rho^2 u_z} + \frac{4\hbar^2 N a_{\mathrm{BG}}\Delta}{\pi u_\rho^4 u_z^2 M} f(u_\rho, u_z, z_0)\,, \end{aligned} \tag{5.9}$$

where we have introduced the integral

$$f(u_\rho, u_z, z_0) = \int_0^\infty d\rho \int_{-\infty}^\infty dz\, \frac{\rho \exp\left[-2\rho^2/u_\rho^2 - 2(z-z_0)^2/u_z^2\right]}{\mathcal{H} + \frac{M\omega_\rho^2}{2\mu_{\mathrm{B}}}\left(\rho^2 + \lambda^2 z^2\right)}. \tag{5.10}$$

From the corresponding Euler-Lagrange equations Eq. (2.31) we obtain the equations of motion for all variational parameters. The phases $\alpha_{\rho,z}$ and $\beta_{\rho,z}$ can be expressed explicitly in terms of first derivatives of the widths u_ρ, u_z, and the center of mass coordinate z_0 according to

$$\alpha_\rho = 0\,, \qquad \alpha_z = \frac{M}{\hbar}\dot{z}_0 - 2z_0\beta_z\,, \qquad \beta_\rho = \frac{M}{2\hbar}\frac{\dot{u}_\rho}{u_\rho}\,, \qquad \beta_z = \frac{M}{2\hbar}\frac{\dot{u}_z}{u_z}\,. \tag{5.11}$$

Inserting Eq. (5.11) into the Euler-Lagrange equations for the width of the condensates u_ρ, u_z, and the center of mass coordinate z_0, we obtain a system of three second order differential equations for u_ρ, u_z, and z_0:

$$\ddot{u}_\rho + \omega_\rho^2 u_\rho - \frac{\hbar^2}{M^2 u_\rho^3} - \sqrt{\frac{2}{\pi}}\frac{a_{\mathrm{BG}} N\hbar^2}{M^2 u_z u_\rho^3}\left[1 - \frac{16\Delta f(u_\rho, u_z, z_0)}{\sqrt{2\pi}u_\rho^2 u_z} + \frac{4\Delta}{\sqrt{2\pi}u_\rho u_z}\frac{\partial f(u_\rho, u_z, z_0)}{\partial u_\rho}\right] = 0\,, \tag{5.12}$$

$$\ddot{u}_z + \lambda^2\omega_\rho^2 u_z - \frac{\hbar^2}{M^2 u_z^3} - \sqrt{\frac{2}{\pi}}\frac{a_{\mathrm{BG}} N\hbar^2}{M^2 u_z^2 u_\rho^2}\left[1 - \frac{16\Delta f(u_\rho, u_z, z_0)}{\sqrt{2\pi}u_\rho^2 u_z} + \frac{8\Delta}{\sqrt{2\pi}u_\rho^2}\frac{\partial f(u_\rho, u_z, z_0)}{\partial u_z}\right] = 0\,, \tag{5.13}$$

$$\ddot{z}_0 + \lambda^2\omega_\rho^2 z_0 - \frac{4\hbar^2 N a_{\mathrm{BG}}\Delta}{\pi M^2 u_\rho^4 u_z^2}\frac{\partial f(u_\rho, u_z, z_0)}{\partial z_0} = 0\,. \tag{5.14}$$

In the following we discuss different approaches how to extract the frequencies of the low-lying collective modes from the equations of motion Eq. (5.12)–(5.14).

5.3. Approximative Solution

In this section we discuss the heuristic approximation of Ref. [121] how to evaluate the integral Eq. (5.10). To this end we assume that the cloud size is much smaller than the oscillating amplitude, which means that the cloud experiences the same field equally at any point, i.e., the scattering length is the same throughout the entire cloud. This is equivalent to stating that the numerator of the integral Eq. (5.10), i. e.

$$\rho \exp\left[-2\rho^2/u_\rho^2 - 2(z-z_0)^2/u_z^2\right]\,, \tag{5.15}$$

is much narrower than the denominator

$$\frac{1}{\mathcal{H} + \frac{M\omega_\rho^2}{2\mu_{\mathrm{B}}}\left(\rho^2 + \lambda^2 z^2\right)}\,, \tag{5.16}$$

which leads to the condition

$$u_\rho \ll \sqrt{\frac{2\mu_\mathrm{B}\mathcal{H}}{M\omega_\rho^2}}\,, \qquad u_z \ll \sqrt{\frac{2\mu_\mathrm{B}\mathcal{H}}{M\omega_\rho^2\lambda^2}}\,. \tag{5.17}$$

Thus, the heuristic approximation of Ref. [121] seems to be valid for a large enough $\mathcal{H}$, i.e. far away from the Feshbach resonance.

In that case, we can expand Eq. (5.16) around the center of mass $\rho = 0$ and $z = z_0$, which gives us in leading order

$$\frac{1}{\mathcal{H} + \frac{M\omega_\rho^2}{2\mu_\mathrm{B}}\left(\rho^2 + \lambda^2 z^2\right)} \approx \frac{1}{\mathcal{H} + \frac{M\omega_\rho^2}{2\mu_\mathrm{B}}\lambda^2 z_0^2}\,. \tag{5.18}$$

Within this approximation, the integral Eq. (5.10) can be evaluated exactly

$$f(u_\rho, u_z, z_0) \approx \frac{\sqrt{2\pi}}{8\mathcal{H}} \frac{u_\rho^2 u_z}{\left(1 + \frac{M\omega_\rho^2\lambda^2 z_0^2}{2\mu_\mathrm{B}\mathcal{H}}\right)}\,. \tag{5.19}$$

By substituting Eq. (5.19) into Eqs. (5.12)–(5.14) and after introducing dimensionless parameters according to Eq. (2.34) with

$$\mathcal{P}_\mathrm{BG} = \sqrt{\frac{2}{\pi}}\frac{N a_\mathrm{BG}}{l}\,, \qquad \varepsilon_0 = \frac{\Delta}{\mathcal{H}}\,, \qquad \varepsilon_1 = \frac{\mathcal{H}\mu_\mathrm{B}}{\hbar\omega_\rho}\,, \tag{5.20}$$

we get a system of three second ordinary differential equations u_ρ, u_z, and z_0 in the dimensionless form

$$\ddot{u}_\rho + u_\rho - \frac{1}{u_\rho^3} - \frac{\mathcal{P}_\mathrm{BG}}{u_z u_\rho^3}\left(1 - \frac{\varepsilon_0}{1 + z_0^2\lambda^2/2\varepsilon_1}\right) = 0\,, \tag{5.21}$$

$$\ddot{u}_z + \lambda^2 u_z - \frac{1}{u_z^3} - \frac{\mathcal{P}_\mathrm{BG}}{u_z^2 u_\rho^2}\left(1 - \frac{\varepsilon_0}{1 + z_0^2\lambda^2/2\varepsilon_1}\right) = 0\,, \tag{5.22}$$

$$\ddot{z}_0 + \lambda^2 z_0\left[1 + \frac{\varepsilon_0\mathcal{P}_\mathrm{BG}}{2\varepsilon_1 u_\rho^2 u_z\left(1 + z_0^2\lambda^2/2\varepsilon_1\right)^2}\right] = 0\,. \tag{5.23}$$

The time-independent solution $u_\rho = u_{\rho 0}$, $u_z = u_{z0}$, and $z_0 = z_{00}$ is determined by setting the accelerations in Eqs. (5.21)–(5.23) to zero:

$$u_{\rho 0} - \frac{1}{u_{\rho 0}^3} - \frac{\mathcal{P}_\mathrm{BG}}{u_{z0} u_{\rho 0}^3}\left(1 - \varepsilon_0\right) = 0\,, \tag{5.24}$$

$$\lambda^2 u_{z0} - \frac{1}{u_{z0}^3} - \frac{\mathcal{P}_\mathrm{BG}}{u_{z0}^2 u_{\rho 0}^2}\left(1 - \varepsilon_0\right) = 0\,, \tag{5.25}$$

$$z_{00} = 0\,. \tag{5.26}$$

Let us now determine the frequencies of collective modes in this approximation which has not been considered in Ref. [121]. To this end we linearize Eqs. (5.21)–(5.23) around these equilibrium positions, so we expand the condensate widths as $u_\rho = u_{\rho 0} + \delta u_\rho$, $u_z = u_{z0} + \delta u_z$, and the center of mass motion $z_0 = z_{00} + \delta z_0$, insert these expressions into the corresponding equations, and expand them around the equilibrium widths by keeping only linear terms. From Eqs. (5.21) and (5.22) we obtain an eigenvalue problem of the form Eq. (2.63), from which we immediately get the frequencies of the breathing and the quadrupole mode

$$\omega_{B,Q}^2 = \frac{1}{2}\left[m_1 + m_3 \pm \sqrt{(m_1 - m_3)^2 + 8m_2^2}\right]\,, \tag{5.27}$$

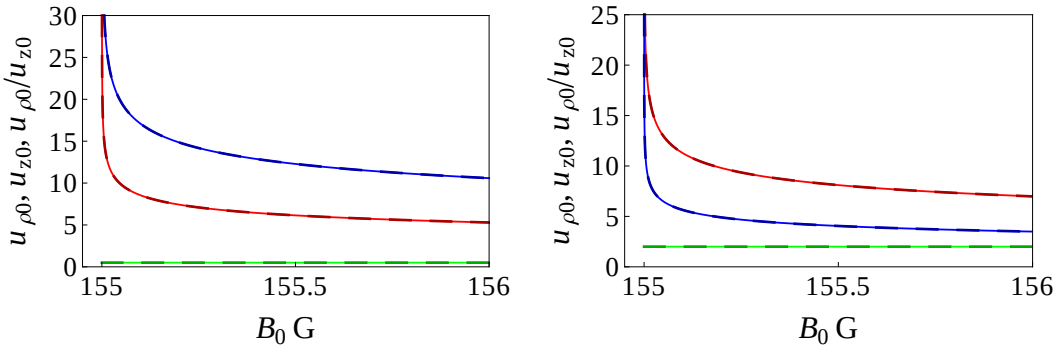

(a) (b)

Figure 5.1.: Equilibrium positions $u_{\rho 0}$ (red curves), u_{z0} (blue curves), and trap aspect ratio $u_{\rho 0}/u_{z0}$ (green curves) as a function of magnetic field B_0 for the experimental dimensionless parameter of the two-body contact interaction $\mathcal{P}_{\rm BG} = -856.732$ with different trap aspect ratios (a) $\lambda = 0.5$ and (b) $\lambda = 2$. The solid and dashed curves correspond to the exact results Eq. (5.24), Eq. (5.25) and the TF approximation Eq. (5.32), respectively.

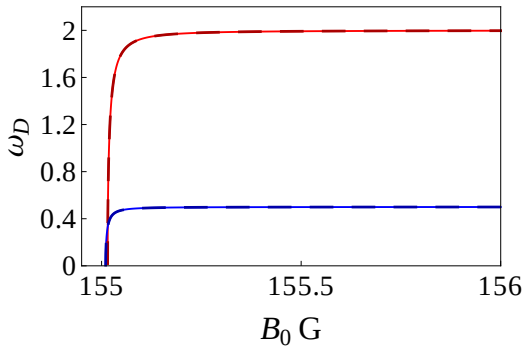

Figure 5.2.: Dipole mode frequency as a function of magnetic field B_0 for the experimental dimensionless parameter of the two-body contact interaction $\mathcal{P}_{\rm BG} = -856.732$ with different trap aspect ratios (a) $\lambda = 0.5$ (blue curves) and (b) $\lambda = 2$ (red curves). The solid and dashed curves correspond to the exact result Eq. (5.31) and the TF approximation Eq. (5.34), respectively.

where the abbreviations m_1, m_2, and m_3 are calculated by using Mathematica [242] and defined as follows

$$m_1 = 1 + \frac{3}{u_{\rho 0}^4} + \frac{3\mathcal{P}_{\rm BG}}{u_{\rho 0}^4 u_{z0}} (1 - \varepsilon_0) \ , \tag{5.28}$$

$$m_2 = \frac{\mathcal{P}_{\rm BG}}{u_{\rho 0}^3 u_{z0}^2} (1 - \varepsilon_0) \ , \tag{5.29}$$

$$m_3 = \lambda^2 + \frac{3}{u_{z0}^4} + \frac{2\mathcal{P}_{\rm BG}}{u_{\rho 0}^2 u_{z0}^3} (1 - \varepsilon_0) \ . \tag{5.30}$$

In addition we obtain from Eq. (5.23) the dipole mode frequency

$$\omega_D^2 = \lambda^2 \left(1 + \frac{\varepsilon_0 \mathcal{P}_{\rm BG}}{2\varepsilon_1 u_{\rho 0}^2 u_{z0}} \right) \ . \tag{5.31}$$

Now, we discuss the Thomas-Fermi approximation to find an analytical expression for the condensate widths $u_{\rho 0}$, u_{z0}, and the ratio of $u_{\rho 0}/u_{z0}$ as well as the frequencies of collective modes. The equilibrium

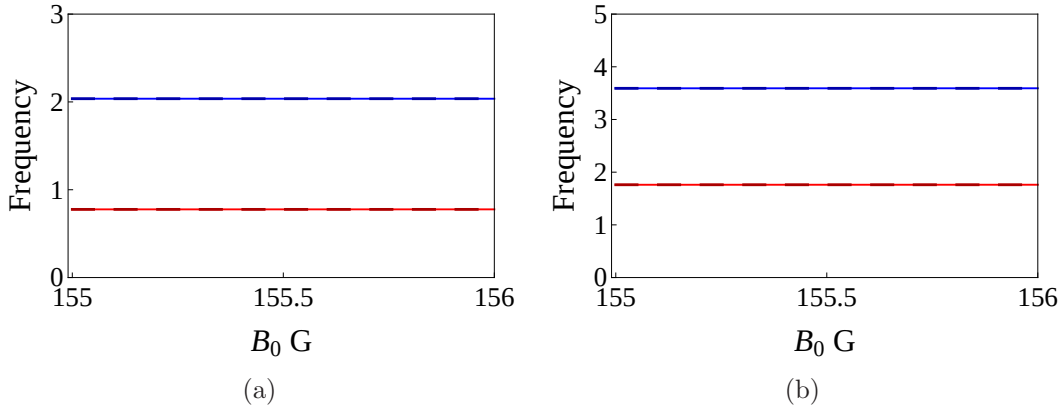

Figure 5.3.: Breathing (blue curves) and quadrupole (red curves) mode frequencies as a function of magnetic field B_0 for the experimental dimensionless parameter of the two-body contact interaction $\mathcal{P}_{\mathrm{BG}} = -856.732$ with different trap aspect ratio (a) $\lambda = 0.5$ and (b) $\lambda = 2$. The solid and dashed curves correspond to the exact results Eq. (5.27) and the TF approximation Eq. (5.33), respectively.

positions Eqs. (5.24) and (5.25) in the TF approximation have the form

$$u_{\rho 0}^5 - \mathcal{P}_{\mathrm{BG}}\lambda\,(1-\varepsilon_0) = 0\,, \qquad \lambda u_{z0} = u_{\rho 0}\,. \tag{5.32}$$

The frequencies of collective modes (5.27) with the abbreviations (5.28)–(5.30) reduce in the TF approximation (5.32) to

$$\omega_{B,Q}^2 = 2 + \frac{3}{2}\lambda^2 \pm \frac{1}{2}\sqrt{16 - 16\lambda^2 + 9\lambda^4}\,, \tag{5.33}$$

thus they coincide with Eq. (4.29) and do not depend on the bias magnetic field B_0. The dipole mode frequency (5.31) in the TF approximation (5.32) has the form

$$\omega_D^2 = \lambda^2\left(1 + \frac{\varepsilon_0\mathcal{P}_{\mathrm{BG}}\lambda}{2\varepsilon_1 u_{\rho 0}^3}\right)\,, \tag{5.34}$$

where the dipole mode frequency is not valid on top of the Feshbach resonance, i.e. for $\varepsilon_1 = 0$.

Figure 5.1 shows the equilibrium widths of the condensate $u_{\rho 0}$, u_{z0}, and the trap aspect ratio $u_{\rho 0}/u_{z0}$ as a function of the bias magnetic field B_0 for the experimental value $\mathcal{P}_{\mathrm{BG}} = -856.732$ [260,264] and the trap anisotropy (a) $\lambda = 0.5$ and (b) $\lambda = 2$. Due to the approximative solution of Ref. [121] both condensates widths are divergent on top of the Feshbach resonance, where $\mathcal{H} \to 0$. The TF approximation Eq. (5.32) agrees quite well with the exact results of the condensate widths Eqs. (5.24) and (5.25). In particular Fig. 5.2 shows that the dipole mode frequency goes to zero just before the Feshbach resonance and we have good agreement between the exact result Eq. (5.31) with the TF approximation Eq. (5.34). In Fig. 5.3 we show the frequencies of collective modes as a function of the bias magnetic field B_0. These frequencies in Eqs. (5.27) have good agreement with the frequencies in the TF approximation Eqs. (5.33) and show that the breathing and quadrupole modes depend only the trap anisotropy λ and do not depend on the bias magnetic field B_0. In the following we show that these consequences of the heuristic approximation Eq. (5.19) from Ref. [121] turn out to be neither correct on top of the Feshbach resonance nor far away from it.

5.4. Schwinger Trick

In the last section we have shown that the approximation Eq. (5.19) of Ref. [121] for the integral Eq. (5.10) seems to be valid far away from the Feshbach resonance. In order to study the frequencies

of collective modes correctly both in the vicinity of the Feshbach resonance and on the right-hand side of the Feshbach resonance, i.e. for $\mathcal{H} > 0$, we develop our own approach by using the Schwinger trick [266] in order to rewrite the integral Eq. (5.10) in form of

$$f = \int_0^\infty d\rho \int_{-\infty}^\infty dz \int_0^\infty ds\ \rho \exp\left[-\frac{2\rho^2}{u_\rho^2} - \frac{2(z-z_0)^2}{u_z^2}\right] \exp\left\{-s\left[\mathcal{H} + \frac{M\omega_\rho^2}{2\mu_\mathrm{B}}\left(\rho^2 + \lambda^2 z^2\right)\right]\right\}. \tag{5.35}$$

Within the linearization of the equations of motions Eqs. (5.12)–(5.14), we have to take into the account that the equilibrium value of the center of mass oscillation vanishes according to Eq. (5.26). This allows to expand the integral of Eq. (5.35) up to the second order of z_0 which yields

$$\begin{aligned} f = \int_0^\infty d\rho \int_{-\infty}^\infty dz \int_0^\infty ds\ \rho \exp\left\{-\frac{2\rho^2}{u_\rho^2} - \frac{2z^2}{u_z^2} - s\left[\mathcal{H} + \frac{M\omega_\rho^2}{2\mu_\mathrm{B}}\left(\rho^2 + \lambda^2 z^2\right)\right]\right\} \\ \times \left(1 + \frac{4zz_0}{u_z^2} - \frac{2z_0^2}{u_z^2} + \frac{8z^2 z_0^2}{u_z^4} + \mathcal{O}[z_0]^3\right). \end{aligned} \tag{5.36}$$

Thus, the corresponding first derivatives read

$$\begin{aligned} \frac{\partial f}{\partial u_\rho} = \int_0^\infty d\rho \int_{-\infty}^\infty dz \int_0^\infty ds\ \rho \exp\left\{-\frac{2\rho^2}{u_\rho^2} - \frac{2z^2}{u_z^2} - s\left[\mathcal{H} + \frac{M\omega_\rho^2}{2\mu_\mathrm{B}}\left(\rho^2 + \lambda^2 z^2\right)\right]\right\} \\ \times \left(\frac{4\rho^2}{u_\rho^3} + \frac{16\rho^2 z z_0}{u_\rho^3 u_z^2} + \mathcal{O}[z_0]^2\right), \end{aligned} \tag{5.37}$$

$$\begin{aligned} \frac{\partial f}{\partial u_z} = \int_0^\infty d\rho \int_{-\infty}^\infty dz \int_0^\infty ds\ \rho \exp\left\{-\frac{2\rho^2}{u_\rho^2} - \frac{2z^2}{u_z^2} - s\left[\mathcal{H} + \frac{M\omega_\rho^2}{2\mu_\mathrm{B}}\left(\rho^2 + \lambda^2 z^2\right)\right]\right\} \\ \times \left(\frac{4z^2}{u_z^3} - \frac{8zz_0}{u_z^3} + \mathcal{O}[z_0]^2\right), \end{aligned} \tag{5.38}$$

$$\begin{aligned} \frac{\partial f}{\partial z_0} = \int_0^\infty d\rho \int_{-\infty}^\infty dz \int_0^\infty ds\ \rho \exp\left\{-\frac{2\rho^2}{u_\rho^2} - \frac{2z^2}{u_z^2} - s\left[\mathcal{H} + \frac{M\omega_\rho^2}{2\mu_\mathrm{B}}\left(\rho^2 + \lambda^2 z^2\right)\right]\right\} \\ \times \left(\frac{4z}{u_z^2} - \frac{4(u_z^2 - 4z^2)z_0}{u_z^4} + \mathcal{O}[z_0]^2\right). \end{aligned} \tag{5.39}$$

In the next two sections we study the consequences of this integral representation both on top and on the right-hand side of the Feshbach resonance.

5.5. On Top of Feshbach Resonance

We discuss in this section the frequencies of collective modes when the bias field B_0 coincides with the resonant magnetic field B_res, i.e. we have $\mathcal{H} = B_0 - B_\mathrm{res} = 0$. In that case the integrals Eqs. (5.36)–(5.39) can be exactly solved, yielding

$$f = \frac{\sqrt{2\pi} u_\rho u_z \mu_\mathrm{B} \mathrm{ArcSec}\left(u_z\lambda/u_\rho\right)}{M\omega_\rho^2 \sqrt{-u_\rho^2 + u_z^2\lambda^2}} + \mathcal{O}[z_0]^2, \tag{5.40}$$

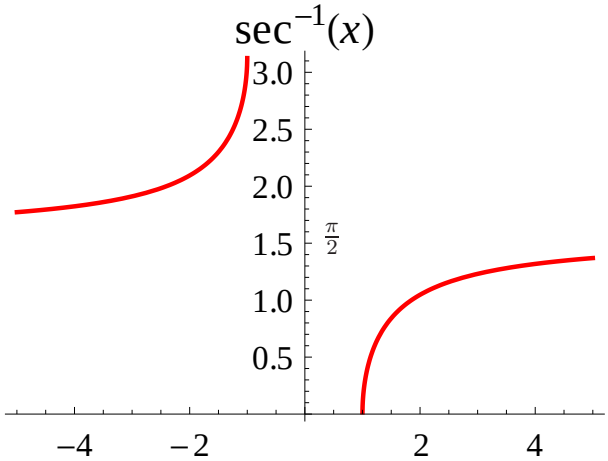

Figure 5.4.: Graph of the arc secant function.

$$\frac{\partial f}{\partial u_\rho} = \frac{\sqrt{2\pi}u_z\mu_{\rm B}}{M\omega_\rho^2\left(u_\rho^2-u_z^2\lambda^2\right)^2}\left[u_\rho^3-u_\rho u_z^2\lambda^2+u_z^2\lambda^2\sqrt{-u_\rho^2+u_z^2\lambda^2}\,\mathrm{ArcSec}\left(u_z\lambda/u_\rho\right)\right]+\mathcal{O}[z_0]^2\,, \tag{5.41}$$

$$\frac{\partial f}{\partial u_z} = -\frac{\sqrt{2\pi}u_\rho^2\mu_{\rm B}}{M\omega_\rho^2\left(u_\rho^2-u_z^2\lambda^2\right)^2}\left[u_\rho^2-u_z^2\lambda^2+u_\rho\sqrt{-u_\rho^2+u_z^2\lambda^2}\,\mathrm{ArcSec}\left(u_z\lambda/u_\rho\right)\right]+\mathcal{O}[z_0]^2\,, \tag{5.42}$$

$$\frac{\partial f}{\partial z_0} = -\frac{4\sqrt{2\pi}u_\rho\mu_{\rm B}z_0}{M\omega_\rho^2u_z\left(u_\rho^2-u_z^2\lambda^2\right)^2}\left[u_\rho^3-u_\rho u_z^2\lambda^2+u_z^2\lambda^2\sqrt{-u_\rho^2+u_z^2\lambda^2}\,\mathrm{ArcSec}\left(u_z\lambda/u_\rho\right)\right]+\mathcal{O}[z_0]^2\,, \tag{5.43}$$

where $\mathrm{ArcSec}(x)=\frac{1}{\mathrm{ArcCos}(x)}$ is inverse of the secant function and it is discontinuous function defined on entire real axis except the $(-1,1)$ range so, its domain is $(-\infty,-1]U[1,\infty)$ [242]. By substituting Eqs. (5.40)–(5.43) into Eqs. (5.12)–(5.14) and after introducing dimensionless parameters according to Eqs. (2.34) and (5.20) with

$$\varepsilon=\varepsilon_0\varepsilon_1=\frac{\Delta\mu_{\rm B}}{\hbar\omega_\rho}\,, \tag{5.44}$$

we get a system of three second ordinary differential equations u_ρ, u_z, and z_0 in the dimensionless form

$$\ddot{u}_\rho+u_\rho-\frac{1}{u_\rho^3}-\frac{\mathcal{P}_{\rm BG}}{u_zu_\rho^3}\left[1-\varepsilon\frac{\left(12u_z^2\lambda^2-16u_\rho^2\right)\mathrm{ArcSec}\left(u_z\lambda/u_\rho\right)}{u_\rho\left(u_z^2\lambda^2-u_\rho^2\right)^{3/2}}-\frac{4\varepsilon}{\left(u_z^2\lambda^2-u_\rho^2\right)}\right]+\mathcal{O}[z_0]^2=0\,, \tag{5.45}$$

$$\ddot{u}_z+\lambda^2u_z-\frac{1}{u_z^3}-\frac{\mathcal{P}_{\rm BG}}{u_z^2u_\rho^2}\left[1+\frac{8\varepsilon\left(u_\rho^2-2u_z^2\lambda^2\right)\mathrm{ArcSec}\left(u_z\lambda/u_\rho\right)}{u_\rho\left(u_z^2\lambda^2-u_\rho^2\right)^{3/2}}+\frac{8\varepsilon}{\left(u_z^2\lambda^2-u_\rho^2\right)}\right]+\mathcal{O}[z_0]^2=0\,, \tag{5.46}$$

$$\ddot{z}_0+\lambda^2z_0+\frac{16\varepsilon\mathcal{P}_{\rm BG}}{u_\rho^3u_z^2}\left[\frac{u_z\lambda^2\mathrm{ArcSec}\left(u_z\lambda/u_\rho\right)}{\left(u_{z0}^2\lambda^2-u_{\rho0}^2\right)^{3/2}}+\frac{u_\rho}{u_z\left(u_\rho^2-u_z^2\lambda^2\right)}\right]z_0+\mathcal{O}[z_0]^2=0\,. \tag{5.47}$$

The experiment in Ref. [260,264] was performed with the following values of dimensionless parameters:

$$\mathcal{P}_{\rm BG}=-856.732\,,\qquad \varepsilon=9.6052\times10^4\,. \tag{5.48}$$

The time-independent solution $u_\rho=u_{\rho0}$, $u_z=u_{z0}$, and $z_0=z_{00}$ are determined by setting the

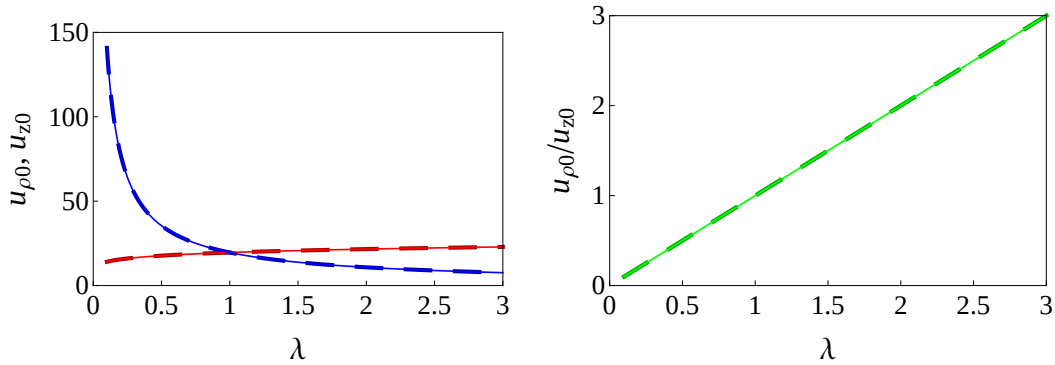

(a) (b)

Figure 5.5.: Equilibrium results for (a) condensate widths $u_{\rho 0}$ (red), u_{z0} (blue) and (b) aspect ratio $u_{\rho 0}/u_{z0}$ (green) as a function of trap aspect ratio λ for the experimental parameters Eq. (5.48). Solid and dashed curves correspond to the exact results Eqs. (5.49), (5.50) and the TF approximation Eqs. (5.60), (5.61), respectively.

accelerations in Eqs. (5.45)–(5.47) to zero

$$u_{\rho 0} - \frac{1}{u_{\rho 0}^3} - \frac{\mathcal{P}_{\mathrm{BG}}}{u_{z0} u_{\rho 0}^3} \left[1 - \frac{\varepsilon \left(12 u_{z0}^2 \lambda^2 - 16 u_{\rho 0}^2\right) \mathrm{ArcSec}\left(\frac{u_{z0}\lambda}{u_{\rho 0}}\right)}{u_{\rho 0} \left(u_{z0}^2 \lambda^2 - u_{\rho 0}^2\right)^{3/2}} - \frac{4\varepsilon}{\left(u_{z0}^2 \lambda^2 - u_{\rho 0}^2\right)} \right] = 0\,, \tag{5.49}$$

$$\lambda^2 u_{z0} - \frac{1}{u_{z0}^3} - \frac{\mathcal{P}_{\mathrm{BG}}}{u_{z0}^2 u_{\rho 0}^2} \left[1 + \frac{8\varepsilon \left(u_{\rho 0}^2 - 2 u_{z0}^2 \lambda^2\right) \mathrm{ArcSec}\left(\frac{u_{z0}\lambda}{u_{\rho 0}}\right)}{u_{\rho 0} \left(u_{z0}^2 \lambda^2 - u_{\rho 0}^2\right)^{3/2}} + \frac{8\varepsilon}{\left(u_{z0}^2 \lambda^2 - u_{\rho 0}^2\right)} \right] = 0\,, \tag{5.50}$$

$$z_{00} = 0\,. \tag{5.51}$$

Afterwards, we determine the frequencies of collective modes. The breathing and quadrupole mode frequencies turn out to be given by Eq. (5.27), where the abbreviations m_1, m_2, and m_3 are calculated by using Mathematica [242] and are defined as follows

$$m_1 = 1 + \frac{3}{u_{\rho 0}^4} + \frac{3\mathcal{P}_{\mathrm{BG}}}{u_{\rho 0}^4 u_{z0}} \left[1 - \frac{4\varepsilon \left(20 u_{\rho 0}^4 - 29 u_{\rho 0}^2 u_{z0}^2 \lambda^2 + 12 u_{z0}^4 \lambda^4\right) \mathrm{ArcSec}\left(\frac{u_{z0}\lambda}{u_{\rho 0}}\right)}{3 u_{\rho 0} \left(-u_{\rho 0}^2 + u_{z0}^2 \lambda^2\right)^{5/2}} - \frac{4\varepsilon \left(-3 u_{\rho 0}^2 + 2 u_{z0}^2 \lambda^2\right)}{\left(u_{\rho 0}^2 - u_{z0}^2 \lambda^2\right)^2} \right], \tag{5.52}$$

$$m_2 = \frac{\mathcal{P}_{\mathrm{BG}}}{u_{\rho 0}^3 u_{z0}^2} \left[1 - \frac{12 u_{\rho 0}^2 \varepsilon}{\left(u_{\rho 0}^2 - u_{z0}^2 \lambda^2\right)^2} - \frac{4\varepsilon \left(4 u_{\rho 0}^4 - 13 u_{\rho 0}^2 u_{z0}^2 \lambda^2 + 6 u_{z0}^4 \lambda^4\right) \mathrm{ArcSec}\left(\frac{u_{z0}\lambda}{u_{\rho 0}}\right)}{u_{\rho 0} \left(-u_{\rho 0}^2 + u_{z0}^2 \lambda^2\right)^{5/2}} \right], \tag{5.53}$$

$$m_3 = \lambda^2 + \frac{3}{u_{z0}^4} + \frac{2\mathcal{P}_{\mathrm{BG}}}{u_{\rho 0}^2 u_{z0}^3} \left[1 - \frac{4\varepsilon \left(2 u_{\rho 0}^4 - 5 u_{\rho 0}^2 u_{z0}^2 \lambda^2 + 6 u_{z0}^4 \lambda^4\right) \mathrm{ArcSec}\left(\frac{u_{z0}\lambda}{u_{\rho 0}}\right)}{u_{\rho 0} \left(-u_{\rho 0}^2 + u_{z0}^2 \lambda^2\right)^{5/2}} - \frac{12 u_{\rho 0}^2 \varepsilon \left(u_{\rho 0}^2 - 2 u_{z0}^2 \lambda^2\right)}{\left(u_{\rho 0}^3 - u_{\rho 0} u_{z0}^2 \lambda^2\right)^2} \right]. \tag{5.54}$$

The dipole mode frequency follows from Eq. (5.47) can be written as

$$\omega_D^2 = \lambda^2 + \frac{16\varepsilon\mathcal{P}_{\mathrm{BG}}}{u_{\rho0}^3 u_{z0}^2}\left[\frac{u_{z0}\lambda^2 \mathrm{ArcSec}\left(\frac{u_{z0}\lambda}{u_{\rho0}}\right)}{\left(u_{z0}^2\lambda^2 - u_{\rho0}^2\right)^{3/2}} + \frac{u_{\rho0}}{u_{z0}\left(u_{\rho0}^2 - u_{z0}^2\lambda^2\right)}\right]. \tag{5.55}$$

From Eqs. (5.49) and (5.50) we read off the useful identity

$$\begin{aligned}\mathrm{ArcSec}\left(\frac{u_{z0}\lambda}{u_{\rho0}}\right) = \frac{\sqrt{-u_{\rho0}^2 + u_{z0}^2\lambda^2}}{40\mathcal{P}_{\mathrm{BG}}u_{\rho0}u_{z0}\varepsilon}\Big(&3u_{\rho0}^4 - \mathcal{P}_{\mathrm{BG}}u_{\rho0}^2u_{z0} - 4u_{\rho0}^2u_{z0}^2 + 4u_{\rho0}^6u_{z0}^2 + 40\mathcal{P}_{\mathrm{BG}}u_{z0}\varepsilon \\ &-3u_{\rho0}^2u_{z0}^2\lambda^2 + \mathcal{P}_{\mathrm{BG}}u_{z0}^3\lambda^2 + 4u_{z0}^4\lambda^2 - 7u_{\rho0}^4u_{z0}^4\lambda^2 + 3u_{\rho0}^2u_{z0}^6\lambda^4\Big),\end{aligned} \tag{5.56}$$

so Eq. (5.55) reduces to

$$\omega_D^2 = \lambda^2 + \frac{4\left(2u_{\rho0}^2 + \mathcal{P}_{\mathrm{BG}}u_{z0} - u_{z0}^2 + u_{\rho0}^4u_{z0}^2 - 2u_{\rho0}^2u_{z0}^4\lambda^2\right)}{5u_{\rho0}^2u_{z0}^4}. \tag{5.57}$$

Figure 5.5 shows the equilibrium widths of the condensate $u_{\rho0}$, u_{z0} and the aspect ratio $u_{\rho0}/u_{z0}$ following from Eqs. (5.49), (5.50) as solid lines versus trap aspect ratio λ and the experimental parameters Eq. (5.48). From Fig. 5.5(b) we read off that the aspect ratio $u_{\rho0}/u_{z0}$ turns out to coincide perfectly with the trap aspect ratio λ. In order to analyze this finding in more detail, we observe that the large values of the experimental parameters Eq. (5.48) suggest to consider the TF approximation. Thus, we neglect the respective second term in Eqs. (5.49) and (5.50), which comes from the kinetic energy. Furthermore, we use the ansatz

$$\frac{u_{z0}\lambda}{u_{\rho0}} = 1 + \eta \tag{5.58}$$

and evaluate the resulting equations in the limit of a vanishing smallness parameter η. By using the Taylor expansion

$$\mathrm{ArcSec}(x) = \sqrt{2}\sqrt{x-1} - \frac{5(x-1)^{3/2}}{6\sqrt{2}} + \frac{43(x-1)^{5/2}}{80\sqrt{2}} + ..., \quad x \geq 1, \tag{5.59}$$

Eqs. (5.49) and (5.50) reduce to

$$u_{\rho0} - \frac{\mathcal{P}_{\mathrm{BG}}}{u_{\rho0}^3u_{z0}}\left(1 - \frac{40\varepsilon}{3u_{\rho0}^2}\right) = 0, \tag{5.60}$$

$$\lambda^2u_{z0} - \frac{\mathcal{P}_{\mathrm{BG}}}{u_{\rho0}^2u_{z0}^2}\left(1 - \frac{40\varepsilon}{3u_{\rho0}^2}\right) = 0, \tag{5.61}$$

which corresponds, indeed, to the identity

$$u_{z0}\lambda = u_{\rho0}. \tag{5.62}$$

Thus, the knowledge of one condensate width, for instance $u_{\rho0}$ from solving

$$u_{\rho0}^5 - \mathcal{P}_{\mathrm{BG}}\lambda\left(1 - \frac{40\varepsilon}{3u_{\rho0}^2}\right) = 0, \tag{5.63}$$

implies that also the other condensate width is known. Fig. 5.5 confirms that the TF approximation Eqs. (5.62), (5.63) agrees quite well with the equilibrium widths determined from Eqs. (5.49), (5.50).

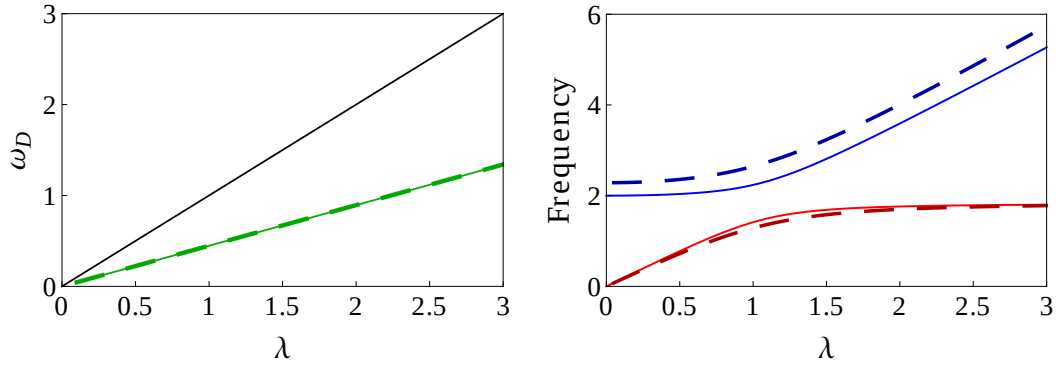

(a) (b)

Figure 5.6.: Frequencies of collective modes results for (a) the dipole mode frequency (green) and (b) the breathing (blue) and quadrupole (red) mode frequencies as a function of trap aspect ratio λ for the experimental parameters Eq. (5.48). (a) Solid black curve corresponds to the dipole mode frequency far away the Feshbach resonance which means that $\omega_D = \lambda$. Solid and dashed curves correspond to the exact result Eq. (5.55) and in the TF approximation Eq. (5.67), respectively. (b) Solid and dashed curves correspond to the Eqs. (2.72) for vanishing three-body interaction strength $\mathcal{K} = 0$ and in the TF approximation Eqs. (5.27), where the abbreviations are defined in Eqs. (5.64)–(5.66), respectively.

In the similar way we insert Eq. (5.58) in the limit $\eta \to 0$ into the frequencies of breathing and quadrupole Eqs. (5.27), where the abbreviations in Eqs. (5.52)–(5.54) reduce to

$$m_1 = 1 + \frac{3\mathcal{P}_{\mathrm{BG}}\lambda}{u_{\rho 0}^5}\left(1 - \frac{856\varepsilon}{45u_{\rho 0}^2}\right), \tag{5.64}$$

$$m_2 = \frac{\mathcal{P}_{\mathrm{BG}}\lambda^2}{u_{\rho 0}^5}\left(1 - \frac{344\varepsilon}{15u_{\rho 0}^2}\right), \tag{5.65}$$

$$m_3 = \lambda^2 + \frac{2\mathcal{P}_{\mathrm{BG}}\lambda^3}{u_{\rho 0}^5}\left(1 - \frac{256\varepsilon}{15u_{\rho 0}^2}\right). \tag{5.66}$$

Correspondingly the dipole mode frequency Eq. (5.57) yields

$$\omega_D^2 = \lambda^2 + \frac{32\varepsilon\lambda^3\mathcal{P}_{\mathrm{BG}}}{3u_{\rho 0}^7}. \tag{5.67}$$

In Fig. 5.6(a) we plot the dipole mode frequency as a function trap anisotropy λ. The solid black curve corresponds to the dipole mode frequency far away from the Feshbach resonance $\omega_D = \lambda$, while the solid green curve corresponds to the exact result of dipole mode frequency on top of the Feshbah resonance Eq. (5.57) and the dashed curve corresponds to the dipole mode in the TF approximation Eq. (5.67) for the experimental parameters Eq. (5.48). This result could be seen as being inconsistent with the Kohn theorem [249], which says that the dipole frequency is equal to the trap frequency and does not depend on the two-body interaction strength. However, the result of the Kohn theorem is a consequence of the translational invariance of the two-body interaction, which is no longer true in our case due to Eq. (5.3). As a consequence the dipole mode frequency Eq. (5.57) and its TF approximation Eq. (5.67) depend on the two-body interaction strength $\mathcal{P}_{\mathrm{BG}}$, the anisotropy of the confining potential λ and the equilibrium values of the condensate widths from Eqs. (5.49) and (5.50). Note that the heuristic approximation of Ref. [121] fails to predict a finite value for the dipole mode frequency on top of the Feshbach resonance according to Eq. (5.34).

In Fig. 5.6(b) we also show the breathing (blue curves) and quadrupole (red curves) mode frequencies as a function of trap anisotropy λ. The solid curves correspond to the frequencies of collective modes far away from the Feshbach resonance, which are described in Eqs. (2.72) for vanishing three-body interaction strength $\mathcal{K} = 0$, while the dashed curves correspond to the frequencies of collective mode on top of the Feshbach resonance and in the TF approximation Eqs. (5.27) for the experimental parameters Eq. (5.48). On top of the Feshbach resonance we observe a significant change of the breathing mode frequency, whereas the quadrupole mode frequency remains basically unaffected.

5.6. Right-Hand Side of Feshbach Resonance

We consider in this section the frequencies of collective modes when the bias field B_0 is larger than the resonant magnetic field $B_{\rm res}$, i.e. $\mathcal{H} = B_0 - B_{\rm res} > 0$. The integrals Eqs. (5.36)–(5.39) reduce then to

$$f = \sqrt{2\pi} u_\rho^2 u_z \mu_{\rm B}^{3/2} \int_0^\infty \frac{ds\ e^{-\mathcal{H}s}}{\left(4\mu_{\rm B} + M\ s\ u_\rho^2\omega_\rho^2\right)\sqrt{4\mu_{\rm B} + M\ s\ u_z^2\lambda^2\omega_\rho^2}} + \mathcal{O}[z_0]^2\,, \tag{5.68}$$

$$\frac{\partial f}{\partial u_\rho} = 8\sqrt{2\pi} u_\rho u_z \mu_{\rm B}^{5/2} \int_0^\infty \frac{ds\ e^{-\mathcal{H}s}}{\left(4\mu_{\rm B} + Msu_\rho^2\omega_\rho^2\right)^2\sqrt{4\mu_{\rm B} + Msu_z^2\lambda^2\omega_\rho^2}} + \mathcal{O}[z_0]^2\,, \tag{5.69}$$

$$\frac{\partial f}{\partial u_z} = 4\sqrt{2\pi} u_\rho^2 \mu_{\rm B}^{5/2} \int_0^\infty \frac{ds\ e^{-\mathcal{H}s}}{\left(4\mu_{\rm B} + Msu_\rho^2\omega_\rho^2\right)\left(4\mu_{\rm B} + Msu_z^2\lambda^2\omega_\rho^2\right)^{3/2}} + \mathcal{O}[z_0]^2\,, \tag{5.70}$$

$$\frac{\partial f}{\partial z_0} = -4M\sqrt{2\pi} u_\rho^2 u_z z_0 \lambda^2 \mu_{\rm B}^{3/2}\omega_\rho^2 \int_0^\infty \frac{ds\ e^{-\mathcal{H}s} s}{\left(4\mu_{\rm B} + Msu_\rho^2\omega_\rho^2\right)\left(4\mu_{\rm B} + Msu_z^2\lambda^2\omega_\rho^2\right)^{3/2}} + \mathcal{O}[z_0]^2\,. \tag{5.71}$$

Thus, we insert now Eq. (5.68)–(5.71) into Eqs. (5.12)–(5.14) and introduce the dimensionless parameters Eq. (2.34) and (5.20) with $\mathcal{S} = \mathcal{H}s$. In this way we obtain a system of three second ordinary differential equations for u_ρ, u_z, and z_0 in the dimensionless form:

$$\ddot{u}_\rho + u_\rho - \frac{1}{u_\rho^3} - \frac{\mathcal{P}_{\rm BG}}{u_z u_\rho^3}\left[1 - 16\varepsilon\ \varepsilon_1^{1/2} \int_0^\infty \frac{d\mathcal{S}\ e^{-\mathcal{S}}\left(2\varepsilon_1 + \mathcal{S}u_\rho^2\right)}{\left(4\varepsilon_1 + \mathcal{S}u_\rho^2\right)^2\sqrt{4\varepsilon_1 + \mathcal{S}u_z^2\lambda^2}}\right] + \mathcal{O}[z_0]^2 = 0, \tag{5.72}$$

$$\ddot{u}_z + \lambda^2 u_z - \frac{1}{u_z^3} - \frac{\mathcal{P}_{\rm BG}}{u_z^2 u_\rho^2}\left[1 - 16\varepsilon\ \varepsilon_1^{1/2} \int_0^\infty \frac{d\mathcal{S}\ e^{-\mathcal{S}}\left(2\varepsilon_1 + \mathcal{S}u_z^2\lambda^2\right)}{\left(4\varepsilon_1 + \mathcal{S}u_\rho^2\right)\left(4\varepsilon_1 + \mathcal{S}u_z^2\lambda^2\right)^{3/2}}\right] + \mathcal{O}[z_0]^2 = 0, \tag{5.73}$$

$$\ddot{z}_0 + \lambda^2\left[1 + \frac{16\mathcal{P}_{\rm BG}}{u_\rho^2 u_z}\varepsilon\ \varepsilon_1^{1/2} \int_0^\infty \frac{d\mathcal{S}\ e^{-\mathcal{S}}\mathcal{S}}{\left(4\varepsilon_1 + \mathcal{S}u_\rho^2\right)\left(4\varepsilon_1 + \mathcal{S}u_z^2\lambda^2\right)^{3/2}}\right] z_0 + \mathcal{O}[z_0]^2 = 0\ . \tag{5.74}$$

The time-independent solution of the condensate widths $u_\rho = u_{\rho 0}$, $u_z = u_{z0}$, and $z_0 = z_{00}$ are now determined from

$$u_{\rho 0} - \frac{1}{u_{\rho 0}^3} - \frac{\mathcal{P}_{\rm BG}}{u_{z0} u_{\rho 0}^3}\left[1 - 16\varepsilon\ \varepsilon_1^{1/2} \int_0^\infty \frac{d\mathcal{S}\ e^{-\mathcal{S}}\left(2\varepsilon_1 + \mathcal{S}u_{\rho 0}^2\right)}{\left(4\varepsilon_1 + \mathcal{S}u_{\rho 0}^2\right)^2\sqrt{4\varepsilon_1 + \mathcal{S}u_{z0}^2\lambda^2}}\right] = 0\,, \tag{5.75}$$

$$\lambda^2 u_{z0} - \frac{1}{u_{z0}^3} - \frac{\mathcal{P}_{\rm BG}}{u_{z0}^2 u_{\rho 0}^2}\left[1 - 16\varepsilon\ \varepsilon_1^{1/2} \int_0^\infty \frac{d\mathcal{S}\ e^{-\mathcal{S}}\left(2\varepsilon_1 + \mathcal{S}u_{z0}^2\lambda^2\right)}{\left(4\varepsilon_1 + \mathcal{S}u_{\rho 0}^2\right)\left(4\varepsilon_1 + \mathcal{S}u_{z0}^2\lambda^2\right)^{3/2}}\right] = 0, \tag{5.76}$$

$$z_{00} = 0\ . \tag{5.77}$$

The breathing and quadrupole mode frequencies are given by Eq. (5.27), where the abbreviations m_1, m_2 and m_3 are calculated by using Mathematica [242]:

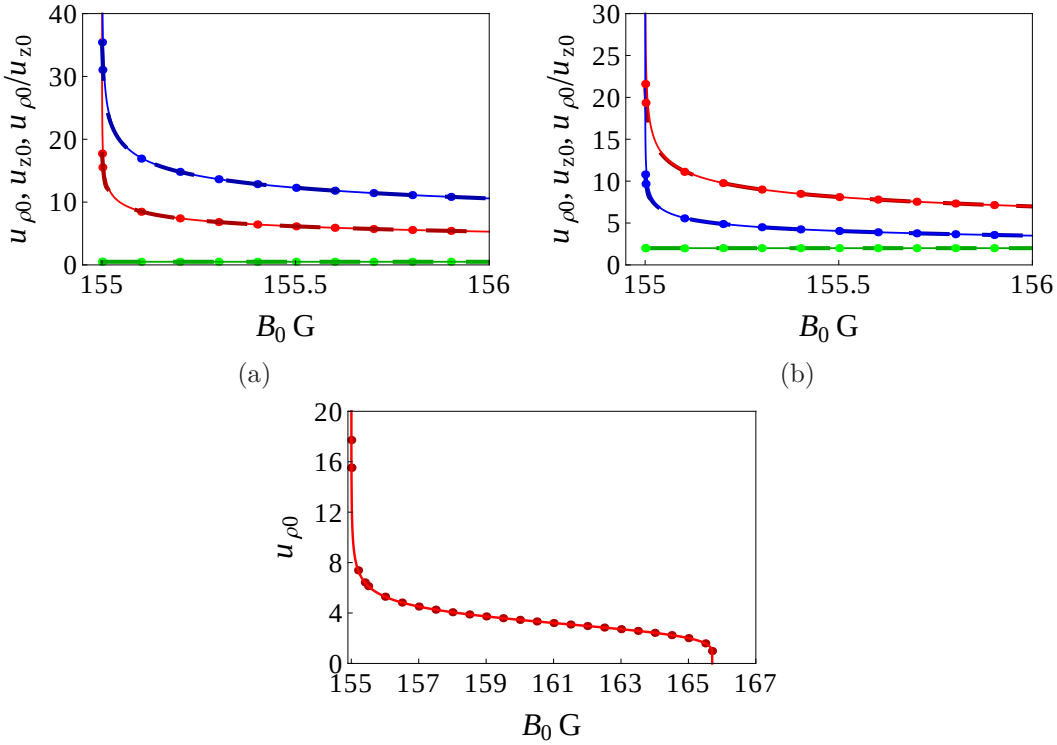

Figure 5.7.: Equilibrium results for condensate widths $u_{\rho 0}$ (red), u_{z0} (blue), and aspect ratio $u_{\rho 0}/u_{z0}$ (green) as a function of a magnetic field B_0 for different trap anisotropy (a), (c) $\lambda = 0.5$ and (b) $\lambda = 2$ for the experimental parameters Eq. (5.48). Solid, dotted, and dashed curves correspond to the approximation solution of Ref. [121] Eqs. (5.24), (5.25) and the exact results Eqs. (5.75), (5.76) and the TF approximation Eqs. (5.82), (5.83), respectively.

$$m_1 = 1 + \frac{3}{u_{\rho 0}^4} + \frac{3\mathcal{P}_{\rm BG}}{u_{\rho 0}^4 u_{z0}} \left[1 - 16\varepsilon\, \varepsilon_1^{1/2} \int_0^\infty \frac{d\mathcal{S} e^{-\mathcal{S}} \left(5\mathcal{S}^2 u_{\rho 0}^4 + 18\mathcal{S} u_{\rho 0}^2 \varepsilon_1 + 24\varepsilon_1^2\right)}{3\left(\mathcal{S} u_{\rho 0}^2 + 4\varepsilon_1\right)^3 \sqrt{4\varepsilon_1 + \mathcal{S} u_{z0}^2 \lambda^2}} \right], \tag{5.78}$$

$$m_2 = \frac{\mathcal{P}_{\rm BG}}{u_{\rho 0}^3 u_{z0}^2} \left[1 - 32\varepsilon\, \varepsilon_1^{1/2} \int_0^\infty \frac{d\mathcal{S} e^{-\mathcal{S}} \left(\mathcal{S} u_{\rho 0}^2 + 2\varepsilon_1\right)\left(2\varepsilon_1 + \mathcal{S} u_{z0}^2 \lambda^2\right)}{\left(\mathcal{S} u_{\rho 0}^2 + 4\varepsilon_1\right)^2 \left(4\varepsilon_1 + \mathcal{S} u_{z0}^2 \lambda^2\right)^{3/2}} \right], \tag{5.79}$$

$$m_3 = \lambda^2 + \frac{3}{u_{z0}^4} + \frac{2\mathcal{P}_{\rm BG}}{u_{\rho 0}^2 u_{z0}^3} \left[1 - 8\varepsilon\, \varepsilon_1^{1/2} \int_0^\infty \frac{d\mathcal{S} e^{-\mathcal{S}} \left(16\varepsilon_1^2 + 10\mathcal{S} u_{z0}^2 \varepsilon_1 \lambda^2 + 3\mathcal{S}^2 u_{z0}^4 \lambda^4\right)}{\left(\mathcal{S} u_{\rho 0}^2 + 4\varepsilon_1\right)\left(4\varepsilon_1 + \mathcal{S} u_{z0}^2 \lambda^2\right)^{5/2}} \right]. \tag{5.80}$$

The dipole mode frequency is given by

$$\omega_D^2 \;=\; \lambda^2 \left[1 + 16\varepsilon\, \varepsilon_1^{1/2} \frac{\mathcal{P}_{\rm BG}}{u_{\rho 0}^2 u_{z0}} \int_0^\infty \frac{d\mathcal{S}\; e^{-\mathcal{S}} \mathcal{S}}{\left(4\varepsilon_1 + \mathcal{S} u_{\rho 0}^2\right)\left(4\varepsilon_1 + \mathcal{S} u_{z0}^2 \lambda^2\right)^{3/2}} \right]. \tag{5.81}$$

Now, we discuss again the Thomas-Fermi approximation to find an analytical description for the condensate widths $u_{\rho 0}$, u_{z0}, and the ratio of $u_{\rho 0}/u_{z0}$ and the frequencies of collective modes. To this end we insert Eq. (5.58) into the time-independent solution $u_{\rho 0}$ and u_{z0} of Eqs. (5.75) and (5.76) and evaluate the expression in the limit $\eta \to 0$, which yields

$$u_{\rho 0} - \frac{\mathcal{P}_{\rm BG}}{u_{z0} u_{\rho 0}^3} \left[1 - 16\varepsilon\, \varepsilon_1^{1/2} \int_0^\infty d\mathcal{S}\; e^{-\mathcal{S}} \frac{\mathcal{S} u_{\rho 0}^2 + 2\varepsilon_1}{\left(\mathcal{S} u_{\rho 0}^2 + 4\varepsilon_1\right)^{5/2}} \right] = 0\,, \tag{5.82}$$

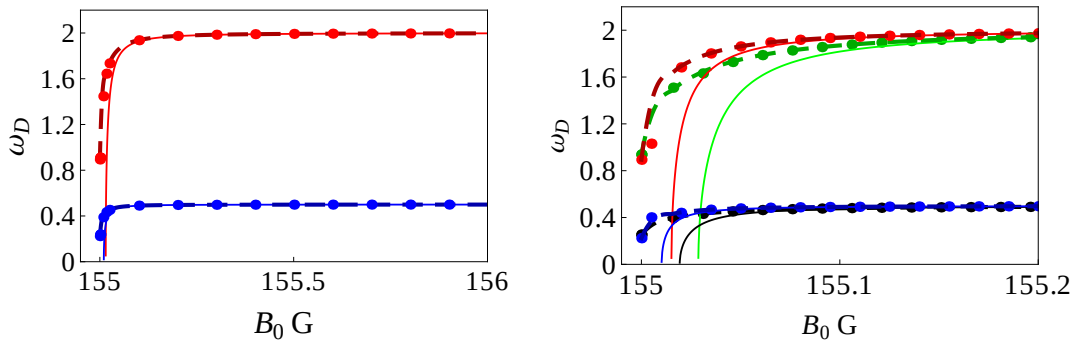

Figure 5.8.: (a) Dipole mode frequency as a function of a magnetic field B_0 for different trap anisotropy $\lambda = 0.5$ (blue) and $\lambda = 2$ (red) for the experimental parameters Eq. (5.48). Solid, dotted, and dashed curves correspond to the approximation solution of Ref. [121] in Eq. (5.31), the exact result Eq. (5.81) and the TF approximation Eq. (5.95), respectively, while (b) focuses on the region of interest for the dipole mode frequency in addition for the hypothetical Feshbach resonance width $\Delta = 100.7$ G with $\lambda = 0.5$ (black) and $\lambda = 2$ (green).

$$\lambda^2 u_{z0} - \frac{\mathcal{P}_{\rm BG}}{u_{z0}^2 u_{\rho 0}^2}\left[1 - 16\varepsilon\, \varepsilon_1^{1/2} \int_0^\infty d\mathcal{S}\; e^{-\mathcal{S}} \frac{\mathcal{S} u_{\rho 0}^2 + 2\varepsilon_1}{\left(\mathcal{S} u_{\rho 0}^2 + 4\varepsilon_1\right)^{5/2}}\right] = 0\,. \tag{5.83}$$

Solving the remaining $\mathcal{S}$-integral we obtain the equilibrium widths $u_{\rho 0}$ and u_{z0} in TF approximation

$$u_{\rho 0}^5 - \mathcal{P}_{\rm BG}\lambda\left[1 - \frac{\varepsilon}{3u_{\rho 0}^5}\left(40u_{\rho 0}^3 + 64u_{\rho 0}\varepsilon_1\right) + 3\kappa u_{\rho 0}^2 + 4\kappa\varepsilon_1\right] = 0\,, \tag{5.84}$$

$$\lambda u_{z0} = u_{\rho 0}\,, \tag{5.85}$$

where we have introduced the abbreviation

$$\kappa = \frac{8\varepsilon\sqrt{\pi\varepsilon_1}}{u_{\rho 0}^5} e^{4\varepsilon_1/u_{\rho 0}^2} \mathrm{Erfc}\left(2\sqrt{\varepsilon_1}/u_{\rho 0}\right)\,, \tag{5.86}$$

with $\mathrm{Erfc}(x)$ representing the complementary error function:

$$\mathrm{Erfc}(x) = \frac{2}{\sqrt{\pi}} \int_x^\infty dt\; e^{-t^2}\,. \tag{5.87}$$

In the similar way we obtain the quadrupole and breathing mode frequencies in TF approximation by inserting Eq. (5.58) into Eqs. (5.78)–(5.80) and and evaluating the limit $\eta \to 0$, where the abbreviations m_1, m_2, and m_3 are defined according to

$$m_1 = 1 + \frac{3\mathcal{P}_{\rm BG}\lambda}{u_{\rho 0}^5}\left[1 - \frac{16\varepsilon\, \varepsilon_1^{1/2}}{3} \int_0^\infty d\mathcal{S}\; e^{-\mathcal{S}} \frac{5\mathcal{S}^2 u_{\rho 0}^4 + 18\mathcal{S} u_{\rho 0}^2 \varepsilon_1 + 24\varepsilon_1^2}{\left(\mathcal{S} u_{\rho 0}^2 + 4\varepsilon_1\right)^{7/2}}\right]\,, \tag{5.88}$$

$$m_2 = \frac{\mathcal{P}_{\rm BG}\lambda^2}{u_{\rho 0}^5}\left[1 - 32\varepsilon\, \varepsilon_1^{1/2} \int_0^\infty d\mathcal{S}\; e^{-\mathcal{S}} \frac{\left(\mathcal{S} u_{\rho 0}^2 + 2\varepsilon_1\right)^2}{\left(\mathcal{S} u_{\rho 0}^2 + 4\varepsilon_1\right)^{7/2}}\right]\,, \tag{5.89}$$

$$m_3 = \lambda^2 + \frac{2\mathcal{P}_{\rm BG}\lambda^3}{u_{\rho 0}^5}\left[1 - 8\varepsilon\, \varepsilon_1^{1/2} \int_0^\infty d\mathcal{S}\; e^{-\mathcal{S}} \frac{3\mathcal{S}^2 u_{\rho 0}^4 + 10\mathcal{S} u_{\rho 0}^2 \varepsilon_1 + 16\varepsilon_1^2}{\left(\mathcal{S} u_{\rho 0}^2 + 4\varepsilon_1\right)^{7/2}}\right]\,. \tag{5.90}$$

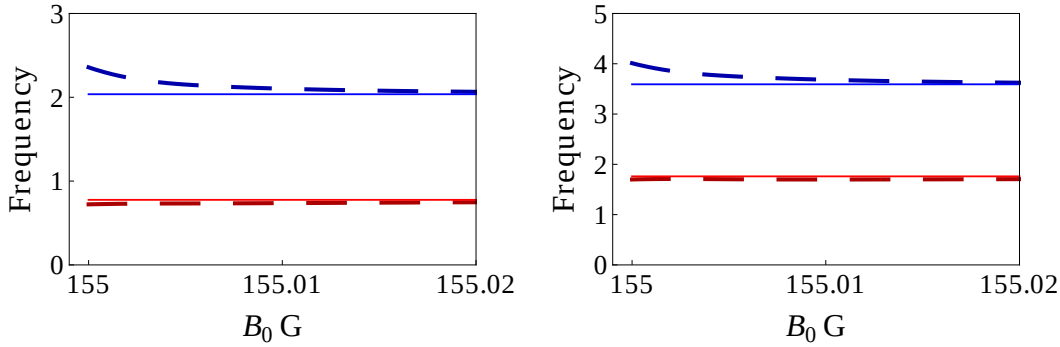

(a) (b)

Figure 5.9.: Frequencies for the quadrupole (red) and the breathing (blue) mode as a function of the magnetic field B_0 for different trap anisotropy (a) $\lambda = 0.5$ and (b) $\lambda = 2$ for the experimental parameters Eq. (5.48). Solid and dashed curves correspond to the approximation solution of Ref. [121] Eq. (5.27) with abbreviations m_1, m_2, and m_3 from Eqs. (5.28)–(5.30) and the TF approximation Eq. (5.27) with abbreviations m_1, m_2, and m_3 from Eqs. (5.92)–(5.94).

The dipole mode frequency Eq. (5.81) reduces correspondingly to

$$\omega_D^2 = \lambda^2 + \frac{16\mathcal{P}_{\mathrm{BG}}\lambda^3}{u_{\rho 0}^3}\,\varepsilon\,\varepsilon_1^{1/2}\int_0^\infty d\mathcal{S}\;e^{-\mathcal{S}}\frac{\mathcal{S}}{\left(4\varepsilon_1+\mathcal{S}u_{\rho 0}^2\right)^{5/2}}\,. \tag{5.91}$$

Solving the remaining $\mathcal{S}$-integrals we obtain the quadrupole and breathing frequencies in TF approximation with

$$\begin{aligned} m_1 &= 1+\frac{3\mathcal{P}_{\mathrm{BG}}\lambda}{u_{\rho 0}^5} \\ &\times\left[1-\frac{8\varepsilon}{45u_{\rho 0}^7}\left(107u_{\rho 0}^5+408u_{\rho 0}^3\varepsilon_1+256u_{\rho 0}\varepsilon_1^2\right)+\frac{\kappa}{45u_{\rho 0}^2}\left(300u_{\rho 0}^4+880\varepsilon_1u_{\rho 0}^2+512\varepsilon_1^2\right)\right], \end{aligned} \tag{5.92}$$

$$\begin{aligned} m_2 &= \frac{\mathcal{P}_{\mathrm{BG}}\lambda^2}{u_{\rho 0}^5} \\ &\times\left[1-\frac{8\varepsilon}{15u_{\rho 0}^7}\left(43u_{\rho 0}^5+152u_{\rho 0}^3\varepsilon_1+64u_{\rho 0}\varepsilon_1^2\right)+\frac{\kappa}{15u_{\rho 0}^2}\left(120u_{\rho 0}^4+320u_{\rho 0}^2\varepsilon_1+128\varepsilon_1^2\right)\right], \end{aligned} \tag{5.93}$$

$$\begin{aligned} m_3 &= \lambda^2+\frac{2\mathcal{P}_{\mathrm{BG}}\lambda^3}{u_{\rho 0}^5} \\ &\times\left[1-\frac{16\varepsilon}{15u_{\rho 0}^7}\left(16u_{\rho 0}^5+64u_{\rho 0}^3\varepsilon_1+48u_{\rho 0}\varepsilon_1^2\right)+\frac{\kappa}{15u_{\rho 0}^2}\left(90u_{\rho 0}^4+280u_{\rho 0}^2\varepsilon_1+192\varepsilon_1^2\right)\right], \end{aligned} \tag{5.94}$$

whereas the dipole mode frequency in TF approximation reads

$$\omega_D^2 = \lambda^2+\frac{32\mathcal{P}_{\mathrm{BG}}\lambda^3\varepsilon}{3u_{\rho 0}^{10}}\left[u_{\rho 0}^3+4u_{\rho 0}\varepsilon_1-\frac{\kappa u_{\rho 0}^5}{8\varepsilon}\left(3u_{\rho 0}^2+8\varepsilon_1\right)\right]. \tag{5.95}$$

We plot in Fig. 5.7 the equilibrium widths of the condensate $u_{\rho 0}$, u_{z0}, and aspect ratio of $u_{\rho 0}/u_{z0}$ as a function of a magnetic field B_0 for the experimental parameters Eq. (5.48) with different trap anisotropy (a) $\lambda = 0.5$ and (b) $\lambda = 2$. The widths of the condensate Eqs. (5.75) and (5.76) are

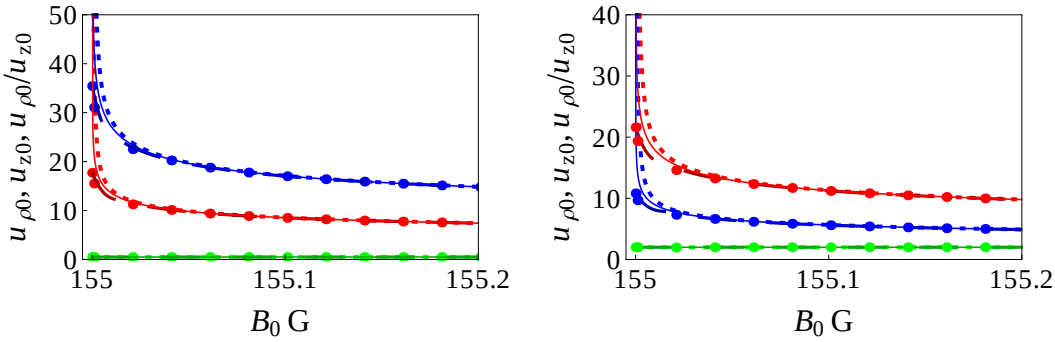

(a) (b)

Figure 5.10.: Equilibrium results for condensate widths $u_{\rho 0}$ (red), u_{z0} (blue), and aspect ratio $u_{\rho 0}/u_{z0}$ (green) as a function of a magnetic field B_0 for different trap anisotropy (a) $\lambda = 0.5$ and (b) $\lambda = 2$ for the experimental parameters Eq. (5.48). Solid, dotted, dashed, and square dotted curves correspond to the approximation solution of Ref. [121] Eqs. (5.24), (5.25) and the exact results Eqs. (5.75), (5.76) and the TF approximation Eqs. (5.82), (5.83), the TF approximation in the limit $\mathcal{H} \to \infty$ or $\varepsilon_1 \to \infty$ results Eqs. (5.98), (5.99), respectively.

coupled, so we solve both equations iteratively. From Fig. 5.7 we read off that the approximative solution of Ref. [121] Eqs. (5.24) and (5.25) is not valid on top of the Feshbach resonance and seems to be valid only far away from the Feshbach resonance. Furthermore, Fig. 5.7 confirms that the TF approximation Eqs. (5.84), (5.85) agrees quite well with the equilibrium widths determined from Eq. (5.75), (5.76). In addition Fig. 5.7(c) shows that the radial condensate width $u_{\rho 0}$ from Eq. (5.75) vanishes at the critical magnetic field $B_{\text{crit}} = B_{\text{res}} + \Delta = 165.7$ G. As already anticipated due to a heuristic argument in Section 5.1, the system on the right-hand side of the Feshbach resonance is not stable beyond this critical magnetic field B_{crit}. Figures 5.8 and 5.9 show the frequencies of the dipole, the breathing, and the quadrupole modes, respectively, for the experimental parameters Eq. (5.48) with different trap anisotropy λ. From these figures we see how the frequencies of collective modes change when one approaches the Feshbach resonance. As already expected in Section 5.1 in Eq. (5.7), the dipole mode frequency on the right-hand side of the Feshbach resonance turns out to be smaller than the dipole mode frequency far away from the Feshbach resonance. In particular we observe that the approximative solution of Ref. [121] in Eqs. (5.27)–(5.31) is not valid on top of the Feshbach resonance. Our results in Section 5.6 and the approximative solution of Ref. [121] for the dipole mode frequency in Fig. 5.8 disagree only 0.05 G above the Feshbach resonance for the experimental parameters Eq. (5.48). However, this still represents an experimentally accessible range as the magnetic field can be controlled up to an accuracy of 1 mG [267]. Furthermore, Fig. 5.8(b) shows how the dipole mode frequency changes with the magnetic bias field for the hypothetical Feshbach resonance width $\Delta = 100.7$ G. Thus, the difference between our predication and the approximative solution of Ref. [121] is more pronounced for a broader Feshbach resonance and for a pancake-like condensate.

Now, as a consistency check for our calculation, we determine the TF approximation for the condensate widths Eq. (5.82), (5.83) and the frequencies of collective modes Eq. (5.27) with abbreviations m_1, m_2, and m_3 are defined in Eqs. (5.92)–(5.95) on top of the Feshbach resonance, i.e. in the limit $\mathcal{H} \to 0$ or $\varepsilon_1 \to 0$. As expected we reproduce all respective findings of Section 5.5, in particular Eqs. (5.62), (5.63) for the condensate widths, Eq. (5.64)–(5.66) for the abbreviations m_1, m_2, and m_3 defining the breathing and quadrupole mode frequencies and Eq. (5.67) for the dipole mode frequency. Thus, approaching the Feshbach resonance and performing the TF limit are commuting procedures

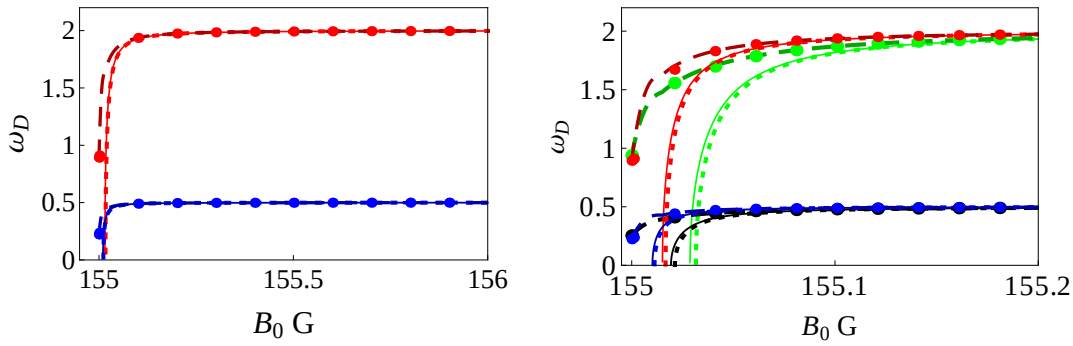

(a) (b)

Figure 5.11.: (a) Dipole mode frequency as a function of a magnetic field B_0 for different trap anisotropy $\lambda = 0.5$ (blue) and $\lambda = 2$ (red) for the experimental parameters Eq. (5.48). Solid, dotted, dashed, and dotted square curves correspond to the approximation solution of Ref. [121] in Eq. (5.31), the exact result Eq. (5.81) and the TF approximation Eq. (5.95) and the TF approximation in the limit $\mathcal{H} \to \infty$ Eq. (5.103), respectively, while (b) focuses on the region of interest for the dipole mode frequency in addition for the hypothetical Feshbach resonance $\Delta = 100.7$ G, with $\lambda = 0.5$ (black) and $\lambda = 2$ (green).

within our theory.

Accordingly, we can also discuss the TF approximation for the condensate widths Eq. (5.82), (5.83) and the frequencies of collective modes Eq. (5.27) with abbreviations m_1, m_2, and m_3 being defined in Eqs. (5.92)–(5.94), (5.95) far away from the Feshbach resonance, i.e. in the limit $\mathcal{H} \to \infty$ or $\varepsilon_1 \to \infty$ and compare the corresponding results with what we have found in Section 5.3 from the heuristic approximation of Ref. [121]. To this end we have to expand the complementary error function Eq. (5.87) for large real x

$$\mathrm{Erfc}(x) = \frac{e^{-x^2}}{\sqrt{\pi}} \left(\frac{1}{x} - \frac{1}{2x^3} + \frac{3}{4x^5} - \frac{15}{8x^7} + \frac{105}{16x^9} - \frac{945}{32x^{11}} + ... \right), x \gg 1\,, \tag{5.96}$$

yielding a corresponding asymptotic expansion for the abbreviation Eq. (5.86)

$$\kappa = 8\varepsilon \left(\frac{1}{2u_{\rho 0}^4} - \frac{1}{16u_{\rho 0}^2 \varepsilon_1} + \frac{3}{128\varepsilon_1^2} - \frac{15u_{\rho 0}^2}{1024\varepsilon_1^3} + \frac{105u_{\rho 0}^4}{8192\varepsilon_1^4} - \frac{945u_{\rho 0}^6}{65536\varepsilon_1^2} + ... \right) . \tag{5.97}$$

Inserting Eq. (5.97) into Eqs. (5.84) and (5.92)–(5.95), we get for

- the condensate widths

$$u_{\rho 0}^5 - \mathcal{P}_{\mathrm{BG}}\lambda \left(1 - \varepsilon_0 + \frac{u_{\rho 0}^2 \varepsilon_0}{8\varepsilon_1} + ... \right) = 0\,, \tag{5.98}$$

$$\lambda u_{z0} = u_{\rho 0}\,, \tag{5.99}$$

- the breathing and quadrupole frequencies:

$$m_1 = 1 + \frac{3\mathcal{P}_{\mathrm{BG}}\lambda}{u_{\rho 0}^5} \left(1 - \varepsilon_0 + \frac{\varepsilon_0 u_{\rho 0}^2}{8\varepsilon_1} - \frac{17u_{\rho 0}^4 \varepsilon_0}{192\varepsilon_1^2} + ... \right), \tag{5.100}$$

$$m_2 = \frac{\mathcal{P}_{\mathrm{BG}}\lambda^2}{u_{\rho 0}^5} \left(1 - \varepsilon_0 - \frac{\varepsilon_0 u_{\rho 0}^2}{8\varepsilon_1} + \frac{17u_{\rho 0}^4 \varepsilon_0}{64\varepsilon_1^2} + ... \right), \tag{5.101}$$

$$m_3 = \lambda^2 + \frac{2\mathcal{P}_{\mathrm{BG}}\lambda^3}{u_{\rho 0}^5} \left(1 - \varepsilon_0 + \frac{\varepsilon_0 u_{\rho 0}^2}{4\varepsilon_1} - \frac{17u_{\rho 0}^4 \varepsilon_0}{64\varepsilon_1^2} + ... \right), \tag{5.102}$$

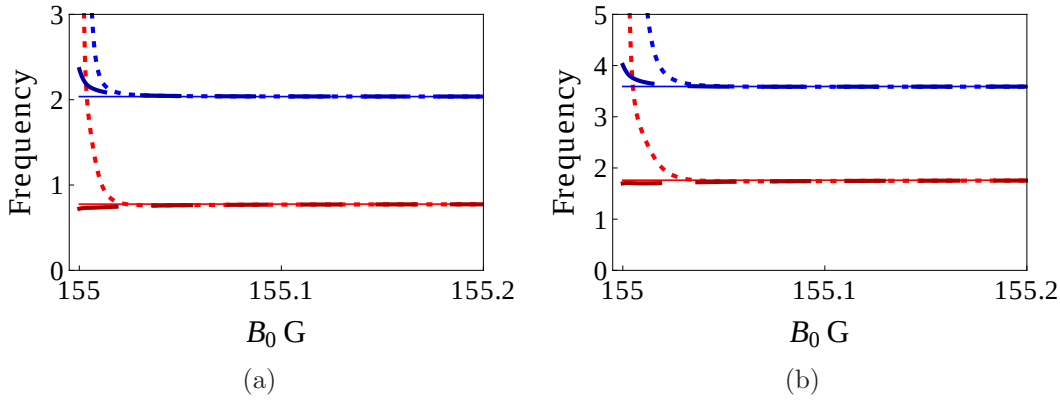

(a) (b)

Figure 5.12.: Frequencies of collective modes results the quadrupole (red) and breathing (blue) as a function of a magnetic field B_0 for different trap anisotropy (a) $\lambda = 0.5$ and (b) $\lambda = 2$ for the experimental parameters Eq. (5.48). Solid, dashed, and square dotted curves correspond to the approximation solution of Ref. [121] from Eq. (5.33) and the TF approximation Eq. (5.27) with abbreviations m_1, m_2, and m_3 from Eqs. (5.92)–(5.94) and the TF approximation in the limit $\mathcal{H} \to \infty$ or $\varepsilon_1 \to \infty$ Eq. (5.27) with abbreviations m_1, m_2, and m_3 being defined in Eqs. (5.100)–(5.102), respectively.

- the dipole mode frequency

$$\omega_D^2 = \lambda^2 \left(1 + \frac{\varepsilon_0 \mathcal{P}_{\mathrm{BG}} \lambda}{2\varepsilon_1 u_{\rho 0}^3} + ... \right) . \tag{5.103}$$

Due to the dependencies $\varepsilon_0 \to 1/\mathcal{H}$ and $\varepsilon_1 \to \mathcal{H}$, the results Eqs. (5.98)–(5.103) represent the $1/\mathcal{H}$ and $1/\mathcal{H}^2$ corrections for the respective quantities, respectively. At first, we observe from comparing Eqs. (5.98), (5.99) with Eq. (5.32) in Fig. 5.10 that the heuristic approximation of Ref. [121] reproduces correctly the $1/\mathcal{H}$ correction for the condensate widths but fails to determine the subsequent $1/\mathcal{H}^2$ correction. This is not surprising as the heuristic approximation Eq.(5.19) for the integral Eq. (5.10) is only exact up to order $1/\mathcal{H}$. But we read off from our results Eq. (5.103) for the dipole mode frequency in Fig. 5.11 that the leading order correction to the Kohn theorem near Feshbach resonance is of the order $1/\mathcal{H}^2$. Therefore, the corresponding predication Eq. (5.34) of the heuristic approximation of Ref. [121] is even incorrect far away from the Feshbach resonance. In addition the same situation for the breathing and quadrupole frequencies show that the leading order of our results Eqs. (5.27), with abbreviations m_1, m_2, and m_3 are defined in Eqs. (5.100)–(5.102) with Fig. 5.11 is $1/\mathcal{H}^2$ and the frequencies depend strongly on the magnetic field B_0 and are divergent on top of the Feshbach resonance, while the frequencies in the TF approximation Eqs. (5.33) depend only on the trap anisotropy λ and do not depend on the bias magnetic field B_0.

6. Bose-Einstein Condensate with Single Vortex

The GP equation (2.12) gives a quantitatively accurate description of both the static and the dynamic properties of the atomic condensate [49,50]. Therefore, the vortex structure and dynamics can be discussed by a more fundamental approach than with superfluid helium, in which the interaction cannot be described in such a simple local form. Furthermore, the diluteness of a gas leads to a relatively large healing length that characterizes the vortex core size, thus enabling a direct experimental visualization of vortex cores [19,169,174,194,268]. To this end we discuss in this chapter the physical properties of a single vortex in condensates by reviewing first that the circulation around a closed contour in the condensate is quantized in Section 6.1. In addition we describe the structure of a single vortex in a condensate trapped by an axially-symmetric harmonic trap and the velocity field around the vortex line in Section 6.2 by solving approximately the time-independent GP equation (2.15) in form of an asymptotic series in the limit of strong two-body interaction strength. Afterwards, Section 6.3 deals with the dynamics of a BEC with a single vortex based on the Thomas-Fermi ansatz for an axially symmetric trap in order to obtain variational equations of motion describing the widths of the condensate and the relative vortex core size. Furthermore, we present the equilibrium positions of the condensate widths as well as the relative vortex core size in Section 6.4 and determine the low-lying collective excitation modes in Section 6.5. Then we discuss in Section 6.6 the energies for a condensate with and without a vortex and obtain the critical rotation frequency for a rotating trap at which a vortex state becomes stable. Finally, we investigate in Section 6.7 the behavior of the condensate during the free expansion after the harmonic trapping potential is turned off.

6.1. Quantization of Circulation

Multiplying the time-dependent GP Eq. (2.12) with $\psi^*(\mathbf{r},t)$ and subtracting its complex conjugate, one gets the continuity equation for the particle density $n_c(\mathbf{r},t) = \psi(\mathbf{r},t)\psi^*(\mathbf{r},t)$

$$\frac{\partial n_c}{\partial t} + \bigtriangledown (n_c \mathbf{v}) = 0, \tag{6.1}$$

where the velocity $\mathbf{v}$ of the condensate is defined by

$$\mathbf{v} = \frac{\hbar}{2Mi} \frac{(\psi^* \bigtriangledown \psi - \psi \bigtriangledown \psi^*)}{\psi\psi^*}. \tag{6.2}$$

Quantized vortices represent phase defects in the superfluid topology of the system. Under the Madelung transformation [168], the macroscopic condensate $\psi(\mathbf{r},t)$ can be expressed in terms of a density $n_c(\mathbf{r},t)$ and a macroscopic phase $S(\mathbf{r},t)$ according to

$$\psi(\mathbf{r},t) = \sqrt{n_c(\mathbf{r},t)} e^{iS(\mathbf{r},t)}. \tag{6.3}$$

Substituting Eq. (6.3) in Eq. (6.2), we get a simple expression for the condensate velocity which depends on the gradient of the phase

$$\mathbf{v} = \frac{\hbar}{M} \nabla S. \tag{6.4}$$

This implies that, unless the phase has a singularity, the velocity field is irrotational i.e.

$$\nabla \times \mathbf{v} = 0. \tag{6.5}$$

From the single-valuedness of the condensate wavefunction it follows that, around a closed loop C, the phase change ΔS must be an integer multiple of 2π. Thus the circulation

$$k = \oint_C \mathbf{v} d\mathbf{r} \tag{6.6}$$

is calculated to be

$$k = 2\pi\gamma \frac{\hbar}{M}, \tag{6.7}$$

where γ is an integer number. A vortex line is now characterized by the appearance of a velocity field which is associated with a non-vanishing, quantized circulation Eq. (6.7). If we assume that the vortex with $\gamma = 1$ is straight and oriented along the z-axis, the quantized circulation takes the simple form

$$\nabla \times \mathbf{v} = 2\pi\gamma \frac{\hbar}{M} \delta^{(2)}(\rho - \rho_0)\hat{\mathbf{z}}, \tag{6.8}$$

where $\delta^{(2)}$ is the two-dimensional Dirac delta function and ρ the polar radius in the xy-plane.

6.2. Structure of Single Vortex

Let us now consider the structure of a single vortex in a condensate trapped by the axially-symmetric harmonic potential. The condensate wave function with a straight vortex line located along the z-axis takes the form

$$\psi(\rho, z, \phi) = f(\rho, z) e^{i\gamma\phi}, \tag{6.9}$$

with $f(\rho, z) = \sqrt{n(\rho, z)}$, an integer winding number γ and cylindrical coordinates (ρ, ϕ, z). Inserting the solution ansatz Eq. (6.9) into the time-independent GP Eq. (2.15) leads to partial differential equation for the amplitude f:

$$-\frac{\hbar^2}{2M}\left[\frac{1}{\rho}\frac{\partial}{\partial\rho}\left(\rho\frac{\partial f}{\partial\rho}\right) + \frac{\partial^2 f}{\partial z^2}\right] + \frac{\hbar^2}{2M\rho^2}\gamma^2 f + \frac{M}{2}\omega_\rho^2\left(\rho^2 + \lambda^2 z^2\right) f + g_2 f^3 = \mu f. \tag{6.10}$$

Equation (6.10) represents the starting point for determining the energy of a vortex in a harmonic trap. The kinetic energy brings a new centrifugal term arising from the velocity flow, which pushes the atoms away from the z-axis. In a rotating condensate in the Thomas-Fermi regime, the vortex core size is on the order of the so-called healing length ξ. The healing length is found by comparing the kinetic energy that is proportional to $\hbar^2/2M\xi^2$ with the interaction energy $g_2 f^2$, which gives

$$\xi = \sqrt{\frac{\hbar^2}{2Mg_2 f(\xi, 0)^2}} = \frac{1}{\sqrt{8\pi a f(\xi, 0)^2}}. \tag{6.11}$$

Here $f(\xi, 0)^2$ represents the Thomas-Fermi density without vortex at the trap center $n_c(\mathbf{0}) = \mu/g_2$ with the chemical potential μ being defined in Eq. (2.21) for vanishing three-body interaction. From this we conclude in the Thomas-Fermi regime that $\xi = l^2/R_\rho$, where the oscillator length l describes the width of a non-interacting BEC and R_ρ denotes the radial extension of the BEC cloud with repulsive two-particle interaction. Thus, a clear separation of length scales $\xi \ll l \ll R_\rho$ holds, i.e., the vortex core size is small compared to the oscillator length, which in turn is small compared to the size of the

condensate R_ρ. Because Eq. (6.10) cannot be solved analytically, we solve Eq. (6.10) approximately for the amplitude f in the two cases $\rho \ll \xi$ and $\xi \ll \rho \ll R_\rho$, respectively.

For $\rho \ll \xi$ the dominant term in Eq. (6.10) arises from the kinetic energy. Therefore, we neglect all other terms and get

$$-\frac{\hbar^2}{2M}\left[\frac{1}{\rho}\frac{\partial}{\partial\rho}\left(\rho\frac{\partial f}{\partial\rho}\right)\right] + \frac{\hbar^2}{2M\rho^2}\gamma^2 f = 0 \tag{6.12}$$

Solving for f yields the ρ-dependence

$$f = c\rho^\gamma, \quad n_c = c^2\rho^{2\gamma}, \quad \rho \ll \xi, \tag{6.13}$$

where c is a suitable constant. For $\xi \ll \rho \ll R_\rho$ the kinetic energy can be neglected and we get the Thomas-Fermi solution

$$n_{\mathrm{TF}}(\rho, z) = \frac{\mu}{g_2}\left[1 - \left(\frac{\rho}{R_\rho}\right)^2 - \left(\frac{z}{R_z}\right)^2\right]. \tag{6.14}$$

Now, we interpolate between both asymptotic forms of Eqs. (6.13) and (6.14) by adopting the following variational ansatz for the density profile of a condensate with a single vortex:

$$\psi(\rho, z, \phi) = C\sqrt{\left(\frac{\rho^2}{\rho^2 + R_\rho^2\beta^2}\right)^\gamma \left[1 - \left(\frac{\rho}{R_\rho}\right)^2 - \left(\frac{z}{R_z}\right)^2\right]}\, e^{i\gamma\phi + iB_\rho\rho^2 + iB_z z^2}. \tag{6.15}$$

Here R_ρ, R_z, β, B_ρ and B_z are time dependent variational parameters, where B_ρ and B_z are included in order to describe the dynamics of the condensate. Furthermore, we have introduced $\beta = \alpha/R_\rho$ as the ratio of the vortex core size and the transverse radius of the BEC. The phase ϕ accounts for the superfluid rotation around the vortex in the usual way [49].

The velocity field around the vortex line follows from Eqs. (6.4) and (6.9):

$$v_\phi = \frac{\gamma\hbar}{M\rho}. \tag{6.16}$$

Thus the energy associated with a single vortex line is dominated by the kinetic energy of the superfluid flow in the vortex, which can be written as

$$E_{\mathrm{v}} = \int d^3r \frac{1}{2} M n_c v_\phi^2 = \frac{\gamma^2\hbar^2}{2M}\int d^3r \frac{n_c}{\rho^2}. \tag{6.17}$$

As we have $E_{\mathrm{v}} \propto \gamma^2$, the energy cost to create one $\gamma = 2$ vortex is twice higher than that to create two $\gamma = 1$ vortices. Thus vortices with $\gamma > 1$ are energetically unfavorable. Therefore, a stable quantized vortex usually has $\gamma = 1$, and, therefore, we mainly concentrate on the case $\gamma = 1$ in the following.

In a uniform medium, the energy per unit length of a vortex with a single quantum of circulation Eq. (6.7) lying along the axis of a cylindrical container of radius ρ is given by [269]

$$\mathcal{E}_{\mathrm{v}} = n_c\pi\frac{\hbar^2}{M}\log\left(1.464\frac{\rho}{\xi}\right), \tag{6.18}$$

where n_c is the density of a uniform medium and ξ is the healing length. Combining Eq. (2.18) and (6.11), we are led to

$$\frac{\xi}{R_\rho} = \frac{\hbar\omega_\rho}{2\mu}, \tag{6.19}$$

where the chemical potential in Eq. (6.19) is related to the central density $n_c(\mathbf{0})$. If the characteristic dimensions of the cloud are large compared with the coherence length at the center of the cloud $\rho \gg \xi$,

we may determine the energy in a simple way by using the result Eq. (6.18) for the energy up to a radius ρ satisfying $\xi \ll \rho \ll R_\rho$ and then by calculating the energy at larger distances in a purely hydrodynamic manner [50]. We obtain from Eqs. (6.17) and (6.18) that the energy per unit length is given by

$$\varepsilon_{\mathrm{v}} = \frac{4\pi n_c(\mathbf{0})\hbar^2 R_z}{3M} \log\left(0.671\frac{R_\rho}{\xi}\right), \tag{6.20}$$

which agrees with the numerical calculations for large clouds [50,192].

6.3. Dynamics of BEC with Single Vortex

In order to obtain the dynamics of a BEC, we use the Thomas-Fermi approach introduced in Refs. [201,270]. This is a time-dependent variational method based on the Thomas-Fermi ansatz for an axially symmetric trap. Inserting Eqs. (2.26) and (6.15) into the Lagrange function Eq. (2.28), we obtain the corresponding Lagrange function for systems of two-body interaction strength and for vanishing three-body interaction strength. The condensate density has to remain positive, which yields a condition for the integration domain for z and ρ:

$$1 - \left[\frac{\rho}{R_\rho}\right]^2 - \left[\frac{z}{R_z}\right]^2 \geq 0. \tag{6.21}$$

The normalization constant C can be calculated by the normalization condition of Eq. (2.13)

$$C = \sqrt{\frac{45N}{8\pi R_\rho^2 R_z A_1}}, \tag{6.22}$$

where A_1 is introduced in appendix A. Thus, the resulting Lagrangian function reads

$$\begin{aligned} L =& -N\hbar\left[\frac{6R_\rho^2\dot{B}_\rho}{7A_1} - \beta^2 R_\rho^2\dot{B}_\rho - \frac{6R_z^2\dot{B}_z}{35A_1} + \frac{R_z^2\dot{B}_z\left(1+\beta^2\right)}{5}\right] - MN\omega_\rho^2\left[\frac{3R_\rho^2}{7A_1} - \frac{\beta^2 R_\rho^2}{2} + \frac{\lambda^2 R_z^2\left(1+\beta^2\right)}{10}\right. \\ &\left. -\frac{3R_z^2\lambda^2}{35A_1}\right] - \frac{N\hbar^2}{M}\left[\frac{12B_\rho^2 R_\rho^2}{7A_1} - 2\beta^2 B_\rho^2 R_\rho^2 - \frac{12B_z^2 R_z^2}{35A_1} + \frac{2\left(1+\beta^2\right)B_z^2 R_z^2}{5} + \frac{5\left(26+33\beta^2\right)}{16A_1 R_\rho^2}\right. \\ &\left. -\frac{15\left(8+16\beta^2+11\beta^4\right)\mathrm{ArcCoth}\left(\sqrt{1+\beta^2}\right)}{16A_1 R_\rho^2\sqrt{1+\beta^2}}\right] - \frac{9g_2N^2}{\pi R_\rho^2 R_z}\left[\frac{9\beta^2}{8A_1} - \frac{27}{28A_1^2} + \frac{1}{2A_1}\right]. \end{aligned} \tag{6.23}$$

The first part of Eq. (6.23) has the time-dependent contribution, while the second and third part are corresponding to the external potential trap and the two-body interaction strength, respectively, and the last term corresponds to the kinetic energy. The Thomas-Fermi approximation corresponds to neglecting the kinetic energy arising from the curvature of the slowly varying condensate background envelope $\sqrt{1-\rho^2/R_\rho^2 - z^2/R_z^2}$. To this end, we follow Ref. [201] and drop all terms which originate from the gradient of this term. On the other hand, it is essential to retain the terms arising from the gradient of the vortex part of the wave function $\sqrt{\rho^2/(\rho^2+R_\rho^2\beta^2)}$, which varies rapidly in the $\hat{\mathbf{e}}_\rho$ direction, as well as the superflow term.

From Euler-Lagrange Eq. (2.31), we obtain the evolution equations for all variational parameters q, i.e. B_i, R_i, β:

1. Minimizing the Lagrange function Eq. (6.23) with respect to R_ρ yields

$$18A_2g_2N + A_3R_\rho^4R_z\left[\frac{M\omega\rho^2}{2} + \frac{2B_\rho^2\hbar^2}{M} + \hbar\dot{B}_\rho\right] - \frac{\hbar^2R_zA_4}{M} = 0. \tag{6.24}$$

2. Minimizing the Lagrange function Eq. (6.23) with respect to R_z yields

$$-45A_2g_2N + A_5R_\rho^2R_z^3\left[\frac{M\lambda^2\omega_\rho^2}{2} + \frac{2B_z^2\hbar^2}{M} + \hbar\dot{B}_z\right] = 0. \tag{6.25}$$

3. Minimizing the Lagrange function Eq. (6.23) with respect to β yields

$$-\frac{9A_6g_2N}{56A_7R_\rho^2R_z} - \frac{M\omega_\rho^2A_8\left(5R_\rho^2 - R_z^2\lambda^2\right)}{A_9} + \frac{\hbar^2\left(A_{13} + A_{11}B_\rho^2R_\rho^4 + A_{12}B_z^2R_\rho^2R_z^2\right)}{MA_{10}R_\rho^2}$$
$$-\frac{2\hbar A_8\left(5R_\rho^2\dot{B}_\rho - R_z^2\dot{B}_z\right)}{A_9} = 0. \tag{6.26}$$

4. Minimizing the Lagrange function Eq. (6.23) with respect to B_ρ yields

$$B_\rho = \frac{M}{2\hbar}\left[\frac{\dot{R}_\rho}{R_\rho} + A_{16}\dot{\beta}\right] \tag{6.27}$$

5. Minimizing the Lagrange function Eq. (6.23) with respect to B_z yields

$$B_z = \frac{M}{2\hbar}\left[\frac{\dot{R}_z}{R_z} + A_{18}\dot{\beta}\right] \tag{6.28}$$

Inserting Eqs. (6.27) and (6.28) into Eqs. (6.24)–(6.26), we obtain a system of three differential equations of second order, for β and the dimensionless radii

$$r_\rho = R_\rho/l, \qquad r_z = R_z/l, \tag{6.29}$$

with the oscillating length l, the dimensionless time $\tau = \omega_\rho t$, and the dimensionless two-body-interaction strength $\mathcal{P}$ defined in Eqs. (2.24) and (2.38), respectively. With this, we obtain for r_ρ, r_z and β the equations of motion

$$\ddot{r}_z + r_z\left[\lambda^2 + \left(A_{17}^2 + A_{18}\right)\dot{\beta}^2 + A_{17}\ddot{\beta}\right] - \frac{360\pi A_2\mathcal{P}}{A_5r_\rho^2r_z^2} + 2A_{17}\dot{r}_z\dot{\beta} = 0\,, \tag{6.30}$$

$$\ddot{r}_\rho + r_\rho\left[1 + \left(A_{15}^2 + A_{16}\right)\dot{\beta}^2 + A_{15}\ddot{\beta}\right] - \frac{2A_4}{A_3r_\rho^3} + \frac{144\pi A_2\mathcal{P}}{A_3r_\rho^3r_z} + 2A_{15}\dot{r}_\rho\dot{\beta} = 0\,, \tag{6.31}$$

$$\left[A_{17}r_z^2 - 5A_{15}r_\rho^2\right]\ddot{\beta} - 5r_\rho^2 + r_z^2\lambda^2 - 5r_\rho\ddot{r}_\rho + r_z\ddot{r}_z + \frac{A_9A_{13}}{A_{10}A_8r_\rho^2} - \frac{9A_6A_9\mathcal{P}}{56A_7A_8r_\rho^2r_z} + \left[5 + \frac{A_9A_{11}}{4A_8A_{10}}\right]\dot{r}_\rho^2$$
$$-\left[1 - \frac{A_9A_{12}}{4A_8A_{10}}\right]\dot{r}_z^2 + \frac{A_9A_{11}A_{15}r_\rho\dot{r}_\rho\dot{\beta}}{2A_8A_{10}} + \frac{A_8A_{12}A_{17}r_z\dot{r}_z\dot{\beta}}{2A_8A_{10}} + \left[\frac{A_9A_{11}A_{15}^2}{4A_8A_{10}} - 5A_{16}\right]r_\rho^2\dot{\beta}^2$$
$$+\left[\frac{A_9A_{12}A_{17}^2}{4A_8A_{10}} + A_{18}\right]r_z^2\dot{\beta}^2 = 0\,. \tag{6.32}$$

Here the respective function $A_i(\beta)$, $i = 1, 2, .., 18$, which depend on the relative vortex core size β, are introduced in Appendix A. With the help of Eqs. (6.30) and (6.31) we can eliminate the derivatives of $\dot{\beta}$ and $\ddot{\beta}$ from Eq. (6.32), therefore, we get

$$\frac{1}{r_\rho^2}\left(\frac{A_{13}A_9}{A_{10}A_8} - \frac{10A_4}{A_3}\right) + \frac{\mathcal{P}}{r_\rho^2r_z}\left(\frac{360A_2\pi}{A_5} - \frac{9A_6A_9}{56A_7A_8} - \frac{720A_2\pi}{A_3}\right) = 0\,. \tag{6.33}$$

Thus, we read off that the variational TF ansatz Eq. (6.15) yields dynamic equations for the radial and axial condensate widths, whereas the relative vortex core size just follows from a static equation.

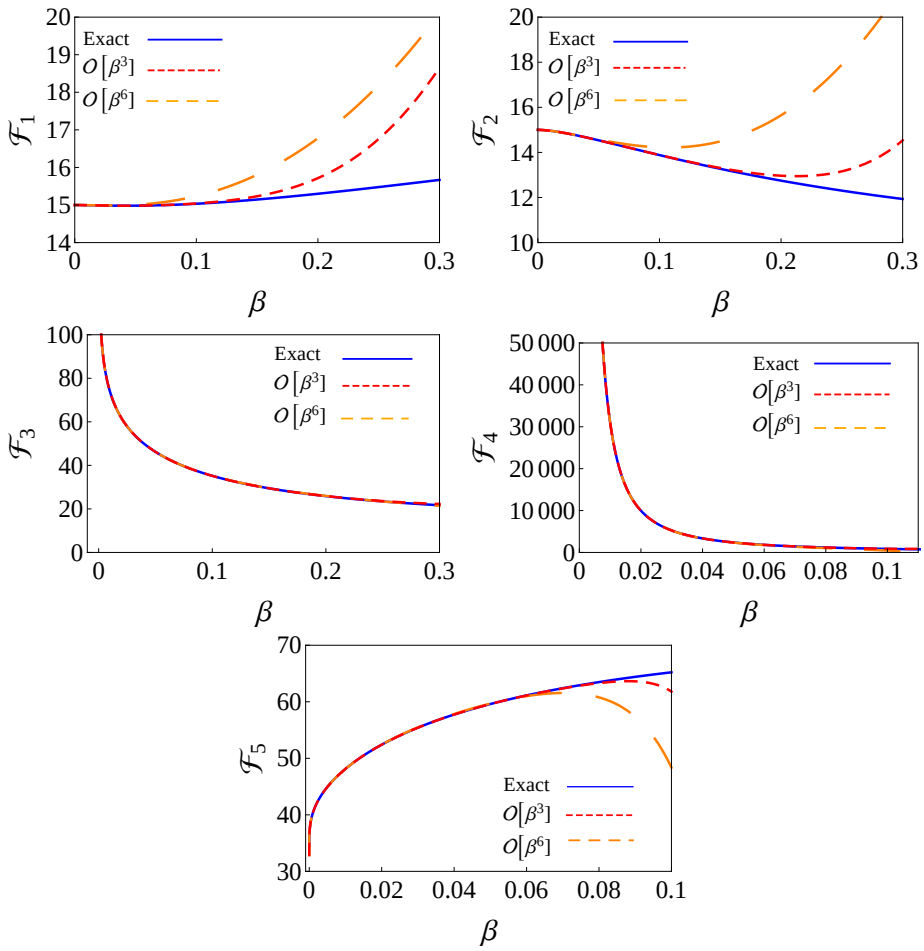

Figure 6.1.: Functions $\mathcal{F}_1(\beta)$–$\mathcal{F}_5(\beta)$ are plotted versus relative vortex core size β. The blue curves represent exact functions from Eqs. (6.35), (6.38), (6.39), (6.43), and (6.44), red dashed curves represent the functions expanded up to second order β according to Eqs. (6.36), (6.40), (6.41), (6.45), and (6.46), whereas orange dashed curves depict the functions expanded up to sixth order β.

6.4. Equilibrium Positions

The stationary solution of Eqs. (6.30), (6.31), and (6.33) is determined by the following algebraic equations:

1. Stationary solution of the axial part

$$\lambda^2 r_{z0} - \frac{\mathcal{P}\mathcal{F}_1(\beta)}{r_{\rho 0}^2 r_{z0}^2} = 0, \tag{6.34}$$

where the function

$$\mathcal{F}_1(\beta) = \frac{360\pi A_2}{A_5}, \tag{6.35}$$

has the second-order approximation in β

$$\mathcal{F}_1(\beta) = 15 + \left(\frac{227}{2} + 30\log\left[2/\beta\right]\right)\beta^2 + \mathcal{O}[\beta]^3. \tag{6.36}$$

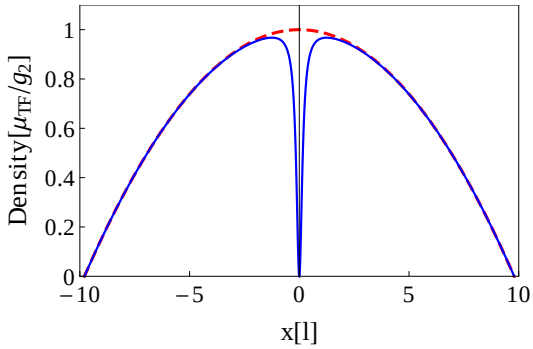

Figure 6.2.: Cross section of the particle density of a BEC with a central vortex (solid curve) and without a vortex (dashed curve) for $\mathcal{P} = 1200$ and $\lambda = 5$ at $y = z = 0$.

2. Stationary solution of the radial part

$$r_{\rho 0} - \frac{\mathcal{P}\mathcal{F}_2(\beta)}{r_{\rho 0}^3 r_{z0}} - \frac{\mathcal{F}_3(\beta)}{r_{\rho 0}^3} = 0, \tag{6.37}$$

with the functions

$$\mathcal{F}_2(\beta) = \frac{-144\pi A_2}{A_3}, \tag{6.38}$$

$$\mathcal{F}_3(\beta) = \frac{2A_4}{A_3}, \tag{6.39}$$

which have the second-order approximations

$$\mathcal{F}_2(\beta) = 15 + (327 + 135\log[2/\beta])\,\beta^2 + \mathcal{O}[\beta]^3, \tag{6.40}$$

$$\mathcal{F}_3(\beta) = \frac{35}{24}(-13 + 12\log[2/\beta]) + \frac{35\beta^2}{24}(-59 + 60\log[2/\beta]) + \mathcal{O}[\beta]^3. \tag{6.41}$$

3. Stationary solution of vortex core

$$\frac{\mathcal{F}_4(\beta)}{r_{\rho 0}^2} + \frac{\mathcal{P}\mathcal{F}_5(\beta)}{r_{\rho 0}^2 r_{z0}} = 0, \tag{6.42}$$

where

$$\mathcal{F}_4(\beta) = \frac{A_{13}A_9}{A_{10}A_8} - \frac{10A_4}{A_3}, \tag{6.43}$$

$$\mathcal{F}_5(\beta) = \frac{360A_2\pi}{A_5} - \frac{9A_6A_9}{56A_7A_8} - \frac{720A_2\pi}{A_3}, \tag{6.44}$$

which have the second-order approximations

$$\begin{aligned}\mathcal{F}_4(\beta) &= \frac{525}{2\beta^2(-76 + 30\log[2/\beta])} + \frac{175(33.722 - 22.104\log[2/\beta])^3}{24(-76 + 30\log[2/\beta])^2} \\ &\quad + \frac{175\beta^2(72.583 - 54.881\log[2/\beta])^4}{96(-76 + 30\log[2/\beta])^3} + \mathcal{O}[\beta]^3, \end{aligned} \tag{6.45}$$

$$\mathcal{F}_5(\beta) = \frac{15(-409 + 120\log[2/\beta])}{-76 + 30\log[2/\beta]} - \frac{75\beta^2(64.122 - 31.87\log[2/\beta])^3}{2(-76 + 30\log[2/\beta])^2} + \mathcal{O}[\beta]^3. \tag{6.46}$$

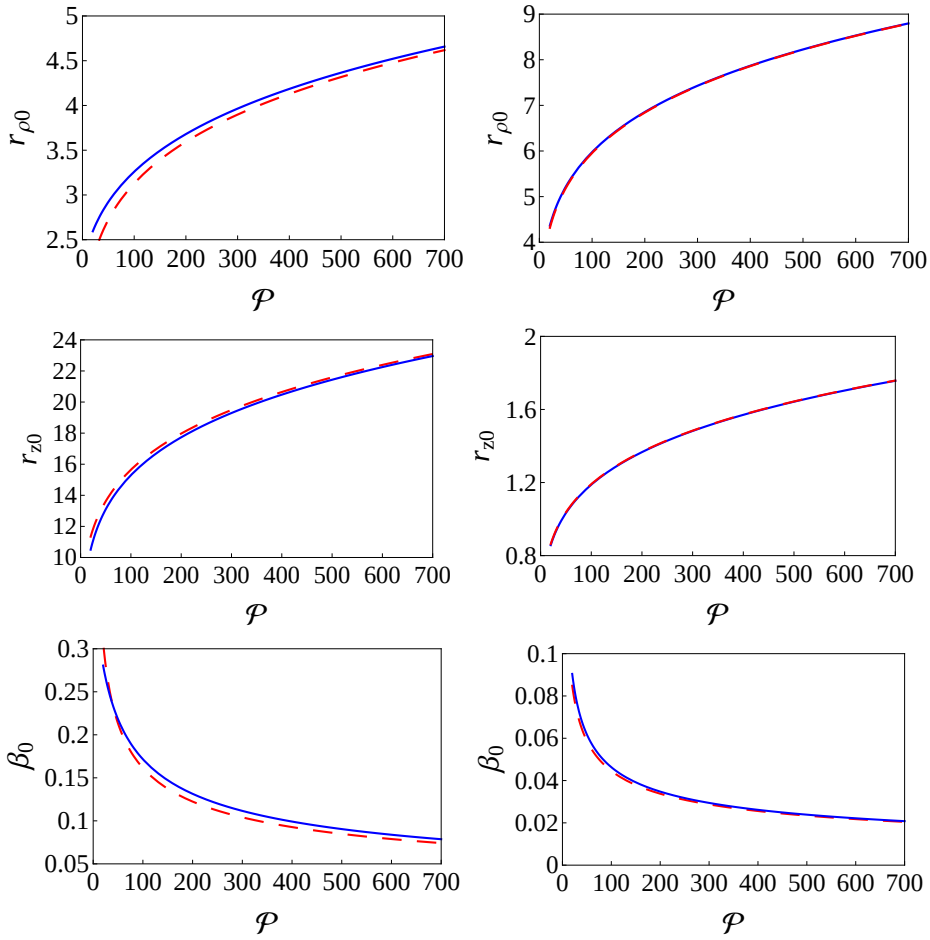

Figure 6.3.: Radial and axial sizes $r_{\rho 0}$ and r_{z0} of a condensate with a vortex as well as the relative vortex size β_0 versus the interaction $\mathcal{P}$. The left curves are denoted for a cigar-like BEC with trap anisotropy $\lambda = 0.2$, while the right curves represent a pancake-like BEC with $\lambda = 5$. Solid blue and dashed red curves correspond to the numerical exact results Eqs. (6.34), (6.37), (6.42) and the analytical approximations Eqs. (6.48)–(6.50), respectively.

We read off from Fig. 6.1 that the 2nd- and 6th-order approximations agree well with the exact functions for small relative vortex core size β.

In order to obtain an approximate analytical expression for the equilibrium positions defined by Eqs. (6.34), (6.37), and (6.42), we assume the following scaling for large $\mathcal{P}$:

$$r_{z0} = c_{z0}\, \mathcal{P}^{1/5}, \qquad r_{\rho 0} = c_{\rho 0}\, \mathcal{P}^{1/5}, \qquad \beta_0 = c_{\beta_0}\, \mathcal{P}^{-\alpha}. \tag{6.47}$$

The dependence of r_{z0} and $r_{\rho 0}$ for large $\mathcal{P}$ is motivated by Eqs. (2.21)–(2.23) as one expects that the vortex has a negligible impact on the TF radii. Substituting Eq. (6.47) into Eqs. (6.34), (6.37), and (6.42) we obtain in the limit $\mathcal{P} \to \infty$ both the exponent α and the constants $c_{\rho 0}$, c_{z0} and $c_{\beta 0}$. Thus the equilibrium positions for large $\mathcal{P}$ read

$$r_{z0} = \frac{r_{\rho 0}}{\lambda}, \tag{6.48}$$

$$r_{\rho 0} = (15\mathcal{P}\lambda)^{1/5}, \tag{6.49}$$

$$\beta_0 = \frac{5^{1/10}}{\sqrt{2}\,(3\mathcal{P}\lambda)^{2/5}}. \tag{6.50}$$

Note that equations Eqs. (6.48) and (6.49) coincide with the TF-Radii R_ρ and R_z from equations Eqs. (2.22) and (2.23) for a condensate without a vortex, while Eq. (6.50) represents the relative vortex core size $\beta = \alpha/R_\rho$. Note, the vortex core size α is of the order of the healing length ξ from Eq. (6.11), according to

$$\alpha = C_0 \xi \,, \tag{6.51}$$

with $C_0 = \sqrt{5/2}$ [43].

We have displayed the cross section of the density profile in Fig. 6.2 for a condensate with a vortex described by our trial function for the stationary case as pointed out in this section. We have also included the density profile of a condensate without a vortex in the Thomas-Fermi limit. The two profiles are very much alike, differing significantly only at the center of the trap where the vortex is located. Fig. 6.3 shows the radial and the axial condensate widths with a vortex for both a cigar-like and a pancake-like BEC. As the scattering length is increased, the radii widens, since the increasing repulsive interaction forces the atoms apart. Comparing the calculated radii to the TF-radii of a condensate without a vortex yields that the spatial extensions of the cloud remain nearly unaltered due to the presence of a vortex. In particular we read off from Fig. 6.3 that in the cigar-like condensate that $r_{\rho 0}$ increases and r_{z0} decreases with a vortex, whereas in the pancake-like condensate the Thomas-Fermi radii remain basically unaffected. Indeed, we see that the relative core radius shrinks as the scattering length is increased.

6.5. Collective Modes

Frequencies of the collective modes are determined by linearizing Eqs. (6.30)–(6.32) around the equilibrium positions. To this end we insert the expansions $r_\rho = r_{\rho 0} + \delta r_\rho$, $r_z = r_{z0} + \delta r_z$ and $\beta = \beta_0 + \delta\beta$ into Eqs. (6.30), (6.31), and (6.33) and get

$$\delta \ddot{r}_z + m_0 \delta \ddot{\beta} + m_1 \delta r_\rho + m_2 \delta u_z + \delta m_3 \beta = 0 \,, \,, \tag{6.52}$$

$$\delta \ddot{r}_\rho + m_4 \delta \ddot{\beta} + m_5 \delta r_\rho + m_6 \delta r_z + m_7 \delta\beta = 0, \tag{6.53}$$

$$m_8 \delta r_\rho + m_9 \delta r_z + m_{10} \delta\beta = 0. \tag{6.54}$$

Here m_i with $i = 1, 2, ..., 10$ are functions which depend on the relative vortex core size β_0 and are calculated by using Mathematica [242].

The coupled set of differential equation Eqs. (6.52)–(6.54) can be rewritten in matrix form

$$M_1 \delta \ddot{\mathbf{r}} + M_2 \delta \mathbf{r} = \mathbf{0} \,, \tag{6.55}$$

with the abbreviations

$$\delta \mathbf{r} = \begin{pmatrix} \delta r_\rho \\ \delta r_z \\ \delta\beta_1 \end{pmatrix} , \quad M_1 = \begin{pmatrix} 1 & 0 & m_4 \\ 0 & 1 & m_0 \\ 0 & 0 & 0 \end{pmatrix} , \quad M_2 = \begin{pmatrix} m_5 & m_6 & m_7 \\ m_1 & m_2 & m_3 \\ m_8 & m_9 & m_{10} \end{pmatrix}. \tag{6.56}$$

If we insert therein the solution ansatz Eq. (2.62), the frequencies of the collective modes are related to the following eigenvalue problem

$$\left(M_2 - \omega^2 M_1\right) \delta \mathbf{r} = 0 \,. \tag{6.57}$$

Non-trivial solutions of this homogenous system exist, provided that

$$\det(M_2 - \omega^2 M_1) = 0, \tag{6.58}$$

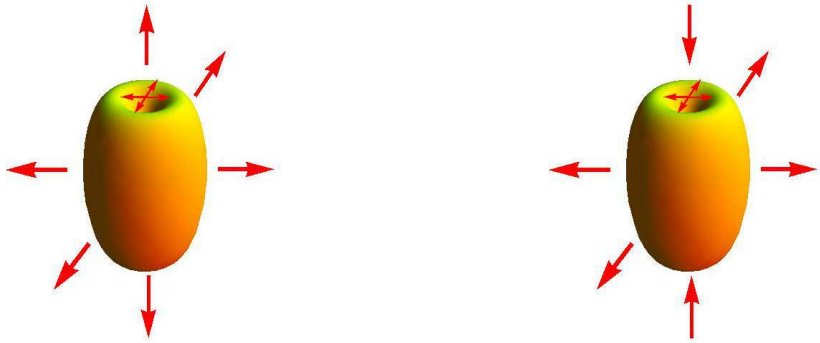

(a) $\delta\mathbf{r}_1$ (b) $\delta\mathbf{r}_2$

Figure 6.4.: Schematic representation of collective modes. (a) mode has all components oscillating in phase. (b) mode has r_z oscillation out of phase with r_ρ and β [272].

which reduces to a quadratic algebraic equation for ω^2:

$$z_1\omega^4 + z_2\omega^2 + z_3 = 0. \tag{6.59}$$

Here we have used the abbreviations

$$z_1 = m_{10} - m_4 m_8 - m_0 m_9\,, \tag{6.60}$$

$$z_2 = -m_{10}m_2 - m_{10}m_5 + m_2 m_4 m_8 - m_0 m_6 m_8 + m_7 m_8 + m_3 m_9 - m_1 m_4 m_9 + m_0 m_5 m_9\,, \tag{6.61}$$

$$z_3 = m_{10}m_2 m_5 - m_1 m_{10} m_6 + m_3 m_6 m_8 - m_2 m_7 m_8 - m_3 m_5 m_9 + m_1 m_7 m_9\,. \tag{6.62}$$

Solving Eq. (6.59), we obtain the frequencies of two collective modes

$$\omega_{1,2}^2 = \frac{-z_2 \pm \sqrt{z_2^2 - 4z_1 z_3}}{2z_1}\,, \tag{6.63}$$

where $\omega_{1,2}$ refers to a plus and a minus sign, respectively. Inserting those collective frequencies into Eq. (6.57), yields the corresponding eigenvectors. Due to the linear dependence of Eq. (6.57), we use the first two lines in order to calculate the eigenvectors of modes. In this way we obtain

$$\delta\mathbf{r}_{1,2} = N_{1,2}\begin{bmatrix} \frac{m_3 m_6 - m_0 m_6 \omega_{1,2}^2 - \left(m_2 m_7 - m_2 m_4 \omega_{1,2}^2 - m_7 \omega_{1,2}^2 + m_4^2 \omega_{1,2}^4\right)}{-m_1 m_6 + m_2 m_5 - m_2 \omega_{1,2}^2 - m_5 \omega_{1,2}^2 + \omega_{1,2}^4} \\ \frac{m_1 m_7 - m_1 m_4 \omega_{1,2}^2 - \left(m_3 m_5 - m_3 \omega_{1,2}^2 - m_0 m_5 \omega_{1,2}^2 - m_0^2 \omega_{1,2}^4\right)}{-m_1 m_6 + m_2 m_5 - m_2 \omega_{1,2}^2 - m_5 \omega_{1,2}^2 + \omega_{1,2}^4} \\ 1 \end{bmatrix}, \tag{6.64}$$

where $N_{1,2}$ denotes some normalization constant. Here the eigenvector $\delta\mathbf{r}_1$ corresponds to in-phase radial and axial oscillations, thus they correspond to the breathing mode frequency ω_1, while the eigenvector $\delta\mathbf{r}_2$ has the lower frequency and is characterized by out-of phase radial and axial oscillations, so they represent the quadrupole mode frequency ω_2. Furthermore, it turns out that the relative vortex core size β oscillates in-phase with the radial width both for the breathing and the quadrupole modes., as shown in Fig. 6.4.

In the limit $\mathcal{P}$ going to infinity, the relative vortex size β_0 goes to zero, whereas $r_{\rho 0}$ and r_{z0} go to infinity according to Eqs. (6.48)–(6.50). One can expand the coefficients m_0,....,m_{10} up to the first order of β_0 and by substituting them into Eqs. (6.60)–(6.62) and by using Eqs. (6.48) and (6.49), we obtain the frequencies of collective modes Eq. (2.72) for vanishing three-body interaction $\mathcal{K} = 0$, we get

$$\omega_{B,Q}^2 = 2 + \frac{3}{2}\lambda^2 \pm \frac{1}{2}\sqrt{16 - 16\lambda^2 + 9\lambda^4}\,. \tag{6.65}$$

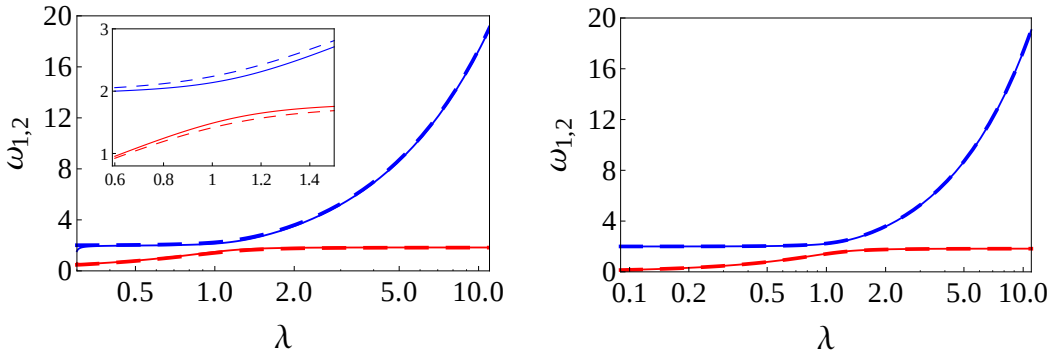

(a) (b)

Figure 6.5.: Frequencies of collective modes: breathing mode (blue curves) and quadrupole mode (red curves) in unit of ω_ρ versus trap anisotropy λ (a) $\mathcal{P} = 170$ and (b) $\mathcal{P} = 800$ [271,272]. Solid and dashed curves correspond to the frequencies of collective modes with a single vortex Eq. (6.63) and the frequencies without vortex in the Thomas-Fermi limit Eq. (6.65), respectively.

In Fig. 6.5 we show the resulting frequencies $\omega_{1,2}$ as a function of trap anisotropy λ, where the solid curves denote the frequencies with a single vortex Eq. (6.63) and the dashed curves relate to the frequencies without vortex in the Thomas-Fermi limit Eq. (6.65), respectively. We read off from Fig. 6.5(a) that the frequencies change slightly in so far as the breathing and the quadrupole frequency decrease and increase in the presence of a single vortex, respectively. Note that our results from Eq. (6.63) in Fig. 6.5(b) coincide perfectly with the frequencies determined in Ref. [272], where the variational TF ansatz Eq. (6.15) is extended in such a way that the relative vortex core size follows from a dynamic equation.

6.6. Critical Rotational Frequency

We now calculate the energy of a single vortex in a trap Bose-Einstein condensate [50,179], which is important determining the lowest angular velocity at which it is energetically favorable for a vortex to enter the cloud. The total energy of the condensate is given by

$$E_{\text{Total}} = \int d^3r \left[\frac{\hbar^2}{2M} \nabla\psi(\mathbf{r},t)\nabla\psi^*(\mathbf{r},t) + V(\mathbf{r})\left|\psi(\mathbf{r},t)\right|^2 + \frac{g_2}{2}\left|\psi(\mathbf{r},t)\right|^4 \right]. \tag{6.66}$$

Note that Eq. (6.66) has already been calculated in Eq. (6.23) as the Lagrangian reduces in the stationary limit, where all accelerations and velocities have to be set to zero to this total energy. Thus the total energy of a condensate in the TF-limit with a central vortex is given by

$$\begin{aligned} E_{\text{Total}} \;=\; & N\hbar\omega_\rho \left[\frac{3r_{\rho 0}^2}{7A_1} - \frac{\beta_0^2 r_{\rho 0}^2}{2} - \frac{3r_{z0}^2\lambda^2}{35A_1} + \frac{\lambda^2 r_{z0}^2\left(1+\beta_0^2\right)}{10} + \frac{36\mathcal{P}}{r_{\rho 0}^2 r_{z0}}\left(\frac{9\beta_0^2}{8A_1} - \frac{27}{28A_1^2} + \frac{1}{2A_1}\right) \right. \\ & \left. - \frac{5\sqrt{1+\beta_0^2}\left(26+33\beta_0^2\right) - 15\left(8+16\beta_0^2+11\beta_0^4\right)\text{ArcCoth}\left[\sqrt{1+\beta_0^2}\right]}{16A_1 r_{\rho 0}^2\sqrt{1+\beta_0^2}} \right]. \end{aligned} \tag{6.67}$$

Figure 6.6 shows the total energy E_{Total}, as defined by Eq. (6.67), of a condensate with a vortex for trap aspect ratio $\lambda = 0.2$ and $\lambda = 5$. In particular the energy with a vortex is larger than with out a vortex for a cigar-like condensate. The agreement of the two curves for the energy with a vortex is

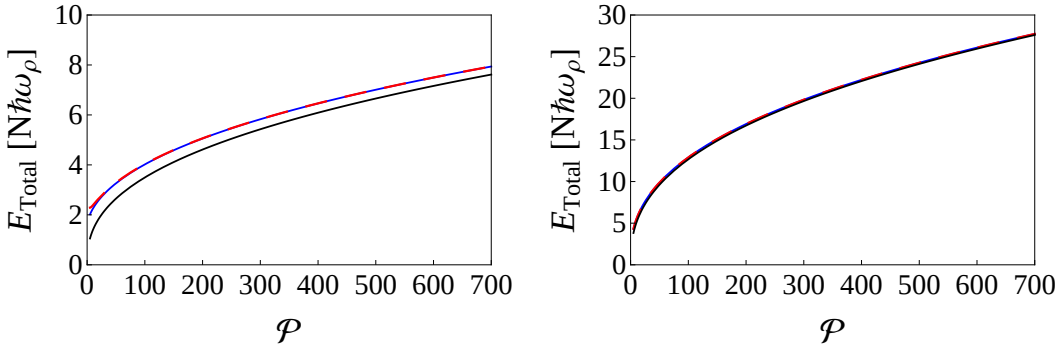

Figure 6.6.: The energy of the condensate with a central vortex scaled in units of $N\hbar\omega_\rho$ versus the dimensionless interaction strength $\mathcal{P}$ for trap aspect ratio (a) $\lambda = 0.2$ and (b) $\lambda = 5$. Blue, red dashed, and black curves correspond to the numerical results Eq. (6.67) by taking into the account the equilibrium condensate widths which are determined from Eqs. (6.34), (6.37), and (6.42), the analytical approximation results Eq. (6.67) are calculated with the equilibrium condensate widths calculated from Eqs. (6.48)–(6.50), and Eq. (6.68), respectively.

excellent. The total energy rises with increasing scattering length as expected, since the part in the energy functional due to the interaction is directly proportional to the s-wave scattering a_s.

The energy of a condensate without a vortex in the TF-limit is determined by substituting Eq. (6.14) with relevant radii from Eq. (2.21)–(2.23) into Eq. (6.66), where, due to Thomas-Fermi approximation, the kinetic energy is neglected. Thus, we obtain

$$E_0 = N\hbar\omega_\rho \frac{5}{14}(15\mathcal{P}\lambda)^{2/5}. \tag{6.68}$$

In general it costs the energy E_{v} to create a vortex which is obtained by subtracting E_0 from E_{Total}

$$E_{\text{v}} = E_{\text{Total}} - E_0\,. \tag{6.69}$$

It is possible to stabilize a vortex state by applying a rotating trap potential [192]. To understand this we consider a frame rotating at angular velocity about the z-axis for which the energy of the system becomes

$$E'_{\text{Total}} = E_{\text{Total}} - \Omega L_z\,. \tag{6.70}$$

For a nonrotating condensate without angular momentum the energy in the rotating frame remains the same as before, whereas for a condensate with a single quantized vortex the energy is reduced. This is due to the fact that every particle carries the angular momentum of $\hbar$ and, consequently, the total angular momentum adds up to $L_z = N\hbar$. We see that, for a condensate in a trap rotating at angular velocity, the vortex state becomes energetically favorable when Ω exceeds a critical rotational frequency at which the energy cost to create a vortex equals the lowering of the energy due to the rotating trap potential. Thus, the critical angular frequency becomes

$$\Omega_C = \frac{E_{\text{v}}}{N\hbar} \tag{6.71}$$

Furthermore an analytical expression for the critical angular velocity obtained by Pethick et al. [50] is included in Fig. 6.7, which is calculated from Eq. (6.71), with E_{v} being defined in Eq. (6.20):

$$\Omega_C = \frac{5\omega_\rho}{2R_\rho^2}\log\left(0.671\frac{R_\rho}{\xi}\right)\,. \tag{6.72}$$

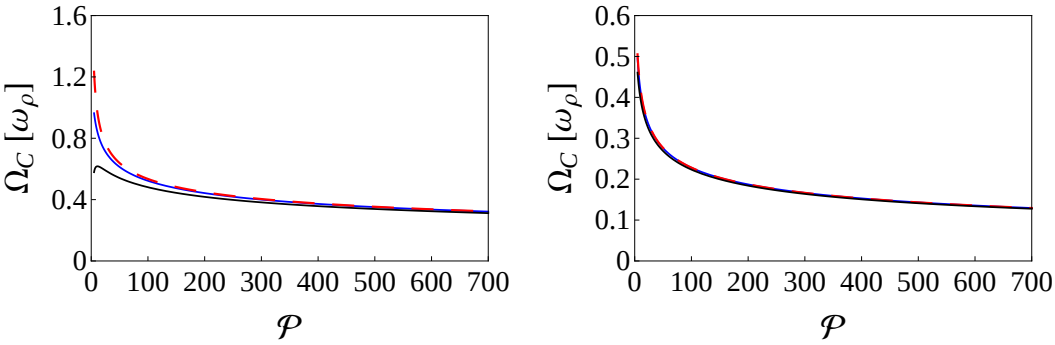

(a) (b)

Figure 6.7.: The critical angular velocity Ω_c of a rotating trap versus two-body interaction strength $\mathcal{P}$ for trap aspect ratio (a) $\lambda = 0.2$ and (b) $\lambda = 5$. Solid blue, dashed red, and black curves correspond to the numerical results Eq. (6.71) obtained by taking into the account the equilibrium condensate widths which are determined from Eqs. (6.34), (6.37), and (6.42), the analytical approximation results Eq. (6.71) are calculated with the equilibrium condensate widths calculated from Eqs. (6.48)–(6.50), and Eq. (6.73), respectively.

Substituting the relative vortex core radius $\beta_0 = \alpha/R_\rho$ from Eq. (6.50) into Eq. (6.72), yields

$$\Omega_C = \omega_\rho \left(\frac{0.579 + 0.339 \log[\mathcal{P}\lambda]}{(\mathcal{P}\lambda)^{2/5}} \right) . \tag{6.73}$$

Figure 6.7 shows the resulting critical rotation frequency Ω_C as defined by Eq. (6.71) for the trap aspect ratio $\lambda = 0.2$ and $\lambda = 5$. To this end, Fig. 6.7 reveals that our analytical result for the critical rotational frequency Eq. (6.71) agrees very well with the numerical result Eq. (6.71) and is, indeed, consistent with the analytical result derived by Pethick et al. [50] from equations Eq. (6.72) and (6.73). Thus the difference between our results Eq. (6.71) and Pethick result Eq. (6.73) is more pronounced for both a cigar-like condensate.

6.7. Time-of-Flight Expansion

In this section we study the free expansion of a trapped condensate with a central vortex in case of an axially-symmetric harmonic trap by solving Eqs. (6.30), (6.31), and (6.33) without the terms, which represent the trap:

$$\ddot{r}_z + r_z \left[\left(A_{17}^2 + A_{18} \right) \dot{\beta}^2 + A_{17} \ddot{\beta} \right] - \frac{360\pi A_2 \mathcal{P}}{A_5 r_\rho^2 r_z^2} + 2A_{17} \dot{r}_z \dot{\beta} = 0 \,, \tag{6.74}$$

$$\ddot{r}_\rho + r_\rho \left[\left(A_{15}^2 + A_{16} \right) \dot{\beta}^2 + A_{15} \ddot{\beta} \right] - \frac{2A_4}{A_3 r_\rho^3} + \frac{144\pi A_2 \mathcal{P}}{A_3 r_\rho^3 r_z} + 2A_{15} \dot{r}_\rho \dot{\beta} = 0 \,, \tag{6.75}$$

$$\frac{1}{r_\rho^2} \left(\frac{A_{13} A_9}{A_{10} A_8} - \frac{10 A_4}{A_3} \right) + \frac{\mathcal{P}}{r_\rho^2 r_z} \left(\frac{360 A_2 \pi}{A_5} - \frac{9 A_6 A_9}{56 A_7 A_8} - \frac{720 A_2 \pi}{A_3} \right) = 0 \,. \tag{6.76}$$

As it is difficult to study these equations exactly, we expand them up to second order of β, yielding

$$\ddot{r}_z - \frac{E_1 P}{r_\rho^2 r_z^2} + E_2 r_z \dot{\beta}^2 + E_3 \dot{r}_z \dot{\beta} + \frac{E_3}{2} r_z \ddot{\beta} = 0 \,, \tag{6.77}$$

$$\ddot{r}_\rho - \frac{E_5}{r_\rho^3} - \frac{E_4 P}{r_\rho^3 r_z} + E_6 \dot{r}_\rho \dot{\beta} + E_7 r_\rho \dot{\beta}^2 + E_8 r_\rho \ddot{\beta} = 0 \,, \tag{6.78}$$

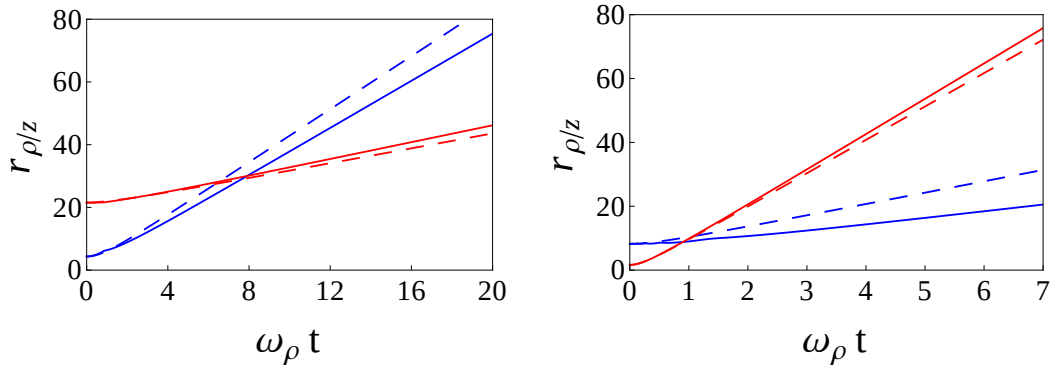

(a) (b)

Figure 6.8.: Time evolution of the spatial extensions r_ρ (blue curves) and r_z (red curves) after turning off the trapping potential for trap anisotropy (a) $\lambda = 0.2$ and (b) $\lambda = 5$ for two-body interaction $\mathcal{P} = 500$. Solid and dashed curves correspond to the radii extensions with a vortex in Eqs. (6.77), (6.78) and without a vortex in Eqs. (6.80), (6.81), respectively.

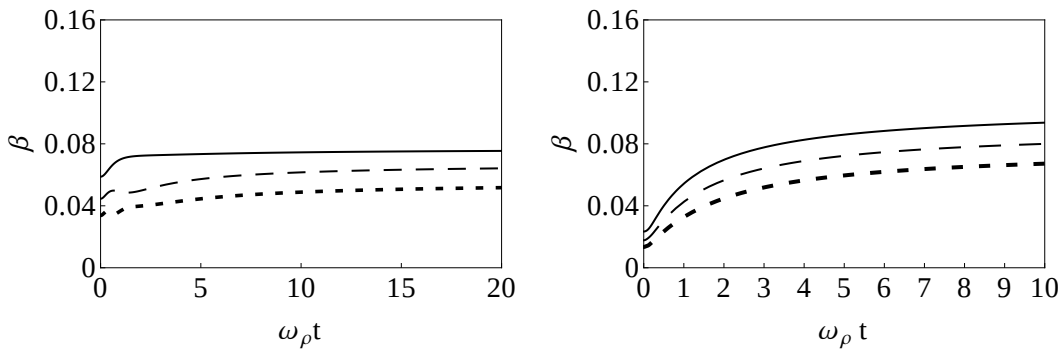

(a) (b)

Figure 6.9.: Evolution in time of relative vortex core size β after turning off the trapping potential for trap anisotropy (a) $\lambda = 0.2$ and (b) $\lambda = 5$ for different two-body interaction $\mathcal{P} = 500$ (solid curves), $\mathcal{P} = 1000$ (dashed curves), and $\mathcal{P} = 2000$ (dotted curves).

$$E_9 + \frac{E_{10}\mathcal{P}}{r_z} = 0\,, \tag{6.79}$$

where the abbreviations E_n, $n = 1, ..., 10$ are defined in Appendix B. To this end we solve these equations numerically for the trap anisotropy $\lambda = 0.2$ and $\lambda = 5$, where we use as initial conditions the numerically determined equilibrium positions for a trapped condensate from Eqs. (6.34), (6.37), and (6.42), where the abbreviations $\mathcal{F}_1(\beta)$–$\mathcal{F}_5(\beta)$ are defined in Eqs. (6.36), (6.40), (6.41), (6.45), and (6.46), respectively.

For a condensate without a vortex is determined by numerically solving the equations of motion obtained by setting all β terms in Eqs. (6.74)–(6.76) to zero, so we get

$$\ddot{r}_z - \frac{15\mathcal{P}}{r_\rho^2 r_z^2} = 0\,, \tag{6.80}$$

$$\ddot{r}_\rho - \frac{15\mathcal{P}}{r_\rho^3 r_z} = 0\,. \tag{6.81}$$

which corresponds to the Thomas-Fermi approximation.

It becomes clear in Fig. 6.8 that the condensate in the cigar-like shape expands much faster in the radial than in the axial direction in time, while the condensate in the pancake-like shape expands

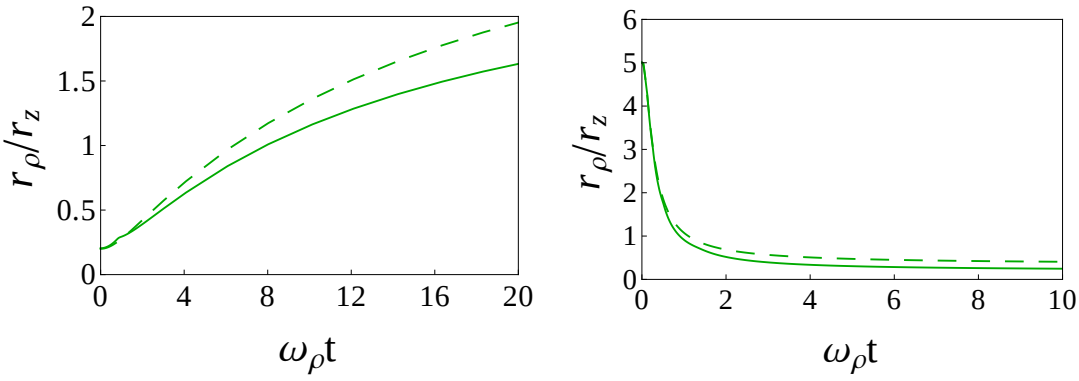

(a) (b)

Figure 6.10.: Trap aspect ratio r_ρ/r_z after turning off the trapping potential for trap anisotropy (a) $\lambda = 0.2$ and (b) $\lambda = 5$ for two-body interaction $\mathcal{P} = 500$. Solid and dashed curves denote to the aspect ratios with a vortex from Eqs. (6.77), (6.78) and without a vortex Eqs. (6.80), (6.81), respectively.

much faster in the axial than in the radial direction in time. In particular we show that the radial expansion with a vortex is slower without a vortex, while the expansion for the axial extension occurs faster with a vortex. The time evolution of the relative vortex core size in Fig. 6.9 shows that the vortex core radius grows less rapid for large two-body interaction. This is an important insight for the experimental detection and the investigation of vortex states. Hence, as β is monotonously increasing, our study qualitatively confirms the result from Ref. [273], which was obtained with a different trial function. Indeed, in the previous study [273] it has been suggested that the vortex core radius expands faster than the radial extension of the cloud, which makes experimental detection feasible by using a time-of-flight method, where the condensate is first set free and then pictures are taken after a short expansion time. Figure 6.10 shows the aspect ratio r_ρ/r_z for a condensate with and without a vortex. Both curves in Fig. 6.10 clearly describe that the aspect ratio is inverted. Furthermore, we conclude that a single vortex decreases the aspect ratio both for a cigar- and a pancake-like condensate. Thus measuring the aspect ratio after free expansion represents an effective quantity to detect single vortex states. Furthermore, the difference between the aspect ratio with and without a vortex is more pronounced for a cigar-like condensate than for a pancake-like condensate.

In Fig. 6.11 the density plot of the condensate in the trapped state after turning off the trapping potential is illustrated. The vortex core region is clearly visible as a bright line and its width increases in time faster than the radial extension.

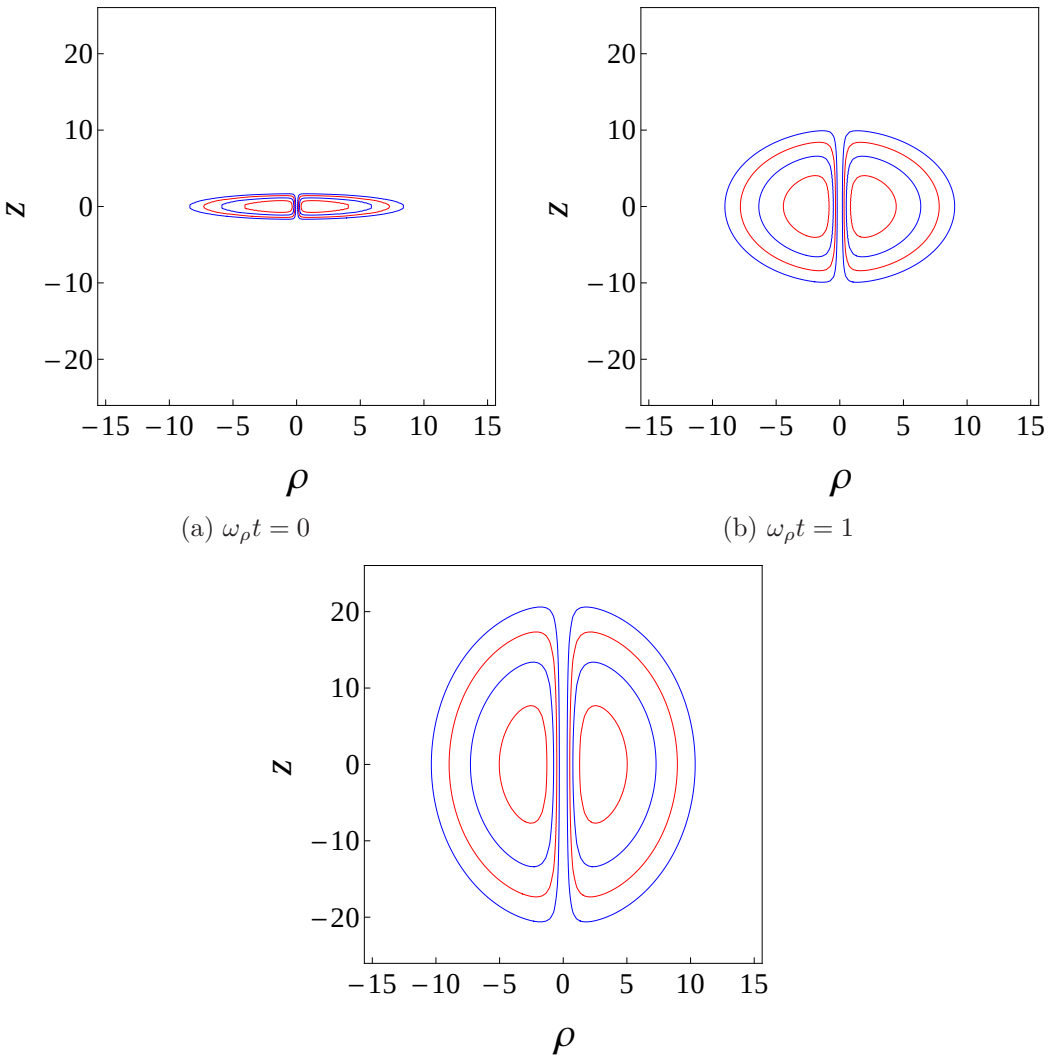

(a) $\omega_\rho t = 0$

(b) $\omega_\rho t = 1$

(c) $\omega_\rho t = 2$

Figure 6.11.: Density profiles of an expanding condensate with a central vortex after turning off the trapping potential for the trap anisotropy $\lambda = 5$ and $\mathcal{P} = 1000$.

7. Conclusion

In this thesis we studied numerically and analytically low-lying collective excitations in Bose-Einstein condensates at when both quantum and thermal fluctuations are negligible. At first, we presented a historical introduction of Bose-Einstein condensates, which are inherently nonlinear quantum many-body systems and lead to a number of interesting effects. For instance, the frequencies of collective oscillation modes can be measured quite accurately and, thus, they represent a valuable source of information about the properties of Bose-Einstein condensates.

The Gross-Pitaevskii mean-field theory of Bose-Einstein condensates was the focus of **Chapter 2**. We started with the second quantised Hamiltonian for an interacting Bose gas with two- and three-body collisions. With this we derived the Gross-Pitaevskii equation Eq. (2.12) from the Heisenberg equation for the field operator in mean-field approximation Eq. (2.9). We discussed the TF approximation of the density profile for a system of two- and three-body interactions Eq. (2.16), where we saw that the TF radii are more sensitive with respective to the three-body interaction for increasing s-wave scattering length Eqs. (2.21)–(2.23). Furthermore, we used a Gaussian variational ansatz to analytically study the dynamical system of a BEC with two- and three-body interactions defined by the time-dependent Gross-Pitaevskii equation Eq. (2.12). We determined the equilibrium positions of the condensate widths Eqs. (2.50)–(2.51), which correspond to stable (unstable) stationary states of a condensate. By linearizing the equations of motion of the condensate widths around the equilibrium positions, we determined the low-lying collective excitation modes Eqs. (2.65)–(2.67). In addition we discussed in detail the stability of BECs with two- and three-body interactions in an axially-symmetric harmonic trap in different cases: repulsive and attractive two-body interactions, attractive two-body and repulsive three-body interactions, and attractive two- and three-body interactions. In particular, we showed in Fig. 2.8 that a small repulsive three-body interaction is able to stabilize the condensate with attractive two-body interaction by increasing the critical number of atoms in the trap. Furthermore switching off the term corresponding to the harmonic trap and solving the resulting equations of motion with the initial conditions provided by the equilibrium positions Eqs. (2.50) and (2.51), we studied the time dependence of the condensate aspect ratio after release from the trap for a system of both two- and three-body interactions.

Motivated by the recent experimental results of Ref. [93], we studied in **Chapter 3** the nonlinear BEC dynamics induced by a harmonically modulated two-body interaction strength. To this end we combined an analytic perturbative approach and based on the Poincaré-Lindstedt method, a numerical analysis based on the Gaussian variational approximation, with numerical simulations of the full time-dependent Gross-Pitaevskii equation. We presented numerically calculated excitation spectra in both a spherical-symmetric trap in Fig. 3.5 and an axially-symmetric trap in Fig. 3.11 and found prominent nonlinear features: mode coupling, higher harmonics generation, and significant shifts in the frequencies of collective modes. In addition, we provided an analytical perturbative framework that captures most of the observed phenomena. The main results are the analytic formulae Eqs. (3.16) and (3.33), which describe how the collective mode frequencies depend on both the modulation amplitude and the external driving frequency for different trap geometries. Most prominently, our numerical results indicate frequency shifts of 10 % even outside the resonant regions according to Figs. 3.8 and 3.13, and this is where experimental measurements should be performed. Furthermore, we used a Fourier analysis with a sufficiently good resolution in order to demonstrate that our analytical results

agree quite well with numerical solutions based on both the Gaussian variational approximation and the full numerical solution of the GP equation in Fig. 3.9.

In **Chapter 4** we studied the nonlinear dynamics of a BEC with two- and three-body interaction by changing the trap anisotropy. Also here we used the perturbative expansion of a Poincaré-Lindstedt analysis within the Gaussian variational approach to study in detail the delicate interplay between nonlinear effects due to two- and three-body interactions as well as the trap geometry. Within the variational approach of the Poincaré-Lindstedt method we calculated frequency shifts and identified the geometric resonances in terms of commensurate frequencies of the quadrupole and the breathing mode of axially symmetric BEC systems in Eqs. (4.24) and (4.28), respectively. We showed that the observed geometric resonances in Fig. 4.4 could be eliminated if two- and three-body interactions are appropriately fine-tuned. In addition, we studied a numerical approach based on the Gaussian variational approximation with excitation spectra in Fig. 4.3 which reveals prominent nonlinear features as, mode coupling, higher harmonics generation, and significant shifts in the frequencies of collective modes. We showed in Fig. 4.6 that our analytical results of the frequency shift, which are based on the third order of perturbation theory, agree well with a corresponding calculation based on the hydrodynamic equations in the Thomas-Fermi approximation [70]. We also studied the resonant mode coupling due to nonlinear interactions between the collective modes of the system. Thus, even if we excite only one of them, the others will be eventually excited due to the nonlinearity of the BEC dynamics.

Subsequently, we studied in **Chapter 5** in detail how the dipole mode frequency and the collective excitation modes of a harmonically trapped Bose-Einstein condensate change in the immediate vicinity of a Feshbach resonance. To this end we derived equations of motion Eq. (5.12)–(5.14) for variational parameters that describe the condensate radial and axial widths as well as the center of mass motion and showed different approaches how to extract the corresponding frequencies of collective modes. At first we discussed the heuristic approximation of Ref. [121] to evaluate the integral Eq. (5.10), which is valid far way from the Feshbach resonance and, thus, can not predict correctly the dynamics on top of the Feshbach resonance. Therefore, we developed our own treatment of the integral Eq. (5.10), which is based on Schwinger trick [266] according to Eq. (5.35). Then we studied the resulting consequences both on top and on the right-hand side of the Feshbach resonance. In this way, we saw how the frequencies of the collective modes change when one approaches the Feshbach resonance as shown in Fig 5.6. As expected in Eq. (5.7) we obtained a large reduction of the dipole mode frequency, so the Kohn theorem is violated, as well as a significant effect for the breathing and the quadrupole mode frequencies on top of the Feshbach resonance. Furthermore, we found that the system on the right-hand side of the Feshbach resonance is not stable beyond a critical magnetic field as shown Fig. 5.7c. Our results and the approximative solution of Ref. [121] disagree about 0.05 G above the Feshbach resonance for the experimental parameters of Refs [260,264] which is still, so large that it could be experimentlly measured that the magnetic field can be tuned up to 1 mG [267].

Finally we studied in **Chapter 6** a Bose-Einstein condensate with a single vortex using a variational approach. To this end we derived equations of motion for variational parameters that describe the radial and axial condensate widths and the relative vortex core size in Eqs. (6.30)–(6.32). Then we discussed the equilibrium positions of the condensate widths as well as the relative vortex core size, for which we determined analytical approximations in the Thomas-Fermi limit Eqs. (6.48)–(6.50). We found that the equilibrium positions of the condensate widths do slightly change in the presence of a vortex, yielding a tiny decrease of the cloud aspect ratio. We then determined the frequencies of collective modes and derived an analytic expression for the breathing and the quadrupole mode frequencies Eqs. (6.63). We observe a significant change of the breathing and quadrupole mode frequencies for a pancake-like condensate, whereas the breathing and quadrupole mode frequencies remains basically unaffected for a ciger-like condensate. Furthermore we presented the frequencies of

collective modes with a single vortex in the Thomas-Fermi limit of two-body interaction Eq. (2.72). It turned out that the relative vortex core size oscillates in phase with both the quadrupole and the breathing modes. Furthermore, we determined the energy of a condensate with a central vortex as well as the critical frequency of a rotating trap at which a single vortex becomes stable. We discussed the time-of-flight expansion of a trapped condensate with a central vortex and we showed that the vortex core expands relatively faster than the radial extension of the cloud.

We conclude that our detailed study of the nonlinear mean-field dynamics of Bose-Einstein condensates at zero temperature could contribute to the design and analysis of future experiments.

A. Abbreviations A_i

Here the abbreviations $A_i(\beta)$ with $i = 1, 2, ..., 19$ are introduced which appear in the equations of motion Eqs. (6.30)–(6.32):

$$A_1 = 3 + 20\beta^2 + 15\beta^4 - 15\beta^2 \left(1+\beta^2\right)^{3/2} \text{ArcCoth}[\sqrt{1+\beta^2}] \tag{A.1}$$

$$A_2 = -54 + 7A_1 \left(4 + 9\beta^2\right) \tag{A.2}$$

$$A_3 = 16\pi A_1 \left(-6 + 7A_1\beta^2\right) \tag{A.3}$$

$$A_4 = 35A_1\pi(26 + 33\beta^2) \tag{A.4}$$

$$A_5 = -\frac{105A_1\pi \left(8 + 16\beta^2 + 11\beta^4\right) \text{ArcCoth}\left[\sqrt{1+\beta^2}\right]}{\sqrt{1+\beta^2}} \tag{A.5}$$

$$A_6 = 16\pi A_1^2 + A_3 \tag{A.6}$$

$$\begin{aligned} A_7 = {} & \beta\sqrt{1+\beta^2}\left(-2454 + 24275\beta^2 + 86835\beta^4 + 102375\beta^6 + 42525\beta^8\right) \\ & -30\beta\left(-24 + 1057\beta^2 + 5288\beta^4 + 10087\beta^6 + 8715\beta^8 + 2835\beta^{10}\right) \text{ArcCoth}\left[\sqrt{1+\beta^2}\right] \\ & +1575\beta^3\left(1+\beta^2\right)^{5/2}\left(8 + 20\beta^2 + 27\beta^4\right) \text{ArcCoth}\left[\sqrt{1+\beta^2}\right]^2 \end{aligned} \tag{A.7}$$

$$A_8 = -\frac{1}{4}A_1^3\sqrt{1+\beta^2} \tag{A.8}$$

$$\begin{aligned} A_9 = {} & \beta\sqrt{1+\beta^2}\left(228 + 1065\beta^2 + 3430\beta^4 + 4200\beta^6 + 1575\beta^8\right) \\ & -15\beta\left(6 + 63\beta^2 + 379\beta^4 + 812\beta^6 + 700\beta^8 + 210\beta^{10}\right) \text{ArcCoth}\left[\sqrt{1+\beta^2}\right] \\ & +1575\beta^5\left(1+\beta^2\right)^{7/2} \text{ArcCoth}\left[\sqrt{1+\beta^2}\right]^2 \end{aligned} \tag{A.9}$$

$$A_{10} = 35A_1^2\sqrt{1+\beta^2} \tag{A.10}$$

$$A_{11} = 280A_1^2\beta\left(1+\beta^2\right)^{3/2} \tag{A.11}$$

$$\begin{aligned} A_{12} = {} & \sqrt{1+\beta^2}\left(-36480\beta^2 - 206880\beta^4 - 719200\beta^6 - 1220800\beta^8 - 924000\beta^{10} - 252000\beta^{12}\right) \\ & +2400\beta^2\left(1+\beta^2\right)^2\left(6 + 57\beta^2 + 322\beta^4 + 490\beta^6 + 210\beta^8\right) \text{ArcCoth}\left[\sqrt{1+\beta^2}\right] \\ & -1575\beta^2\left(1+\beta^2\right)^{3/2}\left(160\beta^4 + 480\beta^6 + 480\beta^8 + 160\beta^{10}\right) \text{ArcCoth}\left[\sqrt{1+\beta^2}\right]^2 \end{aligned} \tag{A.12}$$

$$\begin{aligned} A_{13} = {} & \sqrt{1+\beta^2}\left(7296\beta^2 + 41376\beta^4 + 143840\beta^6 + 244160\beta^8 + 184800\beta^{10} + 50400\beta^{12}\right) \\ & -480\beta^2\left(1+\beta^2\right)^2\left(6 + 57\beta^2 + 322\beta^4 + 490\beta^6 + 210\beta^8\right) \text{ArcCoth}\left[\sqrt{1+\beta^2}\right] \\ & -1575\beta^2\left(1+\beta^2\right)^{3/2}\left(-32\beta^4 - 96\beta^6 - 96\beta^8 - 32\beta^{10}\right) \text{ArcCoth}\left[\sqrt{1+\beta^2}\right]^2 \end{aligned} \tag{A.13}$$

$$A_{14} = \sqrt{1+\beta^2}\left(-6300 + 53200\beta^2 + 197575\beta^4 + 223125\beta^6 + 86625\beta^8\right)$$
$$-525\beta^2\left(254 + 975\beta^2 + 1458\beta^4 + 1070\beta^6 + 330\beta^8\right)\mathrm{ArcCoth}\left[\sqrt{1+\beta^2}\right]$$
$$-1575\beta^2\left(1+\beta^2\right)^{3/2}\left(-40 - 120\beta^2 - 105\beta^4 - 55\beta^6\right)\mathrm{ArcCoth}\left[\sqrt{1+\beta^2}\right]^2 \tag{A.14}$$

$$A_{15} = 40\beta + 60\beta^3 + 15\beta\left(1+\beta^2\right) - 45\beta^3\sqrt{1+\beta^2}\mathrm{ArcCoth}\left[\sqrt{1+\beta^2}\right]$$
$$-30\beta\left(1+\beta^2\right)^{3/2}\mathrm{ArcCoth}\left[\sqrt{1+\beta^2}\right] \tag{A.15}$$

$$A_{16} = \left[-\frac{6A_{15}}{7A_1^2} - 2\beta\right]\Big/\left[\frac{12}{7A_1^2} - 2\beta\right] \tag{A.16}$$

$$A_{17} = \dot{A}_{16} \tag{A.17}$$

$$A_{18} = \left[\frac{6A_{15}}{35A_1^2} + \frac{2\beta}{5}\right]\Big/\left[-\frac{6}{35A_1} + \frac{2}{5}\left(1+\beta^2\right)\right] \tag{A.18}$$

$$A_{19} = \dot{A}_{18} \tag{A.19}$$

B. Abbreviations E_i

Here the abbreviations E_1–E_{14}, defined in Eqs. (6.77)–(6.79), are introduced:

$$E_1 = 15 + \frac{1}{2}\left(227 + 60\log\left[2/\beta\right]\right)\beta^2 \tag{B.1}$$

$$E_2 = \frac{1}{36}\left(212 + 60\log\left[2/\beta\right]\right) + \frac{\beta^2}{324}\left(-76 + 30\left[2/\beta\right]\right)^2 + \frac{\beta^2}{72}\left(-14034 + 14500\log\left[2/\beta\right] - 974.68\log\left[2/\beta\right]^2\right) \tag{B.2}$$

$$E_3 = \frac{1}{9}\left(76 + 30\log\left[2/\beta\right]\right)\beta \tag{B.3}$$

$$E_4 = 15 + \left(327 + 135\log\left[2/\beta\right]\right)\beta^2 \tag{B.4}$$

$$E_5 = \frac{35}{24}\left(-13 + 12\log\left[2/\beta\right]\right) + \frac{35\beta^2}{24}\left(-59 + 60\log\left[2/\beta\right]\right) \tag{B.5}$$

$$E_6 = -76\beta - 798\beta^2 + 30\beta\log\left[2/\beta\right] + 315\beta^2\log\left[2/\beta\right] \tag{B.6}$$

$$E_7 = -53 - \frac{1911\beta}{2} - \frac{26899\beta^2}{2} + 15\log\left[2/\beta\right] + 315\log\left[2/\beta\right]\beta + 255\log\left[2/\beta\right]^2 \tag{B.7}$$

$$E_8 = -38\beta - 399\beta^2 + 15\beta\log\left[2/\beta\right] + \frac{315}{2}\beta^2\log\left[2/\beta\right] \tag{B.8}$$

$$E_9 = \frac{525}{2\beta^2\left(-76 + 30\log\left[2/\beta\right]\right)} + \frac{175\left(33.722 - 22.104\log\left[2/\beta\right]\right)^3}{24\left(-76 + 30\log\left[2/\beta\right]\right)^2} + \frac{175\beta^2\left(72.583 - 54.881\log\left[2/\beta\right]\right)^4}{96\left(-76 + 30\log\left[2/\beta\right]\right)^3} \tag{B.9}$$

$$E_{10} = \frac{15\left(-409 + 120\log\left[2/\beta\right]\right)}{-76 + 30\log\left[2/\beta\right]} - \frac{75\beta^2\left(64.122 - 31.87\log\left[2/\beta\right]\right)^3}{2\left(-76 + 30\log\left[2/\beta\right]\right)^2} \tag{B.10}$$

List of Publications

1. I. Vidanović, A. Balaž, H. Al-Jibbouri, and A. Pelster:
   Nonlinear BEC Dynamics Induced by a Harmonic Modulation of the s-wave Scattering Length;
   Phys. Rev. A **84**, 013618 (2011).

2. I. Vidanović, H. Al-Jibbouri, A. Balaž, and A. Pelster:
   Parametric and Geometric Resonances of Collective Oscillation Modes in Bose-Einstein Condensates;
   Proceedings of the III International School and Conference on Photonics August 29 - September 2, 2011, Belgrade, Serbia;
   Phys. Scr. T **149**, 014003 (2012).

3. H. Al-Jibbouri, I. Vidanović, A. Balaž, and A. Pelster:
   Geometric Resonances in Bose-Einstein Condensates with Two- and Three-Body Interactions;
   J. of Phys. B **46**, 065303 (2013).

4. H. Al-Jibbouri and A. Pelster:
   Breakdown of Kohn Theorem Near Feshbach Resonance in Magnetic Trap;
   Phys. Rev. A **88**, 033621 (2013).

5. H. Al-Jibbouri, A. Balaž, and A. Pelster:
   Collective Excitations of a Bose-Einstein Condensate with a Single Vortex;
   In preparation.

Bibliography

[1] S. Bose, Plancks Gesetz und Lichtquantenhypothese, *Z. Phys* **26**, 178 (1924).

[2] A. Einstein. Quantentheorie des einatomigen idealen Gases. *Sitzungsbericht der Preussichen Akademie der Wissenschaften, Physikalisch-mathematische Klasse* p. 3 (1925).

[3] P. Kapitza, Viscosity of liquid helium below the λ-point, *Nature* **141**, 74 (1938).

[4] J. F. Allen and A. D. Misener, Flow of liquid helium II, *Nature* **141**, 75 (1938).

[5] F. London, The λ-Phenomenon of Liquid Helium and the Bose-Einstein Degeneracy, *Nature* **141**, 643 (1938).

[6] F. London, On the Bose-Einstein Condensation, *Phys. Rev.* **54**, 947 (1938).

[7] O. Penrose and L. Onsager, Bose-Einstein Condensation and Liquid Helium, *Phys. Rev.* **104**, 576 (1956).

[8] T. R. Sosnick, W. M. Snow, and P. E. Sokol, Deep-inelastic neutron scattering from liquid ^{4}He, *Phys. Rev. B* **41**, 11185 (1990).

[9] D. M. Ceperley, Path integrals in the theory of condensed helium, *Rev. Mod. Phys.* **67**, 279 (1995).

[10] N. N. Bogoliubov, On the theory of superfluidity, *J. Phys. (USSR)* **11**, 23 (1947).

[11] L. D. Landau, The theory of superfluidity of helium II, *J. Phys. USSR* **5**, 71 (1941).

[12] R. P. Feynman. Atomic theory of the 2-fluid model of liquid helium. *Phys. Rev.* **94**, 262 (1954).

[13] L. D. Landau and E. M. Lifshitz, *Statistical Physics*, Part I, (Pergamon Press, 1980).

[14] O. Penrose, On the quantum mechanics of helium II, *Philos. Mag.* **42**, 1373 (1951).

[15] L. Onsager, Statistical hydrodynamics, *Nuovo Cimento* **6**, 279 (1949).

[16] R. P. Feynman. *Progress in Low Temperature Physics* (North-Holland Amsterdam, 1955).

[17] H. E. Hall and W. F. Vinen, The Rotation of Liquid Helium II. II. The Theory of Mutual Friction in Uniformly Rotating Helium II, *Proc. R. Soc. A* **238**, 215 (1956).

[18] R. Packard and T. M. Sanders, Observations of Single Vortex Lines in Rotating Superfluid Helium, *Phys. Rev. A* **6**, 799 (1972).

[19] M. R. Matthews, B. P. Anderson, P. C. Haljan, D. S. Hall, C. E. Wieman and E. A. Cornell, Vortices in a Bose-Einstein Condensate, *Phys. Rev. Lett.* **83**, 2498 (1999).

[20] M. H. Anderson, J. R. Ensher, M. R. Matthews, C. E. Wieman, and E. A. Cornell, Observation of Bose-Einstein Condensation in a Dilute Atomic Vapor, *Science* **269**, 198 (1995).

[21] D. S. Jin, M. R. Matthews, J. R. Ensher, C. E. Wieman, and E. A. Cornell, Temperature-Dependent Damping and Frequency Shifts in Collective Excitations of a Dilute Bose-Einstein Condensate, *Phys. Rev. Lett.* **78**, 764 (1997).

[22] K. B. Davis, M. O. Mewes, M. R. Andrews, N. J. van Druten, D. S. Durfee, D. M. Kurn, and W. Ketterle, Bose-Einstein Condensation in a Gas of Sodium Atoms, *Phys. Rev. Lett.* **75**, 3969 (1995).

[23] C. C. Bradley, C. A. Sackett, J. J. Tollett, and R. G. Hulet, Evidence of Bose-Einstein Condensation in an Atomic Gas with Attractive Interactions, *Phys. Rev. Lett.* **75**, 1687 (1995).

[24] C. C. Bradley, C. A. Sackett, and R. G. Hulet, Bose-Einstein Condensation of Lithium: Observation of Limited Condensate Number, *Phys. Rev. Lett.* **78**, 985 (1997).

[25] S. Chu, Nobel Lecture: The manipulation of neutral particles, *Rev. Mod. Phys.* **70**, 685 (1998).

[26] C. N. Cohen-Tannoudji, Nobel Lecture: Manipulating atoms with photons, *Rev. Mod. Phys.* **70**, 707 (1998).

[27] W. D. Phillips, Nobel Lecture: Laser cooling and trapping of neutral atoms, *Rev. Mod. Phys.* **70**, 721 (1998).

[28] D. G. Fried, T. C. Killian, L. Willmann, D. Landhuis, S. C. Moss, D. Kleppner, and T. J. Greytak, Bose-Einstein condensation of atomic hydrogen. *Phys. Rev. Lett.* **81**, 3811 (1998).

[29] JILA BEC Homepage, `http://jilawww.colorado.edu/bec/`

[30] F. P. D. Santos, J. Léonard, J. Wang, C. J. Barrelet, F. Perales, E. Rasel, C. S. Unnikrishnan, M. Leduc, and C. N. Cohen-Tannoudji, Bose-Einstein Condensation of Metastable Helium, *Phys. Rev. Lett.* **86**, 3459 (2001).

[31] G. Modugno, G. Ferrari, G. Roati, R. J. Brecha, A. Simoni, and M. Inguscio, Bose-Einstein Condensation of Potassium Atoms by Sympathetic Cooling, *Science* **294**, 1320 (2001).

[32] T. Weber, J. Herbig, M. Mark, H. Nägerl, and R. Grimm, Bose-Einstein Condensation of Cesium, *Science* **299**, 232 (2003).

[33] T. Yosuke, M. Kenichi, K. Kaduki, T. Tetsushi, H. Kazuhito, K. Mitsutaka, Y. Tsutomu, and T. Yoshiro, Spin-Singlet Bose-Einstein Condensation of Two-Electron Atoms, *Phys. Rev. Lett.* **91**, 040404 (2003).

[34] S. Kraft, F. Vogt, O. Appel, F. Riehle, and U. Sterr, Bose-Einstein Condensation of Alkaline Earth Atoms, ^{40}Ca, *Phys. Rev. Lett.* **103**, 130401 (2009).

[35] S. Stellmer, M. K. Tey, B. Huang, R. Grimm, and F. Schreck, Bose-Einstein Condensation of Strontium, *Phys. Rev. Lett.* **103**, 200401 (2009).

[36] Y. N. M. de Escobar, P. G. Mickelson, M. Yan, B. J. DeSalvo, S. B. Nagel, and T. C. Killian, Bose-Einstein Condensation of ^{84}Sr, *Phys. Rev. Lett.* **103**, 200402 (2009).

[37] A. Griesmaier, J. Werner, S. Hensler, J. Stuhler, and T. Pfau, Bose-Einstein Condensation of Chromium, *Phys. Rev. Lett.* **94**, 160401 (2005).

[38] M. Lu, N. Q. Burdick, S. H. Youn, and B. L. Lev, Strongly Dipolar Bose-Einstein Condensate of Dysprosium, *Phys. Rev. Lett.* **107**, 190401 (2011).

[39] K. Aikawa, A. Frisch, M. Mark, S. Baier, A. Rietzler, R. Grimm, and F. Ferlaino, Bose-Einstein Condensation of Erbium, *Phys. Rev. Lett.* **108**, 210401 (2012).

[40] P. Courteille, R. Freeland, D. Heinzen, F. van Abeelen, and B. Verhaar, Observation of a Feshbach Resonance in Cold Atom Scattering, *Phys. Rev. Lett.* **81**, 69 (1998).

[41] S. Inouye, M. Andrews, J. Stenger, H. J. Miesner, S. Stamper-Kurn, and W. Ketterle, Observation of Feshbach resonances in a Bose-Einstein condensate, *Nature* **392**, 151 (1998).

[42] S. Kato, S. Sugawa, K. Shibata, R. Yamamoto, and Y. Takahashi, Resonant Control of Interaction Between Different Electronic States, *Phys. Rev. Lett.* **110**, 173201 (2013) .

[43] G. Baym and C. J. Pethick, Ground-State Properties of Magnetically Trapped Bose-Condensed Rubidium Gas, *Phys. Rev. Lett.* **76**, 6 (1996).

[44] M. Edwards, P. A. Ruprecht, K. Burnett, R. J. Dodd, and C. W. Clark, Collective Excitations of Atomic Bose-Einstein Condensates, *Phys. Rev. Lett.* **77**, 1671 (1996).

[45] D. S. Rokhsar, Vortex Stability and Persistent Currents in Trapped Bose Gases, *Phys. Rev. Lett.* **79**, 2164 (1997).

[46] D. S. Jin, J. R. Ensher, M. R. Matthews, C. E. Wieman, and E. A. Coernell, Collective Excitations of a Bose-Einstein Condensate in a Dilute Gas, *Phys. Rev. Lett.* **77**, 420 (1996).

[47] E. P. Gross, Structure of a quantized vortex in boson systems *Nuovo Cimento* **20**, 454 (1961).

[48] L. P. Pitaevskii, Vortex Lines in an Imperfect Bose Gases, *Zh. Eksp. Teor. Fiz.* **40**, 646 (1961). *Sov. Phys. JETP.* **13**, 451 (1961).

[49] L. Pitaevskii and S. Stringari, *Bose-Einstein Condensation* (Oxford University Press, Oxford, 2003).

[50] C. J. Pethick and H. Smith, *Bose-Einstein Condensation in Dilute Gases*, Second edition (Cambridge University Press, Cambridge, 2008).

[51] M. Edwards and K. Burnett, Numerical Solution of the Nonlinear Schrödinger Equation for Small Samples of Trapped Neutral Atoms, *Phys. Rev. A.* **51**, 1382 (1995).

[52] C. Sulem and P. L. Sulem, *The Nonlinear Schrödinger Equation* (Springer, Berlin, 1999).

[53] R. J. Marshall, G. H. C. New, K. Burnett, and S. Choi, Exciting, Cooling, and Vortex Trapping in a Bose-Condensed Gas, *Phys. Rev. A* **59**, 2085 (1999).

[54] A. Griffen, Conserving and Gapless Approximations for an Inhomogeneous Bose Gas at Finite Temperatures, *Phys. Rev B* **53**, 9341 (1996).

[55] N. P. Proukakis and K. Burnett, Theory of Bose-Einstein Condensation for Trapped Atoms, *Phil. Trans. R. Soc. Lond. A* **355**, 2235 (1997).

[56] N. P. Proukakis, K. Burnett and H. T. C. Stoof, Microscopic Treatment of Binary Interactions in the Nonequilibrium Dynamics of Partially Bose-Condensed Trapped Gases, *Phys. Rev. A* **57**, 1230 (1998).

[57] S. A. Morgan, A Gapless Theory of Bose-Einstein Condensation in Dilute Gases at Finite Temperature, *J. Phys. B: At. Mol. Opt. Phys.* **33**, 3847 (2000).

[58] K. Xu, Y. Liu, D. E. Miller, J. K. Chin, W. Setiawan, and W. Ketterle, Observation of Strong Quantum Depletion in a Gaseous Bose-Einstein Condensate, *Phys. Rev. Lett.* **96**, 180405 (2006).

[59] A. R. P. Lima, A. Pelster, Quantum Fluctuations in Dipolar Bose Gases, *Phys. Rev. A* **84**, 041604(R) (2011).

[60] A. R. P. Lima and A. Pelster, Beyond Mean-Field Low-Lying Excitations of Dipolar Bose Gases, *Phys. Rev. A* **86**, 063609 (2012).

[61] J. M. Gerton, D. Strekalov, I. Prodan, and R. G. Hulet, Direct Observation of Growth and Collapse of a Bose-Einstein Condensate with Attractive Interactions, *Nature* **408**, 692 (2000).

[62] S. L. Cornish, N. R. Claussen, J. L. Roberts, E. A. Cornell, and C. E. Wieman, Stable ^{85}Rb Bose-Einstein Condensates with Widely Tunable Interactions, *Phys. Rev. Lett.* **85**, 1795 (2000).

[63] J. L. Roberts, N. R. Claussen, S. L. Cornish, E. A. Donley, E. A. Cornell, and C. E. Wieman, Controlled Collapse of a Bose-Einstein Condensate, *Phys. Rev. Lett.* **86**, 4211 (2001).

[64] D. M. Stamper-Kurn, H.-J. Miesner, S. Inouye, M. R. Anderws, and W. Ketterle, Collisionless and Hydrodynamic Excitations of a Bose-Einstein Condensate, *Phys. Rev. Lett.* **81**, 500 (1998).

[65] M.-O. Mewes, M. R. Andrews, N. J. van Druten, D. M. Kurn, D. S. Durfee, C. G. Townsend, and W. Ketterle, Collective Excitations of a Bose-Einstein Condensate in a Magnetic Trap, *Phys. Rev. Lett.* **77**, 988 (1996).

[66] F. Chevy, V. Bretin, P. Rosenbusch, K. W. Madison, and J. Dalibard, Transverse Breathing Mode of an Elongated Bose-Einstein Condensate, *Phys. Rev. Lett.* **88**, 250402 (2002).

[67] H. Ott, J. Fortágh, S. Kraft, A. Günther, D. Komma, and C. Zimmermann, Nonlinear Dynamics of a Bose-Einstein Condensate in a Magnetic Waveguide, *Phys. Rev. Lett.* **91**, 040402 (2003).

[68] MIT BEC Homepage, `http://www.rle.mit.edu/cua\_pub/ketterle\_group/Projects\_1998/Coll\_exc/Collective\_excitations.htm`

[69] Y. Lu, W. Xiao-Rui, L. Ke, T. Xin-Zhou, X. Hong-Wei, and L. Bao-Long, Low-Energy Collective Excitation of Bose-Einstein Condensates in an Anisotropic Magnetic Trap, *Chin. Phys. Lett.* **26**, 076701 (2009).

[70] S. Stringari, Collective Excitations of a Trapped Bose-Condensed Gas, *Phys. Rev. Lett.* **77**, 2360 (1996).

[71] M. Edwards, R. J. Dodd, C. W. Clark, and K. Burnett, Zero-Temperature Mean-Field Theory of Atomic Bose-Einstein Condensates, *J. Res. Nat. Inst. Stand. Technol.* **101**, 553 (1996).

[72] K. G. Singh and D. S. Rokhsar, Collective Excitations of a Confined Bose Condensate, *Phys. Rev. Lett.* **77**, 1667 (1996).

[73] L. You, W. Hoston, and M. Lewenstein, Low Energy Excitations of Trapped Bose Condensates, *Phys. Rev. A* **55**, R1581 (1997).

[74] W. Bao, D. Jaksch, and P. A. Markowich, Numerical Solution of the Gross-Pitaevskii Equation for Bose-Einstein Condensation, *J. Comput. Phys.* **187**, 318 (2003).

[75] W. Bao, S. Jin, and P. A. Markowich, Numerical Study of Time-Splitting Spectral Discretizations of Nonlinear Schrödinger Equations in the Semi-Classical Regimes, *SIAM J. Sci. Comput.* **25**, 27 (2003).

[76] P. Muruganandam and S. K. Adhikari, Numerical and Variational Solutions of the Dipolar Gross-Pitaevskii Equation in Reduced Dimensions, *Laser Phys.* **22**, 813 (2012).

[77] P. A. Ruprecht, M. J. Holland, K. Burrett, and M. Edwards, Time-Dependent Solution of the Nonlinear Schrödinger Equation for Bose-Condensed Trapped Neutral Atoms, *Phys. Rev. A* **51**, 4704 (1995).

[78] S. K. Adhikari, Collapse of Attractive Bose-Einstein Condensed Vortex States in a Cylindrical Trap, *Phys. Rev. E* **65**, 016703 (2002).

[79] S. K. Adhikari and P. Muruganandam, Bose-Einstein Condensation Dynamics from the Numerical Solution of the Gross-Pitaevskii Equation, *J. Phys. B.* **35**, 2831 (2002).

[80] D. Vudragovic, I. Vidanović, A. Balaž, P. Muruganandam, and S. K. Adhikari, C programs for solving the time-dependent Gross-Pitaevskii equation in a fully anisotropic trap, *J. Comput. Phys. Commun.* **183**, 2021 (2012).

[81] S. K. Adhikari, Numerical Solution of the Two-Dimensional Gross-Pitaevskii Equation for Trapped Interacting Atoms, *Phys. Lett. A* **265**, 91 (2000).

[82] S. K. Adhikari, Numerically study of the spherically symmetric Gross-Pitaevskii equation in two space dimensions, *Phys. Rev. E* **62**, 2937 (2000).

[83] W. Bao and W. J. Tang, Ground State Solution of Bose-Einstein Condensate by Directly Minimizing the Energy Functional, *J. Comput. Phys.* **187**, 230 (2003).

[84] V. M. Pérez-García, H. Michinel, J . I. Cirac, M. Lewenstein, and P. Zoller, Low Energy Excitations of a Bose-Einstein Condensate: A Time-Dependent Variational Analysis, *Phys. Rev. Lett.* **77**, 5320 (1996).

[85] V. M. Perez, H. Michinel, J. I. Cirac, M. Lewenstein, and P. Zoller, Dynamics of Bose-Einstein Condensates: Variational Solutions of the Gross-Pitaevskii Equations, *Phys. Rev. A* **56**, 1424 (1997).

[86] E. Tiesinga, B. J. Verhaar, and H. T. C. Stoof, Threshold and Resonance Phenomena in Ultracold Ground-State Collisions, *Phys. Rev. A* **47**, 4114 (1993).

[87] S. E. Pollack, D. Dries, M. Junker, Y. P. Chen, T. A. Corcovilos, and R. G. Hulet, Extreme Tunability of Interactions in a ^{7}Li Bose-Einstein Condensate, *Phys. Rev. Lett.* **102**, 090402 (2009).

[88] H. Feshbach, Unified Theory of Nuclear Reactions, *Ann. Phys. (New York)* **5**, 357 (1958).

[89] U. Fano, Effects of Configuration Interaction on Intensities and Phase Shifts, *Phys. Rev.* **124**, 1866 (1961).

[90] J. Stenger, S. Inouye, M. R. Andrewa, H.-J. Miesner, D. M. Stamper-Kurn, and W. Ketterle, Strongly Enhanced Inelastic Collisions in a Bose-Einstein Condensate near Feshbach Resonances, *Phys. Rev. Lett.* **82**, 2422 (1999).

[91] D. S. Petrov, C. Salomon, and G. V. Shlyapnikov, Weakly Bound Dimers of Fermionic Atoms, *Phys. Rev. Lett.* **93**, 090404 (2004).

[92] E. R. F. Ramos, E. A. L. Henn, J. A. Seman, M. A. Caracanhas, K. M. F. Magalhães, K. Helmerson, V. I. Yukalov, and V. S. Bagnato, Generation of Nonground-State Bose-Einstein Condensates by Modulating Atomic Interactions, *Phys. Rev. A* **78**, 063412 (2008).

[93] S. E. Pollack, D. Dries, R. G. Hulet, K. M. F. Magalhães, E. A. L. Henn, E. R. F. Ramos, M. A. Caracanhas, and V. S. Bagnato, Collective Excitation of a Bose-Einstein Condensate by Modulation of the Atomic Scattering Length, *Phys. Rev. A* **81**, 053627 (2010).

[94] C. Becker, S. Stellmer, P. Soltan-Panahi, S. Dorscher, M. Baumert, E.-M. Richter, J. Kronjager, K. Bongs, and K. Sengstock, Oscillations and Interactions of Dark and Dark-Bright Solitons in Bose-Einstein Condensates, *Nat. Phys.* **4**, 496 (2008).

[95] C. Hamner, J. J. Chang, P. Engels, and M. A. Hoefer, Generation of Dark-Bright Soliton Trains in Superfluid-Superfluid Counterlow, *Phys. Rev. Lett.* **106**, 065302 (2011).

[96] M. Faraday, On a Peculiar Class of Acoustical Figures; and on Certain Forms Assumed by a Group of Particles Upon Vibrating Elastic Surfaces, *Phil. Transac.* **121**, 299 (1831).

[97] M. C. Cross and P. C. Hohenberg, Pattern Formation Outside of Equilibrium, *Rev. Mod. Phys.* **65**, 851 (1993).

[98] J. P. Gollub and J. S. Langer, Pattern Formation in Nonequilibrium Physics, *Rev. Mod. Phys.* **71**, S396 (1999).

[99] A. Balaz and A. I. Nicolin, Faraday Waves in Binary Nonmiscible Bose-Einstein Condensates, *Phys. Rev. A* **85**, 023613 (2012).

[100] P. Engels, C. Atherton, and M. A. Hoefer, Observation of Faraday Waves in a Bose-Einstein Condensate, *Phys. Rev. Lett.* **98**, 095301 (2007).

[101] E. A. L. Henn, J. A. Seman, G. Roati, K. M. F. Magalhes, and V. S. Bagnato, Emergence of Turbulence in an Oscillating Bose-Einstein Condensate, *Phys. Rev. Lett.* **103**, 045301 (2009).

[102] M. Edwards, P. A. Ruprecht, K. Burnett, R. J. Dodd, and C. W. Clark, Collective Excitations of Atomic Bose-Einstein Condensates, *Phys. Rev. Lett.* **77**, 1671 (1996).

[103] Y. Castin and R. Dum, Bose-Einstein Condensates in Time Dependent Traps, *Phys. Rev. Lett.* **77**, 5315 (1996).

[104] J. J. García-Ripoll, V. M. Pérez-García, and P. Torres, Extended Parametric Resonances in Nonlinear Schrödinger Systems, *Phys. Rev. Lett.* **83**, 1715 (1999).

[105] F. Dalfovo, C. Minniti, and L. Pitaevskii, Frequency Shift and Mode Coupling in the Nonlinear Dynamics of a Bose-Condensed Gas, *Phys. Rev. A.* **56**, 4855 (1997).

[106] J. J. García-Ripoll and V. M. Pérez-García, Barrier Resonances in Bose-Einstein Condensation, *Phys. Rev. A* **59**, 2220 (1999).

[107] A. I. Nicolin, Resonant Wave Formation in Bose-Einstein Condensates, *Phys. Rev. E* **84**, 056202 (2011).

[108] S. Sabari, R. V. J. Raja, K. Porsezian, and P. Muruganandam, *J. Phys. B: At. Mol. Opt. Phys.* **43**, 125302 (2010).

[109] I. Vidanović, A. Balaž, H. Al-Jibbouri, and A. Pelster, Nonlinear BEC Dynamics Induced by a Harmonic Modulation of the s-wave Scattering Length, *Phys. Rev. A* **84**, 013618 (2011).

[110] A. I. Nicolin, Faraday Waves in Bose-Einstein Condensates Subject to Anisotropic Transverse Confinement, *Rom. Rep. Phys.* **63**, 1329 (2011).

[111] W. Cairncross, A. Pelster, Parametric Resonance in Bose-Einstein Condensates, `arXiv:1209.3148`.

[112] I. Vidanović, H. Al-Jibbouri, A. Balaž, and A. Pelster, Parametric and Geometric Resonances of Collective Oscillation Modes in Bose-Einstein Condensates, *Phys. Scr. T* **149**, 014003 (2012).

[113] H. Al-Jibbouri, I. Vidanović, A. Balaž, and A. Pelster, Geometric Resonances in Bose-Einstein Condensates with Two- and Three-Body Interactions, *J. Phys B* **46**, 065303 (2013).

[114] G. Hechenblaikner, O. M. Maragò, E. Hodby, J. Arlt, S. Hopkins, and C. J. Foot, Observation of Harmonic Generation and Nonlinear Coupling in the Collective Dynamics of a Bose-Einstein Condensate, *Phys. Rev. Lett.* **85**, 692 (2000).

[115] G. Hechenblaikner, S. A. Morgan, E. Hodby, O. M. Maragò, and C. J. Foot, Calculation of Mode Coupling for Quadrupole Excitations in a Bose-Einstein Condenstate, *Phys. Rev. A.* **65**, 033612 (2002).

[116] L. Pitaevskii and S. Stringari, Landau Damping in Dilute Bose Gases, *Phys. Lett. A* **235**, 398 (1997).

[117] L. Pitaevskii, Phenomenological Theory of Mode Collapse-Revival in a Confined Bose Gas, *Phys. Lett. A.* **229**, 406 (1997).

[118] R. Graham, D. F. Walls, and M. J. Collett, Collapses and Revivals of Collective Excitations in Trapped Bose Condensates, *Phys. Rev. A* **57**, 503 (1998).

[119] Y. Zhou, W. Wen, and H. Guoxiang, Frequency Shift and Mode Coupling of the Collective Modes of Superfluid Fermi Gases in the BCS-BEC Crossover, *Phys. Rev. B* **77**, 104527 (2008).

[120] K. Kasamatsu, M. Tsubota, and M. Ueda, Quadrupole and Scissors Modes and Nonlinear Mode Coupling in Trapped Two-Component Bose-Einstein Condensates, *Phys. Rev. A* **69**, 043621 (2004).

[121] E. R. F. Ramos, F. E. A. dos Santos, M. A. Caracanhas, and V. S. Bagnato, Coupling Collective Modes in a Trapped Superfluid, *Phys. Rev. A* **85**, 033608 (2012).

[122] H. Al-Jibbouri and A. Pelster, Breakdown of Kohn Theorem Near Feshbach Resonance, `arXiv:1306.1988`.

[123] F. Dalfovo, C. Minniti, S. Stringari, and L. Pitaevskii, Nonlinear Dynamics of a Bose Condensed Gas, *Phys. Lett. A* **227**, 259 (1997).

[124] A. E. Leanhardt, A. P. Chikkatur, D. Kielpinski, Y. Shin, T. L. Gustavson, W. Ketterle, and D. E. Pritchard, Propagation of Bose-Einstein Condensates in a Magnetic Waveguide, *Phys. Rev. Lett.* **89**, 040401 (2002).

[125] W. Zhang, E. M. Wright, H. Pu, and P. Meystre, Fundamental Limit for Integrated Atom Optics with Bose-Einstein Condensates, *Phys. Rev. A* **68**, 023605 (2003).

[126] A. X. Zhang and J. K. Xue, Band Structure and Stability of Bose-Einstein Condensates in Optical Lattices with Two- and Three-Atom Interactions, *Phys. Rev. A* **75**, 013624 (2007).

[127] T. Köhler, Three-Body Problem in a Dilute Bose-Einstein Condensate, *Phys. Rev. Lett.* **89**, 210404 (2002).

[128] B. L. Tolra, K. M. O'Hara, J. H. Huckans, W. D. Phillips, S. L. Rolston, and J. V. Porto, Observation of Reduced Three-Body Recombination in a Correlated 1D Degenerate Bose Gas, *Phys. Rev. Lett.* **92**, 190401 (2004).

[129] N. Akhmediev, M. P. Das, and A. V. Vagov, Bose-Einstein Condensation of Atoms with Attarctive Interaction, *Int. J. Mod. Phys. B* **13**, 625 (1999).

[130] A. Gammal, T. Frederico, L. Tomio, and P. Chomaz, Atomic Bose-Einstein Condensation with Three-Body Interactions and Collective Excitations, *J. Phys. B* **33**, 4053 (2000).

[131] F. K. Abdullaev, A. Gammal, L. Tomio, and T. Frederico, Stability of Trapped Bose-Einstein Condensates, *Phys. Rev. A* **63**, 043604 (2001).

[132] S. P. Tewari, P. Silotia, A. Saxena, and L. K. Gupta, Effect of Incorporating Three-Body Interaction in the Low-Density Energy Expansion of Bose-Einstein Condensate of ^{87}Rb Atoms Trapped in a Harmonic Potential, *Phys. Lett. A* **359**, 658 (2006).

[133] E. Wamba, A. Mohamadou, and T. C. Kofane, A Variational Approach to the Modulational Instability of a Bose-Einstein Condensate in a Parabolic Trap, *J. Phys. B: At. Mol. Opt. Phys.* **41**, 225403 (2008).

[134] F. K. Abdullaev and M. Salerno, Gap-Townes Solitons and Localized Excitations in Low-Dimensional Bose-Einstein Condensates in Optical Lattices, *Phys. Rev. A* **72**, 033617 (2005)

[135] C. Bo-Lun, H. Xiao-Bin, and K. Su-Peng, Mott-Hubbard Transition of Bosons in Optical Lattices with Three-Body Interactions, *Phys. Rev. A* **78**, 043603 (2008).

[136] Y. Chen, K.-Z. Zhang and Y. Chen, Dynamic Behaviour of Bose-Einstein Condensates in Optical Lattices with Two- and Three-Body Interactions, *J. Phys. B: At. Mol. Opt. Phys.* **42**, 185302 (2009).

[137] K. Zhou, Z. Liang, and Z. Zhang, Quantum Phases of a Dipolar Bose-Einstein Condensate in an Optical Lattice with Three-Body Interaction, *Phys. Rev. A* **82**, 013634 (2010).

[138] J. Silva-Valencia and A. M. C. Souza, First Mott Lobe of Bosons with Local Two- and Three-Body Interactions, *Phys. Rev. A* **84**, 065601 (2011)

[139] M. Singh, A. Dhar, T. Mishra, R. V. Pai, and B. P. Das, Three Body on-Site Interactions in Ultracold Bosonic Atoms in Optical Lattices and Superlattices, *Phys. Rev. A* **85**, 051604 (2012).

[140] A. Safavi-Naini, J. v. Stecher, B. Capogrosso-Sansone, and S. T. Rittenhouse, First Order Phase Transitions in Optical Lattices with Tunable Three-Body Onsite Interaction, *Phys. Rev. Lett.* **109**, 135302 (2012).

[141] B. Huang, S. Wan, Excitation Spectrum and Momentum Distribution of Bose-Hubbard Model with On-Site Two- and Three-body Interaction, `ArXiv:1212.3762`.

[142] R. Dasgupta, Effects of Three-Body Scattering Processes on BCS-BEC Crossover, *Phys. Rev. A* **82**, 063607 (2010).

[143] U. Roy, R. Atre, C. Sudheesh, C. N. Kumar, and P. K. Panigrahi, Complex Solitons in Bose-Einstein Condensates with Two- and Three-Body Interactions, *J. Phys. B: At. Mol. Opt. Phys.* **43**, 025003 (2010).

[144] A. Mohamadou, E. Wamba, D. Lissouck, and T. C. Kofane, Dynamics of Kink-Dark Solitons in Bose-Einstein Condensates with Both Two- and Three-Body Interactions, *Phys. Rev. E* **85**, 046605 (2012).

[145] M. Juan, L. Zhi, and X. Ju-Kui, Critical Rotation of an Anharmonically Trapped BoseEinstein Condensate, *J. Chin. Phys. B* **18**, 4122 (2009).

[146] M. S. Mashayekhi, J.-S. Bernier, D. Borzov, J.-L. Song, and F. Zhou, Two-Dimensional Bose Gases Near Resonance: Universal Three-Body Effects, *Phys. Rev. Lett.* **110**, 145301 (2013).

[147] Y. Wang, J. Wang, J. P. D'Incao, and C. H. Greene, Universal Three-Body Parameter in Heteronuclear Atomic Systems, *Phys. Rev. Lett.* **109**, 243201 (2012).

[148] L. Guan-Qiang, F. Li-Bin, X. Ju-Kui, C. Xu-Zong, and L. Jie, Collective Excitations of a Bose-Einstein Condensate in an Anharmonic Trap, *Phys. Rev. A* **74**, 055601 (2006).

[149] H. Ji-Xuan, Collective Excitations of a 1D Bose-Einstein Condensate in an Anharmonic Trap, *Phys. Lett. A* **368**, 366 (2007).

[150] L. Guan-Qiang, P. Ping, L. Jian-Ke, and X. Ju-Kui, Collective Excitations and Nonlinear Dynamics of 1D BEC with Two- and Three-body Interactions in Anharmonic Traps, *Commun. Theor. Phys.* **50**, 1129 (2008).

[151] L. Hao-Cai, C. Hai-Jun, and X. Ju-Kui, Bose-Einstein Condensates with Two- and Three-Body Interactions in an Anharmonic Trap at Finite Temperature *Chin. Phys. Lett.* **27**, 030304 (2010).

[152] Y. Wen-Mei, W. Xiu-Fang, Z. Xiao-Yan, and X. Ju-Kui, Stability and Collective Excitation of Two-Dimensional BECs with Two- and Three-Body Interactions in an Anharmonic Trap, *Commun. Theor. Phys.* **51**, 433 (2009).

[153] P. Ping and L. Guan-Qiang, Effects of Three-Body Interaction on Collective Excitation and Stability of Bose-Einstein Condensate, *Chin. Phys. B* **18**, 3221 (2009).

[154] P. A. Ruprecht, M. J. Holland, K. Burnett, and M. Edwards, Time-Dependent Solution of the Nonlinear Schrödinger Equation for Bose-Condensed Trapped Neutral Atoms, *Phys. Rev. A* **51**, 4704 (1995).

[155] M. Edwards and K. Burentt, Numerical Solution of the Nonlinear Schrödinger Equation for Small Samples of Trapped Neutral Atoms, *Phys. Rev. A* **51**, 1382 (1995).

[156] J. Weiner, V. S. Bagnato, S. Zilio, and P. S. Julienne, Experiments and Theory in Cold and Ultracold Collisions, *Rev. Mod. Phys.* **71**, 1 (1999).

[157] Y. Kagen, A. E. Murshev, G. V. Shyapnikov, and J. T. M. Walraven, Bose-Einstein Condensation in Trapped Atomic Gases, *Phys. Rev. Lett.* **76**, 2670 (1996).

[158] A. Gammal, T. Frederico, and L. Tomio, Critical Nnumber of Atoms for Attractive Bose-Einstein Condensates with Cylindrically Symmetrical Traps, *Phys. Rev. A* **64**, 055602 (2001).

[159] L. Tomio, V. S. Filho, A. Gammal, and T. Frederico, Stability of Atomic Condensed Systems with Attractive Two-Body Interactions, *Laser Physics* **13**, 582 (2003).

[160] A. Gammal, L. Tomio, and T. Frederico, Critical Numbers of Attractive Bose-Einstein Condensed Atoms in Asymmetric Traps, *Phys. Rev. A* **66**, 043619 (2002).

[161] A. G. de Sousa, A. B. F. da Silva, G. C. Marques, and V. S. Bagnato, Influence of confining anisotropy on the unstable behavior of a Bose gas with attractive interaction, *Phys. Rev. A* **70**, 063608 (2004).

[162] A. G. de Sousa, V. S. Bagnato, and A. B. F. da Silva, An Analytical Solution for the Critical Number of Particles for Stable Bose-Einstein Condensation Under the Influence of an Anisotropic Potential, *Brazilian J. Phys.* **38**, 1 (2008).

[163] S. F. Victo, A. Gammal, and L. Tomio, Effect of Anharmonicities in the Critical Number of Trapped Condensed Atoms with an Attractive Two-Body Interaction, *Phys. Rev. A* **66**, 043605 (2002).

[164] S. F. Victo, T. Frederico, A. Gammal, and L. Tomio, Stability of the Trapped Nonconservative Gross-Pitaevskii Equation with Attractive Two-Body Interaction, *Phys. Rev. E* **66**, 036225 (2002).

[165] M. Houbiers and H. T. C. Stoof, Stability of Bose condensed Atomic ^{7}Li, *Phys. Rev. A* **54**, 5055 (1996).

[166] A. Gammal, T. Frederico, and L. Tomio, Improved Numerical Approach for the Time-Independent Gross-Pitaevskii Nonlinear Schrödinger Equation, *Phys. Rev. E* **60**, 2421 (1999).

[167] P. G. Saffman, *Vortex Dynamics* (Cambridge University Press, Cambridge, 1992).

[168] R. J. Donnelly, *Quantized Vortices in Helium II* (Cambridge University Press, Cambridge, 1991).

[169] K. W. Madison, F. Chevy, W. Wohlleben, and J. Dalibard, Vortex Formation in a Stirred Bose-Einstein Condensate, *Phys. Rev. Lett.* **84**, 806 (2000).

[170] Y. Shin, M. Saba, M. Vengalattore, T. A. Pasquini, C. Sanner, A. E. Leanhardt, M. Prentiss, D. E. Pritchard, and W. Ketterle, Dynamical Instability of a Doubly Quantized Vortex in a Bose-Einstein Condensate, *Phys. Rev. Lett.* **93**, 160406 (2004).

[171] L. Crasovan, V. Vekslerchik, V. M. Pérez-García, J. P. Torres, D. Mihalache, and L. Torner, Stable Vortex Dipoles in Nonrotating Bose-Einstein Condensates, *Phys. Rev. A* **68**, 063609 (2003).

[172] Q. Zhou and H. Zhai, Vortex Dipole in a Trapped Atomic Bose-Einstein Condensate, *Phys. Rev. A* **70**, 043619 (2004).

[173] B. P. Anderson, P. C. Haljan, C. A. Regal, D. L. Feder, L. A. Collins, C. W. Clark and E. A. Cornell, Watching Dark Solitons Decay into Vortex Rings in a Bose-Einstein Condensate, *Phys. Rev. Lett.* **86**, 2926 (2001).

[174] J. R. Abo-Shaeer, C. Raman, J. M. Vogels, and W. Ketterle, Observation of Vortex Lattices in Bose-Einstein Condensates, *Science* **292**, 476 (2001).

[175] P. Rosenbusch, V. Bretin, and J. Dalibard, Dynamics of a Single Vortex Line in a Bose-Einstein Condensate, *Phys. Rev. Lett.* **89**, 200403 (2002).

[176] J. E. Williams, and M. J. Holland, Preparing Topological States of a Bose-Einstein Condensate, *Nature* **401**, 568 (1999).

[177] A. L. Fetter and A. Svidzinsky, Vortices in a Trapped Dilute Bose-Einstein Condensate, *J. Phys.: Cond. Matter* **13**, R135 (2001).

[178] K. Kasamatsu, M. Tsubota, and M. Ueda, Vortices in Multicomponent Bose-Einstein Condensates, *Int. J. Mod. Phys. B* **19**, 1835 (2005).

[179] A. L. Fetter, Rotating Trapped Bose-Einstein Condensates, *Rev. Mod. Phys.* **81**, 647 (2009).

[180] R. J. Dodd, Approximate Solutions of the Nonlinear Schrödinger Equation for Ground and Excited States of Bose-Einstein Condensates, *J. Res. Nat. Inst. Stand. Technol.* **101**, 545 (1996).

[181] X. Zhi-Jun and C. Ping-Gen, Ground State and Single Vortex for Bose Einstein Condensates in Anisotropic Traps, *Commun. Theor. Phys.* **47**, 1053 (2007).

[182] E. A. L. Henn, J. A. Seman, E. R. F. Ramos, M. Caracanhas, P. Castilho, E. P. Olímpio, G. Roati, D. V. Magalhães, K. M. F. Magalhães, and V. S. Bagnato, Observation of Vortex Formation in an Oscillating Trapped Bose-Einstein Condensate, *Phys. Rev. A* **79**, 043618 (2009)

[183] E. A. L. Henn, J. A. Seman, G. Roati, K. M. F. Magalhães, and V. S. Bagnato, Emergence of Turbulence in an Oscillating Bose-Einstein Condensate, *Phys. Rev. Lett.* **103**, 045301 (2009).

[184] T. K. Ghosh, Collective Excitation Frequencies and Vortices of a Bose-Einstein Condensed State with Gravity-Like Interatomic Attraction, *Phys. Rev. A* **65**, 053616 (2002).

[185] T. K. Ghosh, Vortex Formation in a Slowly Rotating Bose-Einstein Condensate Confined in a Harmonic-Plus-Gaussian Laser Trap, *Eur. Phys. J. D* **31**, 101 (2004).

[186] V. Bretin, S. Stock, Y. Seurin, and J. Dalibard, Fast Rotation of a Bose-Einstein Condensate, *Phys. Rev. Lett.* **92**, 050403 (2004).

[187] T. K. Ghosh, Vortex Formation in a Fast Rotating Bose-Einstein Condensate, *Phys. Rev. A* **69**, 043606 (2004).

[188] M. Juan, L. Zhi, and X. Ju-Kui, Critical Rotation of an Anharmonically Trapped Bose-Einstein Condensate, *Chin. Phys. B* **18**, 4412 (2009).

[189] L. Wen and X. Luo, Formation and Structure of Vortex Lattices in a Rotating Double-Well Bose-Einstein Condensate, *Laser Phys. Lett.* **9**, 618 (2012).

[190] S. Kobayashi, Y. Kawaguchi, M. Nitta, and M. Ueda, Topological Classification of Vortex-Core Structures of Spin-1 Bose-Einstein Condensates, *Phys. Rev. A* **86**, 023612 (2012).

[191] F. Dalfovo and S. Stringari, Bosons in Anisotropic Traps: Ground State and Vortices, *Phys. Rev. A* **53**, 2477 (1996).

[192] E. Lundh, C. J. Pethick, and H. Smith, Zero-Temperature Properties of a Trapped Bose-Condensed Gas: Beyond the Thomas-Fermi Approximation, *Phys. Rev. A* **55**, 2126 (1997).

[193] D. L. Feder, C. W. Clark, and B. I. Schneider, Vortex Stability of Interacting Bose-Einstein Condensates Confined in Anisotropic Harmonic Traps, *Phys. Rev. Lett.* **82**, 4956 (1999).

[194] K. W. Madison, F. Chevy, V. Bretin, and J. Dalibard, Stationary States of a Rotating Bose-Einstein Condensate: Routes to Vortex Nucleation, *Phys. Rev. Lett.* **86**, 4443 (2001).

[195] C. Raman, J. R. Abo-Shaeer, J. M. Vogels, K. Xu, and W. Ketterle, Vortex Nucleation in a Stirred Bose-Einstein Condensate, *Phys. Rev. Lett.* **87**, 210402 (2001).

[196] B. Jackson, J. F. McCann, and C. S. Adams, Vortex Line and Ring Dynamics in Trapped Bose-Einstein Condensates, *Phys. Rev. A* **61**, 013604 (1999).

[197] S. Yi and H. Pu, Vortex Structures in Dipolar Condensates, *Phys. Rev. A* **73**, 061602(R) (2006).

[198] R. M. W. van Bijnen, D. H. J. O'Dell, N. G. Parker, and A. M. Martin, Dynamical Instability of a Rotating Dipolar Bose-Einstein Condensate, *Phys. Rev. Lett.* **98**, 150401 (2007).

[199] R. M. Wilson, S. Ronen, and J. L. Bohn, Stability and Excitations of a Dipolar Bose-Einstein Condensate with a Vortex, *Phys. Rev. A* **79**, 013621 (2009).

[200] C. Yuce and Z. Oztas, Off-Axis Vortex in a Rotating Dipolar Bose-Einstein Condensate, *J. Phys. B: At. Mol. Opt. Phys.* **43**, 135301 (2010).

[201] D. H. J. O' Dell and C. Eberlein, Vortex in a Trapped Bose-Einstein Condensate with Dipole-Dipole Interactions, *Phys. Rev. A* **75**, 013604 (2007).

[202] C. Yuce, Critical Trap Aspect Ratios for Dipolar BEC, *Eur. Phys. J. D* **61**, 695 (2011).

[203] R. K. Kumar and P. Muruganandam, Vortex Dynamics of Rotating Dipolar Bose-Einstein Condensates, *J. Phys. B: At. Mol. Opt. Phys.* **45**, 215301 (2012).

[204] S. K. Adhikari, Dipolar Bose-Einstein Condensate in a Ring or in a Shell, *Phys. Rev. A* **85**, 053631 (2012).

[205] F. Zambelli and S. Stringari, Quantized Vortices and Collective Oscillations of a Trapped Bose-Einstein Condensate, *Phys. Rev. Lett.* **81**, 1754 (1998).

[206] M. Cozzini, A. L. Fetter, B. Jackson, and S. Stringari, Oscillations of a Bose-Einstein Condensate Rotating in a Harmonic Plus Quartic Trap, *Phys. Rev. Lett.* **94**, 100402 (2005).

[207] D. E. Pelinovsky and and P. G. Kevrekidis, Variational Approximations of Trapped Vortices in the Large-Density Limit, *Nonlinearity* **24**, 1271 (2011).

[208] M. Juan and X. Ju-Kui, Superfluid Fermi Gases in a Rotating Anharmonic Trap, *Commun. Theor. Phys.* **55** 434 (2011).

[209] T. Mizushima and K. Machida, Vortex Structures and Zero-Energy States in the BCS-to-BEC Evolution of P-Wave Resonant Fermi Gases, *Phys. Rev. A* **81**, 053605 (2010).

[210] A. J. Allen, E. Zaremba, C. F. Barenghi, and N. P. Proukakis, Observable Vortex Properties in Finite Temperature Bose Gases, *Phys. Rev. A.* **87**, 013630 (2013).

[211] A. L. Fetter and J. D. Walecka, *Quantum Theory of Many-Particle Systems* (McGraw-Hill, San Francisco, 1971).

[212] D. A. W. Hutchinson, E. Zaremba, and A. Griffin, Finite Temperature Excitations of a Trapped Bose Gas, *Phys. Rev. Lett.* **78**, 1842 (1997).

[213] N. P. Proukakis, Microscopic Mean Field Theories of Trapped Bose-Einstein Condensates, DPhil thesis, New College, University of Oxford (1997).

[214] F. Dalfovo, S. Giorgini, L. P. Pitaevskii, and S. Stringari, Theory of Bose-Einstein Condensation in Trapped Gases, *Rev. Mod. Phys.* **71**, 463 (1999).

[215] E. Braaten, H.-W. Hammer, and T. Mehen, Dilute Bose-Einstein Condensate with Large Scattering Length, *Phys. Rev. Lett.* **88**, 040401 (2002).

[216] P. A. Altin, G. R. Dennis, G. D. McDonald, D. Döring, J. E. Debs, J. D. Close, C. M. Savage, and N. P. Robins, Bose-nova and Three-Body loss in a Rb-85 Bose-Einstein Condensate, *Phys. Rev. A* **84**, 033632 (2011).

[217] V. Efimov, Weakly-Bound States of Three Resonantly-Interacting Particles, *Sov. J. Nucl. Phys.* **12**, 589 (1971).

[218] V. Efimov, Low-Energy Properties of Three Resonantly Interacting Particles, *Sov. J. Nucl. Phys.* **29**, 546 (1979).

[219] E. Braaten and A. Nieto, Quantum Corrections to the Energy Density of a Homogeneous Bose Gas, *Eur. Phys. J. B* **11**, 143 (1999).

[220] A. Bulgac, Dilute Quantum Droplets, *Phys. Rev. Lett.* **89**, 050402 (2002).

[221] J. Javanainen, Noncondensate Atoms in a Trapped Bose Gas, *Phys. Rev. A* **54**, R3722 (1996).

[222] A. Griffin, T. Nikuni, and E. Zaremba, *Bose-Condensed Gases at Finite Temperature* (Cambridge University Press, Cambridge, 2009).

[223] A. Griffin, Conserving and Gapless Approximations for an Inhomogeneous Bose Gas at Finite Temperatures, *Phys. Rev. B* **53**, 9341 (1996).

[224] M. Imamović-Tomasović, and A. Griffin, Coupled Hartree-Fock-Bogoliubov Kinetic Equations for a Trapped Bose Gas, *Phys. Rev. A* **60**, 494 (1999).

[225] S. Giorgini, Collisionless Dynamics of Dilute Bose Gases: Role of Quantum and Thermal Fluctuations, *Phys. Rev. A* **61**, 063615 (2000).

[226] A. Minguzzi and M. P. Tosi, Linear Density Response in the Random-Phase Approximation for Confined Bose Vapours at Finite Temperature, *J. Phys.: Cond. Matter* **9**, 10211 (1997).

[227] E. Hodby, O. M. Maragò, G. Hechenblaikner, and C. J. Foot, Experimental Observation of Beliaev Coupling in a Bose-Einstein Condensate, *Phys. Rev. Lett.* **86**, 2196 (2001).

[228] D. Borzov, M. S. Mashayekhi, S. Zhang, J.-L. Song, and F. Zhou, Three-Dimensional Bose Gas Near a Feshbach resonance, *Phys. Rev. A* **85**, 023620 (2012).

[229] E. A. Donley, N. R. Claussen, S. L. Cornish, J. L. Roberts, E. C. Cornell, and C. E. Wieman, Dynamics of Collapsing and Exploding Bose-Einstein Condensates, *Nature* **412**, 295 (2001).

[230] N. R. Claussen, E. A. Donley, S. T. Thompson, and C. E. Wieman, Microscopic Dynamics in a Strongly Interacting Bose-Einstein Condensate, *Phys. Rev. Lett.* **89**, 010401 (2002).

[231] K. Staliunas, S. Longhi, and G. J. de Valcárcel, Faraday Patterns in Bose-Einstein Condensates, *Phys. Rev. Lett.* **89**, 210406 (2002).

[232] S. K. Adhikari, Resonance in Bose-Einstein Condensate Oscillation From a Periodic Variation in Scattering Length, *J. Phys. B* **36**, 1109 (2003).

[233] F. K. Abdullaev, R. M. Galimzyanov, M. Brtka, and R. A. Kraenkel, Resonances in a Trapped 3D Bose-Einstein Condensate Under Periodically Varying Atomic Scattering Length, *J. Phys. B* **37**, 3535 (2004).

[234] F. K. Abdullaev and J. Garnier, Collective Oscillations of One-Dimensional Bose-Einstein Gas in a Time-Varying Trap Potential and Atomic Scattering Length, *Phys. Rev. A* **70**, 053604 (2004).

[235] N. N. Bogoliubov and Y. A. Mitropolsky, *Asymptotic Methods in the Theory of Non-Linear Oscillations* (Gordon and Breach, New York, 1961).

[236] N. Minorsky, *Nonlinear Oscillation* (Van Nostrand, Princeton, 1962).

[237] R. Mickens, *Introduction to Nonlinear Oscillations* (Cambridge University Press, Cambridge, 1981).

[238] A. Pelster, H. Kleinert, and M. Schanz, High-Order Variational Calculation for the Frequency of Time-Periodic Solutions, *Phys. Rev. E* **67**, 016604 (2003).

[239] A. I. Nicolin, R. Carretero-González, and P. G. Kevrekidis, Faraday Waves in Bose-Einstein Condensates, *Phys. Rev. A* **76**, 063609 (2007).

[240] L. Salasnich, A. Parola, and L. Reatto, Dimensional Reduction in Bose-Einstein Condensed Alkali-Metal Vapors, *Phys. Rev. A* **69**, 045601 (2004).

[241] D. Leibfried, R. Blatt, C. Monroe, and D. Wineland, Quantum Dynamics of Single Trapped Ions, *Rev. Mod. Phys.* **75**, 281 (2003).

[242] Mathematica symbolic calculation software package `http://www.wolfram.com/mathematica`.

[243] SCL BEC MATHEMATICA codes, `http://www.scl.rs/scl-research/codes/321`

[244] P. Muruganandam and S. K. Adhikari, Fortran Programs for the Time-Dependent Gross-Pitaevskii Equation in a Fully Anisotropic Trap, *Comp. Phys. Comm.* **180**, 1888 (2009).

[245] A. Bogojević, A. Balaž, and A. Belić, Systematically Accelerated Convergence of Path Integrals, *Phys. Rev. Lett.* **94**, 180403 (2005).

[246] P. Muruganandam and S. K. Adhikari, Fortran Programs for the Time-Dependent Gross-Pitaevskii Equation in a Fully Anisotropic Trap, *Comput. Phys. Commun.* **180**, 1888 (2009).

[247] A. Balaž, A. Bogojević, I. Vidanović, and A. Pelster, Recursive Schrödinger Equation Approach to Faster Converging Path Integrals, *Phys. Rev. E* **79**, 036701 (2009);

[248] A. Balaž, I. Vidanović, A. Bogojević, and A. Pelster, Ultra-Fast Converging Path-Integral Approach for Rotating Ideal Bose-Einstein Condensates, *Phys. Lett. A* **374**, 1539 (2010);

[249] W. Kohn, Cyclotron Resonance and de Haas-van Alphen Oscillations of an Interacting Electron Gas, *Phys. Rev.* **123**, 1242 (1961).

[250] A. L. Fetter and D. Rokhsar, Excited States of a Dilute Bose-Einstein Condensate in a Harmonic Trap, Phys. *Rev. A* **57**, 1191 (1998).

[251] E. Zaremba, T. Nikuni, and A. Griffin, Dynamics of Trapped Bose Gases at Finite Temperature, *J. Low Temp. Phys.* **116**, 277 (1999).

[252] M. J. Bijlsma and H. T. C. Stoof, Collisionless Modes of a Trapped Bose Gas, *Phys. Rev. A* **60**, 3973 (1999).

[253] J. Reidl, G. Bene, R. Graham, and P. Szépfalusy, Kohn Mode for Trapped Bose Gases within the Dielectric Formalism, *Phys. Rev. A* **63**, 043605 (2001).

[254] A. Minguzzi, Sum Rule for the Dynamical Response of a Confined Bose-Einstein Condensed Gas, *Phys. Rev. A* **64**, 033604 (2001).

[255] A. Banerjee, Dipole Oscillations of a Bose-Fermi Mixture: Effect of Unequal Masses of Bose and Fermi Particles, *J. Phys. B: At. Mol. Opt. Phys.* **42**, 235301 (2009).

[256] J.-Y Zhang, S.-C. Ji, Z. Chen, L. Zhang, Z.-D. Du, B. Yan, G.-S. Pan, B. Zhao, Y.-J. Deng, H. Zhai, S. Chen, and J.-W. Pan, Collective Dipole Oscillations of a Spin-Orbit Coupled Bose-Einstein Condensate, *Phys. Rev. Lett.* **109**, 115301 (2012).

[257] Y. Li, G. I. Martone, and S. Stringari, Sum Rules, Dipole Oscillation and Spin Polarizability of a Spin-Orbit Coupled Quantum Gas, *Euro. Phys. Lett.* **99**, 56008 (2012).

[258] F. Ferlaino, R. J. Brecha, P. Hannaford, F. Riboli, G. Roati, G. Modugno, and M. Inguscio, Dipolar Oscillations in a Quantum Degenerate Fermi-Bose Atomic Mixture, *J. Opt. B: Quantum Semiclass. Opt.* **5**, S3 (2003).

[259] S. Chiacchiera, T. Macrì, and A. Trombettoni, Dipole Oscillations in Fermionic Mixtures, *Phys. Rev. A* **81**, 033624 (2010).

[260] P. A. Altin, N. P. Robins, D. Döring, J. E. Debs, R. Poldy, C. Figl, and J. D. Close, ^{85}Rb Tunable-Interaction BoseEinstein Condensate Machine, *Rev. Sci. Instrum.* **81**, 063103 (2010).

[261] H. Al-Jibbouri and A. Pelster, Breakdown of Kohn Theorem Near Feshbach Resonance in Magnetic Trap, *Phys. Rev. A* **88**, 033621 (2013).

[262] A. J. Moerdijk, B. J. Verhaar, and A. Axelsson, Resonances in Ultracold Collisions of ^{6}Li, ^{7}Li, and ^{23}Na, *Phys. Rev. A* **51**, 4852 (1995).

[263] T. Esslinger, I. Bloch, and T. W. Hänsch, Bose-Einstein Condensation in a Quadrupole-Ioffe-Configuration Trap, *Phys. Rev. A* **58**, R2664 (1998).

[264] C. Chin, R. Grimm, P. Julienne, and E. Tiesinga, Feshbach Resonances in Ultracold Gases, *Rev. Mod. Phys.* **82**, 1225 (2010).

[265] S. Yi and L. You. Expansion of a Dipolar Condensate, *Phys. Rev. A* **67**, 045601 (2003).

[266] H. Kleinert and V. Schulte-Frohlinde, *Critical Properties of* Φ^4*-Theories*, (World Scientific, Singapore, 2001).

[267] B. Pasquiou, E. Maréchal, G. Bismut, P. Pedri, L. Vernac, O. Gorceix, and B. Laburthe-Tolra, Spontaneous Demagnetization of a Dipolar Spinor Bose Gas in an Ultralow Magnetic Field, *Phys. Rev. Lett.* **106**, 255303 (2011).

[268] E. Hodby, G. Hechenblaikner, S. A. Hopkins, O. M. Marag'o, and C. J. Foot, Vortex Nucleation in Bose-Einstein Condensates in an Oblate, Purely Magnetic Potential, *Phys. Rev. Lett.* **88**, 010405 (2002).

[269] V. L. Ginzburg and L. P. Pitaevskii, On the Theory of Superfluidity, *Sov. Phys. JETP* **7**, 858 (1958).

[270] N. Zöller, A Single Vortex in a Bose-Einstein Condensate, Bachelor thesis, Freien Universität Berlin (2010).

[271] E. A. de Lima Henn, Ph.D. thesis, Instituto de Física de São Carlos, Universidade de São Paulo, São Carlos (2008).

[272] R. P. Teles, V. S. Bagnato, and F. E. A. dos Santos, Coupling Vortex Dynamics with Collective Excitations in Bose-Einstein Condensates, `arXiv:1306.2534`.

[273] E. Lundh, C. J. Pethick, and H. Smith. Vortices in Bose-Einstein-Condensed Atomic Clouds, *Phys. Rev. A* **58**, 4816 (1998).

Acknowledgments

First and foremost, I would like to express my sincere gratitude to my supervisor Priv.-Doz. Dr. Axel Pelster for his supervision and helpful advices throughout the study, as well as his sound mathematical education, his permanent desire to explain and, not at least, his everlasting good mood are a few characteristics, which are of great value for a PhD student. He is always happy to discuss new ideas, and has a wonderful ability of pointing out the important and interesting aspects of a scientific work.

The opportunity to work in the group of Prof. Dr. Dr. h.c. mult. Hagen Kleinert has been both an honor and a privilege. His wide interest in physics is responsible for creating an intense interchange of ideas.

Most deeply, I would like to acknowledge the help from my co-advisor, Prof. Dr. Jürgen Bosse. In particular, I would like to mention his critical reading of this manuscript, as well as the support letters for extending the PhD scholarship.

I would also like to express grateful thanks to my collaborators, Dr. Antun Balaž and Dr. Ivana Vidanović from the Scientific Computer Laboratory (SCL) Institute of Physics, University of Belgrade, Serbia for their substantial help and contribution to various numerical aspects of my studies.

I am greatly indebted to Jürgen Dietel, Aristeu Lima, Victor Bezerra, Ednilson Santos, Mohammad Mobarak, Mahmoud Ghabour, Christine Gruber, Javed Akram, and Branko Nikolić. I really would like to thank them.

I would like to acknowledge the financial support from German Academic Exchange Service and Ministry of Higher Education and Scientific Research Iraq (DAAD/MoHESRI). I am specially indebted to Ms. Sandra Wojciechowski for her kind help throughout the period of the DAAD-scholarship. I would like to express my sincere gratitude to the Iraqi cultural attaché in Berlin. I would like to thank, Department of Chemistry, College of Science, Al-Qadisiyah University, Iraq, for all the help they rendered me during my study.

I would like to thank my parents, who have given me more love, support and affection than I ever deserved, I hope this thesis evidences that all these years spent thousands of miles from home have been spent somehow wisely. Most deeply, I am grateful to my dear wife Shurooq. I would like to say that your love makes everything worthwhile.